Ion Synthesis of Copper Nanoparticles in Sapphire and Their Modification by High-Power Excimer Laser Pulses: A Review

A. L. Stepanov

Institute of Physics, Erwin Schrödinger Institute for Nanoscale Research,
Karl-Franzens-University, A-8010 Graz, Austria
e-mail: andrey.stepanov@uni-graz.at

Zavoĭskiĭ Physicotechnical Institute, Kazan Scientific Center, Russian Academy of Sciences,
Sibirskiĭ trakt 10/7, Kazan 29, 420029 Tatarstan, Russia
e-mail: anstep@kfti.knc.ru

Received February 16, 2004

Abstract—Composite layers made in sapphire by implantation of 40-keV Cu^+ ions at a dose of 1×10^{17} cm^{-2} and an ion beam current density varying from 2.5 to 10 μA/cm^2 are studied. It is shown that ion implantation makes it possible to synthesize a composite layer containing copper nanoparticles at the surface of the insulator. However, the nanoparticle size distribution in this layer is nonuniform. The composite layer is exposed to high-power excimer laser radiation with the aim of modifying the size and size distribution of the metal nanoparticles in it. The resulting structures are examined by Rutherford backscattering, optical reflection spectroscopy, and atomic force microscopy. It is found that the laser irradiation diminishes copper nanoparticles in the composite layer. Experimental data on laser modification may be explained by photofragmentation and/or melting of the nanoparticles in the sapphire matrix under the action of nanosecond laser pulses. © 2005 Pleiades Publishing, Inc.

INTRODUCTION

Composite materials, such as insulators with metal nanoparticles (MNPs) embedded in them, are promising optoelectronic materials. An example of their application in optoelectronics is a pilot chip that integrates metallic wires as conductors of electric signals with fibers as guides of optical signals. In practice, light guides are frequently made of synthetic sapphire (Al_2O_3) or silicon oxide, which are applied on or buried in semiconductor substrates. In this case, optical emitters and electrooptic detectors that accomplish electric-to-optic signal conversion are fabricated inside the insulating layer. The light signal from a microlaser is focused on a light guide and then transmitted through the optoelectronic chip to a high-speed photodetector, which converts the photon flux to a flux of electrons. It is expected that light guides used instead of metallic conductors will improve the data rate by at least two orders of magnitude. Moreover, there is good reason to believe that optical elements will reduce the energy consumption and heat dissipation, since metallic or semiconductor components of the circuits may be replaced by insulating ones in this case. Pilot optoelectronic chips currently available are capable of handling data streams with a rate of 1 Gbit/s, with 5 Gbit/s in sight.

Key elements of dielectric waveguides are nonlinear optical switches, which must provide conversion of laser pulses as short as several pico- or even femtoseconds. It is known [1, 2] that MNP-containing insulators have a giant third-order nonlinear susceptibility. Because of this, their refractive index changes even if the time of action is ultrashort. Therefore, such materials may be used to advantage in integrated optoelectronic devices. Among the many methods of MNP synthesis in insulators, such as magnetron sputtering, the convective method, ion exchange, sol–gel deposition, etc., ion implantation (II) seems to be the most promising [3, 4]. Today, II is widely used in semiconductor chip fabrication. Using II for MNP synthesis, researchers have reached the highest filling factors for metal atoms embedded in an insulating matrix above the solubility limit. Furthermore, nearly any metal–insulator composition may be fabricated using II. Finally, this method allows for strict control of the doping ion beam position on the sample surface and dopant dose (for example, at ion-beam lithography).

The history of insulator–MNP composites made by II dates back to 1973, when a team of researchers at Lyons University (France) pioneered a method of synthesizing particles of various metals (silver, sodium, calcium, etc.) in LiF and MgO ionic crystals [5, 6]. Later, MNPs were successfully synthesized in various materials, such as polymers, glass, artificial crystals, and minerals. In this work, we consider the formation of MNPs in synthetic sapphire (Al_2O_3), since this material as an MNP-containing insulating matrix has been studied to a much smaller degree than standard waveguide materials, e.g., silicon dioxide.

As follows from the currently available publications concerning ion synthesis of MNPs in Al_2O_3 [7–50] (see

Types of metal nanoparticles and conditions for their synthesis in Al_2O_3 by ion implantation combined with post-implantation heat treatments

Particle type	Matrix type	Radiation energy, keV	Ion dose, cm^{-2}	Current density, $\mu A/cm^2$	Matrix temperature, °C	Postimplantation heat treatment	Particle identification techniques	Refs.
α-Fe	α-Al_2O_3 [0001]	100 160	4.0×10^{16} 7.0×10^{16} 2.0×10^{17}		−200 25		TEM, XRD, CEMS	McHargue *et al.* 1987 [7] 1990 [8] 1991 [9] 1996 [10] 1998 [11]
α-Fe	α-Al_2O_3 [0001]	400	1.0×10^{17}		240	Vacuum annealing at 700–1200°C for 1 h	TEM, XRD VSM	Ohkubo *et al.* 1987 [12] 1989 [13]
α-Fe	α-Al_2O_3 [0001]	160	4.0×10^{16}		45	Annealing in Ar + 4% H_2 at 1500°C for 1 h		Farlow *et al.* 1990 [14]
α-Fe	α-Al_2O_3 polycrist.	110	1.0×10^{17}	10	25		TEM	Donnet *et al.* 1991 [15]
α-Fe	α-Al_2O_3 [0001]	160	1.0×10^{17}	2	25			Sklad *et al.* 1992 [16]
Fe	α-Al_2O_3 policrist.	60	0.2–1.2×10^{17}	2				Jang *et al.* 1997 [17]
Fe	Al_2O_3 [0001]	85	4.0×10^{16} 7.0×10^{16} 1.0×10^{17}	10–15	25		RM	Kobayashi *et al.* 1998 [18]
Fe	Al_2O_3	380	1.0×10^{17} 4.0×10^{17} 1.0×10^{18}	2			RM	Kobayashi *et al.* 1998 [19]
α-Fe	α-Al_2O_3	100	1.0–2.0×10^{17}	2–3	25		CEMS	Sakamoto *et al.* 1999 [20] Hayashi *et al.* 2002 [21] Wakabayashi *et al.* 2002 [22]
Fe	α-Al_2O_3 [0001] [1120]	160	1.0×10^{17} 4.0×10^{17}		25		TEM, GIXRD, VSM	Alves *et al.* 2002 [23]
Fe	α-Al_2O_3	160	1.0×10^{17} 4.0×10^{17}					Monteiro *et al.* 2002 [24]

Particle type	Matrix type	Radiation energy, keV	Ion dose, cm^{-2}	Current density, μA/cm^2	Matrix temperature, °C	Postimplantation heat treatment	Particle identification techniques	Refs.
Fe	Al$_2$O$_3$	350	1.0×10^{17}		−200	Annealing in Ar + 4% H$_2$ at 1100°C for 2 h	XRD	White et al. 2003 [25]
					25		TEM, SQUID	
Co	α-Al$_2$O$_3$	20	$0.5–5.0 \times 10^{17}$		25			Saito et al. 1991 [26]
Co	α-Al$_2$O$_3$ ⟨0001⟩ ⟨0221⟩ ⟨1120⟩	150	5.0×10^{17}		25		SQUID, RS	Marques et al. 2001 [27] 2002 [28]
Co	Al$_2$O$_3$	140	8.0×10^{16}		25	Annealing in Ar + 4% H$_2$ at 1100°C for 2 h	TEM, XRD, SQUID	Meldrum et al. 2003 [29]
					−100			
Ni	α-Al$_2$O$_3$ [0001]	160	4.0×10^{16}		45	Annealing in Ar + 4% H$_2$ at 1500°C for 1 h		Farlow et al. 1990 [14]
Ni	Al$_2$O$_3$ [1120]	3000	1.6×10^{18}	1	20–250		RM	Kobayashi et al. 1996 [30]
Ni	α-Al$_2$O$_3$	64	1.0×10^{17}	0.5			TEM, XRD	Xiang et al. 2004 [31]
Cu	α-Al$_2$O$_3$ polycrist.	110	1.0×10^{17}	10	25		TEM	Donnet et al. 1991 [15]
Cu	α-Al$_2$O$_3$	160	$0.2–2.0 \times 10^{17}$	<2		Annealing in air at 673°C for 1 h		Ila et al. 1998 [32]
Cu	Al$_2$O$_3$	2100	1.0×10^{17}		−170	Vacuum annealing at 770–1270°C for 1 h		Ikeyama et al. 2001 [33] 2002 [34]
Cu	Al$_2$O$_3$	40	1.0×10^{17}	2.5–10	25		RS, AFM	Stepanov et al. 2001 [35] 2002 [36]
Zr	α-Al$_2$O$_3$ polycrist.	110	1.0×10^{17}	10	25		TEM, XRD	Donnet et al. 1991 [15]
Pd	α-Al$_2$O$_3$ polycrist.	2	$1.0–5.0 \times 10^{16}$	0.5			XPS	Battaglin et al. 1999 [37]
				1.0				
Ag	Al$_2$O$_3$	50	$4.0–19.0 \times 10^{16}$	1–5	25		RS	Rahmani et al. 1988 [38]
					−200			Rahmani, Townsend 1989 [39]

Table. (Contd.)

Particle type	Matrix type	Radiation energy, keV	Ion dose, cm^{-2}	Current density, $\mu A/cm^2$	Matrix temperature, °C	Postimplantation heat treatment	Particle identification techniques	Refs.
Ag	Al_2O_3	1500	$0.2–2.0 \times 10^{17}$	<2		Annealing in air at 773°C for 1 h		Ila *et al.* 1998 [32]
Ag	Al_2O_3	25–30	$0.2–2.0 \times 10^{17}$	0.6–6.2	25			Steiner *et al.* 1998 [40]
Sn	Al_2O_3	160	$0.2–2.0 \times 10^{17}$	<2		Annealing in air at 773°C for 1 h		Ila *et al.* 1998 [32]
Pt	Al_2O_3 [0001]	160	5.0×10^{16}	0.4	25			Alves *et al.* 1999b [41]
Pt	Al_2O_3	910	8.2×10^{16}		200	Annealing in Ar + 4% H_2 at 1100°C for 2 h	XRD, TEM, SQUID	White *et al.* 2003 [25]
Au	Al_2O_3 [0001]	400	6.8×10^{16}		1200		TEM	Ohkubo, Suzuki 1988 [42]
Au	Al_2O_3 [0001]	2750	2.2×10^{16}			Annealing in Ar + 4% H_2 at 1100°C for 1 h		Henderson *et al.* 1995 [43]
Au	Al_2O_3	2000	$0.2–2.0 \times 10^{17}$	<2		Annealing in air at 973–1323°C for 1 h		Ila *et al.* 1998 [32]
Au	Al_2O_3	160	1.0×10^{17}				RS	Marques *et al.* 2004 [44]
Eu	Al_2O_3	400	1.0×10^{16}	8 16	34	Annealing in air at 1200°C for 1 h		Can *et al.* 1994 [45] 1995 [46]
FeCo	α-Al_2O_3	100	$1.0–2.0 \times 10^{17}$	2–3	25		CEMS VSM, MR	Sakamoto *et al.* 1999 [20] Hayashi *et al.* 2002 [21] 2003 [47]
FePt	α-Al_2O_3	Fe 350 Pt 910	Fe 1.0×10^{17} Pt $0.5–1.1 \times 10^{17}$		Fe 200–550 Pt 200, 500	Annealing in Ar + 4% H_2 at 1100°C for 2 h	SQUID, TEM XRD	Vallet *et al.* 2002 [48] White *et al.* 2002 [49] 2003 [25] Withrow *et al.* 2003 [50]

Notes: Here, TEM stands for transmission electron microscopy; XPS, for X-ray photoelectron spectroscopy; CEMS, for conversion electron Mössbauer spectroscopy; VSM, for vibrating sample magnetometry; MR, for magnetoresistance measurements; and RM, for resistive measurements (for the other abbreviations, see the text). The ions are listed in the order they follow in the periodic table of elements.

table), this matrix as a basis for a composite was of interest for a long time. The table lists the types of MNPs and conditions of their synthesis directly by II or by II combined with heat treatments. While MNP synthesis in Al_2O_3 has been extensively explored, there are only few studies [15, 32–36, 38–40, 42, 43] devoted to the synthesis of noble metal particles, which are the most effective in terms of nonlinear optical properties.

For nonlinear optics, copper, which is optically close to noble metals, is the most preferable material [1, 2]. However, as follows from the table, II synthesis of copper nanoparticles in Al_2O_3 without using auxiliary postimplantation heat treatments has not been implemented up to now. The feasibility of creating composites by implantation of low-energy (<100 keV) copper ions into a single-crystal sapphire substrate was demonstrated only recently [35, 36]. It should be noted that the early attempts to create composites by irradiating Al_2O_3 by high-energy (130 keV–2.4 MeV) copper ions [51–55] failed (copper particles did not form); therefore, those works are omitted from the table. Subsequent heat treatment of the substrates irradiated by high-energy ions causes, along with the formation of copper nanoparticles [33, 34], the growth of copper oxide particles and $CuAl_2O_4$ spinel phase. Of special interest is work [15], where copper nanoparticles were synthesized in polycrystalline Al_2O_3 by moderate-energy (110 keV) implantation. However, the polycrystalline state of sapphire is strongly different from the single-crystalline one: an elevated density of structure defects, specifically, grain (domain) boundaries, in the former radically changes the MNP synthesis conditions. Therefore, though mentioned in the table, work [15] is beyond the scope of this review.

Thus, this review covers publications devoted to II synthesis of copper nanoparticles of a desired size in a sapphire substrate. Since the linear and nonlinear optical properties of MNPs are directly related to their sizes [56], one may control the optical performance of a composite as a whole by controllably varying the MNP size and MNP size distribution. One way of changing the particle size distribution while keeping a high value of the filling factor is to anneal the composite by high-power excimer laser pulses [57–63].

Emphasis in this work will be on modification of II-synthesized MNPs in Al_2O_3 by exposing the composite to laser radiation.

EXPERIMENTAL

As substrates, we used thin sheets of synthetic polycrystalline sapphire, which offers a high optical transparency in the spectral range 200–1000 nm. The plane exposed to radiation was (1012). The implanted species were 40-keV Cu^+ ions with a dose of 1×10^{17} cm^{-2} and an ion beam current density varying from 2.5 to 12.5 μA/cm^2. Experiments were carried out in an ILU-3 implanter under a pressure of 10^{-5} Torr. Prior to implan-

tation, the substrate was kept at room temperature; in the course of implantation, it was continuously cooled by running water. The samples were analyzed by Rutherford backscattering (RBS) (the energy of $^4He^+$ ions is 2 MeV) on a van de Graaf accelerator. The RBS spectra were converted to copper ion profiles across the Al_2O_3 substrate using the Data Furnace computer program [64]. Optical reflection spectra were recorded with a Monolight one-beam fiber-optic device in the range 380–800 nm at normal incidence of the radiation on the sample. The optical transmission in the range 200–1000 nm was measured with a Perkin Elmer Lambda 19 two-beam spectrophotometer.

After implantation, the Al_2O_3 substrate was subjected to 25-ns-wide pulses from an ALTEX-210 248-nm krypton excimer laser. The pulse repetition rate was 1 Hz, and the total energy was 0.3 J/cm^2 per pulse. The energy variation from pulse to pulse was no more than 2%, as indicated by a DGX FL150A-EX-RP laser energy meter. To improve the laser radiation uniformity, the light beam, before normal incidence on the sample surface, was passed through a circular diaphragm of diameter 2 mm. Immediately before the irradiation by light, which was carried out in air, the substrate was kept at room temperature. Since the irradiation area was small (the light beam was limited by the diaphragm), it was analyzed only by means of optical reflection spectroscopy (RS).

The ion-implanted substrates and those irradiated by the laser were imaged in a Solver-P4 scanning probe microscope operating in the atomic force mode. Imaging was accomplished in the vibration mode, and the vibration amplitude of the sensitive microprobe near the resonance frequency varied from 10 to 100 nm. When the sample surface was scanned line by line, the vertical displacement of the microprobe was detected with a low-intensity laser beam reflecting from the analyzing tip. The surface profile was recorded in the tapping mode. The measurements were performed in air.

LOW-ENERGY ION IMPLANTATION

Ion implantation is a most efficient method of modifying a several-micrometer-thick surface layer by embedding the elementary impurity [3]. The degree of modification depends on the material properties and II parameters, such as the type and energy of an implant, ion current density, substrate temperature, etc. Ion dose F_0, which specifies the implant amount, is one of the basic implantation parameters. According to the impact ion implantation has on insulators being modified, it can be divided into high-dose and low-dose processes (Fig. 1).

In the case of low-dose II ($\sim F_0 \le 5 \times 10^{14}$ cm^{-2}), the ions implanted, after stopping and thermalization, are dispersed throughout the volume of the insulator and are well isolated from each other. The energy of the implant is transferred to the matrix via electron shell
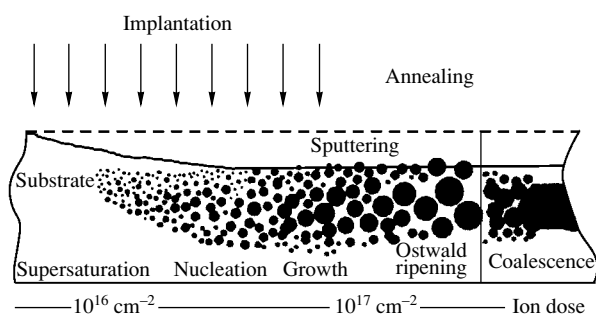
Fig. 1. Basic physical processes (from left to right) involved in the formation of nanoparticles from an implant vs. the ion dose with regard to surface sputtering under irradiation.
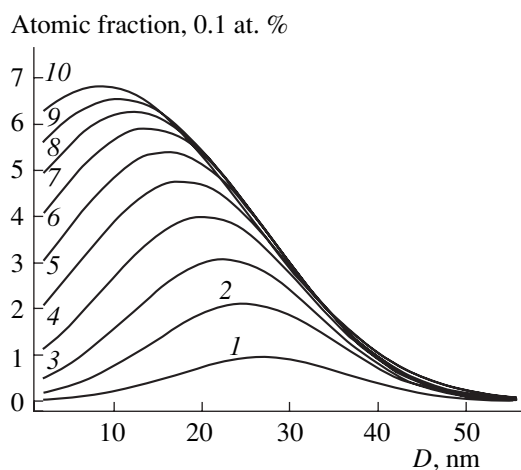

Fig. 2. 40-keV Cu^+ ion profiles in Al_2O_3 calculated with the DYNA algorithm for ion doses of (*1*) 0.1×10^{15}, (*2*) 0.3×10^{15}, (*3*) 0.6×10^{15}, (*4*) 0.9×10^{15}, (*5*) 1.2×10^{15}, (*6*) 1.5×10^{15}, (*7*) 1.8×10^{15}, (*8*) 2.1×10^{15}, (*9*) 2.4×10^{15}, and (*10*) 2.7×10^{15} cm^{-2}. D is the distance inward to the substrate.

excitation (ionization) and nuclear collisions, which induce defects (to radiation-induced defects, one may refer extended and point defects, amorphization and local crystallization, precipitation of a new phase made up of host atoms or implanted ions, etc. [3]). These defects, in turn, may cause reversible and irreversible changes in the material structure. Furthermore, II may intensely sputter the surface of the insulating target, as observed in the case of Cr^+ and Ti^+ implantation into Al_2O_3 or Cu^+ implantation into the $MgAl_2O_3$ spinel matrix and SiO_2 [65, 66] (Fig. 1). Sometimes, sputtering competes with swelling, as in the case of spinels and glasses exposed to extremely high ion current beams [66] or in the case of inert gas ions embedded in polymers [67].

The range of high-dose implantation may be divided into two characteristic dose (irradiation time) subranges (Fig. 1). In the range $10^{15} \leq F_0 \leq 10^{16}$ cm^{-2}, the implant concentration exceeds the solubility limit of metal atoms in insulators (in particular, in sapphire); accordingly, MNPs nucleate and grow. The boundary dose value depends on the type of the insulator and implant. For example, for 25-keV silver ions implanted into $LiNbO_3$, the boundary dose was found to be $F_0 \approx 5.0 \times 10^{15}$ cm^{-2} [68]; for 30-keV silver ions embedded in epoxy resin, $F_0 \sim 10^{16}$ cm^{-2} [69]. The boundary dose (at which MNPs nucleate) for copper implantation into Al_2O_3 has not been reported in the literature.

The next subrange of high-dose implantation, $F_0 \geq 10^{17}$ cm^{-2}, leads to the coalescence of already existing MNPs with the formation of either MNP aggregates or thin quasi-continuous films at the surface of the insulator (Fig. 1). For example, in the case of 40-keV cobalt ions embedded in epoxy resin, a dose exceeding the above value favors the formation of thin-film metallic labyrinth structures [70]. Postimplantation thermal or laser annealing may alter the arrangement of MNPs in an insulator as a result of coalescence or Ostwald ripening [3].

The works considered in this review were aimed at studying composites consisting of the sapphire matrix with isolated copper nanoparticles; i.e., the particles were synthesized by high-dose ($F_0 \sim 10^{17}$ cm^{-2}) implantation. For the case of Cu^+ implantation with a moderate ion energy (40 keV), elastic ion energy losses prevail, which causes oxygen and aluminum atom displacements in the matrix and chemical bond breaking. It is known that implantation of various metal ions into the crystalline Al_2O_3 matrix leads to the amorphization of the ion-doped layer even at relatively low doses (on the order of 10^{15} cm^{-2}) [3, 71].

Acceleration of an implant in the matrix is a long-term process. The implant distribution in the target is routinely described with the TRIM algorithm applied to the statistical Gaussian distribution, which has a symmetric statistical profile [72]. However, as was shown earlier [73–75], the TRIM algorithm works well in describing the metal atom distribution across the insulator at low-energy II (<100 eV) only if the implantation dose is very low ($\ll 10^{15}$ cm^{-2}). This is because TRIM ignores the effect of dynamic surface sputtering (Fig. 1) and the variation of the target atomic composition with the amount of the implant accumulated. Therefore, the DYNA algorithm [76, 77] seems to be more appropriate for simulating the copper distribution in Al_2O_3. DYNA includes pair collisions of the ions with substrate atoms, thereby taking into account the variation of the phase composition in the surface layer with time because of target surface sputtering.

Figure 2 shows how the implant distribution varies with the implantation time, i.e., visualizes the copper accumulation in Al_2O_3. At low doses ($F_0 \leq 0.1 \times 10^{15}$ cm^{-2}), the DYNA- and TRIM-based distributions coincide. However, as the dose grows, the Gaussian profile changes to an asymmetric curve and the implant

concentration maximum shifts closer to the surface. From a dose of 3.0×10^{15} cm^{-2} on, the copper profile in depth of the sapphire is stabilized, i.e., becomes dose-independent. This value manifests the upper bound for the domain of applicability of the DYNA algorithm. At higher doses, the implant concentration in the surface layer will exceed the limiting solubility of copper in sapphire [3] with regard to a low ion energy (40 keV), which DYNA cannot take into account.

METAL NANOPARTICLE FORMATION BY HIGH-DOSE IMPLANTATION

Collisions of the accelerated copper ions with Al$_2$O$_3$ matrix atoms are accompanied by effective electron losses in the latter. As a result, the Cu$^+$ ions deionize with the formation of neutral copper atoms Cu^0. Basically, copper atoms may produce chemical bonds with free matrix atoms, specifically, with oxygen atoms. However, Cu–Cu bonding is energetically more favorable, as can be judged from the change in the Gibbs free energy in copper–oxygen reactions, which is also observed with silver atoms in silicate glass [77].

In view of the fact that copper atoms readily combine with each other, an excess of the copper amount over the solubility limit of copper in Al$_2$O$_3$ leads to the formation of copper nanoparticles in the ion-doped layer. As was noted earlier, the model approach based on pair atomic collisions in a homogeneous amorphous medium (which is involved in the DYNA algorithm) becomes inefficient when the insulator contains metal phase fragments [73]. Yet, the curves calculated at a low dose of 2.7×10^{15} cm^{-2} (Fig. 2) may be helpful in predicting the MNP distribution across the sample at higher doses. Consider the formation and distribution of MNPs at higher doses.

Note first of all that an increase in the absolute copper ion concentration in the depth profiles and the surface sputtering coefficient depend on the implantation time (or the time of implant accumulation) [73]. Therefore, the particle nucleation and growth are also time-dependent processes. Generally, the ion synthesis of MNPs proceeds in several steps: (i) accumulation of Cu^0 atoms in a local near-surface area of sapphire, (ii) supersaturation of this area by Cu^0 atoms, (iii) formation of nuclei consisting of several Cu^0 atoms, and (iv) growth of the nuclei. Clearly, the size of nanoparticles forming at a certain depth from the surface correlates with the filling factor for the metal in the insulator at the same depth, since both parameters depend on the ion concentration profile. Therefore, bearing in mind the asymmetric copper atom distribution obtained for the maximal dose used in the calculations (Fig. 2), one can conclude that, when this dose is exceeded and the distribution becomes asymmetric, larger copper particles (and, accordingly, higher filling factors) will be observed closer to the Al$_2$O$_3$ surface, while finer particles will penetrate deeper into the matrix.
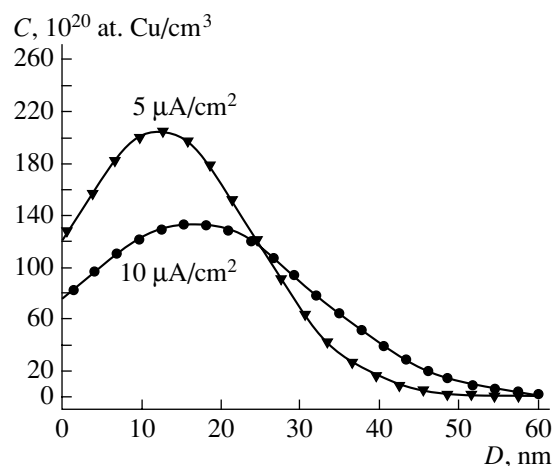
Fig. 3. RBS profiles of copper ions in Al$_2$O$_3$ at an ion dose of 10^{17} cm^{-2} and two ion beam current densities. C is the Cu ion concentration, and D is the distance inward to the substrate.

The model predictions regarding the copper distribution inward to the matrix have been corroborated experimentally. By way of example, Fig. 3 shows the RBS copper atoms profiles near the surface of the sapphire that were taken at a high (10^{17} cm^{-2}) dose. Note that the RBS method gives the distribution of only copper atoms over the volume, ignoring the possible presence of the volume metal phase. In the experimental distributions obtained at two ion current values, the copper concentration reaches a maximum near the surface, decreasing monotonically with depth down to 60 nm. This is in qualitative agreement with the curves shown in Fig. 2. The discrepancy in the positions of the maxima for two ion current values will be discussed below.

Similar distributions of MNPs in depth were also obtained in experiments on high-dose low-energy implantation of ions into other insulators, as follows from the electron microscopy data taken of the cross sections of soda–lime silicate glasses with MNPs [3, 78] or SiO$_2$ with copper particles [79] and also from the measurements of the reflection from the implanted and back sides of silicate glass substrates with silver particles [78, 80].

Figure 4 demonstrates the reflection spectra (thin curves) taken from Al$_2$O$_3$ ion-doped by Cu$^+$ ions at different ion currents. The wide reflection bands in the visible range directly indicate the formation of copper nanoparticles in the sapphire volume. The bands can be attributed to plasmon–polariton resonance (PPR) localized in the particles [56]. By comparing electron microscopic and optical data for MNPs synthesized by different techniques, it was shown that this optical resonance, which is due to collective oscillations of free electrons, is observed in the visible range when the size of copper particles lies between ≈ 2 nm and several tens of nanom-
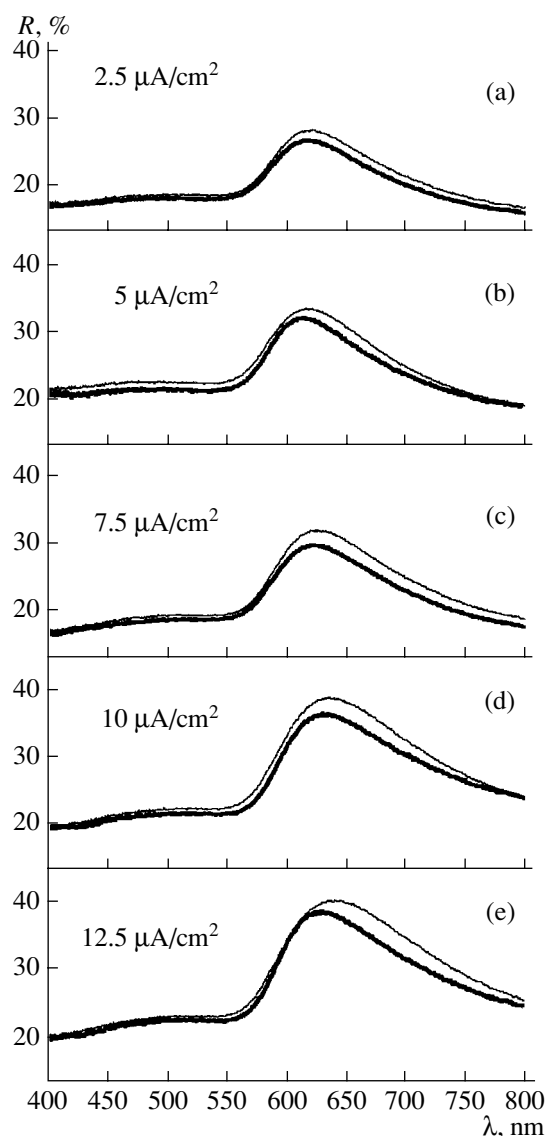
Fig. 4. Optical reflection spectra for copper-ion-implanted Al_2O_3 (thin curves) vs. ion beam current density and the spectra taken from the same samples subjected to post-implantation laser annealing (thick lines).
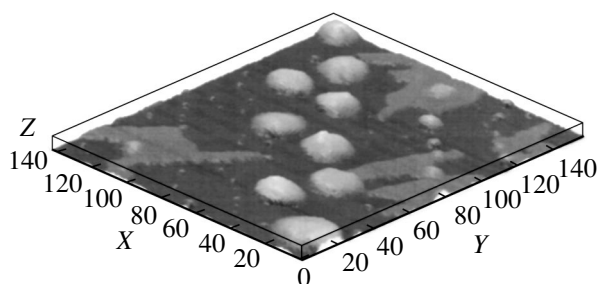

Fig. 5. AFM image of a fragment of the Al_2O_3 surface irradiated by copper ions at an ion beam current density of 7.5 $\mu A/cm^2$. The values plotted in the X and Y axes are given in nanometers. The step is the Z direction is 24 nm.

eters [56]. Such reflection spectra are typical of copper particles in an insulating matrix.

Figure 5 shows a fragment of the Al_2O_3 surface after copper implantation at an ion beam current density of 7.5 $\mu A/cm^2$. This image, obtained in an atomic force microscope (AFM), illustrates characteristic semispherical hillocks of mean size 20 nm, which are absent on the nearly smooth surface of unimplanted Al_2O_3. The hillocks seen in Fig. 5 result from surface sputtering during II and are merely the tops of MNPs having nucleated in the surface layer. It is assumed that sapphire is removed (sputtered) with a higher rate than the metallic phase. Estimates [73, 74] made for high-dose copper implantation into sapphire show that the Al_2O_3 layer sputtered may be several nanometers thick for the doses and energies considered in this work. For Cr^+ and Ti^+ implantation into sapphire (with a dose of ~10^{17} cm^{-2}), similar thicknesses of the layer sputtered from the sapphire surface were observed, as measured by photon tunnel microscopy [65]. At the same time, bare MNPs were observed on the surface after low-energy (<60 keV) high-dose implantation of Au^+ into Al_2O_3 [47] and mica [81]; Fe^+ into SiO_2 [82]; and Ag^+ into Al_2O_3, Ta_2O_3, Si_3N_4, SiO_2 [40, 83, 84], and soda–lime silicate glass [4, 85]. The metal phase on the surface was identified by glancing incidence X-ray diffraction (GIXRD) [83].

As the ion current grows, the maximum of the reflection spectrum shifts from 620 nm for 2.5 $\mu A/cm^2$ to 650 nm for 12.5 $\mu A/cm^2$ (see Fig. 4). Simultaneously, the reflection intensity increases roughly by a factor of 1.5. Generally, interaction of an electromagnetic wave with a single metal particle causes the effects of PPR absorption and scattering if the particle size is less than, or comparable to, the light wavelength [56]. In our case, the size of the largest metal particles does not exceed 20 nm (Fig. 5); therefore, the optical PPR effects dominate (Fig. 4).

The problem of extinction of light when a plane electromagnetic wave interacts with a spherical particle can be solved in terms of classical thermodynamics (the Mie theory) [86, 87]. As for fine particles of noble metals, it is known [56] that Mie spectral resonances are due to PPR effects and analytical Mie spectra may be compared with experimental data. Therefore, the Mie equations will be used to simulate the extinction spectra for copper nanoparticles in Al_2O_3 and the model spectra obtained will be compared with the experiment (Fig. 4), as was successfully done previously for silver particles synthesized in polymers by II [88]. In the calculations described below, we used the complex optical constants for Al_2O_3 [89] and copper [90] corrected for size effects (limitations imposed on the free path of electrons) observed in particles of size ranging from 1 to 200 nm (this range is somewhat wider than in Fig. 5).

The model extinction spectra versus MNP size are shown in Fig. 6, where a broad band covering most of

the visible range is seen. In the MNP size range considered, the PPR maximum shifts toward longer wavelengths with increasing particle size. Simultaneously, the intensity of the extinction band grows and the spectra somewhat broaden, which is in agreement with the changes in the experimental spectra with increasing ion current (Fig. 4). Such behavior of the reflection spectra confirms the statement that copper particles in sapphire grow with ion beam current density.

The most plausible reason for the increase in the particle size is that implantation rises the Al_2O_3 matrix temperature. For example, when low-energy Ag^+ ions were implanted into preheated (from 20 to 60°C) silicate glasses at a moderate ion current density (3 $\mu A/cm^2$ [91]), larger silver particles formed in warmer samples. This is not surprising: an increase in the temperature accelerates diffusion; that is, the mobility of the implanted metal ions rises.

As was noted earlier, the process of MNP synthesis may be subdivided into steps including the incorporation of the accelerated ions, their diffusion, and the nucleation and growth of particles. In our case, however, all the samples were kept under identical conditions (i.e., at room temperature) at the beginning of implantation. It appears that different values of the ion current density result in different rates of incorporation of copper ions into the matrix (different rates of delivery of the ion energy, which heats up Al_2O_3). Thus, we may conclude that the higher the ion current density, the higher the rate of heating of the Al_2O_3 substrate (temperature gradient) and the higher its temperature. It is safe to speak of temperature-enhanced diffusion of the metallic implants in the substrates at high-beam-current implantation. At elevated temperatures and temperature gradients in the Al_2O_3 matrix, the diffusion mobility of copper ions in it grows, the ions drain faster toward nuclei that have already formed, and the particles grow (diffusion growth). In "hot" samples, the amount of ions unattached to the particles, i.e., remaining dispersed in the implanted layer, is smaller than in "cold" ones. Ostwald ripening also may contribute to the growth of the particles: fine nuclei, which have a lower melting point, dissociate into atoms, which serve as building blocks for other (larger) particles. As a result, the total number of the particles decreases.

Under the implantation conditions used in our experiments, the matrix temperature was not so high that the extremely high-power diffusion flux of embedded copper atoms inward to the matrix could prevent particle nucleation. However, as follows from the RBS spectra in Fig. 3, the high ion current raises the copper ion mobility and the RBS spectrum becomes diffuse. In addition, its maximum slightly shifts inward to the substrate, which is one more indication that the copper ion mobility in this matrix is enhanced.

Broadening of the RBS spectrum implies a broad particle size distribution across the depth. Therefore, it would be of interest to estimate the feasibility of modi-
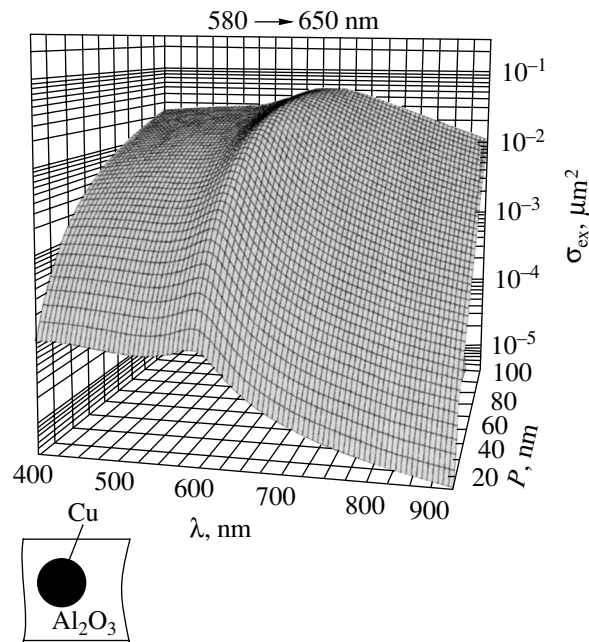

Fig. 6. Calculated spectra of optical extinction σ_{ex} for copper nanoparticles in Al_2O_3 vs. particle size P.

fying implantation-synthesized MNPs by means of laser annealing. This issue is considered in the next section.

MODIFICATION OF METAL NANOPARTICLES BY LASER ANNEALING

In earlier experiments on annealing of ion-implanted structures by an excimer laser (see review [57]), UV radiation was used, which falls into the range of strong absorption by insulators (e.g., soda–lime silicate glass containing silver particles). Such annealing usually leads to melting of the glass surface, including the implanted layer, followed by rapid solidification. As a result, the mean silver particle size diminishes, because the heat of the matrix, which intensely heats up, melts the particles. Melting is favored by a relatively low melting point of the glass used (≈750°C), application of high-power laser pulses, and also the fact that the melting point of dispersed silver is close to the melting point of the glass [57].

In this work, we apply the same approach to MNP modification using an excimer laser. However, the melting point of artificial sapphire is higher (1400°C) than that of soda–lime glass and sapphire is more transparent to 248-nm radiation (Fig. 7). Therefore, one can assume that the laser radiation absorption in sapphire is lower than in the glass and consider the annealing process as direct particle–radiation interaction irrespective of the matrix temperature.

From the spectra shown in Fig. 7, it follows that the post-implantation transmission of the Al_2O_3 matrix in
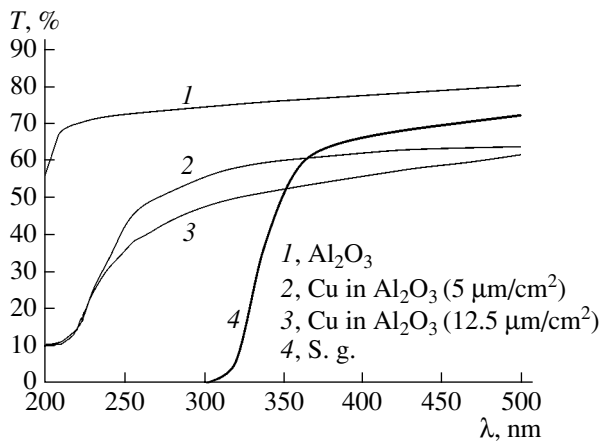
Fig. 7. Optical transmission spectra of Al_2O_3 before and after copper implantation for different values of the ion beam current density. The spectrum for nonirradiated soda–lime silicate glass (S.g.) is given for comparison.
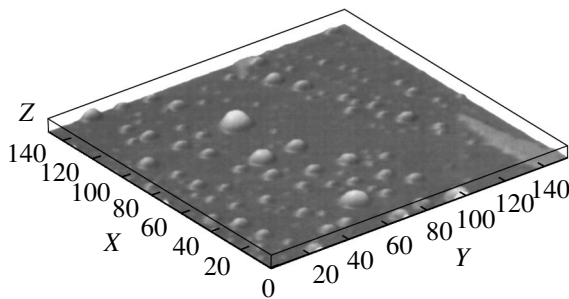

Fig. 8. AFM image of a fragment of the Al_2O_3 surface irradiated by copper ions at an ion beam current density of 7.5 $\mu A/cm^2$ and subjected to laser annealing. The values plotted in the X and Y axes are given in nanometers. The step is the Z direction is 48 nm.

the UV range decreases possibly because of defects induced by radiation [3]. Yet, the matrix remains fairly transparent (35–40%) at the laser wavelength used in the experiments (248 nm) especially versus the transmission of soda–lime glass of the same thickness. It should be noted that synthesized copper nanoparticles also absorb UV radiation due to band-band transitions just as in the bulk metal [56].

The reflection spectra taken from the implanted samples subjected to laser annealing are shown by thick lines in Fig. 4. The selective bands indicate that the nanoparticles are present in the sapphire after the annealing as well. However, in all the samples, the maxima of these reflection bands turn out to be shifted toward shorter waves and they are less high-power than in the spectra taken immediately after implantation. These changes are more pronounced in the case of high-current II; in other words, samples with large copper particles are more sensitive to laser radiation that those with fine particles, which were synthesized at low current densities.

In terms of the Mie theory, which describes the optical properties of fine metal particles (see the previous section, Fig. 6), the short-wavelength shift of the reflection maxima means that laser annealing of sapphire decreases the mean size of the particles. This conclusion is corroborated by AFM examinations. In fact, the hillocks seen in the surface image after laser annealing (Fig. 5) are smaller than those observed after the implantation (Fig. 8) by one order of magnitude.

The features of interaction between high-power laser radiation and a material depend on the laser beam parameters, physicochemical properties of the medium irradiated, and photoexcitation relaxation time. In our composite, one can distinguish the relaxation and excitation processes in the sapphire matrix and in the metal inclusions. The wavelength of the excimer laser, 248 nm, falls into the absorption edge of Al_2O_3 (Fig. 7), so that this radiation generates electron–hole pairs by direct band-to-band electron transitions. In the metal particles, the same radiation excites electrons in both the valence and conduction band. In other words, the optical energy absorbed starts heating the metal virtually at once, while in sapphire, the rate of band-to-band electron transition (i.e., the density of electron–hole pairs) increases gradually [92]. In metals, the time of electron–electron collisions is on the order of 10^{-14}–10^{-13} s and the electron–phonon relaxation takes place one or two orders of magnitude more slowly [93]. In nonmetallic materials, band-to-band electron transitions usually take from 10^{-12} to 10^{-6} s [92].

Note that the time intervals mentioned are much shorter than the duration of laser pulses (25 ns) used in this work. Therefore, although Al_2O_3 is considered as transparent to the laser radiation (Fig. 7), a fraction of the radiation is still absorbed by the sapphire matrix. However, we may roughly assume that most of the energy of the laser radiation is absorbed by the particles and the transparent substrate has no time to heat up. If so, the decrease in the metal nanoparticle size observed in the experiment (Figs. 4, 5, 7) may be due to photofragmentation [94]. This process means a decrease in the total number of the particles in the layer implanted when some of them disintegrate into atoms or tiny molecule-like clusters, which do not exhibit PPR-related absorption (Fig. 9). Clearly, large particles, which have a larger volume and cross-sectional area and, therefore, absorb a greater amount of the laser energy, are more prone to fragmentation. It is just large particles that, when disintegrated, are responsible for the reduction of the PPR band intensity and short-wavelength shift of the PPR band. Earlier, metal particle fragmentation was observed in colloidal solutions exposed to high-power picosecond or nanosecond laser shorts at wavelengths outside the PPR spectral range [94–96]. It was assumed that fragmentation takes place when the laser radiation causes electrons to move to the periphery of the particles, which thereby acquire an appreciable surface charge (Fig. 9).
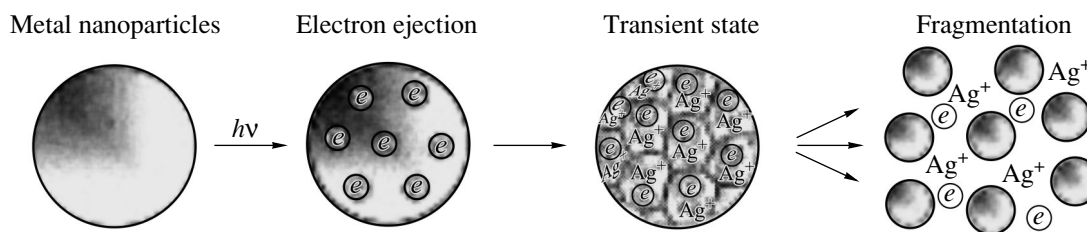
Metal nanoparticles   Electron ejection   Transient state   Fragmentation

$h\nu$

Fig. 9. Stages of silver particle fragmentation under the action of laser irradiation [94].

On the other hand, the conversion of the laser radiation in metal particles may be treated as an energy deposit (relaxation) directly into heating of the metal making up the composite. The temperature may rise to the melting point of copper particles synthesized, since it is known that the melting point of a metal particle, when in a solid matrix, may drop substantially when its size decreases to the nanometer scale [97, 98]. It was reported that the melting point of silver particles less than 50 nm in size declined to ~500°C (cf. the melting point of bulk silver, 960°C) [99, 100]. Consequently, when the temperature of the particles exceeds their melting point, they melt, diminish, and may even collapse. In general, melting of nanoparticles is a nontrivial process and its correct description requires that several sequential stages be considered: surface atom migration (surface premelting), structure fluctuations (quasi-melting), and the formation of mixed (liquid–solid) phases. The particles will collapse in steps, and finer particles will decrease faster than coarser ones. In general, a decrease in the particle size by a given melting mechanism will be reflected in the optical spectra in the same way as in photofragmentation. Therefore, it is still difficult to decide between the two mechanisms of particle decrease at laser annealing. The difference between them is that fragmentation breaks down primarily large particles, while fine particles are more prone to melting. Fragmentation seems to be a more vigorous process and possibly is responsible for the changes observed at laser annealing.

CONCLUSIONS

In this work, we experimentally demonstrate the feasibility of copper nanoparticle synthesis in a sapphire substrate at depths of several tens of nanometers, which meets the requirements for the optoelectronic IC technology. It is found that high ion beam current densities used in the implantation of Cu^+ ions into Al_2O_3 serve to increase the particle size, possibly because of substrate heating and an increase in the copper ion mobility. Basically, this effect opens the door to preparing composites with a desired size of metal particles near the sapphire surface by varying the ion current density during implantation. It is believed that application of ion implantation for MNP synthesis, which is an important step in IC technology, would cheapen opto-electronic chips combining sapphire and a semiconductor.

The irradiation of implanted materials by high-power pulses from an excimer laser decreases the mean particle size and, accordingly, the spread in particle size. Mechanisms behind the MNP modification, such as particle fragmentation and particle melting, are discussed.

The table involving the currently available data on ion synthesis of MNPs in a sapphire substrate in combination with postimplantation heat treatments and listing the relevant publications is the first published engineer's guide of this sort.

REFERENCES

1. C. Flytzanis, F. Hache, M. C. Klein, D. Recard, and P. Rousignol, *Nonlinear Optics in Composite Materials* (Elsevier, Amsterdam, 1991).

2. A. L. Stepanov, I. B. Khaĭbullin, P. Taunsend, *et al.*, RF Patent No. 2,156,490 (2000).

3. P. T. Townsend, P. J. Chandler, and L. Zhang, *Optical Effects of Ion Implantation* (Cambridge Univ. Press, Cambridge, 1994).

4. A. L. Stepanov and D. E. Hole, Recent Res. Devel. Appl. Phys. **5**, 1 (2002).

5. J. Davenas, A. Perez, P. Thevenard, and C. H. S. Dupuy, Phys. Status Solidi A **19**, 679 (1973).

6. M. Treileux, P. Thevenard, G. Ghassagne, and L. H. Hobbs, Phys. Status Solidi A **48**, 425 (1978).

7. C. J. McHargue, G. C. Farlow, P. S. Sklad, *et al.*, Nucl. Instrum. Methods Phys. Res. B **19–20**, 813 (1987).

8. C. J. McHargue, P. S. Sklad, and C. W. White, Nucl. Instrum. Methods Phys. Res. B **46**, 79 (1990).

9. C. J. McHargue, P. S. Sklad, C. W. White, *et al.*, J. Mater. Res. **6**, 2145 (1991).

10. C. J. McHargue, S. X. Ren, P. S. Sklad, *et al.*, Nucl. Instrum. Methods Phys. Res. B **166**, 173 (1996).

11. C. J. McHargue, S. X. Ren, and J. D. Hunn, Mater. Sci. Eng., A **253**, 1 (1998).

12. M. Ohkubo, T. Hioki, and J. Kawamoto, J. Appl. Phys. **62**, 3069 (1987).

13. M. Ohkubo, T. Hioki, N. Suzuki, *et al.*, Nucl. Instrum. Methods Phys. Res. B **39**, 675 (1989).

14. G. C. Farlow, P. S. Sklad, C. W. White, and C. J. McHargue, J. Mater. Res. **5**, 1502 (1990).

15. C. Donnet, G. Marest, N. Moncoffre, *et al.*, Nucl. Instrum. Methods Phys. Res. B **59–60**, 1205 (1991).

16. P. S. Sklad, C. J. McHargue, C. W. White, and G. C. Farlow, J. Mater. Sci. **27**, 5895 (1992).

17. H.-G. Jang, H.-B. Kim, J.-H. Joo, *et al.*, Nucl. Instrum. Methods Phys. Res. B **124**, 528 (1997).

18. T. Kobayashi and T. Terai, Nucl. Instrum. Methods Phys. Res. B **141**, 441 (1998).

19. T. Kobayashi, A. Nakanishi, K. Fukumura, and G. Langouche, J. Appl. Phys. **83**, 4631 (1998).

20. I. Sakamoto, S. Honda, H. Tanoue, *et al.*, Nucl. Instrum. Methods Phys. Res. B **148**, 1039 (1999).

21. N. Hayashi, T. Toriyama, H. Wakabayashi, *et al.*, Nucl. Instrum. Methods Phys. Res. B **158–159**, 193 (2002).

22. H. Wakabayashi, T. Hirai, T. Toriyama, *et al.*, Phys. Status Solidi **189**, 515 (2002).

23. E. Alves, C. MacHargue, R. C. da Silva, *et al.*, Surf. Coat. Technol. **128–129**, 434 (2002).

24. T. Monteiro, C. Boemare, M. J. Soares, *et al.*, Nucl. Instrum. Methods Phys. Res. B **191**, 638 (2002).

25. C. W. White, S. P. Withrow, K. D. Sorge, *et al.*, J. Appl. Phys. **93**, 5656 (2003).

26. Y. Saito, H. Horie, and S. Suganomata, Nucl. Instrum. Methods Phys. Res. B **59–60**, 1173 (1991).

27. C. Marques, M. M. Cruz, R. C. da Silva, and E. Alves, Nucl. Instrum. Methods Phys. Res. B **175–177**, 500 (2001).

28. C. Marques, M. M. Cruz, R. C. da Silva, and E. Alves, Surf. Coat. Technol. **158–159**, 54 (2002).

29. A. Meldrum, L. A. Boatner, and K. Sorge, Nucl. Instrum. Methods Phys. Res. B **207**, 36 (2003).

30. T. Kobayashi, T. Terai, T. Yoneoka, and S. Tanaka, Nucl. Instrum. Methods Phys. Res. B **116**, 187 (1996).

31. X. Xiang, X. T. Zu, S. Zhu, and L. M. Wang, Appl. Phys. Lett. **84**, 52 (2004).

32. D. Ila, E. K. Williams, S. Sarkisov, *et al.*, Mater. Res. Soc. Symp. Proc. **504**, 381 (1998).

33. M. Ikeyama, S. Nakao, M. Tazawa, *et al.*, Nucl. Instrum. Methods Phys. Res. B **175–177**, 652 (2001).

34. M. Ikeyama, S. Nakao, and M. Tazawa, Surf. Coat. Technol. **158–159**, 720 (2002).

35. A. L. Stepanov, U. Kreibig, D. E. Hole, *et al.*, Nucl. Instrum. Methods Phys. Res. B **178**, 120 (2001).

36. A. L. Stepanov, Pis'ma Zh. Tekh. Fiz. **28** (1), 58 (2002) [Tech. Phys. Lett. **28**, 864 (2002)].

37. G. Battaglin, R. Bertoncello, M. Casarin, *et al.*, J. Non-Cryst. Solids **253**, 251 (1999).

38. M. Rahmani, L. H. Abu-Hassan, P. D. Townsend, *et al.*, Nucl. Instrum. Methods Phys. Res. B **32**, 56 (1988).

39. M. Rahmani and P. D. Townsend, Vacuum **39**, 1157 (1989).

40. G. Steiner, M. T. Pham, C. Kuhne, and R. Salzer, Fresenius J. Anal. Chem. **362**, 9 (1998).

41. E. Alves, R. C. da Silva, O. Conde, *et al.*, Nucl. Instrum. Methods Phys. Res. B **148**, 1049 (1999).

42. M. Ohkubo and N. Suzuki, Philos. Mag. Lett. **57**, 261 (1988).

43. D. O. Henderson, R. Mu, M. A. George, *et al.*, J. Vac. Sci. Technol. B **13**, 1198 (1995).

44. C. Marques, E. Alves, R. C. da Silva, *et al.*, Nucl. Instrum. Methods Phys. Res. B **204**, 139 (2004).

45. N. Can, P. D. Townsend, and D. E. Hole, Appl. Phys. Lett. **65**, 1871 (1994).

46. N. Can, P. D. Townsend, D. E. Hole, *et al.*, J. Appl. Phys. **78**, 6737 (1995).

47. N. Hayashi, I. Sakamoto, H. Wakabayashi, *et al.*, J. Appl. Phys. **94**, 2597 (2003).

48. C. E. Vallet, C. W. White, S. P. Withrow, *et al.*, J. Appl. Phys. **92**, 6200 (2002).

49. C. W. White, S. P. Withrow, J. D. Budai, *et al.*, Nucl. Instrum. Methods Phys. Res. B **191**, 437 (2002).

50. S. P. Withrow, C. W. White, J. D. Budai, *et al.*, J. Magn. Magn. Mater. **260**, 319 (2003).

51. G. C. Farlow, P. S. Sklad, C. W. White, and C. J. McHargue, J. Mater. Res. **5**, 1502 (1990).

52. T. Miyano, T. Matsumae, Y. Yoko-o, *et al.*, Nucl. Instrum. Methods Phys. Res. B **59–60**, 1167 (1991).

53. T. Futagami, Y. Aoki, O. Yoda, and S. Nagai, Nucl. Instrum. Methods Phys. Res. B **88**, 261 (1994).

54. J. Bigarre, S. Fayeulle, D. Treheux, and N. Moncoffre, J. Appl. Phys. **82**, 3740 (1997).

55. T. Kobayashi and T. Terai, Nucl. Instrum. Methods Phys. Res. B **148**, 1059 (1999).

56. U. Kreibig and M. Vollmer, *Optical Properties of Metal Clusters* (Springer-Verlag, Berlin, 1995).

57. A. L. Stepanov, Rev. Adv. Mater. Sci. **4**, 123 (2003).

58. R. W. Wood, P. D. Townsend, N. D. Skelland, *et al.*, J. Appl. Phys. **74**, 5754 (1993).

59. A. L. Stepanov, D. E. Hole, A. A. Bukharaev, *et al.*, Appl. Surf. Sci. **136**, 298 (1998).

60. A. L. Stepanov, D. E. Hole, and P. D. Townsend, Nucl. Instrum. Methods Phys. Res. B **149**, 89 (1999).

61. A. L. Stepanov and D. E. Hole, Zh. Prikl. Spektrosk. **68**, 120 (2001).

62. A. L. Stepanov, V. N. Popok, D. E. Hole, and A. A. Bukharaev, Fiz. Tverd. Tela (St. Petersburg) **43**, 2100 (2002) [Phys. Solid State **43**, 2192 (2002)].

63. A. L. Stepanov, Philos. Mag. Lett. **82**, 149 (2002).

64. N. P. Barradas, C. Jeynes, and R. P. Webb, Appl. Phys. Lett. **71**, 291 (1997).

65. J. D. Demaree, S. R. Kirkpatrick, A. R. Kirkpatrick, and J. K. Hirvonen, Nucl. Instrum. Methods Phys. Res. B **127–128**, 603 (1997).

66. C. G. Lee, Y. Takeda, N. Kishimoto, and N. Umeda, J. Appl. Phys. **90**, 2195 (2001).

67. V. B. Odzhaev, I. P. Kozlov, V. N. Popok, and D. V. Sviridov, *Ion Implantation in Polymers* (Belarusk. Gos. Univ., Minsk, 1998) [in Russian].

68. S. Deying, Y. Saito, and S. Suganomata, Jpn. J. Appl. Phys. **33**, L966 (1994).

69. A. L. Stepanov, S. N. Abdullin, R. I. Khaibullin, *et al.*, Mater. Res. Soc. Symp. Proc. **392**, 267 (1995).

70. S. N. Abdullin, A. L. Stepanov, R. I. Khaĭbullin, *et al.*, Fiz. Tverd. Tela (St. Petersburg) **38**, 2574 (1996) [Phys. Solid State **38**, 1412 (1996)].

71. J. Bigarre, S. Fayeulle, D. Treheux, and N. Moncoffre, J. Appl. Phys. **82**, 3740 (1997).

72. J. F. Ziegel, J. P. Biersak, and U. Littmark, *The Stopping and Range of Ions in Solids* (Pergamon, New York, 1996).

73. A. L. Stepanov, V. A. Zhikharev, and I. B. Khaĭbullin, Fiz. Tverd. Tela (St. Petersburg) **43**, 733 (2001) [Phys. Solid State **43**, 766 (2001)].

74. A. L. Stepanov, V. A. Zhikharev, D. E. Hole, *et al.*, Nucl. Instrum. Methods Phys. Res. B **166–167**, 166 (2000).

75. V. M. Konoplev, Radiat. Eff. Lett. Sect. **87**, 207 (1986).

76. V. M. Konoplev, Poverkhnost **2**, 207 (1986).

77. P. W. Wang, Appl. Surf. Sci. **120**, 291 (1997).

78. L. C. Nistor, J. van Landuyt, J. D. Barton, *et al.*, J. Non-Cryst. Solids **162**, 217 (1992).

79. N. Kishimoto, N. Umeda, Y. Takeda, *et al.*, Nucl. Instrum. Methods Phys. Res. B **148**, 1017 (1999).

80. A. L. Stepanov, Opt. Spektrosk. **89**, 444 (2000) [Opt. Spectrosc. **89**, 408 (2000)].

81. D. O. Henderson, R. Mu, A. Ueda, *et al.*, J. Non-Cryst. Solids **205–207**, 788 (1996).

82. A. A. Bukharaev, V. M. Janduganov, E. A. Samarsky, and N. V. Berdunov, Appl. Surf. Sci. **103**, 49 (1996).

83. M. T. Pham, W. Matz, and H. Seifarth, Anal. Chim. Acta **350**, 209 (1997).

84. A. L. Stepanov and V. N. Popok, Pis'ma Zh. Tekh. Fiz. **29** (1), 20 (2003) [Tech. Phys. Lett. **29**, 977 (2003)].

85. A. L. Stepanov and V. N. Popok, Surf. Sci. **566–568**, 1250 (2004).

86. G. Mie, Ann. Phys. **25**, 377 (1908).

87. M. Born and E. Wolf, *Principles of Optics*, 4th ed. (Pergamon Press, Oxford, 1969; Nauka, Moscow, 1973).

88. A. L. Stepanov, in *Metal–Polymer Nanocomposites*, Ed. by L. Nicolais and G. Carotenuto (Wiley, New York, 2004), Chap. 8.

89. E. D. Palik, *Handbook of Optical Constants of Solids* (Academic, New York, 1985).

90. P. B. Johnson and R. W. Christy, Phys. Rev. B **6**, 4370 (1972).

91. A. L. Stepanov, D. E. Hole, and P. D. Townsend, J. Non-Cryst. Solids **260**, 65 (1999).

92. D. Baüerle, *Laser Processing and Chemistry* (Springer-Verlag, Berlin, 1996).

93. J. Y. Bigot, J. C. Merle, O. Cregut, and A. Daunois, Phys. Rev. Lett. **75**, 4702 (1995).

94. P. V. Kamat, M. Flumiani, and G. V. Harland, J. Phys. Chem. B **102**, 3123 (1998).

95. S. Link, C. Burda, M. B. Mohamed, *et al.*, J. Chem. Phys. B **103**, 1165 (1999).

96. S. Link and M. A. El-Sayed, Annu. Rev. Phys. Chem. **54**, 331 (2003).

97. D. Dalacu and L. Martinu, Appl. Phys. Lett. **77**, 4283 (2000).

98. K. Dick, T. Dhanasekaran, Z. Zhang, and D. Meisel, J. Am. Chem. Soc. **124**, 2312 (2002).

99. T. Castro, R. Reifenberg, E. Choi, and R. P. Andres, Phys. Rev. B **42**, 8548 (1990).

100. J. Roiz, A. Oliver, E. Munoz, *et al.*, J. Appl. Phys. **95**, 1783 (2004).

Translated by V. Isaakyan

THEORETICAL
AND MATHEMATICAL PHYSICS

Collective Cherenkov Effect and Anomalous Doppler Effect in a Bounded Spatial Region

I. N. Kartashov*, M. V. Kuzelev*, A. A. Rukhadze**, and N. Sepehri Javan***

* Moscow State University, Vorob'evy gory, Moscow, 119992 Russia
e-mail: kartashov@ph-elec.phys.msu.su
** Prokhorov Institute of General Physics, Russian Academy of Sciences,
ul. Vavilova 38, Moscow, 119991 Russia
*** Zanjan University, Zanjan, Iran
Received June 1, 2004

Abstract—The problem of the development of instability in a bounded spatial region due to the collective Cherenkov effect or the anomalous Doppler effect is studied in the linear approximation. Threshold conditions for the onset of the convective and absolute instabilities of different longitudinal modes and their growth rates are determined with allowance for reflections from the boundaries of the system. The dynamics of the development of an initial perturbation during convective instability is simulated. © 2005 Pleiades Publishing, Inc.

1. FORMULATION OF THE PROBLEM AND BASIC EQUATIONS

The collective Cherenkov effect is one of the fundamental mechanisms for stimulated emission from electron beams in media with slowed waves. The physical nature of the effect was considered in detail in [1, 2]. In the electrodynamics of plasmas and plasmalike media, the collective Cherenkov effect is classified as being related to the wave–wave interactions [3] in which the energy of one of the interacting waves is negative. Nezlin [4] pointed out the analogy between stimulated emission from a beam in the case of a negative energy of one of the interacting waves, on the one hand, and another fundamental emission mechanism—the anomalous Doppler effect—on the other hand. In the literature on plasma physics, the collective Cherenkov effect is often treated as one of the numerous beam instabilities [5, 6]. With this approach, which is of course quite justified, the fundamental role played by the collective effect remains virtually untouched, however. At the same time, the methods and terminology of the general theory of instabilities, which was developed in plasma physics and in the allied fields of science [7–9], can be successfully applied to study the collective Cherenkov effect. Such an attempt will be made here.

We start with the following set of equations, which describe the interaction of a straight electron beam with an electrodynamic waveguide system in the linear approximation [10]:

$$\left(\left(\frac{\partial}{\partial t} + U\frac{\partial}{\partial z}\right)^2 + G_b(\hat{\omega}, \hat{k})\omega_b^2\right)A_b = -\omega_b^2 S_b(\hat{\omega}, \hat{k})A_w,$$

$$D_w(\hat{\omega}, \hat{k})A_w = -\omega_w^2 S_w(\hat{\omega}, \hat{k})A_b. \tag{1}$$

Here, the functions $A_b(t, z)$ and $A_w(t, z)$ characterize the states of the electron beam and electrodynamic system, respectively; the differential operator $D_w(\hat{\omega}, \hat{k})$ describes the dynamics of the electrodynamic system; G_b, S_b, and S_w are dimensionless operators; ω_w is a quantity having the dimensionality of frequency; ω_b is the Langmuir frequency of the beam electrons; and the frequency operator $\hat{\omega}$ and the longitudinal wavenumber operator $\hat{k}$ are defined as

$$\hat{\omega} = i\frac{\partial}{\partial t}, \quad \hat{k} = -i\frac{\partial}{\partial z}. \tag{2}$$

Equations (1) were derived under the assumption that an electron beam propagates with the velocity U along an electrodynamic system oriented in the z direction. Thus, for an infinitely long electron beam propagating in an infinite electron plasma, we have [5] $G_b = S_b = S_w = 1$, $\omega_w = \omega_p$, and $D_w(\hat{\omega}, \hat{k}) = -\hat{\omega} + \omega_p^2 + 3\hat{k}^2 V_{Te}^2$, where ω_p is the Langmuir frequency of the plasma electrons and V_{Te} is their thermal velocity.

An electron beam can interact resonantly with an electrodynamic system only under conditions for which the equations

$$(\omega - kU)^2 - G_b(\omega, k)\omega_b^2 = 0,$$
$$D_w(\omega, k) = 0 \tag{3}$$

(where ω and k are the frequency and wavenumber) have a solution.

We assume that Eqs. (3), which determine a resonant point in the (k, ω) plane, have the solution $k = k_0$ and $\omega = \omega_0$. Restricting our analysis to the resonant

interaction between an electron beam and an electrodynamic system, we represent the solution to Eqs. (1) in the form

$$A_b(t, z) = \tilde{A}_b(t, z)\exp(-i\omega_0 t + ik_0 z),$$
$$A_w(t, z) = \tilde{A}_w(t, z)\exp(-i\omega_0 t + ik_0 z), \tag{4}$$

where $\tilde{A}_w(t, z)$ is the amplitude of an eigenwave of the system. We also assume that the amplitude $\tilde{A}_w(t, z)$ varies slowly in both space and time, i.e., that the following inequalities are satisfied:

$$\left|\frac{\partial \tilde{A}_w}{\partial t}\right| \ll |\omega_0 \tilde{A}_w|, \quad \left|\frac{\partial \tilde{A}_w}{\partial z}\right| \ll |k_0 \tilde{A}_w|. \tag{5}$$

At this point, the beam wave amplitude $\tilde{A}_b(t, z)$ is not yet assumed to be slowly varying. We substitute solution (4) into Eqs. (1) and take into account the relationships $(\omega_0 - k_0 U)^2 - G_b(\omega_0, k_0)\omega_b^2 = 0$ and $D_w(\omega_0, k_0) = 0$, which hold at the resonant point. Using inequalities (5), we then arrive at the following equations for the amplitudes $\tilde{A}_b(t, z)$ and $\tilde{A}_w(t, z)$ (from which the tilde will be omitted for brevity):

$$\left(\frac{\partial}{\partial t} + U\frac{\partial}{\partial z}\right)^2 A_b \mp 2i\sqrt{G_b(\omega_0, k_0)}\omega_b\left(\frac{\partial}{\partial t} + U\frac{\partial}{\partial z}\right)A_b$$
$$= -\omega_b^2 S_b(\omega_0, k_0)A_w, \tag{6}$$
$$\left(\frac{\partial}{\partial t} + V_g\frac{\partial}{\partial z}\right)A_w = -i\omega_w^2 S_w(\omega_0, k_0)\left|\frac{\partial D_w(\omega_0, k_0)}{\partial \omega}\right|^{-1}A_b.$$

Here, V_g is the group velocity of the natural wave in an electrodynamic system that is not perturbed by the electron beam. These fairly general equations describe two limiting regimes in which an electron beam is stimulated to emit natural waves of an electrodynamic system: those of collective Cherenkov effect and single-particle Cherenkov effect [1, 2] (and, of course, a transitional regime between them). In the regime of collective Cherenkov effect, in which we are only interested here, the inequality

$$\left|\left(\frac{\partial}{\partial t} + U\frac{\partial}{\partial z}\right)A_b\right| \ll \left|\sqrt{G_b}\omega_b A_b\right| \tag{7}$$

is satisfied and Eqs. (6) read

$$\left(\frac{\partial}{\partial t} + U\frac{\partial}{\partial z}\right)A_b = \mp\frac{1}{2}i\omega_b\frac{S_b(\omega_0, k_0)}{\sqrt{G_b(\omega_0, k_0)}}A_w,$$
$$\left(\frac{\partial}{\partial t} + V_g\frac{\partial}{\partial z}\right)A_w = -i\omega_w^2 S_w(\omega_0, k_0)\left|\frac{\partial D_w(\omega_0, k_0)}{\partial \omega}\right|^{-1}A_b. \tag{8}$$

The upper and lower signs in the first of Eqs. (8) refer to the resonance of the electrodynamic wave with the fast and slow beam waves, respectively. The collective Cherenkov effect is the resonant interaction of the

electrodynamic wave with just the slow beam wave, whose energy is negative. This is why we choose the lower sign (the plus sign) in these equations and redefine the amplitude A_b to write them as

$$\left(\frac{\partial}{\partial t} + U\frac{\partial}{\partial z}\right)A_b = ia^2 A_w,$$
$$\left(\frac{\partial}{\partial t} + V_g\frac{\partial}{\partial z}\right)A_w = -iA_b, \tag{9}$$

where

$$a^2 = \frac{1}{2}\omega_b\omega_w^2\frac{S_b(\omega_0, k_0)S_w(\omega_0, k_0)}{\sqrt{G_b(\omega_0, k_0)}}$$
$$\times\left|\frac{\partial D_w(\omega_0, k_0)}{\partial \omega}\right|^{-1} > 0 \tag{10}$$

is the parameter containing all information about the physical nature of the particular system under consideration (derivations of Eqs. (9) for various vacuum and plasma systems can be found in [6]).

In what follows, the collective Cherenkov effect will be considered in a bounded spatial region $0 < z < L$. Consequently, it is necessary to take into account reflections of the beam-emitted electromagnetic wave from the boundaries $z = 0$ and $z = L$. We denote by B_w the amplitude of the electromagnetic wave propagating in the opposite direction to the emitted wave of amplitude A_w. Assuming that the oppositely propagating wave does not interact with the electron beam, we write the following obvious equation for its amplitude B_w:

$$\left(\frac{\partial}{\partial t} - V_g\frac{\partial}{\partial z}\right)B_w = 0. \tag{11}$$

Equations (9) and (11) should be supplemented with the conditions for the wave amplitudes at the boundaries $z = 0$ and $z = L$. These conditions are essentially dependent on the sign of the group velocity V_g. When $V_g > 0$, it is said that the beam interacts with the forward (copropagating) wave of the electrodynamic system; the case $V_g < 0$ refers to the interaction with the backward (counterpropagating) wave. For $V_g > 0$, Eqs. (9) and (11) are supplemented with the boundary conditions

$$A_b(t, 0) = 0, \quad A_w(t, 0) = \kappa_1 B_w(t, 0),$$
$$B_w(t, L) = \kappa_2 A_w(t, L), \tag{12}$$

where κ_1 and κ_2 are the coefficients of reflection of an electromagnetic wave from the boundaries $z = 0$ and $z = L$, respectively. The first of conditions (12) implies that the electron beam remains unperturbed when it reaches the boundary $z = 0$ (we assume that the beam velocity is positive, $U > 0$, i.e., that the beam propagates in the positive direction of the z axis).

For $V_g < 0$, the boundary conditions have a different form:

$$A_b(t, 0) = 0, \quad B_w(t, 0) = \kappa_1 A_w(t, 0),$$
$$A_w(t, L) = \kappa_2 B_w(t, L). \tag{13}$$

The objective of further analysis is to consider the boundary-value problem given by Eqs. (9) and (11) and boundary conditions (12), as well as that given by the same equations and boundary conditions (13). Note that boundary-value problems for Eqs. (9) were solved by Gorbunov [11], who, however, treated them in a somewhat different formulation and did not take into account the wave described by Eq. (11).

2. COLLECTIVE CHERENKOV EFFECT IN THE INTERACTION WITH THE FORWARD WAVE ($V_g > 0$)

We begin by considering the case $V_g > 0$, in which the emitted wave propagates in the same direction as the beam. In other words, we analyze the excitation of a forward wave in a bounded spatial region. We represent the solutions to Eqs. (9) and (11) in an exponential form, $\sim\exp(-i\omega t + ikz)$, and obtain the dispersion relations

$$D_1(\omega, k) \equiv (\omega - kU)(\omega - kV_g) + a^2 = 0,$$
$$D_2(\omega, k) \equiv (\omega + kV_g) = 0. \tag{14}$$

Note that the quantities ω and k in these dispersion relations are not actually a frequency and a wavenumber but rather, in accordance with formulas (4), they are deviations from the resonant values ω_0 and k_0.

Using dispersion relations (14), we write the general solution to Eqs. (9) and (11) in the form

$$A_w(z) = A\exp(ik_1(\omega)z) + B\exp(ik_2(\omega)z),$$

$$A_b(z) = -\frac{a^2}{(\omega - k_1 U)}A\exp(ik_1(\omega)z)$$
$$-\frac{a^2}{(\omega - k_2 U)}B\exp(ik_2(\omega)z), \tag{15}$$

$$B_w(z) = C\exp(ik_3(\omega)z),$$

where the common factor $\exp(-i\omega t)$ is omitted and the wavenumbers

$$k_{1,2} = \frac{1}{2}\omega\left(\frac{1}{V_g} + \frac{1}{U}\right) \pm \sqrt{\frac{1}{4}\omega^2\left(\frac{1}{V_g} - \frac{1}{U}\right)^2 - \frac{a^2}{V_g U}},$$
$$k_3 = -\frac{\omega}{V_g} \tag{16}$$

are solutions to these dispersion relations (14) regarded as equations for the wavenumber k.

In doing so, we can determine the condition under which the process of emission from the beam can actu-

ally be treated as a collective Cherenkov effect. The sought condition is derived by inserting solution (15) into inequality (7):

$$a \ll \sqrt{G_b \frac{V_g}{U}\omega_b}, \tag{17}$$

which implies that the beam electron density should be sufficiently high ($a \sim \sqrt{\omega_b}$).[1]

Substituting solution (15) into boundary conditions (12) and eliminating constants A, B, and C yields the following characteristic equation for determining the frequency ω:

$$\exp(ik_3 L) = \kappa_1\kappa_2\left[\frac{\omega_0 - k_1 U}{(k_2 - k_1)U}\exp(ik_1 L)\right.$$
$$\left. + \frac{\omega - k_2 U}{(k_1 - k_2)U}\exp(ik_2 L)\right]. \tag{18}$$

Since, in the general case, Eq. (18) can only be solved numerically, we consider two limiting cases. For $a = 0$ (i.e., when there is no electron beam), Eq. (18) simplifies to

$$\kappa_1\kappa_2\exp\left(2i\frac{\omega}{V_g}L\right) = 1. \tag{19}$$

Introducing the notation $\kappa_1\kappa_2 = |\kappa_1\kappa_2|\exp(-i\phi)$, we obtain from Eq. (19) the expression

$$\omega = -i\frac{V_g}{2L}\ln\frac{1}{|\kappa_1\kappa_2|} + \phi\frac{V_g}{2L}. \tag{20}$$

The imaginary part of this expression is the conventional damping rate of the electromagnetic waves that escape from the region $0 < z < L$ through its semitransparent ($|\kappa_1\kappa_2| < 1$) boundaries $z = 0$ and $z = L$.

Another limiting case is given by the inequality

$$|\omega|^2\frac{(U - V_g)^2}{UV_g} \ll a^2. \tag{21}$$

In this case, we expand the functions $k_{1,2}(\omega)$ in the vicinity of zero and substitute the expansions into Eq. (18) to obtain the expression

$$\omega = \left(\frac{L}{V_g} + \frac{L}{W_g}\right)^{-1}$$
$$\times\left[i\ln\left(|\kappa_1\kappa_2|\cosh\left(\frac{a}{\sqrt{UV_g}}L\right)\right) + \phi\right], \tag{22}$$

---

[1] Inequalities (5) reduce to the inequality $a \ll \sqrt{V_g/U}\,\omega_0$ (usually, $\omega_b \ll \omega_0$), which is weaker than condition (17).

where

$$W_g = \left(\frac{\partial k_{1,2}}{\partial \omega}(0)\right)^{-1} = \frac{2UV_g}{U + V_g} \tag{23}$$

is the so-called group velocity of amplified waves [7–9]. Under the inequality

$$|\kappa_1 \kappa_2| \cosh\left(\frac{a}{\sqrt{UV_g}}L\right) > 1 \tag{24}$$

the imaginary part of expression (22) is positive, which indicates that the system is unstable. It is known [7–9] that the collective Cherenkov effect in the interaction with the forward wave is a convective instability during which any of the finite-amplitude perturbations is displaced in the beam propagation direction and, as a result, is damped at each spatial point as $t \longrightarrow \infty$. The presence of the boundaries prevents the perturbations from being displaced and, under threshold condition (24), leads to their growth at each point z in the interval $[0, L]$.

It should be noted that the collective Cherenkov effect, as well as some other beam instabilities, is of considerable interest for many branches of physics, including microwave electronics. Thus, the collective Cherenkov effect[2] in the interaction with the forward wave underlies certain operating modes of a traveling wave tube (TWT) [12, 13]. Inequality (24) is the condition for an amplifier to be self-excited, i.e., to start to function as an oscillator. Plasma TWT oscillators operating in the regime of stimulated collective Cherenkov effect were considered in [10, 14, 15].

3. COLLECTIVE CHERENKOV EFFECT IN THE INTERACTION WITH THE BACKWARD WAVE ($V_g < 0$)

Here, we investigate the case $V_g < 0$, in which the emitted wave propagates in the direction opposite to the propagation direction of the beam. In other words, we analyze the excitation of a backward wave in a bounded spatial region. Formulas (14)–(16) also hold for this case but with V_g replaced by $-V_g$. We begin by considering a simple particular situation in which the boundary $z = L$ is perfectly transparent to electromagnetic radiation. Substituting solution (15) into boundary conditions (13) with $\kappa_2 = 0$ gives the following characteristic equation:

$$\exp(i(k_1 - k_2)L) = \frac{\omega - k_2 U}{\omega - k_1 U}. \tag{25}$$

It is expedient to examine this equation separately for the simplest case in which the beam velocity is

equal to the group velocity, $|V_g| = U$. In this case, Eq. (25) reduces to

$$\exp(2ik_0 L) = \frac{\omega + k_0 U}{\omega - k_0 U}, \quad k_0 = \frac{1}{U}\sqrt{\omega^2 + a^2}. \tag{26}$$

It can be easily shown that Eq. (26) has zero solutions, $\omega = 0$, when

$$2a\frac{L}{U} = \pi(2n + 1); \quad n = 0, 1, 2, \ldots. \tag{27}$$

It is also easy to show that the solution $\omega = 0$ is the only real solution to Eq. (26). Let us find the frequency assuming that equality (27) for $n = 0$ is slightly violated. Setting

$$\frac{a}{U} = \frac{\pi}{2L} + \delta, \quad |\delta| \ll 1/L, \tag{28}$$

we obtain the following expression for the frequency:

$$\omega \approx i\frac{2}{\pi}a(\sqrt{1 + \pi L\delta} - 1). \tag{29}$$

Frequency (29) is purely imaginary; moreover, we have $\text{Im}\,\omega > 0$ only for $\delta > 0$. This circumstance and representation (28) yield the following threshold condition for the onset of the instability due to the collective Cherenkov effect in the interaction with the backward wave in a system of finite length:

$$a > \frac{\pi}{2}\frac{U}{L}. \tag{30}$$

For $\pi L\delta \ll 1$, expression (29) can be represented as

$$\omega = iaL\delta = ia\frac{L}{U}\left(a - \frac{\pi}{2}\frac{U}{L}\right). \tag{31}$$

In the general case, even the simplest equation (26) can only be solved numerically. We introduce the dimensionless frequency x and the beam density parameter σ by the relationships

$$x = \frac{\omega}{a}, \quad \sigma = 2a\frac{L}{U}. \tag{32}$$

In these new variables, Eq. (26) takes the form

$$\exp(i\sigma\sqrt{1 + x^2}) = \frac{x + \sqrt{1 + x^2}}{1 - \sqrt{1 + x^2}}. \tag{33}$$

Figure 1 shows how the dimensionless frequency x depends on the beam density parameter σ. We can see that there are an infinite number of longitudinal modes. As has already been mentioned, the thresholds for the onset of the instabilities of each of the modes are given by the expressions $\sigma = \pi(2n + 1)$. The frequency of the $n = 0$ mode is purely imaginary. As the parameter σ changes from zero to plus infinity, the imaginary frequency $\text{Im}\,x$ of the corresponding mode changes from minus infinity to unity. For small σ values, the imaginary parts $\text{Im}\,x$ of the frequencies of the remaining

---

[2] In this case, in vacuum microwave electrons, it has become common to speak of a large high-frequency beam space charge.
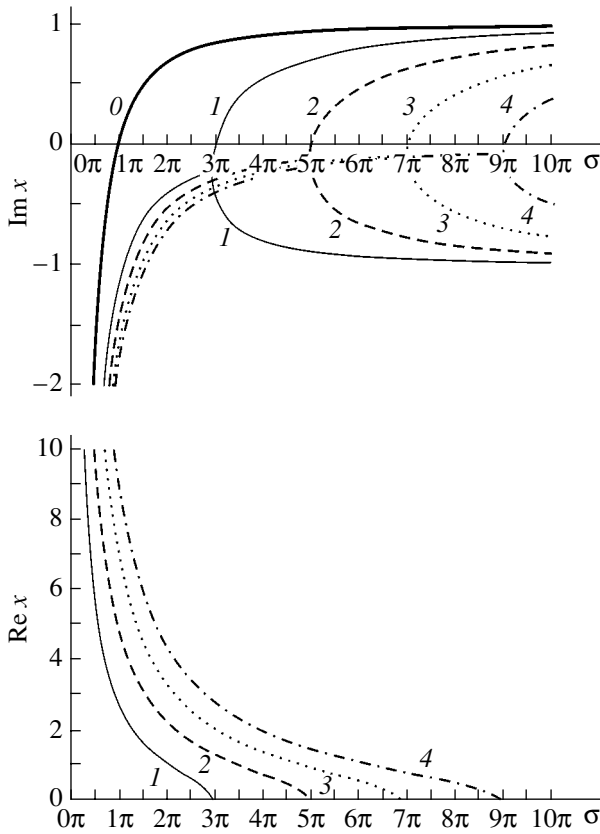
Fig. 1. Dimensionless frequency x vs. beam density parameter σ in the absence of reflections, $\kappa = 0$.
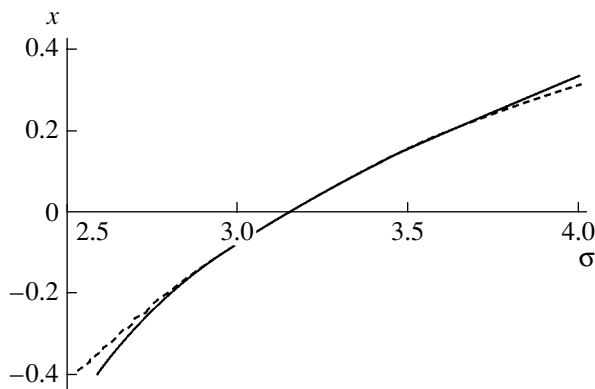

Fig. 2. Dimensionless growth rate $\mathrm{Im}\,x$ vs. beam density parameter σ near the instability threshold. The solid curve shows analytical solution (34), and the dashed curve presents the numerical solution to Eq. (33).

modes with the numbers $n = 1, 2, 3, \ldots$ also increase and, in addition, the real parts $\mathrm{Re}\,x$ of the frequencies of these modes are nonzero (more precisely, there are two solutions with the same value of the imaginary part $\mathrm{Im}\,x$ and with the real part $\mathrm{Re}\,x$ of the same magnitude but opposite sign; in Fig. 1, only the modes with $\mathrm{Re}\,x \geq 0$ are shown). Near the instability thresholds for each of the modes with the numbers $n = 1, 2, 3, \ldots$, the real part

$\mathrm{Re}\,x$ vanishes. As the parameter σ increases further, both solutions are such that the real part is zero, $\mathrm{Re}\,x = 0$, and the imaginary part $\mathrm{Im}\,x$ has two branches: one that increases to unity and the other that decreases to minus unity.

In terms of variables (32), solution (29) is given by the formula

$$x = i\frac{2}{\pi}\left(\sqrt{1 + \frac{\pi}{2}(\sigma - \pi)} - 1\right). \tag{34}$$

Figure 2 compares analytical solution (34) near the instability threshold (solid curve) with the corresponding numerical solution to Eq. (33) (dashed curve). The analytical solution is seen to coincide well with the numerical one.

Let us discuss the physical meaning of threshold condition (30). Recall that the collective Cherenkov effect in the interaction with the backward wave is an absolute instability during which the perturbations grow without bound at any spatial point [7–9]. For $V_g < 0$ and $|V_g| = U$, the eigenfrequencies determined by the first of dispersion relations (14) are given by the formulas

$$\omega = \pm\sqrt{k^2 U^2 - a^2}. \tag{35}$$

Consequently, the instability occurs only within the wavenumber range

$$|k| < \frac{a}{U}. \tag{36}$$

In a system of length L, the wavelengths of the perturbations cannot exceed the value $\lambda_{\max} = 4L$; therefore, the minimal wavenumber is described by the relationship

$$k_{\min} = \frac{2\pi}{\lambda_{\max}} = \frac{\pi}{2L}. \tag{37}$$

Relationships (36) and (37) imply that the instability in a system of finite length is possible under the condition

$$k_{\min} = \frac{\pi}{2L} < \frac{a}{U}, \tag{38}$$

which coincides with the original condition (30). Hence, threshold condition (30) stems from the fact that absolute instability cannot develop in a sufficiently short system. As for the wave damping in such a system (from expression (29) and Fig. 1, we see that the imaginary part of the frequency can be negative), it is of course associated with the escape of radiation through the boundaries $z = 0$ and $z = L$.

We now consider a more general case $|V_g| \neq U$, assuming again that $\kappa_2 = 0$. We introduce the notation

$$\xi = \frac{U}{|V_g|}, \quad \chi_0 = \frac{1}{U}\sqrt{\frac{1}{4}\omega^2(1 + \xi)^2 + \xi a^2}, \tag{39}$$

to represent Eq. (25) in the form

$$\exp(2i\chi_0 L) = \frac{\omega(1 + \xi)/2 + \chi_0 U}{\omega(1 + \xi)/2 - \chi_0 U}. \quad (40)$$

As is the case with Eq. (26), Eq. (40) has the solution $\omega = 0$, provided that $2\chi_0 L = \pi(2n + 1)$ (see equality (27)). This circumstance yields the following threshold condition for the onset of the instability of the longitudinal $n = 0$ mode, which is a generalization of condition (30):

$$a > \frac{\pi}{2}\frac{\sqrt{|V_g|U}}{L}. \quad (41)$$

Near the instability threshold for the $n = 0$ mode, the frequency is given by the expression (see expression (31))

$$\omega = ia\frac{2L}{(|V_g| + U)}\sqrt{\frac{U}{|V_g|}}\left(a - \frac{\pi}{2}\frac{\sqrt{|V_g|U}}{L}\right). \quad (42)$$

Introducing the analogues of quantities (32),

$$x = \frac{\omega}{a}, \quad \sigma = 2a\frac{L}{\sqrt{|V_g|U}}, \quad \mu = \frac{1 + \xi}{2\sqrt{\xi}}, \quad (43)$$

we transform Eq. (40) to the equation

$$\exp(i\sigma\sqrt{1 + \mu^2 x^2}) = \frac{\mu x + \sqrt{1 + \mu^2 x^2}}{\mu x - \sqrt{1 + \mu^2 x^2}}. \quad (44)$$

The replacement $\mu x \longrightarrow x$ reduces Eq. (44) to Eq. (33), so numerical solutions to Eq. (44) contain no new information as compared to Fig. 1.

We now take into account reflections from the boundaries of the system. Substituting solution (15) into general boundary conditions (13) with $\kappa_{1,2} \neq 0$ gives the characteristic equation

$$\exp(i(k_1 - k_2)L) = \frac{\omega - k_2 U}{\omega - k_1 U}$$
$$+ \kappa_1\kappa_2\frac{(k_2 - k_1)U}{(\omega - k_1 U)}\exp(i(k_3 - k_2)L). \quad (45)$$

Note that, for a zero beam density ($a = 0$), Eq. (45) should have solution (20), as is indeed the case. As in the absence of reflections, the case of different wave velocities reduces to the case $|V_g| = U$, to which we are restricting the analysis here. For simplicity, we also assume that $\kappa_1\kappa_2 = \kappa > 0$, where κ is a positive real constant.[3] In terms of variables (32), we convert Eq. (45) to

---

[3] The argument of quantity $\kappa_1\kappa_2$ determines how the wave phases change in reflections and yields an insignificant correction to the real part of the frequency, without changing its imaginary part.

a form convenient for further analysis:

$$\exp(i\sigma\sqrt{1 + x^2}) = \frac{x + \sqrt{1 + x^2}}{1 - \sqrt{1 + x^2}}$$
$$- \kappa\frac{2\sqrt{1 + x^2}}{x - \sqrt{1 + x^2}}\exp\left(i\frac{\sigma}{2}\sqrt{1 + x^2}\right)\exp\left(i\frac{\sigma}{2}x\right). \quad (46)$$

We first find the thresholds for the onset of the instability. To do this, we set $x = 0$ in Eq. (46) and reduce it to

$$\exp(i\sigma) = -1 + 2\kappa\exp(i\sigma/2). \quad (47)$$

Since $\kappa^2 \leq 1$, Eq. (47) can be cast into the form

$$\cos(\sigma/2) = \kappa. \quad (48)$$

If we arrange the roots σ of Eq. (48) in increasing order, then we arrive at the threshold conditions for the onset of the instabilities of the longitudinal modes with the numbers $n = 0, 1, \ldots$, respectively. Thus, the threshold condition for the $n = 0$ mode has the form

$$a > \frac{U}{L}\arccos(\kappa). \quad (49)$$

For $\kappa = 0$, inequality (49) passes over to threshold condition (30). Taking into account the inequalities $x \ll 1$ and $(\sigma - 2\arccos\kappa) \ll 1$, which hold near the instability threshold given by inequality (49), we obtain from Eq. (46) the following expression for the dimensionless frequency:

$$x \approx i\frac{\sigma/2 - \arccos\kappa}{1 + \dfrac{\kappa\arccos\kappa}{\sqrt{1 - \kappa^2}}}. \quad (50)$$

Figures 3 and 4 show how the dimensionless frequency x depends on the beam density parameter σ for $\kappa = 0.5$ and 1, respectively. We see that the imaginary parts of the upper branches of the pairs of neighboring modes (namely, those with $n = 1$ and 2, with $n = 3$ and 4, etc.) are reconnected to one another. The lower branches of these pairs of modes have the same values of $\mathrm{Im}\,x$, the real parts $\mathrm{Re}\,x$ being of the same magnitude but opposite sign. As κ increases to unity, the parameter σ corresponding to the threshold $x = 0$ approaches the values 0, 4π, 8π, etc. (Fig. 4).

Of particular interest is the dynamics of the formation (relaxation) of the longitudinal mode in the collective Cherenkov effect in the interaction with the backward wave. Let us consider the situation in which an electron beam is perturbed at the initial time $\tau = \omega_0 t = 0$ by a solitary electromagnetic field pulse

$$A_w(\zeta, 0) = \begin{cases} A_0\sin^2\left(\dfrac{\zeta}{2n_\lambda}\right), & \zeta = k_0 z \in [0, 2\pi n_\lambda] \\ 0, & \zeta \notin [0, 2\pi n_\lambda], \end{cases} \quad (51)$$
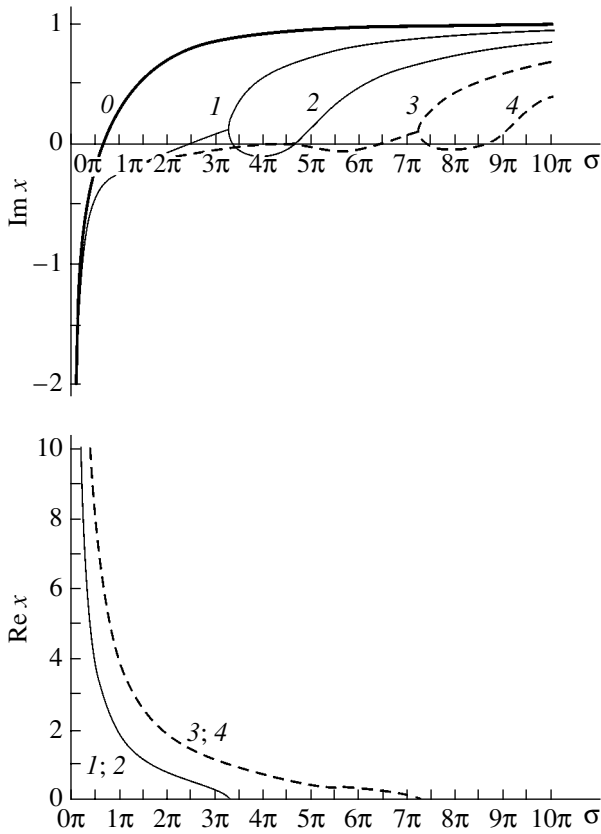
Fig. 3. Dimensionless frequency x vs. beam density parameter σ for $\kappa = 0.5$.
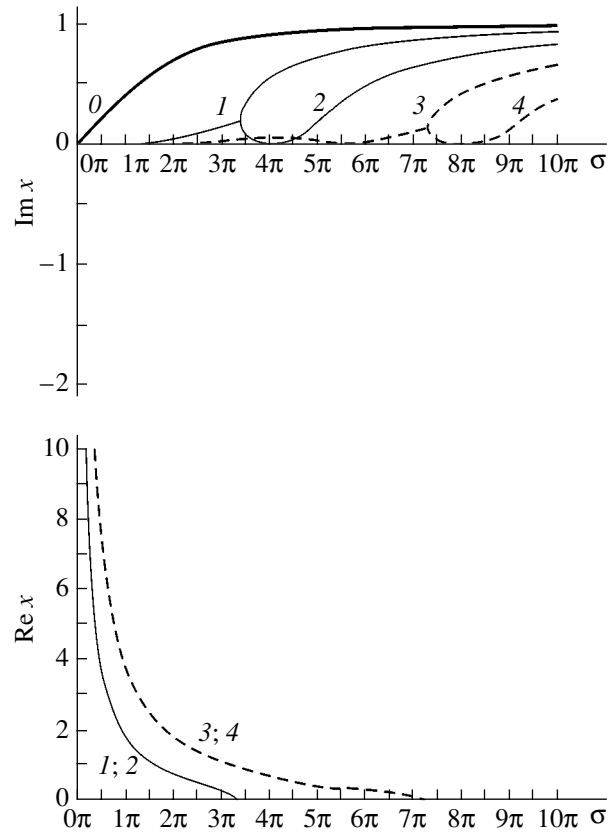

Fig. 4. Dimensionless frequency x vs. beam density parameter σ for $\kappa = 1$.

where $n_\lambda = 6$ is the dimensionless length of the pulse (in units of wavelengths) and $A_0 = 1^{-4}$ is its amplitude.

We specify the following parameter values: the beam density (normalized to ω_0) is $a = 0.01$, the velocities (normalized to ω_0/k_0) are $U = |V_g| = 1$, the total reflection coefficient is $\kappa = 0$, and the system length is equal to 50 wavelengths. Corresponding to this set of values is $\sigma = 2\pi$, which indicates that only the longitudinal $n = 0$ mode is unstable (according to Fig. 1, we have $\mathrm{Im}\,x \approx 0.7$). The pulse dynamics for the above parameter values is illustrated in Fig. 5. An electrodynamic pulse of amplitude A_w propagates in the negative direction of the z axis. An electron beam that enters the system through the boundary $z = 0$ and propagates in the positive direction of the z axis is modulated and excites a wave of amplitude A_w. As a result of the onset of the absolute instability of the zeroth longitudinal mode and the displacement of a wave packet accompanied by the escape of radiation through nonreflecting boundaries of the system, the oscillations relax to the following quasi-steady pattern (in which the amplitudes grow exponentially according to the law $\sim\exp(xa\tau) \approx \exp(0.007\tau)$): the beam modulation amplitude A_b increases with z, reaches its maximal value at a certain internal point of the system, and then decreases toward the right boundary, while the amplitude of the

electromagnetic wave is zero at the boundary $z = L$ (because this boundary is nonreflecting), increases away from it, reaches its maximal value at an intermediate point, and then decreases toward the boundary $z = 0$. The behavior of the amplitudes A_w and A_b is nonmonotonic because it is deep inside the system that the interaction between an electromagnetic wave and a beam is strongest (at the left boundary, we have $A_b = 0$, and, at the right boundary, we have $A_w = 0$). By the time $\tau \sim 800$–900 (which is as short as only several units of the reciprocal of the growth rate), the longitudinal profiles of the amplitudes completely "forget" the structure of initial perturbation (51). The case of a low group velocity of the electromagnetic wave, $|V_g| = 0.1$ (Fig. 6), is analogous to the previous one. Since electromagnetic perturbations are displaced at low velocities, the amplitude A_w is maximal very near the right boundary of the system.

Figure 7 illustrates the dynamics of the development of electromagnetic pulse (51) during the absolute instability for the same parameters as those in Fig. 5 but for the reflection coefficients $\kappa_1 = 1$ and $\kappa_2 = 0.5$ (i.e., for $\kappa = 0.5$). An initial pulse of amplitude A_w propagates in the negative direction and is totally reflected from the boundary $z = 0$ (at the time $\tau = 80$). The reflected pulse of amplitude B_w does not interact with the beam, prop-
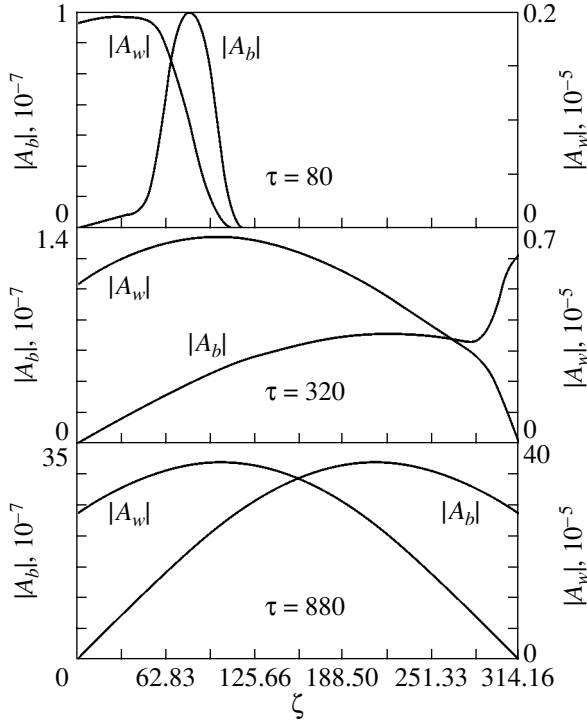
Fig. 5. Relaxation dynamics of oscillations during the absolute instability in the absence of reflections for $a = 0.01$ and $U = |V_g| = 1$.

Fig. 6. Relaxation dynamics of oscillations during the absolute instability in the absence of reflections for $a = 0.01$, $U = 1$, and $|V_g| = 0.1$.

agates to the right, reaches the boundary $z = L$ (at the time $\tau = 320$), and is reflected from it, the reflection coefficient being $\kappa_2 = 0.5$. The pulse of amplitude A_w that is reflected from the boundary $z = L$ propagates toward the boundary $z = 0$, and so on. Because of the Cherenkov interaction of the electromagnetic wave of amplitude A_w with the beam, the wave amplitude A_w and beam modulation amplitude A_b increase. By the time $\tau \sim 1200$ (which is as short as only several units of the reciprocal of the dimensionless growth rate), the oscillations relax to the following quasi-steady pattern: the wave amplitudes increase exponentially, while their spatial profiles do not change with time. Moreover, the longitudinal profiles of the amplitudes A_w and A_b are analogous to those shown in Figs. 5 and 6, whereas the amplitude B_w decreases exponentially with increasing z because of the delayed displacement of the perturbations.

Note that the collective Cherenkov effect in the interaction with the backward wave underlies certain operating modes of a backward wave tube (BWT) [12, 13]. In conventional BWTs, the high-frequency beam space charge either is low or moderately high [16]; in the terminology used here, this corresponds to the single-particle Cherenkov effect. In the present paper, we have considered the opposite limiting case. The methods that we have applied in our study differ from those used to investigate BWTs in vacuum microwave electronics. This is why the above results provide
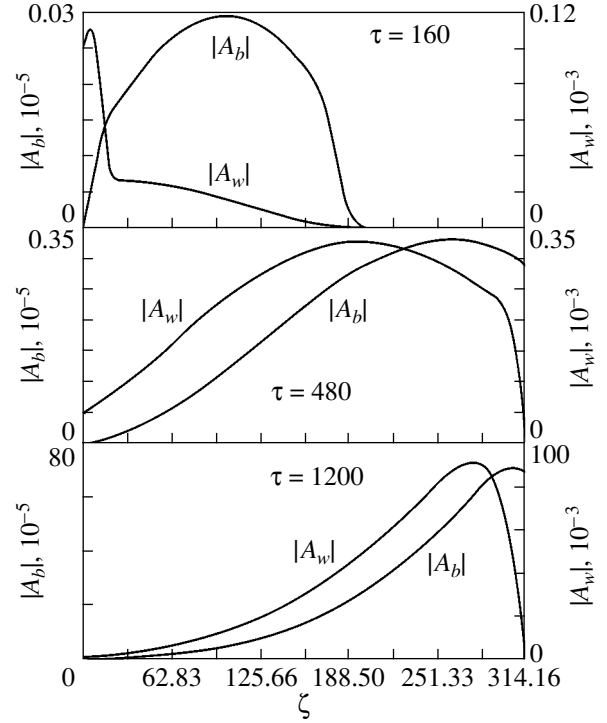
additional essential information on the physics of absolute instabilities in bounded spatial regions. TWT amplifiers based on the stimulated collective Cherenkov effect can be designed as beam–plasma waveguides in a finite-amplitude external magnetic field, like those considered in [17, 18].

4. ANOMALOUS DOPPLER EFFECT IN A FINITE SPATIAL REGION

We consider a monoenergetic electron beam that propagates along the z axis and penetrates through a dielectric layer $0 < z < L$ oriented perpendicular to its propagation direction. Let there be an external magnetic field B directed along the beam. Assuming that the quantities characterizing such a system are independent of the transverse coordinates x and y, we write the following set of linear equations for the transverse components of the electron velocity, $V_\perp = V_x + iV_y$, and of the vector potential of the electromagnetic field, $A_\perp = A_x + iA_y$:

$$\frac{\partial V_\perp}{\partial t} + U\frac{\partial V_\perp}{\partial z} + i\omega_B V_\perp = -\frac{e}{mc}\left(\frac{\partial A_\perp}{\partial t} + U\frac{\partial A_\perp}{\partial z}\right),$$

$$\frac{\partial^2 A_\perp}{\partial t^2} - c_0^2\frac{\partial^2 A_\perp}{\partial z^2} = \frac{mc}{e}\frac{\omega_b^2}{\varepsilon}V_\perp. \tag{52}$$
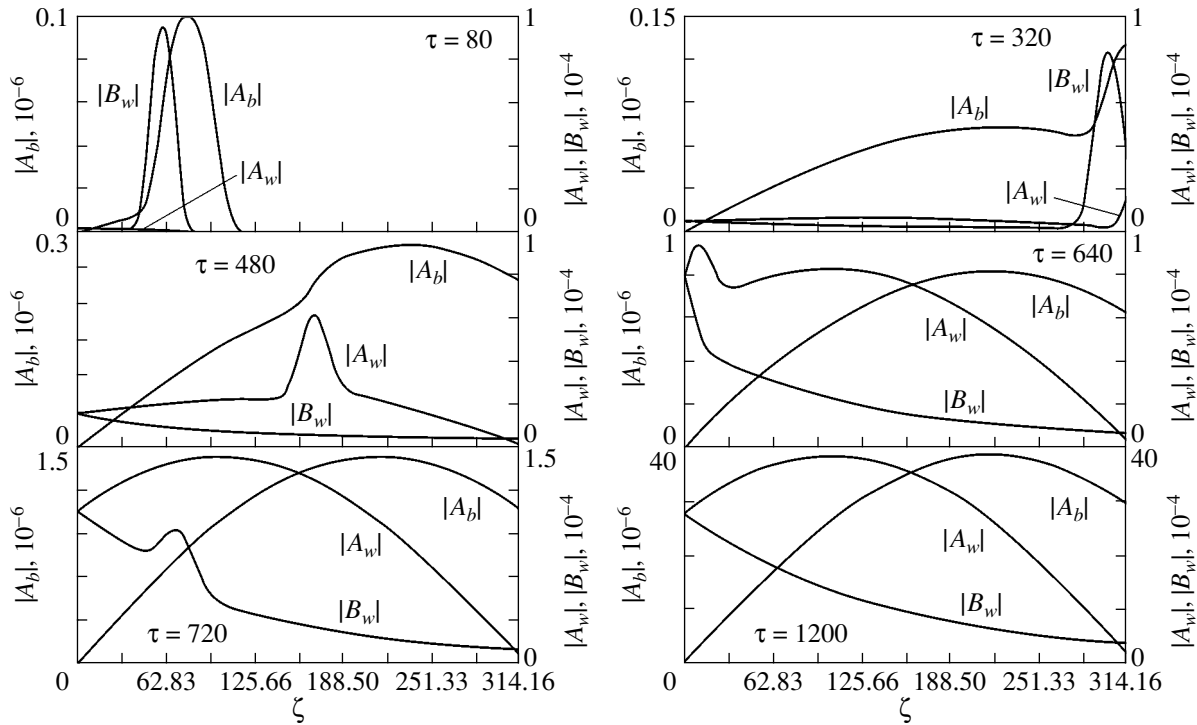
Fig. 7. Relaxation dynamics of oscillations during the absolute instability for $\kappa_1 = 1$, $\kappa_2 = 0.5$, $a = 0.01$, and $U = |V_g| = 1$.

Here, $\omega_B = eB/mc$ is the electron gyrofrequency and $c_0 = c/\sqrt{\varepsilon}$, with ε being the dielectric constant. Equations (52) describe circularly polarized perturbations; for definiteness, we assume that $\omega_B > 0$.

Let us investigate the interactions between an electromagnetic wave and an electron cyclotron wave. At $\omega = \omega_0$ and $k = k_0$, the interaction between these two waves is resonant and is described by the equations

$$\omega = kU - \omega_B, \quad \omega = \pm kc_0, \tag{53}$$

which yield

$$\omega_0 = \omega_B \frac{c_0}{U - c_0} \quad \text{and} \quad \omega_0 = -\omega_B \frac{c_0}{U + c_0}. \tag{54}$$

The plus and minus signs in Eqs. (53) and two different frequencies in relationships (54) indicate that an electron beam can interact with both a forward and a backward electromagnetic wave.

Using representation (4) for the solution to Eqs. (52), we obtain from them the following equations for the slowly varying amplitudes:

$$\left(\frac{\partial}{\partial t} + U\frac{\partial}{\partial z}\right)V_\perp = ia^2 A_\perp,$$

$$\left(\frac{\partial}{\partial t} + V_g\frac{\partial}{\partial z}\right)A_\perp = -iV_\perp, \tag{55}$$

where

$$V_g = \frac{k_0 c_0^2}{\omega_0} = \pm c_0, \quad a^2 = \frac{1}{2}\frac{\omega_b^2}{\varepsilon}\frac{\omega_B}{\omega_0} \tag{56}$$

and the rest of the notation is the same as in Eqs. (52).

Equations (55) have the same form as Eqs. (9) (which have been considered above), provided that the parameter a^2 introduced by the second of formulas (56) is positive (see expression (10)). This is why it is necessary to examine the sign of this parameter. For $c_0 > U$, both frequencies (54) are negative, so we have $a^2 < 0$, i.e., all solutions to Eqs. (55) are stable. This result is quite natural because, for slower-than-light motions, the radiation is emitted under conditions of the normal Doppler effect [1, 2]. In such circumstances, the role of the energy source for radiation is played by the energy of the transverse motion of an electron; in the case at hand, this energy is $m|V_\perp|^2/2$. Consequently, under conditions of the normal Doppler effect, the amplitude $|A_\perp|$ increases only when the velocity $|V_\perp|$ decreases; for $V_\perp(t, 0) = 0$, the beam electrons do not emit radiation at all.

For $c_0 < U$, the first of frequencies (54) is positive; in this case, we have $a^2 > 0$ and Eqs. (55) have unstable solutions that grow at the rate $\omega = ia$. This corresponds to radiation emitted by a "superluminous" beam under conditions of the anomalous Doppler effect [1, 2, 4]. In order to describe the interaction of a beam with an electromagnetic wave at the first of frequencies (54), it is

necessary to set $V_g = c_0 > 0$ in the second of Eqs. (55). Hence, the anomalous Doppler effect in a dielectric layer is described in exactly the same manner as the collective Cherenkov effect in the interaction with the forward wave (which has been analyzed in detail in Section 2). This is why we do not give here any additional explanations concerning the anomalous Doppler effect. Note only that, in special slowing-down structures (such as periodic structures, as well as plasma waveguides in a finite external magnetic field), the anomalous Doppler effect can also occur in the interaction with the backward wave. Obviously, the results that have been obtained in Section 3 of the present study apply almost wholly to this case of the Doppler effect.

ACKNOWLEDGMENTS

REFERENCES

1. M. V. Kuzelev and A. A. Rukhadze, in *Problems of Theoretical Physics and Astrophysics (70th Anniversary of V. L. Ginzburg)* (Nauka, Moscow, 1989), pp. 70–92 [in Russian].

2. M. V. Kuzelev and A. A. Rukhadze, Usp. Fiz. Nauk **152**, 285 (1987) [Sov. Phys. Usp. **30**, 507 (1987)].

3. B. B. Kadomtsev, *Cooperative Effects in Plasmas,* Vol. 22 of *Reviews of Plasma Physics*, Ed. by V. D. Shafranov (Nauka, Moscow, 1988; Consultants Bureau, New York, 2001).

4. M. V. Nezlin, Usp. Fiz. Nauk **120**, 481 (1976) [Sov. Phys. Usp. **19**, 946 (1976)].

5. A. F. Aleksandrov, L. S. Bogdankevich, and A. A. Rukhadze, *Principles of Plasma Electrodynamics* (Vysshaya Shkola, Moscow, 1988; Springer-Verlag, Berlin, 1984).

6. M. V. Kuzelev and A. A. Rukhadze, *Electrodynamics of Dense Electron Bunches in a Plasma* (Nauka, Moscow, 1990) [in Russian].

7. A. I. Akhiezer, *Plasma Electrodynamics* (Nauka, Moscow, 1974; Pergamon, Oxford, 1975).

8. E. M. Lifshitz and L. P. Pitaevskiĭ, *Physical Kinetics* (Nauka, Moscow, 1979; Pergamon, Oxford, 1981).

9. A. M. Fedorchenko and N. Ya. Kotsarenko, *Absolute and Convective Instability in Plasmas and Solids* (Nauka, Moscow, 1981) [in Russian].

10. M. V. Kuzelev, A. A. Rukhadze, and P. S. Strelkov, *Plasma Relativistic Microwave Electronics* (MGTU im. N. E. Baumana, Moscow, 2002) [in Russian].

11. L. M. Gorbunov, Zh. Éksp. Teor. Fiz. **67**, 1386 (1974) [Sov. Phys. JETP **40**, 689 (1974)].

12. V. N. Shevchik and D. I. Trubetskov, *Analytical Numerical Methods in Microwave Electronics* (Sov. Radio, Moscow, 1970) [in Russian].

13. D. I. Trubetskov and A. E. Khramov, *Lectures on Microwave Electronics for Physicists* (Fizmatlit, Moscow, 2003), Vol. 1 [in Russian].

14. M. V. Kuzelev and A. A. Rukhadze, Fiz. Plazmy **26**, 231 (2000) [Plasma Phys. Rep. **26**, 231 (2000)].

15. M. V. Kuzelev, O. T. Loza, A. A. Rukhadze, *et al.*, Fiz. Plazmy **27**, 710 (2001) [Plasma Phys. Rep. **27**, 669 (2001)].

16. N. S. Ginzburg, S. P. Kuznetsov, and T. N. Fedoseeva, Izv. Vyssh. Uchebn. Zaved. Radiofiz. **21**, 1037 (1978).

17. M. V. Kuzelev, Fiz. Plazmy **28**, 544 (2002) [Plasma Phys. Rep. **28**, 501 (2002)].

18. I. N. Kartashov, M. V. Kuzelev, and A. A. Rukhadze, Fiz. Plazmy **30**, 60 (2004) [Plasma Phys. Rep. **30**, 56 (2004)].

Translated by O. Khadin

Elastic Scattering of an Electron by the Negative Lithium Ion

V. V. Semenikhina, V. K. Ivanov, and K. V. Lapkin

St. Petersburg State Polytechnical University, ul. Politekhnicheskaya 29, St. Petersburg, 195251 Russia
e-mail: ivanov@tuexph.stu.neva.ru
Received May 20, 2004; in final form, August 31, 2004

Abstract—In the framework of the many-body theory, the differential and total cross sections of elastic scattering of slow electrons by the negative lithium ion Li⁻ are obtained. Calculations are performed both in the Hartree–Fock single-particle approximation and with regard to many-electron correlations, which take into account the dynamic polarization of the core. Features observed in the behavior of the phases and cross sections for *p* and *d* partial waves are associated with resonance scattering of electron waves. Considering the dynamic polarization of the core by an incident electron heightens the diffraction character of the scattering. The real process is compared with particle scattering in models with a repulsive potential. © 2005 Pleiades Publishing, Inc.

INTRODUCTION

Great interest has been recently shown in the process of photoabsorption by negative ions (see [1, 2] and Refs. therein), which is due to an important role of many-electron correlations in this process and its intriguing features, which distinguish it from photoabsorption by neutral atoms. To date, negative ions have been studied much more poorly than atoms or positive ions (because dense beams of negative ions are hard to produce). However, experimental potentialities for a wider use of powerful sources of radiation, in particular, synchrotron radiation, have been increased in recent years. Electron scattering by negative ions has been understood in a still smaller degree than electron photodetachment and is scarcely referred to in the literature, though this process is of no less interest than photoabsorption. This is particularly true for the influence of various polarization effects on the scattering process, since the negative ion is a rather "loose" highly polarizable system. Notwithstanding the fact that Coulomb repulsive interaction between the ion and an incident electron generally prevails, it turns out that the polarization of the ion considerably affects the behavior of the phases and changes the scattering differential cross section.

In this work, we theoretically study elastic collisions between electrons and negative ions. The object of investigation is the Li⁻ ion, which has been extensively studied in recent years in the context of photodetachment processes [2]. To determine the scattering characteristics, such as the phase, amplitude, and partial and total cross sections, we apply the methods of the many-body theory, which have been advantageously applied to neutral atoms. As the zeroth-order approximation, the Hartree–Fock single-particle approach [3] is taken. The polarization of the core by an incident electron, which has a profound effect on the collisions, is taken into account in terms of the Dyson equation [4].

The Li⁻ ion has a closed outer shell and is spherically symmetric. This allows us to perform calculations with simple models and, comparing the calculation results with those obtained from the first principles, gain a better insight into elastic scattering of electrons by this ion.

In this paper, the atomic system of units is used, $m = e = h/2\pi = 1$ (the energy is given in rydbergs (Ry)).

CALCULATIONS IN THE FRAMEWORK OF SINGLE-PARTICLE APPROXIMATIONS

The wave functions of the ground state of a negative ion are calculated in the Hartree–Fock (HF) approximation. The HF method of self-consistent field is based on the assumption that the electrons in the atom move independently in some average field and takes into account electron–electron interaction only partly [3]. However, this method, being consistent with the idea of independent motion of electrons in the average field of an ion, usually serves as the zeroth-order approximation in taking into account many-electron correlations [5].

The elastic scattering cross section for electrons with energy E and momentum $k = \sqrt{E}$ is expressed through the scattering phases $\delta_l(E)$ of partial waves l by the formula [6]

$$\sigma(E) = \sum_{l=0}^{\infty} \sigma_l(E)$$
$$= \frac{\pi}{k^2} \sum_{l=0}^{\infty} (2l+1)\left|1 - \exp(2i\delta_l(k))\right|^2, \tag{1}$$

where $\delta_l(k)$ is the phase of elastic scattering of partial wave l. It is determined from the asymptotic behavior of the wave function of a scattered particle [6],

$$\psi_\mathbf{k}(\mathbf{r}) = \frac{i}{2kr}\sum_{l=0}^{\infty}(2l+1)P_l(\cos\theta)[(-1)^l\exp(-ikr) \\ - \exp(2i\delta_l(k)+ikr)]. \qquad (2)$$

Knowing an expression for the wave function at $r \longrightarrow \infty$, one can determine the phases of the partial waves and the elastic scattering cross section.

The scattering phases are found in two ways: (i) by solving the HF equation for an incident electron in the field of the frozen core (i.e., in the field of the negative ion obtained in the HF approximation) and (ii) by solving an integral equation that includes the polarization potential of the core. The phase of an lth partial wave of elastic scattering of an incident electron with momentum k is found by the standard formula [5]

$$\delta_l = \arcsin\left(-\sqrt{\frac{\pi}{k}}\int_0^\infty J_l(kr)V(r)P_{N+1}(r)dr\right). \qquad (3)$$

Here, $J_l(kr)$ is the Bessel function. The value of $V(r)$, the scattering potential, is determined through combinations of the integrals of radial wave functions $P_j(r) = rR_j(r)$ [5], where subscript j runs from 1 to S (S is the number of shells in the ground state of the ion),

$$V(r) = \frac{2}{r}[Z - Y(r)], \qquad (4)$$

$$Y_i(r) = \sum_{j=1}^{S}N_jY_{jj}^0(r) \\ - \sum_{j=1}^{S}\frac{2}{N_{j+1}}\sum_{\mu>0}\gamma_\mu(S+1,j)Y_{jj}^\mu(r), \qquad (5)$$

$$Y_{ij}^\mu(r) = r\int_0^\infty\frac{r_<^\infty}{r_>^{\varpi+1}}P_i(r')P_j(r')dr'. \qquad (6)$$

Here, Z is the nuclear charge of the negative ion, $\gamma_\mu(S + 1, j)$ are the angular coefficients of direct interaction between the incident electron and the electrons of a jth shell, and N_j is the number of electrons on a jth level.

METHOD OF PHASE FUNCTIONS

To explain the behavior of the HF phase, we used simplified models of scattering of an electron by the negative ion, namely, the scattering by a uniformly charged ball and the scattering by a uniformly charged sphere. The radii of the ball and sphere were set equal to the average radius of the lithium ion Li$^-$ ($R = 1.89$ a.u.) and their charges Z, equal to –1. The so-called short-range part of the potential of the uniformly

charged ball is of the simple form $U(r) = (3R^2 - r^2)/3R^3$, $r \le R$. Beyond the uniformly charged ball, the potential is equal to the Coulomb potential, $V(r) = 1/r$ ($r > R$).

The method of phase functions consists in passing from the Schrödinger equation to an equation for a desired quantity (the scattering phase in our case) [7]. For this purpose, two functions, $\delta_l(r)$ and $A(r)$, are introduced into consideration. Physically, they have the meaning of the scattering phase and the asymptotic amplitude of the wave functions for scattering by a sequence of "truncated" potentials of different range. The asymptotic value of function $\delta_l(r)$ as $r \longrightarrow \infty$ is equal to the desired phase of scattering by the total potential, $\delta_l(\infty) = \delta_l$. Moreover, the equation for the phase function is free of amplitude function $A(r)$,

$$\frac{d}{dr}\delta_l(r) = -\frac{1}{k}U(r)[\cos\delta_l(r)F_l(kr,\eta) \\ + \sin\delta_l(r)G_l(kr,\eta)]^2, \qquad (7)$$
$$\delta_l(0) = 0,$$

which significantly simplifies the solution of the problem. Here, $U(r)$ is the short-range part of the potential. It should be emphasized that this phase also depends on Coulomb parameter $\eta = 1/k$ because of the interference with the short-range potential. Equation (7) involves Coulomb functions [8] $F_l(kr, \eta)$ and $G_l(kr, \eta)$, which are regular and irregular (at $r = 0$) solutions to the Schrödinger equation with the Coulomb potential. Solutions to Eq. (7) rapidly converge to desired values $\delta_l(\infty)$.

DYNAMIC POLARIZATION POTENTIAL

The HF approximation, as well as the models considered above, disregard many-electron effects, in particular, the polarization of the core by an incident electron, though it is well known that negative ions are highly polarizable, since the binding energy of outer-shell electrons is rather low. Therefore, to adequately describe and determine the phases, amplitudes, and cross section of elastic scattering, one should go beyond the scope of the single-particle approximation. In this paper, the dynamic polarization of the negative ion by an incident electron is taken onto account in terms of the Dyson equation [4, 9]. In matrix form, the Dyson equation for the reducible properly energy part of a one-particle Green's function, $\tilde\Sigma(\mathbf{r}, \mathbf{r}', E)$, is written as [4, 9]

$$\langle E_1 l|\tilde\Sigma(E)|E_2 l\rangle = \langle E_1 l|\Sigma(E)|E_2 l\rangle \\ + \nu p\int\langle E_2 l|\Sigma(E)|E'l\rangle\langle E'l|\tilde\Sigma(E)|E_2 l\rangle\frac{dE'}{E - E'}, \qquad (8)$$

where $|El\rangle$ are the one-particle wave functions of the electron, $\langle|\Sigma(E)|\rangle$ is the irreducible properly energy part

of the Green's function, and the integral is taken in the sense of the principal value.

Irreducible properly energy part $\Sigma(E)$ has the meaning of the nonlocal polarization potential that depends on electron energy E and embodies the electron–core correlation interaction.

The irreducible properly energy part $\Sigma(E)$ of the one-particle Green's function is convenient to partition into two components, namely, the Hartree–Fock component and the one defined by correlation interaction [4],

$$\Sigma(E) = \Sigma^{HF}(E) + \Sigma^{cor}(E). \qquad (9)$$

The properly energy part in the HF approximation, Σ^{HF}, is the self-consistent average field by which an atom (ion) acts upon an electron being scattered. It is determined, along with electron scattering phase δ_l^{HF}, by calculating the wave functions in the HF system of equations.

Thus, our goal is to calculate the correlation part of the potential. Since the HF approximation includes the first order of the perturbation theory in Coulomb interaction, matrix element $\Sigma^{cor}(E)$ in the lowest order of the perturbation theory may be represented by the flow diagram [4]

$$(10)$$
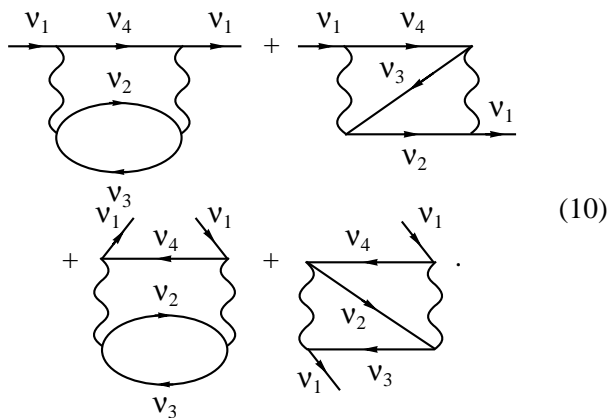
Here, the right-arrowed lines correspond to the incident electron ($\nu_1 = (E, l)$) and to the excited electrons of the ion (ν_2); the left-arrowed, to the resulting vacancy (hole); and the wavy line, to Coulomb interaction. As was shown by previous calculations [4, 5], the contribution of the third-order diagrams to the properly energy part is usually less than 10% of that from the second-order ones. Therefore, the calculation of the correlation polarization potential is restricted to diagrams (10).

A correction to the HF scattering phase is determined through the matrix element of reducible properly energy part (8) in which the irreducible properly energy part now includes only the correlation interaction,

$$\Delta\delta_l(E) = \arctan(-\pi\langle El|\tilde{\Sigma}(E)|El\rangle). \qquad (11)$$

Correction (11) was calculated with the modified software used earlier in atomic calculations [5]. First, the wave functions of the ground state of the negative

lithium ion were calculated in the HF approximation. Then, the HF wave functions and the scattering phases of an incident electron in the frozen HF field of the negative ion were found. It is known that these wave functions constitute a complete orthonormal basis for determining many-electron correlations [5]. The HF wave functions were calculated with a relative accuracy of 10^{-7}, and the corresponding HF phase was found with an accuracy of $\leq 5\%$. With these wave functions, matrix element $\Sigma^{cor}(E)$ was calculated using the second-order perturbation theory (see (10)) with regard to the transferred monopole, dipole, and quadrupole moments ($\Delta l = 0, 1, 2$) in terms of Coulomb interaction, as was done in [4]. Then, the reducible properly energy part of the Green's function was determined by solving integral equation (8) and corrections to the scattering phase were found.

RESULTS AND DISCUSSION

At the first stage, the phases and partial cross sections were found by the HF method and the results obtained were compared with the known results for scattering by the Coulomb repulsive field. In the general case (with allowance for orbital moment l), the phase of scattering by the Coulomb field is determined through the gamma function [10],

$$\eta_l = \arg\Gamma\left(l + 1 + i\frac{1}{k}\right). \qquad (12)$$

The phases of scattering of various partial waves by the Coulomb repulsive field are smooth functions of the incident electron energy and tend to zero as $k = \sqrt{\varepsilon} \longrightarrow 0$. The HF phase of the *s* wave also monotonically decreases with an increase in the electron energy. However, the energy dependences of the HF scattering phases of the *p* and *d* waves were found to behave differently from the Coulomb case. In particular, the phase of the *p* wave exhibits a peak about $\pi/4$ high at $\varepsilon \approx 5.4$ eV (Figs. 1, 2).

To determine the contribution of exchange interaction to the behavior of the phases and, in particular, to see whether it is responsible for the specific shape of the *p* and *d* waves, the scattering phases of the electrons were calculated in the Hartree approximation (without regard to exchange interaction). Comparison of the results obtained in terms of the HF and Hartree approximations indicates that neglect of exchange interaction changes the height of the peak in the *p* and *d* phases insignificantly, although it shifts this singularity by 3.4 eV toward higher energies of the incident electron (curve *3* in Fig. 2). The scattering phase curves for the *s* wave undergo a similar shift. This effect can be explained by the attractive character of the exchange potential in the HF equations. However, it should be noted that, if the energy of the incident electron exceeds 13 eV, the shifts of the phase curves obtained in the model and HF calculations differ considerably, appar-
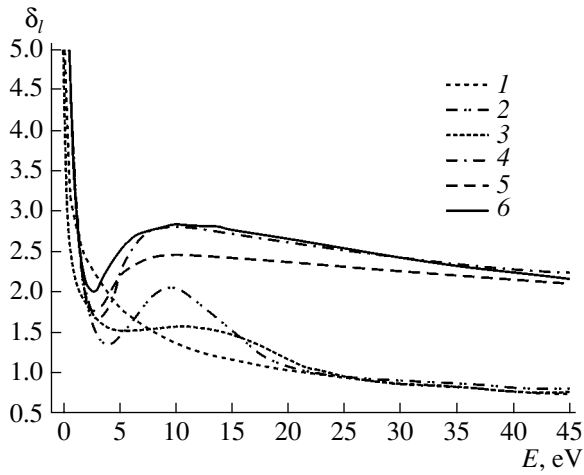
Fig. 1. Energy dependence of the scattering phase for the partial *p* wave in different approximations. Model calculations: (*1*) Coulomb repulsive field, (*2*) uniformly charged ball, and (*3*) uniformly charged sphere. Calculations of scattering by the Li⁻ ion: (*4*) local parametric potential taking into account the polarization of the core by an incident electron ($\alpha = 162$ a.u., $r_0 = 5.2$ a.u.), (*5*) Hartree–Fock approximation, and (*6*) Dyson equation.
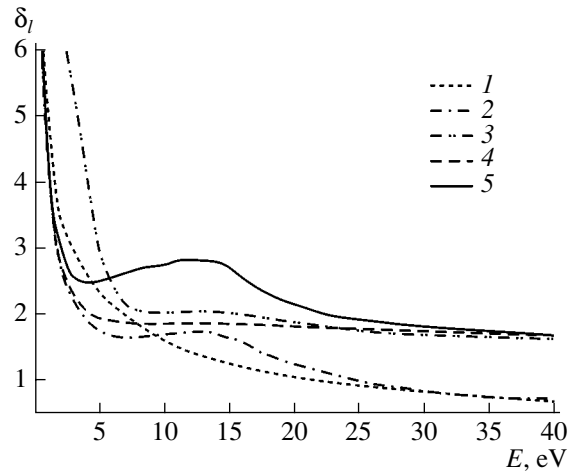

Fig. 2. Energy dependence of the scattering phase for the partial *d* wave in different approximations. Model calculations: (*1*) Coulomb repulsive field and (*2*) uniformly charged ball. Calculations of scattering by the negative Li⁻ ion: (*3*) Hartree approximation, (*4*) Hartree–Fock approximation, and (*5*) Dyson equation.

ently because of the difference in the short-range behavior of the Coulomb and HF potentials. To be sure of this, we calculated a correction to the *p* phase within the perturbation theory [10],

$$\Delta \delta_l = -\int_0^\infty \Delta U(r)[J_{l+1/2}(kr)]^2 r\,dr. \qquad (13)$$

Here, $\Delta U(r)$ is the difference between the Coulomb and Hartree potentials and $J_{l+1/2}(kr)$ is the Bessel function.

With this correction, the Hartree phase approaches the Coulomb phase more rapidly at high energies, the general behavior remaining unchanged.

It is also clear that the singularities in the behavior of the *p* and *d* phases are due to diffraction of the electron waves by the structure of the negative ion. To gain greater insight into the physical nature of the singularities in the scattering phases, we solved simple model problems: scattering by a uniformly charged ball and by a uniformly charged sphere. It turned out that the phases of the *p* and *d* waves also vary nonmonotonically and exhibit singularities of about $\pi/4$ and $\pi/6$, respectively (Figs. 1, 2). Considering the variation of these phases with the radius of the ball (sphere) unveils the position of these singularities versus the radius of the scattering field (Fig. 3). With increasing (decreasing) radius of the model potential, this singularity shifts toward higher (lower) energies. As field radius *R* tends to zero, the scattering phase turns into the Coulomb phase. Thus, the results of model calculations corroborate the diffraction nature of the singularities observed in the behavior of the scattering phases.

The elastic scattering phases were also found using the local parametric potential

$$V_{\mathrm{pol}} = -\frac{\alpha}{(r^2 + r_0^2)^2}, \qquad (14)$$

which takes into account the polarization of the core by an incident electron. Here, α is the dipole polarizability and r_0 is the range of the potential.

The parameters were chosen in such a way that the behavior of the *p* phase approximated its behavior in the dynamic potential as closely as possible. The dipole polarizability calculated was found to be close to the polarizability of a Li atom, $\alpha = 162$ a.u., and parameter r_0 was equal to 5.2 a.u. The results of calculation of this phase using parametric potential (14) are presented in Fig. 1 (curve *4*).

Figures 1 and 2 also show the scattering phase of the *p* and *d* waves that was calculated with the Dyson equation, i.e., with regard to the dynamic polarization of the core by an incident electron. The inclusion of the polarization potential is seen to significantly affect the behavior of the partial scattering phases. While the polarization potential merely heightens the phase peak to $\pi/2$ for the *p* wave (Fig. 1), the phase peak of the partial *d* wave (Fig. 2), which reaches $\pi/3$ at an energy of 13.6 eV, can be almost completely attributed to many-electron effects. However, the effect of the polarization potential on partial scattering waves of higher multipole order weakens rapidly with growing *l*.

The partial and total cross sections were calculated by formula (1). The phase peaks in the *p* wave exert a scarce influence on the scattering partial cross section, while the minor phase singularity in the *d* wave noticeably changes the partial cross section at energies higher
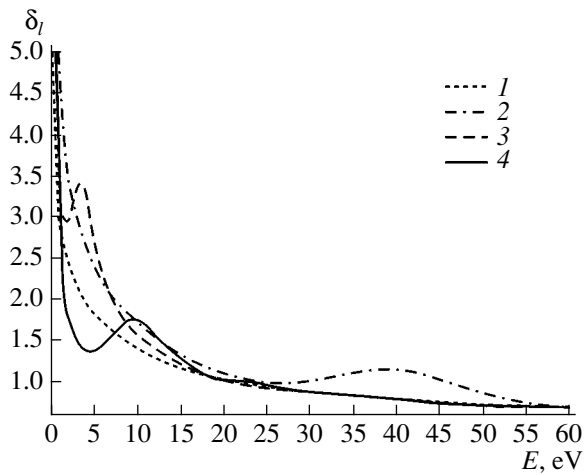
Fig. 3. Model calculations of the scattering phase for the *p* wave. (*1*) Coulomb repulsive field. The dependence of the phase on the radius of the uniformly charged scattering ball ($R = 1.89$ a.u.) of radius (*2*) $R/2$, (*3*) $2R$, and (*4*) R.

Fig. 4. Energy dependence of the partial cross section for the *d* wave in different approximations. Model calculations: (*1*) Coulomb repulsive field and (*2*) uniformly charged ball. Calculations of the scattering by the negative $\bar{\text{Li}}^-$ ion: (*3*) Hartree–Fock approximation and (*4*) taking account of polarization with the Dyson equation.
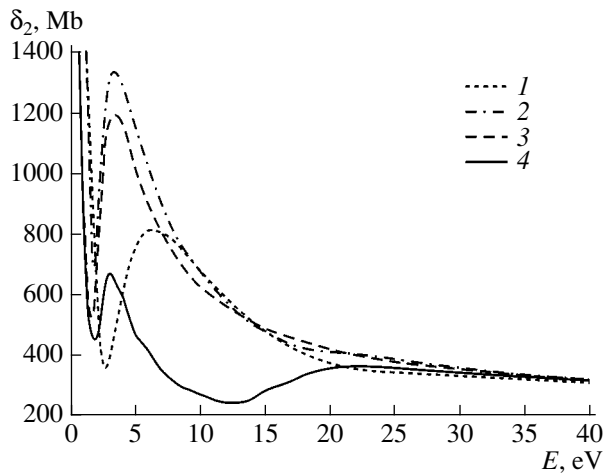

Fig. 5. Energy dependence of the total cross section of elastic scattering of electrons by the negative lithium ion: (*1*) Coulomb repulsive field, (*2*) uniformly charged ball, (*3*) Hartree–Fock approximation, and (*4*) taking account of polarization with the Dyson equation.
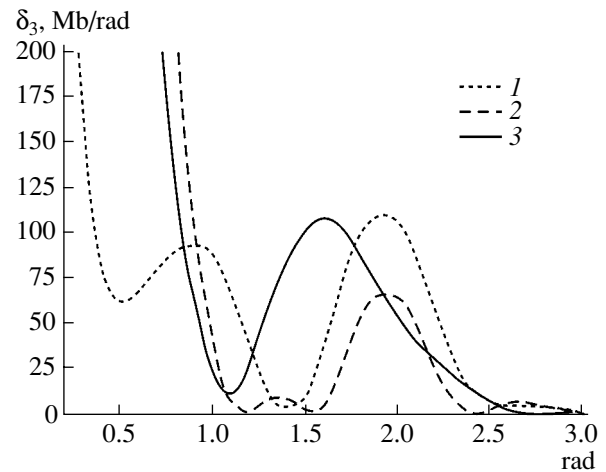
Fig. 6. Differential cross section of elastic scattering of electrons by the negative lithium ion for an electron energy of (*1*) 5, (*2*) 15.5, and (*3*) 36 eV.

than 2.7 eV. Figure 4 compares the partial cross sections of scattering of the *d* wave that were found in different approximations. The cross section obtained with allowance for many-electron effects is seen to have an extra interference minimum at an energy of ≈2.7 eV, where the phase of the *d* wave approaches π. For the total cross section of elastic scattering of electrons by the negative lithium ion, the interference structure is similar (Fig. 5). The cross sections obtained with the Dyson equation and in the Hartree–Fock approximation differ most considerably at incident electron energies of 2.7–20 eV. This means that the effects associated with the dynamic polarization of the core become essential in this range of electron energies [11].
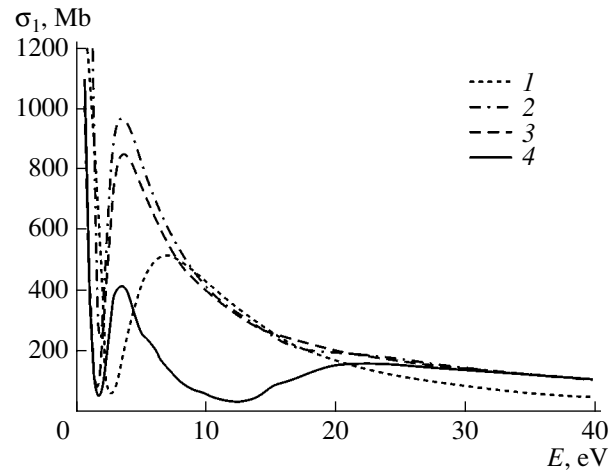
Obviously, the phase singularities of the waves scattered are bound to be more pronounced in the elastic scattering differential cross section [6],

$$d\sigma = 2\pi \sin\theta |f(\theta)|^2 d\theta, \qquad (15)$$

where

$$f(\theta) = \frac{1}{2ik} \sum_{l=0} (2l+1)(\exp(2i\delta_l) - 1) P_l(\cos\theta) \quad (16)$$

is the amplitude of electron scattering by angle θ. The electron scattering amplitude peaks at θ = 0 and declines with increasing θ, changing sign, so that the

differential cross section exhibits diffraction maxima and minima.

The elastic scattering differential cross sections calculated with regard to many-electron effects are shown in Fig. 6. The main features of the diffraction pattern are observed at the same energy values (3.5 and 15.5 eV) at which the behavior of the p and d waves becomes nonmonotonic. For these values of the electron energy, the second-order diffraction maxima are more intense than the first maximum. The inclusion of dynamic polarization enhances the difference between the intensities of the first- and second-order maxima, as was shown in [12]. At low energies ($E < 2.7$ eV) and energies exceeding 34 eV, the second- and higher-order maxima are always less intense than the first maximum.

CONCLUSIONS

Elastic scattering of electrons by negative ions still remains a poorly studied domain of the physics of collisions. However, the results on electron photodetachment from negative ions and electron scattering obtained in this paper uncover intriguing effects. In particular, it is demonstrated that the structure of the negative ion is responsible for the nonmonotone behavior of the phases of p and d partial waves, which are caused by the diffraction of electron waves on a finite-radius object. This feature is absent in scattering of a symmetric s wave. It is shown that many-electron correlations, in particular, the dynamic polarization of the core electrons by an incident particle, should be taken into consideration in description of elastic scattering of slow electrons. Electron diffraction that arises in electron scattering by negatively charged ions brings about perceptible qualitative changes in the scattering characteristics. The results obtained may be able to be used in studying scattering by other negative ions and various negatively charged clusters, including fullerenes.

ACKNOWLEDGMENTS

REFERENCES

1. S. Buckman and C. W. Clark, Rev. Mod. Phys. **66**, 539 (1994).

2. V. K. Ivanov, Radiat. Phys. Chem. **70**, 345 (2004).

3. D. Hartree, *The Calculation of Atomic Structure* (Wiley, New York, 1957; Inostrannaya Literatura, Moscow, 1960).

4. G. F. Gribakin, B. V. Gul'tsev, V. K. Ivanov, and M. Yu. Kuchiev, J. Phys. B **23**, 4505 (1990).

5. M. Ya. Amus'ya and L. V. Chernysheva, *Computerized System for Numerical Investigation of the Atomic Structure* (Nauka, Leningrad, 1983) [in Russian].

6. N. F. Mott and H. S. W. Massey, *The Theory of Atomic Collisions* (Clarendon, Oxford, 1965; Mir, Moscow, 1969).

7. V. V. Babikov, *The Method of Phase Equations in Quantum Mechanics* (Nauka, Moscow, 1967) [in Russian].

8. G. F. Drukarev, *Collisions of Electrons with Atoms and Molecules* (Nauka, Moscow, 1978; Plenum, New York, 1987).

9. L. Zülicke, *Quantenchemie, Ein Lehrgang* (Deutscher Verlag der Wissenschaften, Berlin, 1973; Mir, Moscow, 1976).

10. L. D. Landau and E. M. Lifshitz, *Course of Theoretical Physics*, Vol. 3: *Quantum Mechanics: Non-Relativistic Theory* (Nauka, Moscow, 1989; Pergamon, Oxford, New York, 1977).

11. V. V. Semenikhina, V. K. Ivanov, A. N. Ipatov, and C. V. Lapkin, Proc. SPIE **5127**, 41 (2003).

12. V. V. Semenikhina, V. K. Ivanov, and C. V. Lapkin, Proc. SPIE **5400**, 46 (2004).

Translated by A. Pankrat'ev

GASES
AND LIQUIDS

Rate of Unsteady Evaporation of a Spherical Drop with Regard to Concentration and Temperature Discontinuities at Its Surface

Yu. I. Yalamov and M. K. Kuzmin

Moscow State Regional University, ul. Radio 10a, Moscow, 105005 Russia
Received June 16, 2004

Abstract—Unsteady evaporation and condensation growth of a quiescent spherical drop are studied in the case when the surface temperature and the saturated vapor concentration on the surface of the drop are variable and experience a jump in the Knudsen layer. A general (i.e., valid for any time scale) expression for the rate of change of the radius as a function of time is found. From this expression, first approximations for infinitesimal and large times are derived separately by asymptotically expanding relevant functions. The formulas derived are analyzed and compared with those known from the conventional theories, for which purpose the rate of evaporation of the drop in air is calculated in a wide range of initial conditions. © 2005 Pleiades Publishing, Inc.

INTRODUCTION AND PROBLEM DEFINITION

In [1, 2], we elaborated a theory of unsteady evaporation and condensation growth of a quiescent spherical drop that takes into account concentration and temperature discontinuities in the Knudsen layer near the surface of the drop. A general (in the sense that it applies to any time scale) expression for the rate of change of the radius of the drop as a function of time was found, and formulas for infinitesimal and large times separately were derived from that expression. Also, the domain of applicability of the formulas derived previously for the quasi-steady and unsteady variation of the radius was determined. When posing the boundary conditions, we assumed that the saturated vapor concentration on the surface of the drop is constant, while the temperature may slightly vary.

In this work, we consider a more general case when the temperature and saturated vapor concentration on the surface of the drop are variable and are related, in a linear approximation, via the Clapeyron–Clausius equation.

The constituents of a binary gaseous mixture are molecules of the substance of the drop and a carrier gas that does not experience phase transitions in a given temperature range. Following Maxwell [3], we assume that the vapor concentration at the surface is equal to the saturated vapor concentration at a given surface temperature. It is also assumed that the radius R of the drop is much larger than the free path of gas molecules at a given temperature ($R \gg \lambda$) but is not so large that concentration and temperature discontinuities may be disregarded. The (relative) vapor concentration c_1 and

the temperature T of the vapor–gas mixture are described by the set of equations

$$\frac{\partial c_1}{\partial t} = D\left(\frac{\partial^2 c_1}{\partial r^2} + \frac{2}{r}\frac{\partial c_1}{\partial r}\right), \qquad (1)$$

$$\frac{\partial T}{\partial t} = a\left(\frac{\partial^2 T}{\partial r^2} + \frac{2}{r}\frac{\partial T}{\partial r}\right), \qquad (2)$$

with the initial and boundary conditions

$$c_1(r,t)|_{t=0} = c_{10}, \quad c_1(r,t)|_{r \to +\infty} = c_{1\infty} = c_{10}, \quad (3)$$

$$T(r,t)|_{t=0} = T_0, \quad T(r,t)|_{r \to +\infty} = T_\infty = T_0, \quad (4)$$

$$[c_1(r,t) - c_{1s}(t)]|_{r=R} = \left(K_c^{(c)}\frac{\partial c_1}{\partial r} + K_c^{(T)}\frac{1}{T_0}\frac{\partial T}{\partial r}\right)\bigg|_{r=R}, (5)$$

$$[T(r,t) - T_s(t)]|_{r=R} = \left(K_T^{(T)}\frac{\partial T}{\partial r} + K_T^{(c)}T_0\frac{\partial c_1}{\partial r}\right)\bigg|_{r=R}, (6)$$

$$LDnm_1\frac{\partial c_1}{\partial r}\bigg|_{r=R} = -\kappa\frac{\partial T}{\partial r}\bigg|_{r=R}. \qquad (7)$$

Here, r is the radial coordinate of the spherical coordinate system with the origin at the center of the drop; t is the time; $D = nm_2 D_{12}/\rho$, where D_{12} is the coefficient of interdiffusion of the binary mixture components; $n = n_1 + n_2$; n_1, m_1 and n_2, m_2 are the molecular concentrations and masses of the first and second components, respectively; ρ is the density of the binary vapor–gas mixture; and a is the diffusivity of the binary mixture. In boundary conditions (5)–(7), $K_c^{(c)}$, $K_c^{(T)}$, $K_T^{(T)}$, and

$K_T^{(c)}$ are the gasdynamic coefficients of concentration and temperature discontinuities [4, 5]; L is the specific heat of the phase transition for the substance of the drop; and κ is the thermal conductivity of the vapor–gas mixture.

Equations (1) and (2) and conditions (3)–(7) should be complemented by the approximate linear Clapeyron–Clausius equation [6]

$$c_{1s}(t) = c_{1s0}\{1 + \nu_{s0}[T_s(t) - T_{s0}]\}, \qquad (8)$$

which is valid for a small variation of the surface temperature. Here, $c_{1s}(t) = c_1(T_s) = n_1(T_s)/n$, where $n_1(T_s)$ is the concentration of the saturated vapor of the substance of the drop at a surface temperature $T_s = T_s(t)$,

$$c_{1s}(t)|_{t=0} = c_{1s0}, \quad T_s(t)|_{t=0} = T_{s0},$$

$$\nu_{s0} = \frac{Lm_1 - kT_{s0}}{kT_{s0}^2}, \qquad (9)$$

and k is the Boltzmann constant.

It should be noted that quantity Lm_1 involved in expression (9) is one order of magnitude higher than kT_{s0} for most liquids (including water, alcohols, and ethers) when the surface temperature of the drop is below the melting point [7]. Therefore, we put $\nu_{s0} > 0$.

In view of (7), boundary conditions (5) and (6) can be represented in a form that is more convenient to analyze:

$$[c_1(r, t) - c_{1s}(t)]|_{r=R} = \chi_c \frac{\partial c_1}{\partial r}\bigg|_{r=R}, \qquad (10)$$

$$[T(r, t) - T_s(t)]|_{r=R} = \chi_c \frac{\partial T}{\partial r}\bigg|_{r=R}, \qquad (11)$$

where

$$\chi_c = K_c^{(c)} - \frac{l}{\kappa T_0}K_c^{(T)}, \quad \chi_T = K_T^{(T)} - \frac{\kappa T_0}{l}K_T^{(c)},$$

$$l = LDnm_1.$$

Quantities χ_c and χ_T, which were first introduced by us in [1, 2], are called the composite coefficients of concentration and temperature discontinuities, respectively. They are generally nonnegative. Vanishing of either of them is the necessary and sufficient condition for the existence of the corresponding discontinuity. The left-hand sides of (10) and (11), which are functions of t, will be referred to as

$$J_c(t) = [c_1(r, t) - c_{1s}(t)]|_{r=R},$$
$$J_T(t) = [T(r, t) - T_s(t)]|_{r=R}. \qquad (12)$$

SOLUTION METHOD

We will solve the problem using the integral Laplace transformations [8] designated as follows:

$$S(r, p) = \int_0^\infty c_1(r, t)\exp(-pt)dt,$$

$$\theta(r, p) = \int_0^\infty T(r, t)\exp(-pt)dt.$$

With boundary conditions (3) and (4), we find the maps of Eqs. (1) and (2),

$$DS'' + \frac{2D}{r}S' - pS + c_{10} = 0,$$

$$a\theta'' + \frac{2a}{r}\theta' - p\theta + T_0 = 0,$$

which are the ordinary second-order differential equations in unknown functions $S(r, p)$ and $\theta(t, p)$, where r is an independent variable and p is a parameter. The general solutions to either of the linear equations with variable coefficients have the form [9]

$$S(r, p) - \frac{c_{10}}{p} = \frac{A}{r}\exp\left(-\sqrt{\frac{p}{D}}r\right) + \frac{A'}{r}\exp\left(\sqrt{\frac{p}{D}}r\right), \quad (13)$$

$$\theta(r, p) - \frac{T_0}{p} = \frac{B}{r}\exp\left(-\sqrt{\frac{p}{a}}r\right) + \frac{B'}{r}\exp\left(\sqrt{\frac{p}{a}}r\right), \quad (14)$$

where A, A', B, and B' ("constants" of integration) depend on the conditions of the problem.

First, in view of boundary conditions (3) and (4), we find that

$$A' = B' = 0. \qquad (15)$$

Now, introducing the designations

$$S_s(p) = \int_0^\infty c_{1s}(t)\exp(-pt)dt,$$

$$\theta_s(p) = \int_0^\infty T_s(t)\exp(-pt)dt,$$

we write boundary conditions (7), (8), (10), and (11) in the mapping space,

$$\left.\begin{array}{l} (1 + \chi_c p_1)q_1 A - RS_s = -\dfrac{c_{10}R}{p} \\[2ex] (1 + \chi_T p_2)q_2 B - R\theta_s = -\dfrac{T_0 R}{p} \\[2ex] lp_1 q_1 A + \kappa p_2 q_2 B = 0 \\[2ex] S_s - c_{1s0}\nu_{s0}\theta_s = \dfrac{c_{1s0}}{p}(1 - \nu_{s0}T_{s0}), \end{array}\right\} \qquad (16)$$

where

$$p_1 = \frac{1}{R} + \sqrt{\frac{p}{D}}, \quad p_2 = \frac{1}{R} + \sqrt{\frac{p}{a}},$$

$$q_1 = \exp\left(-\sqrt{\frac{p}{D}}R\right), \quad q_2 = \exp\left(-\sqrt{\frac{p}{a}}R\right).$$

Solving algebraic set of equations (16) yields

$$A = -\varepsilon\kappa R\sqrt{Da}\frac{p_2}{p\delta q_1}, \quad B = \varepsilon l R\sqrt{Da}\frac{p_1}{p\delta q_2}, \quad (17)$$

$$S_s = \frac{1}{p}\left[c_{10} - \frac{\varepsilon\kappa}{\delta}(\chi_c p + a_1\sqrt{p} + a_2)\right], \quad (18)$$

$$\theta_s = \frac{1}{p}\left[T_0 + \frac{\varepsilon l}{\delta}(\chi_T p + b_1\sqrt{p} + b_2)\right], \quad (19)$$

where

$$\varepsilon = \varepsilon_c - c_{1s0}\nu_{s0}\varepsilon_T, \quad \varepsilon_c = J_c(t)|_{t=0}, \quad \varepsilon_T = J_T(t)|_{t=0};$$

$$\delta = g_0 p + g_1\sqrt{p} + g_2;$$

$$g_0 = \kappa\chi_c + c_{1s0}\nu_{s0}l\chi_T, \quad g_1 = \kappa a_1 + c_{1s0}\nu_{s0}lb_1,$$
$$g_2 = \kappa a_2 + c_{1s0}\nu_{s0}lb_2; \quad (20)$$

$$a_1 = \frac{\chi_c}{R}(\sqrt{D} + \sqrt{a}) + \sqrt{D}, \quad a_2 = \frac{\sqrt{Da}}{R^2}(R + \chi_c);$$

$$b_1 = \frac{\chi_T}{R}(\sqrt{D} + \sqrt{a}) + \sqrt{a}, \quad b_2 = \frac{\sqrt{Da}}{R^2}(R + \chi_T).$$

Denoting p as z, we will consider the quadratic trinomial $\delta = g_0 z^2 + g_1 z + g_2$. Its zeros z_1 and z_2 are real and different, since

$$D_\delta = g_1^2 - 4g_0 g_2 = \left[\frac{g_0}{R}(\sqrt{D} - \sqrt{a}) + \kappa\sqrt{D} - c_{1s0}\nu_{s0}l\sqrt{a}\right]^2$$

$$+ 4\kappa c_{1s0}\nu_{s0}l\sqrt{Da} > 0.$$

If

$$\beta_1 = -z_1 = (g_1 - \sqrt{D_\delta})/2g_0,$$

$$\beta_2 = -z_2 = (g_1 + \sqrt{D_\delta})/2g_0$$

are positive quantities, we have

$$\delta = g_0(\sqrt{p} + \beta_1)(\sqrt{p} + \beta_2).$$

By virtue of relationships (15) and (17), functions (13) and (14) can be expressed as

$$S(r, p) = \frac{c_{10}}{p} - \frac{\varepsilon\kappa R\sqrt{Da}}{r}\frac{p_2}{p\delta}\exp(-\alpha_c\sqrt{p}), \quad (21)$$

$$\theta(r, p) = \frac{T_0}{p} - \frac{\varepsilon l R\sqrt{Da}}{r}\frac{p_1}{p\delta}\exp(-\alpha_T\sqrt{p}), \quad (22)$$

where $\alpha_c = (r - R)/\sqrt{D}$ and $\alpha_T = (r - R)/\sqrt{a}$.

The functions that will be frequently used below in the original space are designated as follows:

$$\Phi(\alpha, \beta, t) = \text{erfc}\left(\frac{\alpha}{2\sqrt{t}}\right)$$

$$- \exp(\beta^2 t + \alpha\beta)\text{erfc}\left(\frac{\alpha}{2\sqrt{t}} + \beta\sqrt{t}\right),$$

$$\varphi(\beta, t) = 1 - \Phi(0, \beta, t) = \exp(\beta^2 t)\text{erfc}(\beta\sqrt{t}).$$

Passing to the original space by formulas (18) and (19), we find, respectively, the time dependences of the saturated vapor concentration and temperature on the surface of the drop,

$$c_{1s}(t) = c_{10} - \varepsilon\kappa\left[\frac{a_2}{g_2} + \sum_{j=1}^{2} A_s(\beta_j)\varphi(\beta_j, t)\right], \quad (23)$$

$$T_s(t) = T_0 - \varepsilon l\left[\frac{b_2}{g_2} + \sum_{j=1}^{2} B_s(\beta_j)\varphi(\beta_j, k)\right], \quad (24)$$

where

$$A_s(\beta_j) = \frac{\chi_c\beta_j^2 - a_1\beta_j + a_2}{g_0\beta_j^2 - g_2}, \quad B_s(\beta_j) = \frac{\chi_T\beta_j^2 - b_1\beta_j + b_2}{g_0\beta_j^2 - g_2}.$$

From maps (21) and (22), we find in the original space, respectively, the concentration distribution and temperature field in the medium around the drop,

$$c_1(r, t) = c_{10} - \frac{\varepsilon\kappa\sqrt{D}}{r}\sum_{j=1}^{2} A(\beta_j)\Phi(\alpha_c, \beta_j, t), \quad (25)$$

$$T(r, t) = T_0 - \frac{\varepsilon l\sqrt{a}}{r}\sum_{j=1}^{2} B(\beta_j)\Phi(\alpha_c, \beta_j, t), \quad (26)$$

where

$$A(\beta_j) = \frac{R\beta_1 - \sqrt{a}}{g_0\beta_j^2 - g_2}, \quad B(\beta_j) = \frac{R\beta_j - \sqrt{D}}{g_0\beta_j^2 - g_2}.$$

Up to now, the radius R of the drop was assumed to be constant. Such an assumption, however, is valid only if the weight of the drop far exceeds the weight of the evaporant that left the surface of the drop during the process considered.

It is known [3, 10] that the rate of unsteady variation of the radius is given by the formula

$$\frac{dR}{dt} = \frac{Dnm_1}{\gamma}\frac{\partial c_1}{\partial r}\bigg|_{r=R},$$

where γ is the density of the drop and $(\partial c_1/\partial r)|_{r=R}$ is found from Eq. (25).

Thus, we have

$$\frac{dR}{dt} = \frac{\varepsilon Dnm_1\kappa}{\gamma R^2}\left[\frac{\sqrt{Da}}{g_2} + \sum_{j=1}^{2} C(\beta_j)\varphi(\beta_j, t)\right], \quad (27)$$

where

$$C(\beta_j) = \frac{R^2\beta_j^2 - R(\sqrt{D} + \sqrt{a})\beta_j + \sqrt{Da}}{g_0\beta_j^2 - g_2}.$$

ANALYSIS OF THE SOLUTIONS

Functions (23)–(27) found in the original space linearly depend on $\varepsilon \neq 0$, which is given by expression (20). Then, it is clear that evaporation ($dR/dt < 0$) or condensation growth ($dR/dt > 0$) of an aerosol drop will take place only if $\varepsilon \neq 0$; otherwise, $dR/dt = 0$, as follows from (27).

It is easy to check (for example, using maps (18) and (19) of respective functions (23) and (24)) that the temperature and the saturated vapor concentration on the surface of the drop can be constant iff

$$D = a, \quad \chi_c = \chi_T.$$

Consider the behavior of Eqs. (23) and (24) at $t \longrightarrow 0_+$. In this limit, we have

$$c_{1s}(t) \longrightarrow c_{10} - \frac{\varepsilon\kappa\chi_c}{g_0}, \quad T_s(t) \longrightarrow T_0 + \frac{\varepsilon l\chi_T}{g_0}.$$

Generally, this means that

$$c_{1s}(t)|_{t \to 0_+} \neq c_{1s}(t)|_{t=0} = c_{1s0},$$

$$T_s(t)|_{t \to 0_+} \neq T_s(t)|_{t=0} = T_{s0}.$$

Designating $\Delta c_{1s} = c_{1s}(t)|_{t \to 0_+} - c_{1s}(t)|_{t=0}$, $\Delta T_s = T_s(t)|_{t \to 0_+} - T_s(t)|_{t=0}$, we find that

$$\Delta c_{1s} = \frac{c_{1s0}\nu_{s0}}{g_0}(\varepsilon_c l\chi_T + \varepsilon_T\kappa\chi_c),$$

$$\Delta T_s = \frac{1}{g_0}(\varepsilon_c l\chi_T + \varepsilon_T\kappa\chi_c).$$

Thus, at $t = 0$, functions $c_{1s}(t)$ and $T_s(t)$ experience a jump in the sense adopted in this paper. It can be said that functions (12) experience a similar jump at $t = 0$.

It is of interest to contrast the vapor and temperature distributions at the outer boundary of the Knudsen layer and on the surface of the drop (i.e., inside this layer). From expressions (25) and (26) at $r = R$ (i.e., at the outer boundary of the Knudsen layer), we get

$$c_1(r, t)|_{r=R}$$

$$= c_{10} - \frac{\varepsilon\kappa\sqrt{D}}{R}\left[\frac{\sqrt{a}}{g_2} - \sum_{j=1}^{2} A(\beta_j)\varphi(\beta_j, t)\right], \quad (28)$$

$$T(r, t)|_{r=R}$$

$$= T_0 - \frac{\varepsilon l\sqrt{a}}{R}\left[\frac{\sqrt{D}}{g_2} - \sum_{j=1}^{2} B(\beta_j)\varphi(\beta_j, t)\right]. \quad (29)$$

The difference between the values following from (28), (29) and from (23), (24) is a quantitative measure of the effect of the Knudsen layer.

Let us now discuss at length expression (27) for the rate of unsteady variation of the radius, which was derived for any allowable time from 0 to $+\infty$. Note first of all that formula (27) is a generalization of the formula

$$\frac{dR}{dt} = \frac{\xi}{R + \chi_c}\left[1 + \frac{R}{\chi_c}\varphi(\beta, t)\right], \quad (30)$$

where $\xi = D(c_{1\infty} - c_{1s0})nm_1/\gamma$ and $\beta = (R + \chi_c)\sqrt{D}/\chi_cR$ [1, 2].

Formula (30) follows from (27) at $\nu_{s0} = 0$.

Consider asymptotic expansions of function $\varphi(\beta_j, t)$ for infinitesimal and large values of t,

$$\varphi(\beta_j, t) = \left[1 + \sum_{k=1}^{\infty} \frac{(\beta_j^2 t)^k}{k!}\right]$$

$$\times \left\{1 - 2\beta_j\sqrt{\frac{t}{\pi}}\left[1 + \sum_{m=1}^{\infty} \frac{(-1)^m(\beta_j^2 t)^m}{m!(2m+1)}\right]\right\}, \quad (31)$$

$$\varphi(\beta_j, t)$$

$$= \frac{1}{\beta_j\sqrt{\pi t}}\left[1 + \sum_{m=1}^{\infty} (-1)^m\frac{1 \cdot 3 \cdot \ldots \cdot (2m-1)}{(2\beta_j^2 t)^m}\right]. \quad (32)$$

Leaving the zeroth- and first-order terms in (31) and (32), we get the corresponding approximations of formula (27),

$$\frac{dR}{dt} = \frac{\varepsilon Dnm_1\kappa}{\gamma g_0},$$

$$\frac{dR}{dt} = \frac{\varepsilon Dnm_1\kappa}{\gamma g_0}\left[1 - \frac{2}{g_0}\sqrt{\frac{t}{\pi}}(\kappa\sqrt{D} + c_{1s0}\nu_{s0}l\sqrt{a})\right], \quad (33)$$

$$\frac{dR}{dt} = \frac{\varepsilon Dnm_1\kappa\sqrt{Da}}{\gamma g_0 R^2},$$

$$\frac{dR}{dt} = \frac{\varepsilon Dnm_1\kappa\sqrt{Da}}{\gamma g_0 R^2} \quad (34)$$

$$\times \left[1 + \frac{1}{g_2\sqrt{\pi t}}(\kappa\sqrt{a} + c_{1s0}\nu_{s0}l\sqrt{D})\right].$$

It is worth noting that formulas (34) derived for $t \gg 0$ are the generalizations of the well-known formulas [3, 10]

$$\frac{dR}{dt} = \frac{\xi}{R}, \quad \frac{dR}{dt} = \frac{\xi}{R}\left(1 + \frac{R}{\sqrt{\pi Dt}}\right), \quad (35)$$

which are usually derived by solving only one stationary or, accordingly, nonstationary equation of diffusion that disregards concentration discontinuities (as well as temperature discontinuities, since the process of heat conduction is neglected). Formulas (35) are obtained from (34) at $\chi_c \longrightarrow 0$ and $\nu_{s0} \longrightarrow 0$ ($\chi_T \longrightarrow 0$).

From general formula (27) and formula (33), we find that

$$\lim_{t \to 0_+} \frac{dR}{dt} = \frac{\varepsilon Dnm_1 \kappa}{\gamma g_0}$$

is a finite quantity. At the same time, from the second formula in (35), dR/dt tends to infinity at $t \longrightarrow 0_+$. At $t \longrightarrow +\infty$, we find from (27) and (34) that

$$\frac{dR}{dt} \longrightarrow \frac{\varepsilon Dnm_1 \kappa \sqrt{Da}}{\gamma g_2 R^2}.$$

To gain a better understanding of the effect of the factors taken into consideration in this paper on unsteady evaporation and condensation growth of a spherical drop, let us calculate the rate of change of its radius by formulas (33)–(35) for the case when water drops evaporate ($\varepsilon < 0$, $\xi < 0$) in air. To be brief, we will hereafter write "the rate of evaporation" instead of "the rate of change of the radius of the drop." It is of interest to compare the numerical values of the rate of evapora-

tion that are calculated by newly derived formulas (33) and (34) for infinitesimal and large times not only with each other but also with those calculated by formulas (35). Such a comparison is of value, since expressions (33) and (34) involve the composite coefficients of concentration and temperature discontinuities, while formulas (35), which were derived in terms of earlier theories [3, 10], do not take into account these discontinuities. Moreover, the temperature does not enter into (35) in explicit form. Therefore, when comparing the rates of evaporation found by formulas (33) and (34) with those found by formulas (35), we put $T_0 = T_{s0}$ in (33) and (34) and hence, $\xi = \varepsilon Dnm_1/\gamma$.

Clearly, the first equations in (33)–(35) are easily integrated to give the average rate of evaporation, $v = (R_2 - R_1)/(t_2 - t_1)$. Subscripts 0, ∞, and q used below mean that the velocity is found from the formula for infinitesimal times, that for large times, or the quasi-stationary formula:

$$v_0 = \frac{\xi \kappa}{g_0}, \quad v_\infty = \frac{\xi \kappa}{g_0 + (\kappa + c_{1s0}\nu_{s0}l)R_m}, \quad v_q = \frac{\xi}{R_m},$$

where $R_m = (R_1 + R_2)/2$ is the mean radius.

Putting

$$v_0 = \alpha_{0\infty} v_\infty, \quad v_0 = \alpha_{0q} v_q, \quad v_q = \alpha_{q\infty} v_\infty,$$

we obtain the following expressions for the positive quantities:

$$\alpha_{0\infty} = 1 + (1 + \zeta)\alpha_{0q}, \quad \alpha_{0q} = \frac{\kappa R_m}{g_0},$$

$$\alpha_{q\infty} = 1 + \zeta + \frac{1}{\alpha_{0q}}, \quad (36)$$

where $\zeta = c_{1s0}\nu_{s0}l/\kappa > 0$, from which it follows that

$$|v_\infty| < |v_0|, \quad |v_\infty| < |v_q|.$$

Since α_{0q} is proportional to R_m, the discrepancy between velocities v_0 and v_q also varies in proportion to R_m. The numerical values of $\alpha_{0\infty}$, α_{0q}, and $\alpha_{q\infty}$ that were determined from formulas (36) for $R_m = 1$ μm, 5 μm, and 10 μm are listed in Tables 1–3 for a number of initial temperatures.

Based on $\alpha_{0\infty}$ listed in Table 1, one can argue that the rates of evaporation calculated by the first formulas in (33) and (34) (infinitesimal and large times, respectively) differ substantially. Within the initial temperature interval considered, the ratio between the rates varies insignificantly, while varying considerably with R_m at the same temperature; namely, $|(dR/dt)_\infty|$ sharply decreases with size of the drop. The value of α_{0q} declines with temperature. The values of $\alpha_{q\infty}$ in Table 3 indicate that the ratio between rates v_q and v_∞ is weakly dependent on the size of the drop. Also, the discrepancy between the rates increases with rising initial temperature, being not very large at $T_0 = 283$ K, $v_q \approx 2.5 v_\infty$.

Table 1. Values of coefficient $\alpha_{0\infty} = v_0/v_\infty$

T_0, K		283	293	303	313	323
$R_m \times 10^{-6}$, m	1	7.77	7.19	6.74	6.62	6.64
	5	34.84	31.95	29.72	29.09	29.20
	10	68.69	62.89	58.44	57.17	57.40

Table 2. Values of coefficient $\alpha_{0q} = v_0/v_q$

T_0, K		283	293	303	313	323
$R_m \times 10^{-6}$, m	1	2.80	1.78	1.12	0.73	0.49
	5	13.98	8.90	5.58	3.65	2.45
	10	27.97	17.79	11.17	7.30	4.90

Table 3. Values of coefficient $\alpha_{q\infty} = v_q/v_\infty$

T_0, K		283	293	303	313	323
$R_m \times 10^{-6}$, m	1	2.78	4.04	6.04	9.06	13.55
	5	2.49	3.59	5.32	7.97	11.92
	10	2.46	3.54	5.23	7.83	11.72

Table 4

T_0, K	α
283	0.937
293	0.935
303	0.941
313	0.964
323	1.004

Table 5

T_0, K	$v_0 \times 10$, m/s
283	−6.22
293	−7.79
303	−9.20
313	−10.89
323	−12.78

It turns out that the discrepancies between the rates of evaporation calculated by the first and second formulas in (34) and (35) (for the initial conditions being the same) are nearly identical. To check the validity of this statement, we note that the second formulas differ from the first ones solely in the parenthesized factors. The expression of interest from the second formula in (34) can be represented in the form $1 + \alpha R/\sqrt{\pi D t}$, where $\alpha = (1 + \zeta\sqrt{D/a})/(1 + \zeta + g_0/\kappa R)$. For evaporation of water drops in air at $R = \lambda 10^2$, this expression takes the values given in Table 4.

Parameter R influences α insignificantly, so that we may take $\alpha \approx 1$ irrespective of the size of an evaporating drop. Thus, the expressions that differentiate the second formulas from the first ones in formulas (34) and (35) have nearly the same values for water drops evaporating in air.

The quantitative comparison of the velocities (Tables 1–3) should be complemented by a table of rates of evaporation calculated by one of the formulas discussed under the same initial conditions. For the first of formulas (33), we obtain Table 5, which lists the rates of evaporation of a water drop in dry air for several initial temperatures.
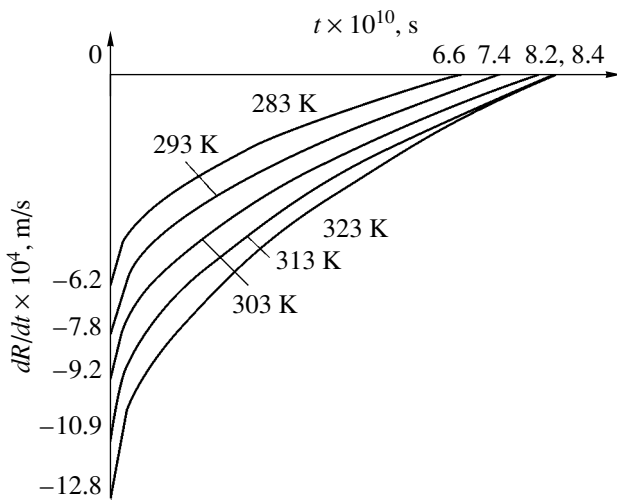
It is noteworthy that, according to this formula, the average and instantaneous rates coincide; that is, $v_0 = (dR/dt)_0$. Note also that general formula (27) for the rate of change of the radius coincides with the right-hand side of the first of formulas (33) in the limit $t \longrightarrow 0_+$. Consequently, it is correct to say that Table 5 lists the rates of evaporation of water drops in dry air at the zero time of the process (at $T_0 = T_{s0}$).

In (33)–(35), it remains for us to analyze the second formula of (33). Unlike the right-hand side of the first formula, that of the second one is time-dependent and, therefore, may shed light on the variation of the radius during the evaporation process. For water drops evaporating in air at different initial temperatures, the second formula of (33) gives dependences plotted in the figure. The rate of evaporation is seen to vanish over a short period of time (less than a nanosecond).

CONCLUSIONS

In this work, we obtained a general (valid for any time scale) expression for the rate of unsteady change of the radius of the drop and derived its approximants for infinitesimal and large times. Taken together, the formulas make it possible to take into account a large number of factors considerably influencing the process. These formulas show that the rate of unsteady evaporation of water drops in air rapidly decreases within a short time interval after the beginning of the process and strongly depends on the initial temperature and size of the drop. Comparing the rates of evaporation calculated by these formulas and by the formulas for quasi-steady and unsteady evaporation from the earlier theories, which ignore concentration and temperature drops, suggests that the latter are of limited applicability and can be replaced by more adequate (more general) formulas obtained in this work.

Figure.

REFERENCES

1. Yu. I. Yalamov and M. K. Kuzmin, Dokl. Akad. Nauk **392**, 44 (2003) [Dokl. Phys. **48**, 474 (2003)].

2. Yu. I. Yalamov and M. K. Kuzmin, Teplofiz. Vys. Temp. **41**, 779 (2003).

3. N. A. Fuks, *Evaporation and Growth of Drops in Gaseous Media* (Akad. Nauk SSSR, Moscow, 1958) [in Russian].

4. Yu. I. Yalamov and V. S. Galoyan, *Dynamics of Drops in Inhomogeneous Viscous Media* (Luǐs, Yerevan, 1985) [in Russian].

5. E. I. Alekhin and Yu. I. Yalamov, *Solution Approaches to Boundary-Value Problems in the Kinetic Theory of Multicomponent Gases near the Condensed Phase* (Moskovsk. Pedagog. Univ., Moscow, 1991) [in Russian].

6. N. Nix and N. Fukuta, J. Chem. Phys. **58**, 1735 (1973).

7. N. B. Vargaftik, *Tables of the Thermophysical Properties of Liquids and Gases* (Nauka, Moscow, 1972; Halsted Press, New York, 1975).

8. G. Dötsch, *Guide to the Applications of Laplace Transforms* (Van Nostrand, London, 1963; Nauka, Moscow, 1965).

9. L. S. Pontryagin, *Ordinary Differential Equations* (Addison-Wesley, London, l962; Nauka, Moscow, 1982).

10. I. Ya. Kolesnik, Kolloidn. Zh. **30**, 527 (1968).

Translated by V. Isaakyan

GASES
AND LIQUIDS

Nonlinear Oscillations of an Uncharged Conducting Drop in an External Uniform Electrostatic Field

S. O. Shiryaeva, M. V. Volkova, and A. I. Grigor'ev

Demidov State University, Sovetskaya ul. 14, Yaroslavl, 150000 Russia
e-mail: grig@uniyar.ac.ru
Received July 16, 2004

Abstract—The problem of nonlinear oscillations of the finite amplitude of an uncharged drop of an ideal incompressible conducting liquid in an external uniform electrostatic field is solved for the first time by analytical asymptotic methods. The problem is solved in an approximation quadratic in amplitude of the initial deformation of the equilibrium shape of the drop and in eccentricity of its equilibrium spheroidal deformation. Compared with the case of nonlinear oscillations of charged drops in the absence of the field, the curvature of the vertices of uncharged drops nonlinearly oscillating in the field is noticeably higher, whereas the number of resonant situations (in the sense of internal resonant interaction of modes) is much smaller. © *2005 Pleiades Publishing, Inc.*

(1) Investigation into free nonlinear oscillations of a charged drop, which was pioneered two decades ago and is being continued today [1–10], is of both scientific and applied value. Researchers have gained better insight into the physics of the oscillations and instability of drops against their self-charge. Unfortunately, the same cannot be said of nonlinear oscillations of a drop placed in an electrostatic field although this physical object is also frequently encountered in many applications. A charged drop in an electric field is much more difficult to treat analytically, because several small parameters are involved in the problem. To date, no efforts to asymptotically investigate the nonlinear oscillations and stability of an uncharged drop in external fields in the second-order approximation (let alone higher order approximations) in oscillation amplitude have been made. A distortion of the equilibrium spherical shape of the drop in external electric, acoustic, and aerodynamic fields, as well as in the field of centrifugal forces, is obviously bound to change the oscillation characteristics, as was noted in [3]. For example, when placed in an electrostatic field, the drop takes a shape that is close to an elongate spheroid. Unfortunately, the oscillations of spheroidal uncharged and charged drops in a uniform external field have been calculated only in the approximation linear in oscillation amplitude [11–16].

A deviation of the equilibrium shape of a spheroidal drop from the shape of an equivoluminar sphere can be considered as a small steady deformation of the spherical shape. As a dimensionless parameter characterizing such a deviation, it is natural to take eccentricity e of the drop. The ratio of the amplitude ξ of capillary oscillations of a spheroidal drop to the radius R of an equivoluminar sphere is taken to be the second small parameter, $\varepsilon \equiv \xi/R$. Actually, calculations of the oscilla-

tions of a spheroidal drop in the first-order approximation in dimensionless oscillation amplitude ε must also include the second-order approximation in eccentricity ε (i.e., in dimensionless electrostatic field strength) [11–16]. Then, using expansions in both small parameters and leaving terms $\sim\varepsilon e^2$ in the solution makes the problem virtually nonlinear.

In asymptotic calculations using several small parameters, one must properly select the orders of smallness of the parameters left. For example, let $\varepsilon \sim e^2$ [13, 14, 16] in the problem considered. Then, calculation in an approximation $\sim\varepsilon e^2$ must also take into account terms $\sim e^2$, which was not done in [13, 14, 16]. Therefore, the results obtained in those papers are incorrect.

If we assume that e^2 is much larger than ε (see [11, 12, 15, 17]), terms $\sim\varepsilon^2$ may be omitted in calculation of order εe^2. However, works [11, 12, 15, 17] were aimed at deriving and analyzing dispersion relations for charged spheroidal drops rather than at studying the time evolution of the initial deformation, which is routine in solving nonlinear problems. The basic result of the studies conducted in an approximation that is linear in oscillation amplitude and quadratic in eccentricity e of the drop (i.e., in an approximation of order εe^2 under the condition that $e^2 \gg \varepsilon$) was a dispersion relation derived for three-dimensional oscillations of an extended charged spheroidal drop. If mode interaction is neglected, the oscillations are given by [15]

$$\omega^2 = -\{n(n-1)(n+2)\alpha_n$$
$$- 3e^2[n^3 + (2n-1)(n+2)\alpha_n]\kappa_n^m\};$$

$$\alpha_n \equiv \left(1 - \frac{W_q}{n+2}\right), \quad W_q \equiv \frac{Q^2}{4\pi R^3 \sigma},$$

$$\kappa_n^m \equiv \frac{[n(n+1) - 3m^2]}{3(2n-1)(2n+3)},$$

where n is the mode number, m is the azimuth eigenvalue, and dimensionless parameter W_q (Rayleigh parameter) characterizes the stability of the drop against its self-charge. The critical value of parameter W_q, $W_q \equiv W_{q*}$, is four [1].

From the above dispersion relation, it is seen that the oscillation frequencies of all modes of a spheroidal drop decline with increasing e. By equating the frequency squared with zero, it is easy to find the critical value of parameter W_q, $W_{q\text{sph}}$ at which an extended spheroidal drop becomes unstable against nonaxisymmetric oscillations as a function of n, m, and the drop eccentricity,

$$W_{q\text{sph}} = (n+2)[1 - (e^2 3n^2 \kappa_n^m /(n-1)(n+2))].$$

At $n = 2$ and $m = 0$, it is easy to obtain an expression for the critical value of parameter W for the fundamental mode of axisymmetric oscillations that specifies the stability of the entire drop, $W_{q\text{sph}} = 4[1 - (2e^2/7)]$.

According to [17], for a drop in the form of an oblate spheroid, the expressions written above remain valid if the eccentricity squared changes sign. In particular, the critical value of parameter W for an oblately spheroidal drop takes the form

$$W_{q\text{sph}}$$
$$= (n+2)\left[1 + e^2 \frac{[n(n+1) - 3m^2]n^2}{(n-1)(n+2)(2n-1)(2n+3)}\right].$$

This expression implies that a charged oblately spheroidal drop is stable against virtual axisymmetric perturbations and nonaxisymmetric perturbations with an azimuth eigenvalue meeting the condition $m^2 \leq (n(n+1)/3)$. Otherwise, $m^2 > (n(n+1)/3)$, nonaxisymmetric modes with corresponding azimuth eigenvalues are unstable. For example, a charged oblately spheroidal drop is unstable against virtual deformations $\sim P_2^2$, P_3^3, and so on.

The aforesaid is also true for nonspheroidal distortions of the equilibrium shapes of drops suspended in an electromagnetic field [18]. In that case, the oscillation spectrum was calculated in the $(\varepsilon\beta)$-order approximation, where β is a small dimensionless parameter characterizing the equilibrium deformation of the drop in a magnetic field and ε is the dimensionless oscillation amplitude.

In this work, we analyze nonlinear oscillations of an uncharged drop placed in a uniform electrostatic field, assuming that $\varepsilon \sim e^2$ and leaving terms $\sim \varepsilon e^2$ and $\sim \varepsilon^2$.

(2) Consider the time evolution of the surface shape of an uncharged liquid drop nonlinearly oscillating in uniform electrostatic field $\mathbf{E}_0$. We assume that the liquid is ideal, incompressible, and perfectly conducting and has density ρ and surface tension coefficient σ.

In the absence of an external field, the drop has a spherical shape of radius R. The presence of weak external electrostatic field $\mathbf{E}_0$ causes a small distortion of the equilibrium shape. In the spherical coordinates, this distortion can be represented in the form of expansion in Legendre polynomials,

$$r(\theta) = R + \sum_{n=0}^{\infty} a_n P_n(\cos(\theta)),$$

where amplitudes a_n ($|a_n| \ll R$) are determined from the pressure balance at the equilibrium surface of the drop. It should be taken into account that electric field pressure p_E, which gives rise the distortion of the equilibrium spherical shape, must have the same order of smallness as the distortion, $p_E \sim E_0^2 \sim a_n$. Writing the pressure of the surface tension forces, $p_\sigma^{(\text{eq})}$, and electric field pressure $p_E^{(\text{eq})}$ up to terms $\sim a_n$,

$$p_\sigma^{(\text{eq})} \approx \frac{2\sigma}{R} - \frac{\sigma}{R^2} \sum_{n=0}^{\infty} (2 - n(n+1)) a_n P_n(\cos(\theta)) + O(a_n^2),$$

$$p_E^{(\text{eq})} \approx \frac{9E_0^2}{8\pi} \cos(\theta) + O(a_n^2)$$

$$\times \frac{3E_0^2}{8\pi} (2P_2(\cos(\theta)) + P_0(\cos(\theta))) + O(a_n^2),$$

and setting up the pressure balance, we obtain

$$r(\theta) \approx R\left(1 + \frac{3E_0^2 R}{16\pi\sigma} P_2(\cos(\theta))\right) + O(E_0^4).$$

Comparing this expression with the equation of a spheroidal surface that is written up to terms $\sim e^2$,

$$r_{\text{sph}} \approx R\left(1 + \frac{1}{3}e^2 P_2(\cos(\theta))\right) + O(e^4),$$

one sees that the equilibrium surface shape of an uncharged drop in a weak electrostatic field may be viewed (up to terms $\sim e^2$) as a spheroid whose eccentricity is related to the field strength as $e^2 = (9E_0^2 R/16\pi\sigma)$.

Note that the dimensionless combination $W_E \equiv E_0^2 R/\sigma$ (the so-called Taylor parameter) characterizes the stability of the drop against its surface charge induced by external uniform electrostatic field E_0. The value of parameter W_E that is critical in terms of such instability, $W_E \equiv W_{E*}$, is equal to ≈ 2.62 [12].

Let an equilibrium weakly spheroidal drop with eccentricity e initially ($t = 0$) undergo axisymmetric perturbation $\xi(\theta, t)$ of fixed amplitude ε that is considerably smaller than the radius of the drop. Our goal is to find the resulting spectrum of capillary oscillations of the drop (i.e., the shape of the drop) at $t > 0$. We assume that the drop is always axisymmetric. Then, in the spherical coordinate system with the origin at the center of mass of the drop, the equation for the surface of the drop written in dimensionless variables such that $\rho = \sigma = R = 1$ has the form

$$r(\theta, t) = r(\theta) + \xi(\theta, t)$$
$$= 1 + \frac{1}{3}e^2 P_2(\cos(\theta)) + \xi(\theta, t); \tag{1}$$

$$e^2 = \frac{9E_0^2}{16\pi}; \quad |\xi| \ll 1.$$

The flow of the liquid in the drop that is caused by the distortion of the equilibrium surface is assumed to be potential with velocity field potential $\psi(\mathbf{r}, t)$. The velocity field is defined via potential gradient as $\mathbf{V}(\mathbf{r}, t) = \mathrm{grad}(\psi(\mathbf{r}, t))$. Assuming that the velocities of hydrodynamic flows in the drop are much lower than the propagation velocity of electromagnetic interactions, we will consider the electric field near the drop as electrostatic and describe it through potential $\Phi(\mathbf{r}, t)$, which, in turn, is related to field strength $\mathbf{E}$ by the well-known relationship $\mathbf{E} = -\mathrm{grad}(\Phi)$.

The mathematical statement of the problem is as follows:

$$\Delta\psi(\mathbf{r}, t) = 0; \quad \Delta\Phi(\mathbf{r}, t) = 0; \tag{2}$$

$$r \longrightarrow 0: \psi(\mathbf{r}, t) \longrightarrow 0; \tag{3}$$

$$r \longrightarrow \infty: \Phi(\mathbf{r}, t) \longrightarrow -E_0 r\cos(\theta); \tag{4}$$

$$r = r(\theta) + \xi(\theta, t): \frac{\partial\xi}{\partial t} = \frac{\partial\psi}{\partial r} - \frac{1}{r^2}\frac{\partial\xi}{\partial\theta}\frac{\partial\psi}{\partial\theta}; \tag{5}$$

$$\Delta p - \frac{\partial\psi}{\partial t} - \frac{1}{2}(\nabla\psi)^2 + p_E = p_\sigma; \tag{6}$$

$$\Phi(\mathbf{r}, t) = \Phi_S(t); \tag{7}$$

$$\int_V r^2 dr\sin\theta d\theta d\varphi = \frac{4}{3\pi}; \tag{8}$$

$$V = [0 \le r \le r(\theta) + \xi(\theta, t), 0 \le \theta \le \pi, 0 \le \varphi \le 2\pi];$$

$$\int_V \mathbf{e_r} \cdot r^3 dr\sin\theta d\theta d\varphi = 0; \tag{9}$$

$$\oint_V (\mathbf{n} \cdot \nabla\Phi)ds = 0, \tag{10}$$

$$S = [r = r(\theta) + \xi(\theta, t), 0 \le \theta \le \pi, 0 \le \varphi \le 2\pi];$$

$$t = 0: \xi(\theta, t) = \xi_0 P_0(\cos(\theta))$$

$$+ \xi_1 P_1(\cos(\theta)) + \varepsilon\sum_{i \in \Xi} h_i P_i(\cos(\theta)), \tag{11}$$

$$\frac{\partial\xi(\theta, t)}{\partial t} = 0; \quad \sum_{i \in \Xi} h_i = 1.$$

Here, Δ is the Laplacian (except for the symbol before pressure p). Conditions (8) and (9) must be fulfilled at any (including the initial) time instant. Therefore, at $t = 0$, they specify the amplitudes of the zeroth, ξ_0, and first, ξ_1, modes in the expansion of initial perturbation $\xi(\theta)$ in Legendre polynomials; that is, the amplitudes of the zeroth and first modes are specified by the initial deformation rather than being arbitrary.

In expressions (6)–(11), Δp is the difference between the constant pressures inside and outside the drop in equilibrium;

$$P_E = \frac{1}{8\pi}(\nabla\Phi)^2,$$

the electric field pressure; $p_\sigma = \mathrm{div}_S\mathbf{n}$, the pressure of surface tension forces (div_S is the surface divergence); $\mathbf{n}$, the unit normal to the surface given by (1); $\Phi_S(t)$, the electric potential that is constant over the surface; ε, the amplitude of the initial perturbation of the surface shape (small parameter of the problem); h_i is the coefficient defining the partial contribution of an ith vibrational mode to the initial perturbation; Ξ, a set of the numbers of initially excited vibrational modes; and

$$\xi_0 \approx -\sum_{i \in \Xi}\left[\varepsilon^2\frac{h_i^2}{(2i+1)} + \varepsilon e^2\frac{2}{15}h_i\delta_{i,2}\right] + O(\varepsilon^3); \tag{12}$$

$$\xi_1 \approx -\sum_{i \in \Xi}\left[\varepsilon^2\frac{9ih_{i-1}h_i}{(2i-1)(2i+1)} + \varepsilon e^2\frac{9}{35}h_i\delta_{i,3}\right] + O(\varepsilon^3)$$

are the constants determined from conditions (8) and (9) at the zero time up to terms $\sim\varepsilon e^2$ and $\sim\varepsilon^2$.

To simplify the following mathematics and easily separate out terms due to the spheroidal shape of the equilibrium drop in final expressions, we introduce a formal parameter β, $e^2 \approx \beta\varepsilon$. Since it was assumed that $e^2 \sim \varepsilon$, $\beta \sim 1$. This parameter is needed only in order that the product $\varepsilon\beta$ can be changed to e^2. It is remembered, in addition, that, when seeking for the equilibrium shape of the drop in the field, we obtained the relationship between the eccentricity and electric field strength, which has the form

$$e^2 = \frac{9}{16\pi}E_0^2$$

in the dimensionless variables.

(3) To find a solution to the problem stated, we will apply the method of many scales, as was done previously in [1–10, 12–14, 16, 18]. Desired functions $\xi(\theta, t)$, $\psi(\mathbf{r}, t)$, and $\Phi(\mathbf{r}, t)$ are represented in the form of

expansions in powers of small parameter ε and are considered to be dependent not merely on time t but on various time scales introduced via small parameter ε: $T_m \equiv \varepsilon^m t$ ($m = 0, 1, 2, \ldots$). We restrict our consideration to the quadratic approximation and so will look for dependences of the desired quantities only on two time scales T_0 and T_1,

$$\xi(\theta, t) = \varepsilon \xi^{(1)}(\theta, T_0, T_1) + \varepsilon^2 \xi^{(2)}(\theta, T_0) + O(\varepsilon^3);$$

$$\psi(\mathbf{r}, t) = \varepsilon \psi^{(1)}(\theta, T_0, T_1) + \varepsilon^2 \psi^{(2)}(\theta, T_0) + O(\varepsilon^3); \quad (13)$$

$$\Phi(\mathbf{r}, t) = \varepsilon^{1/2}(\Phi^{(0)}(r, \theta) + \varepsilon \Phi^{(1)}(r, \theta, T_0))O(\varepsilon^{5/2}).$$

The electric field potential is expanded in half-integer powers of parameter ε, since $E_0 \sim \varepsilon^{1/2}$. Component $\Phi^{(0)}(r, \theta)$ of the potential defines the equilibrium weakly spheroidal shape of the drop in the field,

$$\Phi^{(0)}(r, \theta) = \left(\frac{16\pi}{9}\beta\right)\frac{1}{r^2}(1 - r^3)\cos(\theta), \quad (14)$$

while increment $\Phi^{(1)}(r, \theta, T_0)$ characterizes the distortion of the equilibrium surface.

The pressures of the electric field, p_E, and surface tension forces, p_σ, entering in dynamic boundary condition (6), are given by the following expansions:

$$p_E = p_E^{(eq)} + \varepsilon^2 p_E^{(2)}(\xi) + O(\varepsilon^3),$$
$$p_\sigma = p_\sigma^{(eq)} + \varepsilon p_\sigma^{(1)}(\xi) + \varepsilon^2 p_\sigma^{(2)}(\xi) + O(\varepsilon^3), \quad (15)$$

where components

$$p_E^{(eq)} = \frac{\varepsilon}{8\pi}(\nabla\Phi^{(0)})^2\Big|_{r = r(\theta)} \text{ and } p_\sigma^{(eq)} = \text{div}_S \overline{n^{(eq)}}\Big|_{r = r(\theta)}$$

are independent on perturbation $\xi(\theta, t)$, being the pressures at the equilibrium surface of the spheroidal drop. They meet the equilibrium pressures balance

$$r = r(\theta): \Delta p + p_E^{(eq)} = p_\sigma^{(eq)} \quad (16)$$

and, consequently, cancel one another.

Substituting expansions (13) and (15) into the set of Eqs. (2)–(11) yields a set of boundary-value problems of different orders of smallness for finding functions $\xi^{(m)}$, $\psi^{(m)}$ ($m = 1, 2$), and $\Phi^{(1)}$. It is obvious that each of functions $\psi^{(m)}$ and $\Phi^{(1)}$ has to satisfy linear equations (2).

Solutions to Eqs. (2) for the first- and second-order functions meeting conditions (3) and (4) are written in the form

$$\psi^{(m)}(r, \theta, T_0, T_1)$$

$$= \sum_{n = 1}^{\infty} D_n^{(m)}(T_0, T_1)r^n P_n(\cos(\theta)) \; (m = 1, 2); \quad (17)$$

$$\Phi^{(1)}(r, \theta, T_0) = \sum_{n = 0}^{\infty} F_n^{(1)}(T_0)r^{-(n+1)}P_n(\cos(\theta)).$$

Corrections to the equilibrium surface of the drop are also represented in the form of expansions in Legendre polynomials,

$$\xi^{(m)}(\theta, T_0, T_1) = \sum_{n = 0}^{\infty} M_n^{(m)}(T_0, T_1)P_n(\cos(\theta)) \quad (18)$$
$$(m = 1, 2).$$

(4) A set of equations for first-order coefficients $D_n^{(1)}(T_0, T_1)$ and $M_n^{(1)}(T_0, T_1)$ in the solutions obtained for hydrodynamic potential $\psi^{(1)}(r, \theta, T_0, T_1)$ and surface perturbation $\xi^{(1)}(\theta, T_0, T_1)$ is derived from boundary conditions (5), (6), (8), and (9) after grouping the terms linear in parameter ε, which specify the distortion of the equilibrium shape.

Recall that relationships (16) must be taken into account in the expansion of dynamic boundary condition (6). Because of this, the set of the first-order boundary conditions for $D_n^{(1)}(T_0, T_1)$ and $M_n^{(1)}(T_0, T_1)$ that is derived from (5) and (6) is no different from a set for first-order coefficients in the problem of oscillations of an uncharged spherical drop in the absence of an external field,

$$r = 1: \frac{\partial\xi^{(1)}}{\partial T_0} - \frac{\partial\psi^{(1)}}{\partial r} = 0; \quad \frac{\partial\psi^{(1)}}{\partial T_0} + p_\sigma^{(1)}(\xi) = 0,$$

where

$$p_\sigma^{(1)}(\xi) \equiv -(2 + \Delta_\theta)\xi^{(1)}; \quad \Delta_\theta \equiv \frac{1}{\sin\theta}\frac{\partial}{\partial\theta}\left(\sin\theta\frac{\partial}{\partial\theta}\right).$$

(i) After straightforward transformations, we get differential equations in coefficients $M_n^{(1)}(T_0, T_1)$,

$$\frac{\partial M_n^{(1)}(T_0, T_1)}{\partial T_0^2} + \omega_n^2 M_n^{(1)}(T_0, T_1) = 0; \quad (19)$$
$$\omega_n^2 = n(n-1)(n+2).$$

The solutions to Eqs. (19) are harmonic functions of time T_0 (at $n \geq 2$) with T_1-dependent coefficients,

$$M_n^{(1)}(T_0, T_1) = A_n^{(1)}(T_1)\exp(i\omega_n T_0) + \text{c.c.}; \quad (20)$$
$$A_n^{(1)}(T_1) = a_n^{(1)}(T_1)\exp(ib_n^{(1)}(T_1)).$$

Hereafter, c.c. means terms complex conjugate to the terms written and $a_n^{(1)}(T_1)$ and $b_n^{(1)}(T_1)$ are real functions for which the T_1 dependence can be found from consideration of the problem in the next order of smallness.

From conditions (8) and (9), written in the linear approximation in ε, it follows that

$$M_0^{(1)}(T_0, T_1) = 0; \quad M_1^{(1)}(T_0, T_1) = 0. \quad (21)$$

Note that expressions (21) do not contradict (19) at $n = 0$ and 1.

(ii) Equations in coefficients $F_n^{(1)}(T_0)$ appearing in solution (17) are derived from conditions (7) and (10) by grouping terms $\sim \varepsilon^{3/2}$, which are due to distortion $\xi(\theta, t)$ of the equilibrium spheroidal shape,

$$r = 1: \Phi^{(1)} + \frac{\partial \Phi^{(0)}}{\partial r}\xi^{(1)} = \Phi_S^{(1)};$$

$$\int_0^\pi \left[\frac{\partial \Phi^{(1)}}{\partial r} + \frac{\partial}{\partial r}\left(r^2 \frac{\partial \Phi^{(0)}}{\partial r}\right)\xi^{(1)} - \frac{\partial \Phi^{(0)}}{\partial \theta}\frac{\partial \xi^{(1)}}{\partial \theta}\right]\sin(\theta)d\theta = 0.$$

Substituting the expressions for $\Phi^{(0)}$ and $\Phi^{(1)}$ into these expressions yields

$$F_n^{(1)}(T_0) = \sqrt{16\pi}\beta[K_{1,n+1,n}M_{n+1}^{(1)}(T_0)$$
$$+ K_{1,n-1,n}M_{n-1}^{(1)}(T_0)] \quad (n > 0); \quad (22)$$

$$F_0^{(1)}(T_0) = 0; \quad \Phi_S^{(1)} = 0; \quad K_{lmn} = [C_{l0m0}^{n0}]^2,$$

where C_{l0m0}^{n0} are the Clebsch–Gordan coefficients.

(5) (i) A set of the second-order boundary conditions that is derived from (5) and (6) will contain both terms quadratic in surface perturbation $\xi(\theta, t)$ and those allowing for interaction between perturbation $\xi(\theta, t)$ and the equilibrium shape of the spheroidal drop,

$$r = 1: \frac{\partial \xi^{(2)}}{\partial T_0} - \frac{\partial \psi^{(2)}}{\partial r} = -\frac{\partial \xi^{(1)}}{\partial T_1}$$

$$+ \frac{\partial^2 \psi^{(1)}}{\partial r^2}\left(\xi^{(1)} + \frac{\beta}{3}P_2(\cos(\theta))\right) - \frac{\partial \xi^{(1)}}{\partial \theta}\frac{\partial \psi^{(1)}}{\partial \theta};$$

$$\frac{\partial \psi^{(2)}}{\partial T_0} + p_\sigma^{(2)}(\xi) = p_E^{(2)}(\xi) - \frac{\partial \psi^{(1)}}{\partial T_1}$$

$$- \frac{\partial^2 \psi^{(1)}}{\partial r \partial T_0}\left(\xi^{(1)} + \frac{\beta}{3}P_2(\cos(\theta))\right) - \frac{1}{2}\left(\left(\frac{\partial \psi^{(1)}}{\partial r}\right)^2 + \left(\frac{\partial \psi^{(1)}}{\partial \theta}\right)^2\right);$$

where

$$p_\sigma^{(2)}(\xi) = -(2 + \Delta_\theta)\xi^{(2)} + 2\xi^{(1)}(1 + \Delta_\theta)\xi^{(1)}$$

$$- 2\frac{\beta}{2}P_2(\cos(\theta))(4 - \Delta_\theta)\xi^{(1)};$$

$$p_E^{(2)}(\xi) = \frac{1}{8\pi}\left[\frac{\partial}{\partial r}((\nabla\Phi^{(0)})^2)\xi^{(1)} + 2\nabla\Phi^{(0)} \cdot \nabla\Phi^{(1)}\right].$$

Substituting lower order solutions (14), (17), (18), and (20)–(22) into the above equations, we obtain, after

tedious transformations, an equation for desired second-order coefficients $M_n^{(2)}(T_0)$,

$$\frac{\partial M_n^{(2)}(T_0)}{\partial T_0^2} + \omega_n^2 M_n^{(2)}(T_0) = \left[-2i\omega_n\frac{dA_n^{(1)}(T_1)}{dT_1}\right.$$

$$+ \beta G1(n)A_n^{(1)}(T_1)\Bigg]\exp(i\omega_n T_0)$$

$$+ \beta[G2(n)A_{n+2}^{(1)}\exp(i\omega_{n+2}T_0)$$

$$+ G3(n)A_{n-2}^{(1)}\exp(i\omega_{n-2}T_0)]$$

$$+ \sum_{l=2}^\infty\sum_{m=2}^\infty \{(\gamma_{lmn} + \omega_l\omega_m\eta_{lmn})A_l^{(1)}A_m^{(1)}$$

$$\times \exp(i(\omega_l + \omega_m)T_0) + (\gamma_{lmn} - \omega_l\omega_m\eta_{lmn})$$

$$\times A_l^{(1)}\overline{A_m^{(1)}}\exp(i(\omega_l - \omega_m)T_0)\} + (c.c.);$$

$$G1(n) \equiv \frac{n}{3}[(3n(n+1) - 10)K_{2,n,n}$$

$$+ 12(nK_{1,n-1,n}K_{1,n,n-1}$$

$$+ (n+2)K_{1,n+1,n}K_{1,n,n+1}) - 8]; \quad (23)$$

$$G2(n) \equiv \frac{1}{3}[(n^3 + 3n^2 - 10n - 8)K_{2,n+2,n}$$

$$+ 12n(n+2)K_{1,n+1,n}K_{1,n+2,n+1}];$$

$$G3(n) \equiv \frac{n}{3}[(5n^2 - 21n + 14)K_{2,n-2,n}$$

$$+ 12nK_{1,n-1,n}K_{1,n-2,n-1}];$$

$$\gamma_{lmn} = K_{lmn}[\omega_m^2(n - m + 1) + 2n(m(m+1) - 1)]$$

$$+ \alpha_{lmn}\frac{1}{m}\omega_m^2;$$

$$\eta_{lmn} = K_{lmn}\left(\frac{n}{2} - m + 1\right) + \alpha_{lmn}\frac{1}{m}\left(1 + \frac{n}{2l}\right);$$

$$\alpha_{lmn} = -\sqrt{l(l+1)m(m+1)}C_{l0m0}^{n0}C_{l(-1)m1}^{n0}.$$

It is remembered that the Clebsch–Gordan coefficients are different from zero only if their subscripts meet the conditions

$$|l - m| \leq n \leq (l + m);$$
$$(l + m + n) = 2g \quad (g = 1, 2, 3, \ldots). \quad (24)$$

In order that a solution to Eq. (23) be free of secular terms (i.e., terms indefinitely increasing with time), it is necessary that the inhomogeneity function (the right of (23)) be free of terms proportional to $\exp(i\omega_n T_0)$ (i.e., of terms describing a periodic external action with fre-

quency ω_n equal to the natural frequency of an *n*th mode). To this end, the condition

$$-2i\omega_n \frac{dA_n^{(1)}(T_1)}{dT_1} + \beta G1(n)A_n^{(1)}(T_1) = 0, \qquad (25)$$

from which one can find the dependences of the first-order amplitudes on "slow" time T_1, must be met. Expressing $A_n^{(1)}(T_1)$ in (25) via real functions $a_n^{(1)}(T_1)$ and $b_n^{(1)}(T_1)$ and requiring that the real and imaginary parts of the equation vanish, one easily obtains

$$a_n^{(1)}(T_1) = a_n^{(0)}, \quad b_n^{(1)}(T_1) = -\frac{\beta}{2\omega_n}G1(n)T_1 + b_n^{(0)},(26)$$

where $a_n^{(0)}$ and $b_n^{(0)}$ are constants determined from the initial conditions.

With (26), one can write, instead of (20), an expression for amplitudes $M_n^{(1)}(T_0, T_1)$ that includes the dependences on both time scales,

$$M_n^{(1)}(t) = 2a_n^{(0)}\cos\left[\left(\omega_n - \frac{e^2}{2\omega_n}G1(n)\right)t + b_n^{(0)}\right]. \quad (27)$$

Solving Eqs. (23) subject to relation (25), we obtain an expression for amplitudes $M_n^{(2)}(T_0)$ ($n \le 2$),

$$M_n^{(2)}(T_0) = A_n^{(2)}\exp(i\omega_n T_0)$$
$$+ \beta[\mu_{n+2}A_{n+2}^{(1)}\exp(i\omega_{n+2}T_0)$$
$$+ \mu_{n-2}A_{n-2}^{(1)}\exp(i\omega_{n-2}T_0)] \qquad (28)$$
$$\times \sum_{l=2}^{\infty}\sum_{m=2}^{\infty}\{\lambda_{lmn}^{(+)}A_l^{(1)}A_m^{(1)}\exp(i(\omega_l+\omega_m)T_0)$$
$$+ \lambda_{lmn}^{(-)}A_l^{(1)}\overline{A_m^{(1)}}\exp(i(\omega_l-\omega_m)T_0)\} + (\text{c.c.}),$$

where

$$\mu_{n+2} = \frac{G2(n)}{(\omega_n^2-\omega_{n+2}^2)}, \quad \mu_{n-2} = \frac{G3(n)}{(\omega_n^2-\omega_{n-2}^2)},$$

$$\lambda_{lmn}^{(\pm)} = \frac{(\gamma_{lmn}\pm\omega_l\omega_m\eta_{lmn})}{[\omega_n^2-(\omega_l\pm\omega_m)^2]}.$$

Note that, since this quadratic-in-ε approximation allows us to find the dependences of coefficients $M_n^{(2)}$ only on time scale T_0, it suffices to take in (28) that $A_n^{(2)} = a_n^{(2)}\exp(ib_n^{(2)})$, where $a_n^{(2)}$ and $b_n^{(2)}$ are real constants. The dependences of coefficients $A_j^{(1)}$ on time T_1 may be disregarded in this case; i.e., $A_j^{(1)} = a_j^{(0)}\exp(ib_j^{(0)})$.

Considering the terms due to perturbation $\xi(\theta, t)$ of the equilibrium surface of the spheroidal drop in the second order of smallness in ε, we can find, from conditions (8) and (9), expressions for nonlinear corrections to the amplitudes of the zeroth- and first-order modes,

$$M_0^{(2)}(T_0) = -\frac{2}{15}\beta M_2^{(1)}(T_0) - \sum_{n=2}^{\infty}\frac{1}{(2n+1)}[M_n^{(1)}(T_0)]^2,$$

$$M_1^{(2)}(T_0) = -\frac{9}{35}\beta M_3^{(1)}(T_0) \qquad (29)$$

$$-\sum_{n=2}^{\infty}\frac{9n}{(2n-1)(2n+1)}M_{n-1}^{(1)}(T_0)M_n^{(1)}(T_0),$$

(ii) With expansions (13) substituted into initial conditions (11), the latter transform into a set of equations for functions ξ in the first and second order of smallness,

$$t = 0: \xi^{(1)}(\theta, t) = \sum_{i \in \Xi}h_i P_i(\cos(\theta)); \quad \frac{\partial\xi^{(1)}(\theta, t)}{\partial T_0} = 0;$$

$$\xi^{(2)}(\theta, t) = \frac{1}{\varepsilon^2}[\xi_0 P_0(\cos(\theta)) + \xi_1 P_1(\cos(\theta))];$$

$$\frac{\partial\xi^{(2)}(\theta, t)}{\partial T_0} = -\frac{\partial\xi^{(1)}(\theta, t)}{\partial T_1}.$$

From these equations, one can find real constants $a_n^{(0)}$, $b_n^{(0)}$, $a_n^{(2)}$, and $b_n^{(2)}$ appearing in (27) and (28).

Satisfying the initial conditions in the first approximation in ε, we obtain $a_n^{(0)} = \frac{1}{2}h_i\delta_{n,i}$ and $b_n^{(0)} = 0$ ($i \in \Xi$, $n = 0, 1, 2, \ldots$); in the second approximation in ε, we find

$$a_n^{(2)} = -\frac{\beta}{2}\sum_{i \in \Xi}h_i(\mu_{n+2}\delta_{i,n+2} + \mu_{n-2}\mu_{i,n-2})$$

$$-\frac{1}{4}\sum_{i \in \Xi}\sum_{j \in \Xi}h_ih_j(\lambda_{ijn}^{(+)} + \lambda_{ijn}^{(-)}); \quad b_n^{(2)} = 0,$$

where $\delta_{n,i}$ is the Kronecker delta.

Using these expressions, we write the first- and second-order amplitudes in expansion (18) for the shape of the vibrating drop in the final form,

$$M_n^{(1)}(t) = \delta_{n,i}h_i\cos\left[\left(\omega_n - \frac{e^2}{2\omega_n}G1(n)\right)t\right];$$

$$M_0^{(2)}(t)$$

$$= -\sum_{i \in \Xi} \left[\frac{2}{15} \beta \delta_{i,2} h_i \cos(\omega_i t) + \frac{h_i^2}{(2i+1)} (\cos(\omega_i t))^2 \right];$$

$$M_1^{(2)}(t) = -\sum_{i \in \Xi} \left[\frac{9}{35} \beta \delta_{i,3} \cos(\omega_i t) \right.$$

$$\left. + \frac{9 i h_{i-1} h_i}{(2i-1)(2i+1)} \cos(\omega_{i-1} t) \cos(\omega_i t) \right] \ (\forall n \geq 2),$$

$$(30)$$

$$M_n^{(2)}(t) = \sum_{i \in \Xi} h_i \beta \{ \delta_{i,n+2} \mu_{n+2} [\cos(\omega_{n+2} t) - \cos(\omega_n t)]$$

$$+ \delta_{i,n-2} \mu_{n-2} [\cos(\omega_{n-2} t) - \cos(\omega_n t)] \}$$

$$+ \frac{1}{2} \sum_{i \in \Xi} \sum_{j \in \Xi} h_i h_j \{ \lambda_{lijn}^{(+)} [\cos((\omega_i + \omega_j) t) - \cos(\omega_n t)]$$

$$+ \lambda_{lijn}^{(-)} [\cos((\omega_i - \omega_j) t) - \cos(\omega_n t)] \}.$$

Thus, with (1), (13), and (18), we find an analytical expression for the shape of the oscillating surface of an uncharged drop exposed to an external uniform electric field as follows:

$$r(\theta, t) = 1 + \frac{1}{3} e^2 P_2(\cos(\theta)) + \varepsilon \sum_{n=0}^{\infty} M_n^{(1)}(t) P_n(\cos(\theta))$$

$$(31)$$

$$+ \varepsilon^2 \sum_{n=0}^{\infty} M_n^{(2)}(t) P_n(\cos(\theta)) + O(\varepsilon^3),$$

where amplitude coefficients $M_n^{(i)}(t)$ $(i = 1,2)$ are defined by (30).

Figures 1a and 3a show the calculated (by (31)) nonlinearly oscillating shapes of an uncharged conducting drop in uniform electrostatic field E_0 (at $W_E \approx 0.5 W_{E*}$). The zero time ($t = 0$) is represented by the thin curve, while the thick curve corresponds to $t = (2\pi/\omega_2)$, that is, to the situation at the end of the oscillation period of the fundamental mode ($n = 2$). For comparison, Figs. 1b and 3b show the calculated [5] nonlinearly oscillating shapes of a charged drop for $W_q \approx 0.5 W_{q*}$ at the same initial deformation and at the same time instants. It is easy to see that the curvature of the vertices, as well as the field strength and the probability of initiating a corona discharge [19] near the surface of a nonlinearly oscillating drop, increases with the number of modes responsible for the initial deformation of the drop. Other conditions being equal (i.e., the Rayleigh and Taylor parameters being roughly equal to half their critical values), the curvature of the vertices of uncharged drops in a uniform electrostatic field is larger than for charged drops in the absence of the field.

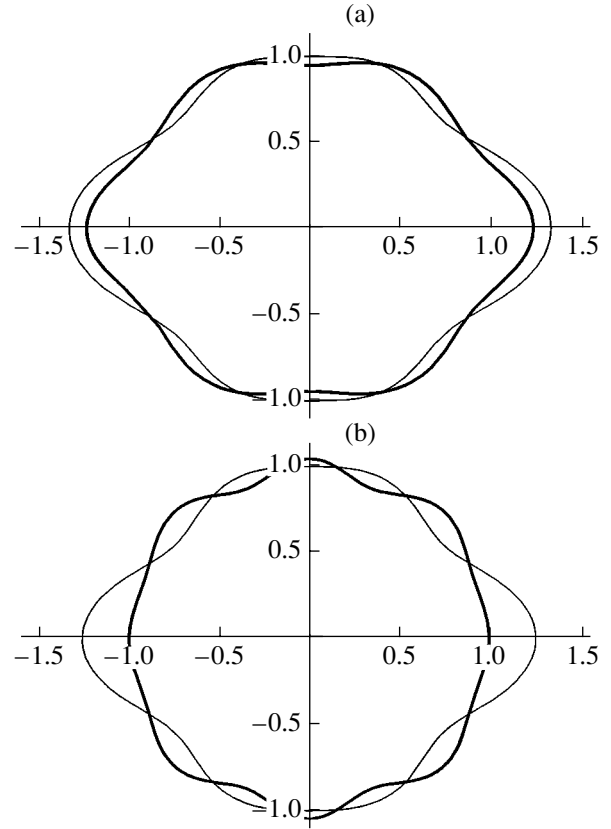(6) From expressions (30) and (31) for nonlinear amplitude corrections $M_n^{(2)}$ and from the form of coef-

Fig. 1. Contours of the nonlinearly oscillating shape of the drop at the zero time (thin curve) and at the end of the oscillation period of the fundamental mode (thick curve) for the case when the initial deformation is specified by a superposition of the fourth and sixth modes at $h_4 = h_6 = 0.5$ and $\varepsilon = 0.25$. (a) Uncharged drop in a uniform external electrostatic field and (b) charged drop.

ficients $\lambda_{lijn}^{(\pm)}$ (see (28)), it is seen that nonlinear corrections $M_n^{(2)}$ to the oscillation amplitude exhibit a resonance: when $\omega_n^2 - (\omega_l \pm \omega_m)^2 = 0$ (the frequencies are defined by relationship (19)), they diverge, indicating an internal resonant interaction between nth, lth, and mth modes [6, 8]. Calculations show that there exist only two resonant situations at $n, l, m < 100$: $n = 8, l = m = 5$ and $n = 16, l = m = 10$. Both resonances are degenerate and take place when the shape of an uncharged spherical drop executes nonlinear oscillations [20]. In the third order of smallness in oscillation amplitude, the frequencies in the resonance condition $\omega_n^2 - (\omega_l \pm \omega_m)^2 = 0$ are obviously defined by relationships allowing for the influence of the external field (with regard to corrections for sphericity),

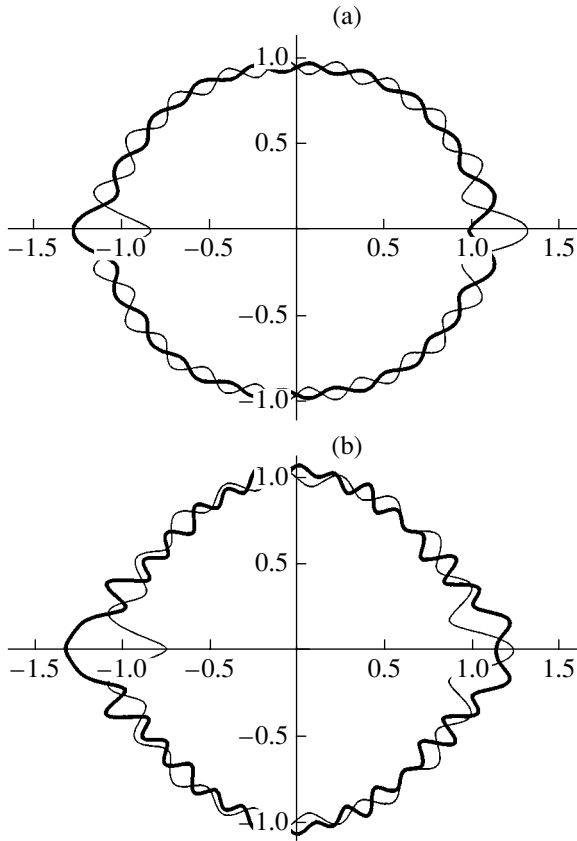$$\sqrt{n(n-1)(n+2)} - \frac{e^2}{2\sqrt{n(n-1)(n+2)}} G1(n),$$

(a)

(b)

Fig. 2. Same as in Fig.1 when the initial deformation is specified by the 19th mode alone at $h_{19} = 1$ and $\varepsilon = 0.25$.
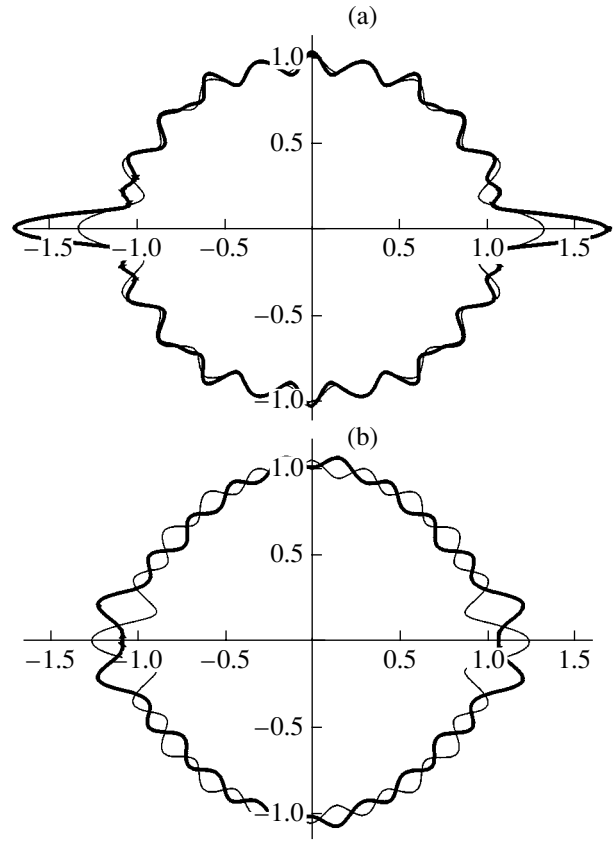

(a)

(b)

Fig. 3. Same as in Fig.1 when the initial deformation is specified by the 20th mode at $h_{20} = 1$ and $\varepsilon = 0.25$.

(see (27)), or, equivalently,

$$\sqrt{n(n-1)(n+2)} - \frac{9E_0^2}{32\pi\sqrt{n(n-1)(n+2)}}G1(n).$$

In such a case, the number of resonances increases drastically; however, this situation is more appropriate to study in the third order of smallness.

(7) In the above analysis, it has been assumed that the field-induced eccentricity squared has the same order of smallness as the surface oscillation amplitude, $e^2 \sim \varepsilon$. It should be noted, however, that these parameters are independent. Moreover, for example, drops in thunderstorm clouds are featured by an oblongness of several tenths of the drop radius, which can be considered as a quantity of the zeroth order of smallness. If the problem under consideration is stated under the assumption that $e^2 \gg \varepsilon$, the second-order electric field pressure component

$$p_E^{(2)}(\xi) = \frac{1}{8\pi}\left[\frac{\partial}{\partial r}((\nabla\Phi^{(0)})^2)\xi^{(1)} + 2\nabla\Phi^{(0)} \cdot \nabla\Phi^{(1)}\right]$$

should be viewed as a first-order parameter and included into the set of boundary conditions for the first-order amplitudes,

$$r = 1: \frac{\partial\xi^{(1)}}{\partial T_0} - \frac{\partial\psi^{(1)}}{\partial r} = 0;$$

$$\frac{\partial\psi^{(1)}}{\partial T_0} - p_E^{(2)}(\xi) + p_\sigma^{(1)}(\xi) = 0.$$

In this case, instead of (19), we arrive at the differential equation

$$\frac{\partial M_n^{(1)}(t)}{\partial T_0^2} + \omega_n^2 M_n^{(1)}(t) - n\frac{3E_0^2}{4\pi}[A(n)M_{n-2}^{(1)}(t) \qquad (32)$$
$$+ C(n)M_{n+2}^{(1)}(t)] = 0,$$

where the frequency is defined by the expression

$$\omega_n^2 \equiv n\left[(n-1)(n+2) - \frac{3E_0^2}{4\pi}B(n)\right]$$
$$\equiv n\left[(n-1)(n+2) - \frac{4e^2}{3}B(n)\right]. \qquad (33)$$

In (32) and (33),

$$A(n) \equiv -4K_{2,n-2,n} + 3nK_{1,n-1,n}K_{1,n-2,n-1};$$

$$B(n) \equiv -4K_{2,n,n} + 3(nK_{1,n-1,n}K_{1,n,n-1}$$
$$+ (n+2)K_{1,n+1,n}K_{1,n,n+1}) - 2;$$

$$C(n) \equiv -4K_{2,n+2,n} + 3(n+2)K_{1,n+1,n}K_{1,n+2,n+1}.$$

If mode interaction in Eq. (32) is neglected (that is, the terms $\sim M_{n-2}^{(1)}(t)$ and $M_{n+2}^{(1)}(t)$ are omitted), expression (33) turns into a dispersion relation for the problem of surface oscillations of an uncharged drop exposed to a uniform electrostatic field on the assumption $e^2 \gg \varepsilon$.

CONCLUSIONS

It is shown that nonlinear oscillations of an uncharged drop of an electrically conducting liquid in an external uniform electrostatic field are qualitatively similar to nonlinear oscillations of a charged drop (see [1–10]). The quantitative discrepancy is associated with the equilibrium sphericity of the drop in the field. The most considerable difference between the physical objects compared that is revealed in the calculations of the second order of smallness in oscillation amplitude shows up as an appreciable decrease in the number of resonant situations for nonlinear oscillations of an uncharged drop in the field.

REFERENCES

1. J. A. Tsamopoulos and R. A. Brown, J. Fluid Mech. **147**, 373 (1984).
2. J. A. Tsamopoulos, T. R. Akylas, and R. A. Brown, Proc. R. Soc. London, Ser. A **401**, 67 (1985).
3. R. Natarayan and R. A. Brown, Proc. R. Soc. London, Ser. A **410**, 209 (1987).
4. Z. C. Feng, J. Fluid Mech. **333**, 1 (1997).
5. S. O. Shiryaeva, Izv. Ross. Akad. Nauk, Mekh. Zhidk. Gaza, No. 3, 173 (2001).
6. S. O. Shiryaeva, Zh. Tekh. Fiz. **72** (4), 15 (2002) [Tech. Phys. **47**, 673 (2002)].
7. S. O. Shiryaeva, Zh. Tekh. Fiz. **73** (2), 19 (2003) [Tech. Phys. **48**, 152 (2003)].
8. S. O. Shiryaeva, Pis'ma Zh. Tekh. Fiz. **29** (17), 28 (2003) [Tech. Phys. Lett. **29**, 714 (2003)].
9. A. N. Zharov, S. O. Shiryaeva, and A. I. Grigor'ev, Zh. Tekh. Fiz. **73** (12), 9 (2003) [Tech. Phys. **48**, 1511 (2003)].
10. S. O. Shiryaeva, A. N. Zharov, and A. I. Grigor'ev, Zh. Tekh. Fiz. **74** (1), 10 (2004) [Tech. Phys. **49**, 8 (2004)].
11. K. J. Cheng, Phys. Lett. A **112**, 392 (1985).
12. A. I. Grigor'ev and O. A. Sinkevich, Izv. Akad. Nauk SSSR, Mekh. Zhidk. Gaza, No. 6, 10 (1985).
13. Z. C. Feng, Quarterly Appl. Math. **47**, 555 (1990).
14. Z. C. Feng and K. V. Beard, Proc. R. Soc. London **430**, 133 (1990).
15. S. O. Shiryaeva and A. I. Grigor'ev, Zh. Tekh. Fiz. **66** (9), 12 (1996) [Tech. Phys. **41**, 865 (1996)].
16. Z. C. Feng and K. V. Beard, J. Fluid Mech. **227**, 429 (1991).
17. A. I. Grigor'ev and S. O. Shiryaeva, Zh. Tekh. Fiz. **69** (7), 10 (1999) [Tech. Phys. **44**, 745 (1999)].
18. A. Bratz and I. Egry, J. Fluid Mech. **298**, 341 (1995).
19. A. I. Grigor'ev, S. O. Shiryaeva, and M. V. Volkova, Zh. Tekh. Fiz. **73** (11), 31 (2003) [Tech. Phys. **48**, 1389 (2003)].
20. J. A. Tsamopolos and R. A. Brown, J. Fluid Mech. **127**, 519 (1983).

Translated by N. Mende

GASES
AND LIQUIDS

Decay of Longitudinal Pressure Oscillations in a Cylindrical Cell

A. A. Pikulev

All-Russia Research Institute of Experimental Physics, Russian Federal Nuclear Center,
Sarov, Nizhni Novgorod Oblast, 607190 Russia
e-mail: pikulev@expd.vniief.ru
Received June 9, 2004

Abstract—Longitudinal acoustic oscillations in a cylindrical cell are considered. The temperature and velocity distributions over a periodically unsteady boundary layer are found. An expression for the characteristic decay time of pressure oscillations is derived. © 2005 Pleiades Publishing, Inc.

INTRODUCTION

Longitudinal pressure oscillation in cylindrical cavities is a widespread phenomenon. A typical example is wind instruments, such as a flute, organ, etc., where sounding is based on the self-oscillation effect [1]. The timbre (tone quality) depends on the instrument material and design, as well as on the manner of sound extracting. Also, the timbre is known to depend on the acoustic power distribution over higher spectral harmonics. Next, the spectral radiation power depends on the difference between the energy spent by an external source per unit time to generate a given harmonic and the dissipation power. Finally, the dissipation power is related primarily to the effects of viscosity and heat conduction and depends on the geometry of the acoustic resonator.

Along with wind instruments, longitudinal pressure oscillations (which inevitably pose threats) are observed in water pipes, where these pressure waves are also associated with the self-oscillation effect [2].

One more example is hermetically sealed cells of nuclear-pumped lasers, where longitudinal pressure waves are due to longitudinally nonuniform impulsive heating of the gas mixture [3]. After the impulse, damped pressure oscillations are observed in the cells [4, 5]. The pressure specifies the amount of energy introduced into the lasing medium and characterizes gas-dynamic processes taking place in the laser cell. Therefore, it is usually used as a key parameter in testing the results of numerical simulation of gas dynamics in nuclear-pumped lasers. On the other hand, numerical simulation of damped longitudinal pressure oscillations is rather difficult. This is because the dimension of the problem rises and two length scales appear in the direction normal to the side walls of the cell: the mainstream flow and the much thinner boundary layer. These features of the flow may introduce large errors into the simulation results: in [4], making allowance for the effect of numerical viscosity [6] led to much faster decay of pressure oscillations than was observed in the experiments.

This author suggests a gas-dynamic model of longitudinal acoustic pressure oscillations in a cylindrical cell. This model makes it possible to describe the structure of a temperature–velocity boundary layer with periodically unsteady temperature and velocity and derive a simple expression for the characteristic time of pressure wave decay.

1. BASIC EQUATIONS

A complete system of gas-dynamic equations consists of the equations of conservation of momentum and energy, as well as the continuity equation. With the dissipation energy neglected, the system is written as [7, 8]

$$
\begin{cases}
\partial_t \rho \mathbf{u} + (\nabla \cdot \mathbf{u})\rho \mathbf{u} = -\nabla p + (\nabla \cdot \mu \nabla)\mathbf{u} + \nabla\{\mu(\nabla \cdot \mathbf{u})\}/3 \\
\partial_t \rho + (\nabla \cdot \rho \mathbf{u}) = 0 \\
\partial_t\{p/(\gamma - 1) + \rho \mathbf{u}^2/2\} \\
+ (\nabla \cdot \mathbf{u}\{\gamma p/(\gamma - 1) + \rho \mathbf{u}^2/2\}) = (\nabla \cdot \lambda \nabla)T.
\end{cases}
\tag{1}
$$

Here, $\mathbf{u} \equiv (u, v, w)$, ρ, T, and p are the velocity vector, density, temperature, and pressure of the gas, respectively; μ is the dynamic viscosity; λ is the thermal conductivity; and γ is the adiabatic exponent.

Let coordinate axis $0z$ be directed parallel to the generatrix of the cylindrical surface and the cell length be $2L$. The geometry of the problem is shown in Fig. 1.

Consider pressure oscillations in an acoustic approximation, assuming that the following relationships are valid:

$$\begin{cases} \rho = \rho_0 + \Delta\rho, & |\Delta\rho| \ll \rho_0 \\ p = P_0 + \Delta p, & |\Delta p| \ll P_0. \end{cases} \quad (2)$$

Here, P_0 and ρ_0 are the mean pressure and density of the gas in the cell.

Using Eq. (2) and neglecting second- and higher-order terms, we obtain from system (1)

$$\begin{cases} \rho_0 \partial_t \mathbf{u} = -\nabla(\Delta p) + \mu \nabla^2 \mathbf{u} + \mu \nabla(\nabla \cdot \mathbf{u})/3 \\ \partial_t \Delta\rho + \rho_0(\nabla \cdot \mathbf{u}) = 0 \\ \partial_t \Delta p + \gamma P_0 (\nabla \cdot \mathbf{u}) = (\gamma - 1)\lambda \nabla^2 T. \end{cases} \quad (3)$$

The main reasons for longitudinal pressure oscillation decay are viscous stresses at the side walls of the cell (the effect of viscosity) and heat conduction through these walls (the effect of heat conduction). Since the pressure varies periodically, the effects of viscosity and heat conduction are significant only in the near-wall region (boundary layer) with characteristic size δ. Below, we assume that all the linear dimensions of the cell (length, width, and radius of curvature of the side walls) are much larger than the characteristic thickness of the temperature–velocity boundary layer. With this condition satisfied, the influence of the cross-sectional shape on the structure of the boundary layer may be neglected in Eqs. (3) and the boundary layer may be considered as locally planar. Moreover, in Eqs. (3), the terms due to longitudinal diffusion may be neglected in comparison with those of transverse diffusion; i.e., we may put $\nabla^2 \approx \nabla^2_{x,y}$, where $\nabla^2_{x,y} = \partial^2_{xx} + \partial^2_{yy}$ is the transversal Laplace operator.

Because of the presence of the boundary layer, the pressure distribution over the cross section of the cell is nonuniform even if longitudinal acoustic waves alone are excited. The characteristic time of pressure transverse relaxation is $\tau \sim \delta/\upsilon$, where υ is the speed of sound. Similarly, the characteristic time of pressure longitudinal relaxation is $T \sim L/\upsilon$, which is much longer than the transverse relaxation time, $T \gg \tau$. Therefore, the pressure distribution over the cross section of the cell may be regarded uniform on time scales exceeding the transverse relaxation time.

To derive an equation for the pressure, we average system (3) over cross section S of the cell. Taking into consideration attachment conditions at the side walls and neglecting the longitudinal viscosity and thermal conductivity (which are much lower than the transverse parameters), we recast the first and third equations in
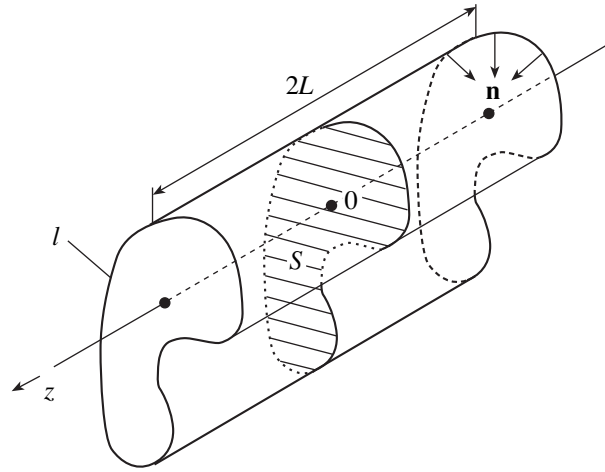
Fig. 1. Schematic of the cylindrical cell.

(3) (normal n is directed into the cell) as

$$\begin{cases} \rho_0 \partial_t \langle w \rangle = -\partial_z \Delta p - \dfrac{1}{S} \oint_l \mu \dfrac{\partial w}{\partial n} dl \\ \dfrac{\partial_t \Delta p}{\gamma - 1} + \dfrac{\gamma P_0 \partial_z \langle w \rangle}{\gamma - 1} = -\dfrac{1}{S} \oint_l \lambda \dfrac{\partial T}{\partial n} dl. \end{cases} \quad (4)$$

Here, $\langle \ldots \rangle$ means averaging over the cross section and l is the cross-sectional perimeter.

The correction to the pressure satisfies the relationship $\langle \Delta p \rangle \cong \Delta p$. From system (4), we obtain an inhomogeneous wave equation for the pressure,

$$\partial^2_{tt} \Delta p - \upsilon^2 \partial^2_{zz} \Delta p$$
$$= -\frac{\gamma - 1}{S} \frac{\partial}{\partial t} \oint_l \lambda \frac{\partial T}{\partial n} dl + \frac{\gamma P_0}{\rho_0 S} \frac{\partial}{\partial z} \oint_l \mu \frac{\partial w}{\partial z} dl. \quad (5)$$

The pressure, temperature, and density of an ideal gas are related by the Clapeyron ideal gas law [7]. In the acoustic approximation, it has the form

$$\Delta p/(\gamma - 1) = c_v T_0 \Delta\rho + c_V \rho_0 \Delta T. \quad (6)$$

Here, c_v is the specific heat at constant volume; T_0 is the gas mean temperature in the cell, which is equal to the wall temperature; and ΔT is the temperature correction, $T = T_0 + \Delta T$.

Using Eq. (6) and the continuity equation (the second equation in system (3)), we bring the momentum equation along axis $0z$ and energy equation into the form

$$\begin{cases} \rho_0 \partial_t w = -\partial_z \Delta p + \mu \nabla^2_{x,y} w \\ c_p \rho_0 \partial_t \Delta T = \partial_t \Delta p + \lambda \nabla^2_{x,y} \Delta T, \end{cases} \quad (7)$$

where c_p is the specific heat at constant pressure.

Equations (5) and (7) constitute a closed system of integro-differential equations of damped longitudinal pressure oscillations in the acoustic approximation.

Let us solve this system under the assumption of weak decay. In this case, a solution to Eq. (5) is the interference of standing waves with slowly varying amplitudes P_n,

$$\Delta p = \sum_{n=1}^{\infty} P_n \cos(k_n z) \exp(i\omega_n t + i\varphi_n), \quad (8)$$

where $k = \pi n/L$ is the wavenumber, $\omega_n = k_n \upsilon$ is the circular frequency of an nth oscillation mode, and φ_n is the oscillation phase.

In Eq. (8), the boundary conditions at the end faces of the cell are $\partial_z \Delta p(t, \pm L) = 0$. From the condition of slow decay, the condition $|\partial_t P_n| \ll \omega_n P_n$ follows; therefore, the pressure in system (7) has the form of (8) and amplitudes P_n may be regarded as time-independent (quasi-stationary).

2. CALCULATION OF VISCOUS FORCE AND HEAT FLUX TO THE WALL OF THE CELL

Since system (7) is linear, a general solution to it can be sought as a superposition of solutions for pressure waves of type

$$p_n = P_n \exp(i\omega_n t \pm i k_n z + i\varphi_n) \quad (9)$$

(for convenience of calculations, here traveling waves are used instead of standing ones), where the plus and minus signs refer to waves propagating from right to left and vice versa, respectively.

Standing waves (8) result when two counterpropagating waves with equal amplitudes superpose. Substi-

Fig. 2. Distribution of the temperature and velocity in the boundary layer (the figures by the curves indicate the mode number).

tuting Eq. (9) into system (7) yields

$$\begin{cases} \rho_0 \partial_t w_n = \pm i k_n p_n + \mu \partial_{xx}^2 w_n \\ c_p \rho_0 \partial_t T_n = i\omega_n p_n + \lambda \partial_{xx}^2 T_n \end{cases} \quad (10)$$

(here, x is the coordinate along the inner normal to the wall; $x = 0$ at the wall). As boundary conditions for system (10), we use the attachment condition $w_n(0, z, t) = 0$ and the equality of the gas and wall temperatures, $T_n(0, z, t) = 0$. At infinity, the velocity and temperature are set finite, $|w_n(+\infty, z, t)| < \infty$ and $|T_n(+\infty, z, t)| < \infty$. Below, we are interested in a solution at $t \longrightarrow \infty$, i.e., only in a particular solution to system (10). Therefore, initial conditions are omitted. A solution of system (10) is sought in the form

$$\begin{cases} w_n = W_n(x) \exp(i\omega_n t \pm i k_n z + i\varphi_n), \\ T_n = T_n(x) \exp(i\omega_n t \pm i k_n z + i\varphi_n). \end{cases} \quad (11)$$

Substituting Eqs. (9) and (11) into system (10) yields the following differential equations for amplitudes W_n and $\hat{T}_n$:

$$\begin{cases} \mu \partial_{xx}^2 W_n - i\omega_n \rho_0 W_n = \mp i k_n P_n \\ \lambda \partial_{xx}^2 \hat{T}_n - i\omega_n c_p \rho_0 \hat{T}_n = -i\omega_n P_n. \end{cases} \quad (12)$$

Particular solutions to system (12) subject to the boundary conditions mentioned above are

$$\begin{cases} W_n = \pm P_n(1 - \exp\{-x(i+1)(\omega_n/2\nu)^{1/2}\})/\rho_0 \upsilon \\ \hat{T}_n = P_n(1 - \exp\{-x(i+1)(\omega_n/2\chi)^{1/2}\})/c_p \rho_0, \end{cases} \quad (13)$$

where $\nu = \mu/\rho_0$ is the kinematic viscosity and $\chi = \lambda/c_p\rho_0$ is the diffusivity.

It is seen from system (13) that the thickness of the boundary layer for an nth mode in the case of steady pressure oscillations is time-independent and equals $\delta_n^\upsilon = (2\nu/\omega_n)^{1/2}$ for the velocity boundary layer and $\delta_n^T = (2\chi/\omega_n)^{1/2}$ for the temperature boundary layer. The velocity–temperature distribution for several oscillation modes in the boundary layer is shown in Fig. 2. This distribution is uniquely described by the function $f_n(x) = 1 - \exp(-x/\delta_n)\cos(x/\delta_n)$.

From Eqs. (11) and (13), one can easily determine the viscous stress acting on the wall of the cell and the heat flux density through the wall. The phases of both are $\pi/4$ ahead of that of the pressure,

$$\begin{cases} \mu \partial_x w_n(0, z, t) = \pm p_n(\nu\omega_n)^{1/2} \exp(i\pi/4)/\upsilon \\ \lambda \partial_x T_n(0, z, t) = p_n(\chi\omega_n)^{1/2} \exp(i\pi/4). \end{cases} \quad (14)$$
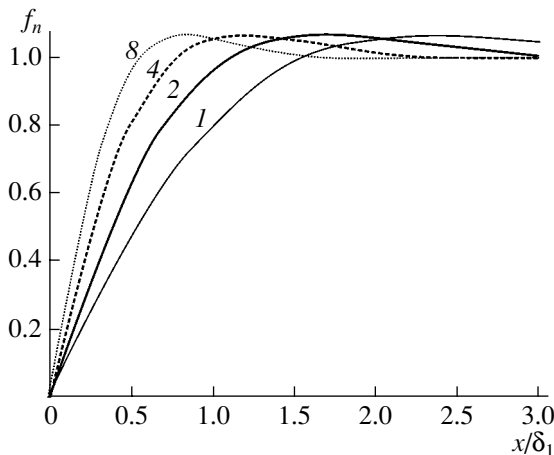
Parameters of the fundamental mode of pressure oscillations in the laser cells of the LUNA-2M setup [9] for several inert gases

	He		Ne		Ar	
P_0, atm	1	2	0.7	1	0.25	0.5
δ_1^v, mm	0.29	0.21	0.30	0.25	0.35	0.25
δ_1^T, mm	0.35	0.25	0.35	0.3	0.42	0.3
τ_1, ms	13	19	29	35	34	49
$\Delta\omega_1/\omega_1$, %	3.0	2.1	3.0	2.5	3.6	2.5

3. PRESSURE OSCILLATION DECAY

To determine the rate of pressure oscillation decay, we substitute expressions (14) for the viscous stress and heat flow density into Eq. (5). Taking into account the condition of slowly varying pressure oscillation amplitude, $|\partial_t P_n| \ll \omega_n P_n$, we arrive at the equation

$$\partial_{tt}^2 p_n - \upsilon^2 \partial_{zz}^2 p_n$$
$$= -ilp_n\omega_n^{3/2}\{\nu^{1/2} + (\gamma - 1)\chi^{1/2}\}\exp(i\pi/4)/S. \tag{15}$$

Note that the form of Eq. (15) does not depend on the traveling wave direction; i.e., the time variation of the oscillation amplitude is identical for both traveling and standing waves. A solution to Eq. (15) is sought in the form

$$p_n = P_n\exp(i\omega_n t - i\Delta\omega_n t - ik_n z - t/\tau_n), \tag{16}$$

where $\Delta\omega_n \ll \omega_n$ is the oscillation frequency pulling and $\tau_n \gg 1/\omega_n$ is the characteristic decay time of pressure oscillations for an nth mode.

Substituting Eq. (16) into Eq. (15) and neglecting terms of the second order of smallness yields the final expression

$$1/\tau_n = \Delta\omega_n = l\omega_n^{1/2}\{\nu^{1/2} + (\gamma - 1)\chi^{1/2}\}/\{2^{3/2}S\}. \tag{17}$$

It follows from Eq. (17) that higher modes decay faster ($\tau_n \sim 1/n^{1/2}$) than lower ones; as a result, the free oscillation spectrum degenerates to the fundamental mode with time.

Thus, taking into account viscosity and heat conduction generates two effects: (i) exponential decay of pressure oscillations and (ii) oscillation frequency pulling. The second effect is weak and may be neglected in most cases. It follows from Eq. (17) that the characteristic decay time increases with cross-sectional area of the cell. For example, in the case of a circular cell, $\tau_n \sim r$, where r is the radius of the cell.

The table lists a number of characteristic parameters for the fundamental mode of pressure oscillations for several inert gases for a LUNA-2M laser setup [9]. The total length of the laser cells is 2.4 m; the cross-sectional area, $S = 2.1 \times 10^{-3}$ m²; and the cross-sectional perimeter, $l = 0.48$ m [9]. In the calculation, we took $T_0 = 300$ K. In this case, the contribution of heat conduction to the rate of pressure oscillation decay is about 45%, while that of viscosity is about 55%. It is seen from the table that the thickness of the temperature–velocity boundary layer equals two- or three-tenths of a millimeter; the typical decay time, several tens of milliseconds; and the relative oscillation frequency pulling, several percent. These values are typical of hermetically sealed cells used in nuclear-pumped lasers.

REFERENCES

1. *Musics Encyclopedia: A Dictionary*, Ed. by G. V. Keldysh (Sov. Éntsiklopediya, Moscow, 1990) [in Russian].
2. A. D. Girgidov, *Fluid Mechanics (Hydraulics)* (St. Petersb. State Polytech. Univ., St. Petersburg, 2003) [in Russian].
3. A. A. Sinyanskii and S. P. Melnikov, Proc. SPIE **3686**, 43 (1999).
4. A. A. Androsenko, P. A. Androsenko, N. V. Gusev, and P. P. D'yachenko, in *Proceedings of the Conference "Physics of Nuclear-Excited Plasma and Nuclear-Pumped Lasers," Obninsk, 1993*, Vol. 2, pp. 23–44.
5. J. R. Torczynski, R. J. Gross, G. N. Hays, *et al.*, Nucl. Sci. Eng. **101**, 280 (1989).
6. C. A. J. Fletcher, *Computational Techniques for Fluid Dynamics* (Springer-Verlag, New York, 1988; Mir, Moscow, 1991), Vol. 2.
7. L. G. Loitsyansky, *Mechanics of Liquids and Gases* (Nauka, Moscow, 1973; Begell House, New York, 1995).
8. L. D. Landau and E. M. Lifshitz, *Course of Theoretical Physics*, Vol. 6: *Fluid Mechanics* (Nauka, Moscow, 1986; Pergamon, New York, 1987).
9. A. M. Voinov, L. E. Dovbysh, V. N. Krivonosov, *et al.*, Vopr. At. Nauki Tekh., Ser.: Fiz. Yad. Reaktorov, Nos. 2–3, 63 (2000).

Translated by M. Astrov

=================== **SOLIDS** ===================

Pulsed Magnetic Technique of Material Testing under Impulsive Loading

S. I. Krivosheev

St. Petersburg State Polytechnical University, ul. Politekhnicheskaya 29, St. Petersburg, 195251 Russia
e-mail: ksi@SK3153.spb.edu
Received May 26, 2004

Abstract—A pulsed magnetic technique for generating mechanical pressure impulses is developed. Using this technique, polymethyl methacrylate and gabbrodiabase are tested in various loading schemes. It is shown that the experimental data are reasonable to analyze in terms of a structure-and-time approach. © *2005 Pleiades Publishing, Inc.*

Material fracture is a complex process involving different scale levels, as follows from the extensive body of fractographic and X-ray diffraction data taken from materials subjected to rupturing loads. In statics, rupturing loads are routinely described in terms of the static strength and cracking resistance (stress intensity factor) of a material. Under dynamic loading, one more coordinate, time, appears, which makes the process description more difficult: fracture now proceeds not only on different scale levels but also evolves in time. It has been shown in a number of works that the strain-rate dependences of the strength and cracking resistance, which also traditionally characterize the material at fracture, are valid for only a particular loading scheme (see, e.g., [1]). In other situations, they cannot adequately describe the material behavior.

An account of fracture under dynamic loading can be given with the approach developed in [2]. The basic static parameters (strength and cracking resistance) are complemented by a parameter characterizing the process evolution in time: the incubation (structural) time to fracture. Within this time interval, which is a material characteristic, the damage builds up and reaches a critical level under threshold loads. Processes preceding fracture on the macrolevel may differ considerably: emergence of dislocations at grain boundaries (in metals), rotation of molecular globules, formation of voids, etc. In dynamic, as also in static, tests, threshold loads causing fracture of the material on the macrolevel are determined given the parameters of a loading impulse.

PULSED MAGNETIC LOADING TECHNIQUE

Central to investigating material fracture under impulsive loading are knowledge of the pressure impulse parameters and application of loading schemes such that the stressed state can be determined by solving relevant problems of continuum mechanics.

The available methods of determining the pressure impulse in a solid may be divided into two major groups. The first one embraces those methods in which the loading impulse parameters are found from the velocity of the specimen's free surface. The velocity (or displacement) of the free boundary may be measured, e.g., by a laser interferometer or with a capacitive or inductive sensor. The methods of this group share the following drawbacks: the need for reconstructing the pressure impulse from the free surface velocity under the assumption that elastic perturbations arising in the material under loading are small (the acoustic approximation) and the need for special loading schemes to determine a particular stressed state. The second group covers the methods using pressure transducers, which generate a signal depending on the pressure impulse parameters. The complicated amplitude–frequency response (AFR) of the transducers provides reliable measurements only in narrow time and amplitude intervals. Therefore, one must have a set of transducers with AFRs fitting well different parts of the amplitude–frequency spectrum of the signal expected.

One can greatly simplify analysis of material fracture by applying a pulsed magnetic method to generate a loading impulse. It is known that the current passing in conductors generates a magnetic field and, interacting with this field, gives rise to a ponderomotive force. Generally, the direction and distribution of the acting forces depend on the current distribution over the cross section of the conductors, as well as on their geometry and arrangement. In a perfect conductor, a unit surface is subjected to the force (magnetic pressure)

$$\bar{\mathbf{P}}_{\mathrm{m}} = \frac{1}{2}[\bar{\mathbf{J}} \times \bar{\mathbf{B}}], \qquad (1)$$

which is directed normally to it. Here, $\bar{\mathbf{J}}$ and $\bar{\mathbf{B}}$ are the surface current density and magnetic induction at a point on the surface.

In the case of plane-parallel s-thick wires h distant from each other ($h \ll b$, where b is the width of the wires), the edge effect can be neglected (accurate to the order of h/b) and the current (magnetic pressure) distribution may be assumed to be uniform [3]. Then, the instantaneous value of magnetic pressure P_m is given by

$$P_{\mathrm{m}} = \frac{1}{2}\frac{I}{b}B = \frac{1}{2}H\mu H = \frac{B^2}{2\mu}, \qquad (2)$$

where B is the magnetic induction and μ is the permeability (for a nonmagnetic material, $\mu = \mu_0 = 4\pi \times 10^{-7}$ H/m).

To reduce the error in pressure impulse determination that is due to the compression work of the wires, their thickness is minimized through the current integral

$$I_{\mathrm{c}} = \int\limits_0^{t_{\mathrm{c}}} (I(t)/(sb))^2 dt, \qquad (3)$$

where $I(t)$ and t_{c} are the instantaneous current and the time of its action, respectively.

The ultimate value of the current integral at which, e.g., copper is still in the solid phase equals 0.89×10^{17} A^2 s/m^4 [4].

At a certain relationship between the dimensions of the plane wires, their inductance can be minimized and the energy may be rapidly introduced into the magnetic field of the system.

Discharge of a capacitor bank directly through a low-inductance load, specifically, through a set of plane wires or a one-turn solenoid, is the most efficient and simplest way of generating high current pulses.

For the given configuration, the shape of the pressure impulse depends on that of the current passing in the plane wires. In the equivalent circuit of a pulsed current generator (PCG) (Fig. 1), the transient is described by the equation

$$L\frac{d^2 I}{dt^2} + \frac{d(RI)}{dt} + \frac{1}{C}I = 0, \qquad (4)$$

provided that the inductance is constant. This equation is solvable under the initial ($t = 0$) conditions $I = 0$, $U = U_0$, and $dI/dt = U_0/L$, where L, R, and C are the inductance, resistance, and capacitance of the circuit, respectively; U_0 is the voltage across the capacitor; and I is the current in the circuit.

A nonlinear resistor inserted in the current circuit greatly affects the shape of the current pulses. In particular, it makes it possible to generate unipolar current pulses. In the technology of high pulsed currents, nonlinear resistors made of Vilit, Tervit, and zinc oxide have gained most acceptance [5–7].

As a pulsed current source, we used a specially designed PCG that forms current pulses of amplitude to
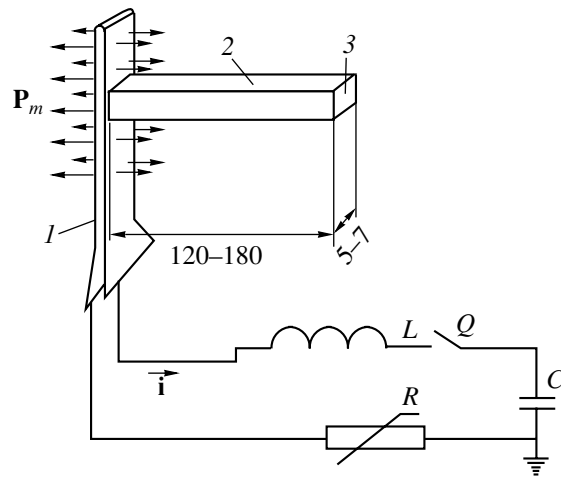

Fig. 1. Pulsed current generator and loading scheme. (*1*) Loading unit, (*2*) test specimen, and (*3*) mirror plane. L, inductance; C, capacitance; and R, nonlinear resistance.

1.2 MA with a pulse rise time of 1.5 µs at an inductive load of 25 nH [8]. The shape of the pulse is controlled using a set of 16-mm-high resistors (Vilit disks) of diameter 72 mm. Precalibrated resistors from one lot that were used in the experiments had the I–V characteristic of form

$$U_R = a_0 h_R \left|\frac{I}{s_R}\right|^\alpha \mathrm{sgn}(I), \qquad (5)$$

where $a_0 = 1100$ [V cm^{-1}(A/s m^2)$^{-\alpha}$] and $\alpha = 0.14$ [V A$^{-\alpha}$ s m$^{2\alpha-1}$] are the material parameters and h_R and S_R are, respectively, the height and cross-sectional area of the resistor.

To reduce the inductance of the resistor set, four parallel-connected branches with two disks in each were applied.

INTEROMETRIC TEST

If the current is uniformly distributed over the cross section of b-wide wires, the parameters of the pressure impulse acting on the wires and the parameters of the current pulse are uniquely related by expression (2).

To check the correspondence between the magnetic pressure impulse and the pressure impulse applied to the specimen, we used the method of laser interferometry. The test specimen is covered by a reflecting coating (evaporated aluminum). A loading assembly (plane wires) is mounted on the opposite side of the specimen and tightly pressed against it. Castor oil is used to improve the acoustic contact. The dimensions of the loading assembly provide generation of a plane compression shock wave in the specimen, and the size of the specimen excludes the arrival of surface waves at the detection zone throughout the measurement process.
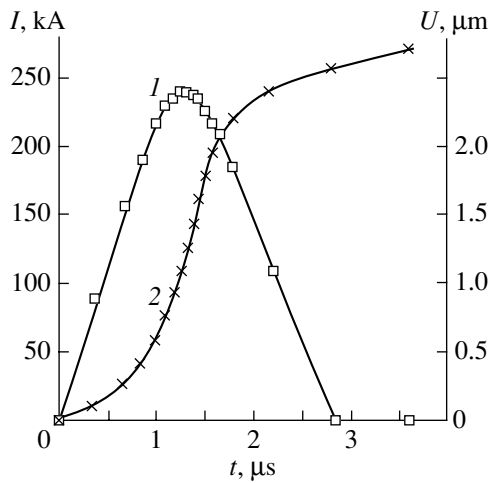
Fig. 2. (*1*) Current *I* in the load and (*2*) displacement *U* of the free surface of the sphere-plastic specimen.

Fig. 3. (*1*) Magnetic pressure impulse and (*2*) mechanical pressure impulse recovered from the measured free boundary velocity.

The interferometer used in the experiments was similar to a two-channel Michelson interferometer and measured the displacement of the reflecting surface [9]. The signal was recorded with a TDS-457C oscilloscope.

Laser interferometry allows one not only to detect the shape of a loading impulse but also to measure the velocity of a longitudinal wave in the material. Figure 2 shows the current pulse in the sphere-plastic specimen and the displacement of its free surface that are reconstructed from the interferogram.

In the acoustic approximation, the displacement velocity of a boundary may be set equal to the double mass velocity of particles in an incident wave [10]. Differentiating the free surface displacement with respect to time, one can determine the mass velocity of the particles and reconstruct the pressure impulse, using the simple relationship

$$P = \rho C_1 u/2, \qquad (6)$$

where ρ_0 is the density of the material, C_1 is the speed of sound in the material, and u is the velocity of the free surface.

Figure 3 shows the magnetic pressure impulse corresponding to the current in Fig. 2 and the mechanical pressure impulse reconstructed by the above technique from the time dependence of the free surface displacement (see also Fig. 2). Test specimens were made of polymethyl methacrylate (PMMA) and sphere plastics. The impulses differ by 5–7% in amplitude possibly because of difficulties in differentiation (a finite number of points are taken on the interferogram that visualizes the time dependence of the free surface displacement when the velocity of the surface is found from the decay of the wave in the material) and the acoustic approximation inaccuracy.
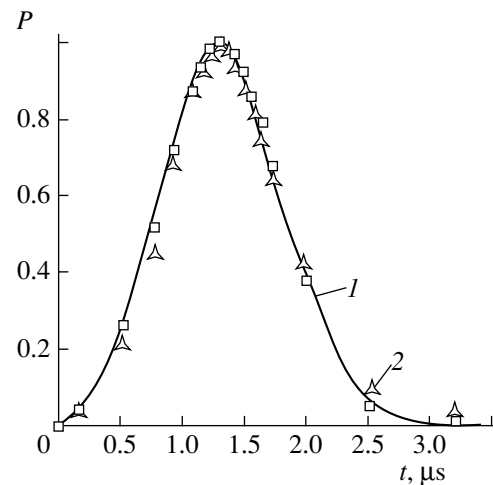
EXPERIMENTAL TECHNIQUES OF DETERMINING THRESHOLD RUPTURING LOADS

Material fracture is obviously a multistage process including formation of the stressed state, which may cause damage and its buildup; cracking; and crack propagation. It is reasonable to study the process at the least possible rupturing loads. In this case, there is no need to analyze the amount of the energy spent on cracking and crack propagation. Prior to cracking, the stressed state can be analyzed in terms of continuum mechanics and linear mechanics of fracture. When designing the experiment, one should bear in mind that there may appear the need to treat the stressed state not only analytically but also numerically (the analytical treatment is preferable).

The pulsed magnetic technique of loading suggested in this work allows for various loading schemes and conditions [11].

(i) Wave loading of cracked specimens. In the case of specimens that have macrodefects like cracks, the following scheme may be realized (Fig. 4). In the plane specimen, a 2- to 3-mm-wide notch is made that terminates in a groove 2–3 mm long and 0.2 mm wide. Thin copper wires of width equal to the thickness of the specimen are inserted into the groove and brought into acoustic contact with the edges of the notch. The current passing along the wires generates a pressure (equal to the magnetic pressure) that uniformly acts on the edges of the notch throughout its length. The test results for several materials are given in Figs. 5 and 6. Threshold rupturing loads $P_{tr, r}$ were found by extrapolating the length L_{cr} of a developed crack to zero ($L_{cr} \longrightarrow 0$).

(ii) Testing of specimens with quasi-static stabilization of the wave field. Clearly, the wave stressed state cannot form if the specimen sizes are much
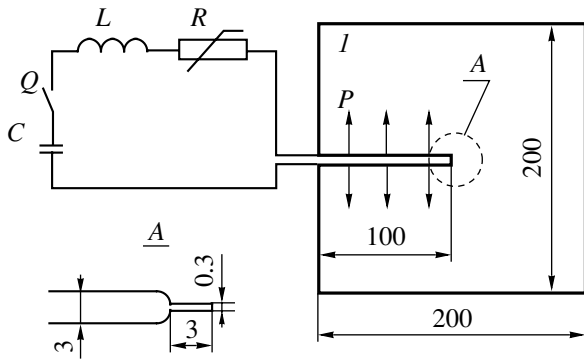
Fig. 4. Electric circuit of the setup and loading scheme. *C* and *L* are the storage capacitance and self-inductance of the pulsed current generator, respectively; *Q* is the high-voltage switch; and *R* is the nonlinear resistance. (*1*) Test specimen. The dimensions are given in millimeters.
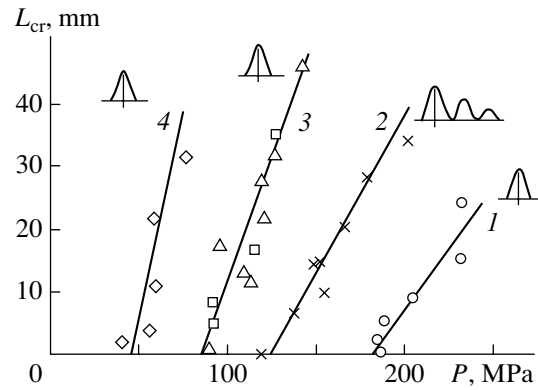

Fig. 5. Experimental data for the brittle fracture threshold for 10-mm thick specimens made of organic glass. The time to maximum is (*1, 2*) 1.0, (*3*) 2.0, and (*4*) 4.3 μm. (□) Data obtained on the ξ-2 setup.

Fig. 6. Experimental data for the brittle fracture threshold for 12-mm thick gabbrodiabase specimens. Loading by a single impulse of duration (*1*) 8.2 and (*2*) 3.6 μs.

Fig. 7. Equivalent electrical circuit of the pulsed magnetic setup and loading scheme. P_m, magnetic pressure; *i*, current; *C*, total capacitance of the capacitor bank; *Q*, switch; *R*, impulse-shaping Vilit resistance; *L*, self-inductance of the capacitor bank; *1*, loading unit (copper wires); *2*, striker; *3*, test specimen; and *4*, fixed supports.

smaller than the loading impulse wavelength, i.e., if

$$c_1 T \gg D, \tag{7}$$

where c_1 is the velocity of the wave, T is the pressure impulse duration, and D is the characteristic size of the specimen.

Therefore, with small specimens meeting this condition, one can carry out high-loading-rate experiments without considering the wave character of loading. In this case, the stressed state can be found by solving relevant static problems.

The scheme of the experiments with small specimens is shown in Fig. 7. The $24 \times 5 \times 6$-mm specimen with a central notch 2 mm deep and 0.2 mm wide was placed on rigid supports. Loading is accomplished by a striker, which is in acoustic contact with the wires. A magnetic pressure produced by the current in the wires is converted to a force that is transferred to the striker. This force is proportional to the contact surface of the striker and the magnetic pressure. The striker imparts this force to the specimen. Thus, three-point dynamic loading is realized, for which the stressed state of the specimen is well known.

In this way, we determined the threshold rupturing loads for PMMA and gabbrodiabase specimens with sizes meeting condition (8).

Static tests were performed with R-05 and RMU-0.05 testing machines. The experimental results are summarized in Table 1.

(iii) Wave loading of defect-free specimens. Defect-free specimens are routinely tested under cleavage conditions. The striker generates a compression wave (impulse) at one end of the specimen, and the wave, having passed through the specimen, reflects from the other (free) end as a rarefaction wave. The parameters of the initial pressure impulse are recovered from the velocity of the free surface and depend on the
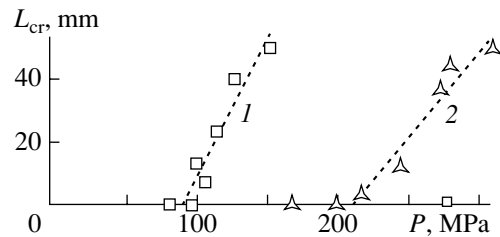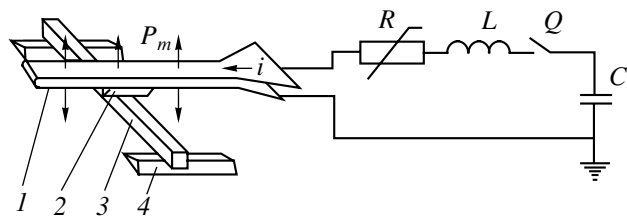
velocity and size of the striker, as well on the properties of the material it is made of.

In our case, plane wires of different configurations providing the validity of formula (2) served as a loading unit. The specimens to be shock loaded were gabbrodiabase and PMMA rods measuring $180 \times 5 \times 6$ mm. The wires were glued to the polished end face of the rod with a monomolecular adhesive, and the PCG was switched on. The loading scheme is depicted in Fig. 1. The threshold rupturing load amplitude was found by raising the load up to fracture. Each of the specimens was loaded once.
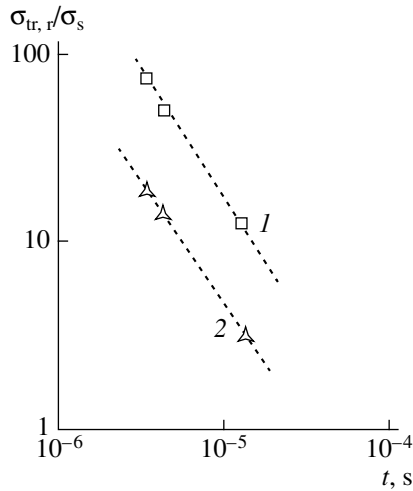
Fig. 8. Rupturing stress vs. impulse duration. $\sigma_{tr, r}$ and σ_s are the dynamic and static strength, respectively. (*1*) Gabbrodiabase and (*2*) PMMA.

It should be noted that these experiments were aimed at determining the dynamic rupture strength at the macrolevel. The pressure impulse amplitude below which the specimen did not disintegrate into two parts was determined. In other words, the macroscopic fracture threshold was found. The shape of the current pulse was specified by the nonlinear resistor and corre-

Table 1. Experimental data for small specimen fracture

	Notch depth, mm	Impulse duration, μs	Rupturing force, N
PMMA	2.5 ± 0.1	Statics	68 ± 6
PMMA	2.5 ± 0.1	7.0	805 ± 40
Gabbrodiabase	2 ± 0.1	Statics	195 ± 6
Gabbrodiabase	2 ± 0.1	4.1	3920 ± 30

Table 2. Parameters of PMMA and gabbrodiabase

Parameter	PMMA	Gabbro-diabase
σ_s, static strength (MPa)	72	17.54
K_{1c}, static cracking resistance (stress intensity factor) (MPa $\sqrt{m}$)	1.1	2.4
τ, structural time to fracture found in experiment (1) (μs)	32 ± 3	130 ± 5
τ, structural time to fracture found in experiment (2) (μs)	34 ± 5	77 ± 5
τ, structural time to fracture found in experiment (3) (μs)	32 ± 3	72 ± 5
c_1, longitudinal wave velocity (m/s)	2350	5630
c_r, wave velocity in the rod (m/s)	2130	5000
ρ_0, density (kg/m³)	1180	2890

sponded to the first half-cycle of a sinusoid. The rupturing load amplitude versus impulse duration is shown in Fig. 8.

STRUCTURE-AND-TIME APPROACH TO ANALYZING EXPERIMENTAL DATA

From the experimental data, one can determine the stressed state of the specimen and select a fracture criterion. A structural–time criterion seems to be the most suitable for analyzing the experimental data, since it generally takes into account space–time nonuniformities of the stress field in the specimen.

In the general case, such a criterion (first introduced in [2]) has the form

$$\frac{1}{\tau} \int_{t-\tau}^{t} \frac{1}{d} \int_{0}^{d} \sigma(r, \theta, t') dr dt' \leq \sigma_s. \tag{8}$$

Here, d and τ are the structural size and structural time to fracture, r and θ are the polar coordinates, σ_s is the material static strength, and $\sigma(r, \theta, t)$ is the tension at the crack tip ($r = 0$). Criterion (8) makes it possible to generalize the principles of linear mechanics of fracture to fracture dynamics. For the plane stress state, structural size d, which is determined from quasi-static tests of cracked specimens, can be expressed through the quasi-static fracture toughness (critical stress intensity factor) and quasi-static strength by the simple formula [1]; $d = 2K_{1c}^2/(\pi\sigma_s^2)$. According to the approach adopted, σ_s, K_{1c}, and τ constitute a set of basic parameters characterizing the strength properties of the material. This criterion allows one to study media with and without macrodefects from a unified point of view. Let us analyze the experimental data by solving relevant problem using the structural–time criterion.

(1) It was shown [12, 13] that, prior to arrival of the waves reflected from the specimen boundary, the experimental conditions correspond to the following problem. An infinite elastic plane with a semi-infinite notch, $R^2 \backslash \{(x, y) : x \leq 0, y = 0\}$, experiences impulsive loading applied to the edges of the notch, $\sigma_y = -p(t)$, $\sigma_{xy} = 0$, subject to $U|_{t \leq 0} = 0$ (initial condition) and $\forall t > 0 : U = \text{const} + O(r^\beta)$, $r \longrightarrow 0$, $\beta > 0$ (this condition provides the uniqueness of a solution to the problem). In the experiments, the load was applied as unipolar impulses, $p(t) = P_m Q(t)$.

For cracked specimens, the structural–time criterion can be rearranged to the form

$$\int_{t-\tau}^{t} K_1(s) ds \leq K_{1c}\tau, \tag{9}$$

where $K_1(t)$ is the current stress intensity factor and τ is the structural (incubation) time to fracture.

From (9), it follows that the lowest (threshold) rupturing amplitude of the loading impulse is found by the formula

$$P = \tau K_{1c}/\varphi(c_1, c_2)\max \int_{t-\tau}^{t} f(s)ds, \qquad (10)$$

where

$$\varphi(c_1, c_2) = 4c_2\sqrt{c_1^2 - c_2^2}/(c_1\sqrt{\pi c_1})$$

is the function of the longitudinal and shear waves and function

$$f(t) = \int_0^t Q(s)f_0(t-s)ds, \quad f_0(t) = 1/2t^{-1/2}$$

is found by solving the dynamic problem with initial and boundary conditions.

Threshold rupturing loads are determined from experimental data. With (10), one may find the structural time to fracture. For the PMMA, this time equaled 32 μm. For the gabbrodiabase, the structural (incubation) time to fracture determined by (10) was found to be $\tau = 130$ μm. This time far exceeds the time the wave load takes to travel the double distance from the crack edge to the specimen boundary, $2l/c_1$. Hence, by the time of fracture, the stressed state no longer meets the conditions of the problem, unlike the PMMA [12, 13], and parameter τ determined from (10) for the gabbrodiabase does not meet the experimental conditions. It can be argued that this parameter for gabbrodiabase lies in the interval $2l/c_1 < \tau \le 130$ μs.

(2) Consider the case when the striker (steel prism) is in direct contact with the specimen to be tested and wires. The striker is subjected to an impulsive force $F(t) = P(t)s$, where $P = P_m(\sin(\omega t))^2$ is the pressure exerted by the wires, s is the area of the striker base that the force acts on, and t_1 is the duration of the impulsive force.

It was shown [14] that the inertia of the system has a considerable effect on the parameters of an impulsive load acting on the specimen. In a linear elastic approximation, the force transferred to the specimen is given by

$$G(t) = \begin{cases} \dfrac{A}{\omega^2 - \nu^2}\left(\omega^2\sin^2\dfrac{\nu t}{2} - \nu^2\sin^2\dfrac{\omega t}{2}\right) & \text{for } 0 \le t \le t_1 \\[2ex] \dfrac{1}{1-(\nu/\omega)^2}\sin\dfrac{\nu t_1}{2}\sin\nu\left(t - \dfrac{t_1}{2}\right) & \text{for } t > t_1, \end{cases} \qquad (11)$$

where $\nu = \sqrt{k/m}$ is the natural oscillation frequency of the system, m is the mass of the striker, k is the stiffness, and A is the amplitude.

According to (11), the duration and amplitude of the impulse acting on the specimen have the form

$$t_2 = \frac{\pi}{\nu} + \frac{t_1}{2}, \quad G_{max} = \frac{A}{1-(\nu/\omega)^2}\sin\frac{\nu t_1}{2}. \qquad (12)$$

It is obvious from these relationships that the inertia of the loading unit's components (striker) significantly affects the impulsive load parameters. Specifically, the amplitude of the impulse declines, while its duration grows. For example, an impulse of duration 12.7 μs transforms into a 217-μs-long impulse.

Since we are dealing with the quasi-static mode of stress field stabilization in this case, the stress intensity factor may be taken to be proportional to the applied load in the form

$$K_1(t) = \frac{K_{1c}}{G_s}G(t), \qquad (13)$$

where G_s is the rupturing force under static loading.

The structural time to fracture is determined from (10), (11), and (13).

(3) In cleavage experiments, a pulsed tension is produced by the rarefaction wave, which arises after the compression wave has reflected from the free end face of the specimen. Here, not only the material properties are responsible for fracture but also the amplitude, shape, and duration of the impulse. The stressed state observed in these experiments is analytically the easiest, since it is completely specified by the rarefaction wave. Under these conditions, the structural–time criterion turns into

$$\frac{1}{\tau}\int_{t-\tau}^{t}\sigma(s, x)ds \le \sigma_s, \qquad (14)$$

where $\sigma(s, x)$ is the stress at a point x at a time s, τ is the structural time to fracture, and σ_s is the static strength of the material.

When an impulsive load is generated by the pulsed magnetic technique, the parameters of the impulse are known exactly. Therefore, the structural time of the material can be found if the threshold value of the impulse amplitude is known.

Table 2 lists the physicomechanic parameters of the materials tested, along with the structural times determined from the experimental data. The experiments on dynamic fracture were carried out with a PCG-50/250 pulsed current generator at the St. Petersburg State Polytechnical University and a ξ-2 setup at the St. Petersburg State University.

CONCLUSIONS

The pulsed magnetic technique of loading greatly simplifies related experiments and allows one to determine the parameters of an impulsive pressure applied to the specimen accurate to 5%.

A unique relationship between the impulsive pressure parameters and current distribution in the loading unit makes a desired loading scheme in specimens of different configuration feasible.

The experiments revealed that fracture is a threshold-type process and also that the rupturing load amplitude increases as the impulsive load duration decreases.

Analysis of the experimental data in terms of the structure-and-time approach showed that the structural time to fracture in various loading schemes is virtually the same. Therefore, the structural time to fracture may be included in the set of basic material parameters.

The material characteristics found experimentally (static strength, cracking resistance, structural time to fracture, etc.) in combination with the structure-and-time approach make it possible to predict the material behavior under impulsive loading of any type.

ACKNOWLEDGMENTS

REFERENCES

1. N. F. Morozov and Yu. V. Petrov, *Fracture Dynamics in Solids* (St. Petersb. State Univ., St. Petersburg, 1997) [in Russian].

2. N. F. Morozov, Yu. V. Petrov, and A. A. Utkin, Dokl. Akad. Nauk SSSR **313**, 276 (1990) [Sov. Phys. Dokl. **35**, 646 (1990)].

3. G. A. Shneerson, *Fields and Transient Processes in Super-High-Current Devices* (Énergoatomizdat, Moscow, 1992) [in Russian].

4. H. Knoepfel, *Pulsed High Magnetic Fields* (North-Holland, Amsterdam, 1970; Mir, Moscow, 1971).

5. P. N. Dashuk, S. L. Zaĭents, V. S. Komel'kov, *et al.*, *Technology of High Pulsed Currents and Magnetic Fields* (Atomizdat, Moscow, 1979) [in Russian].

6. A. I. Afanas'ev, I. M. Bogatenkov, and N. I. Feĭzulaev, *Overshoot Suppressors in High-Voltage Circuits* (St. Petersb. State Tech. Univ., St. Petersburg, 2000) [in Russian].

7. A. I. Afanas'ev and I. M. Bogatenkov, *High-Voltage Testing of Electrical Devices* (St. Petersb. State Tech. Univ., St. Petersburg, 1998) [in Russian].

8. Y. E. Adamian, S. I. Krivosheev, V. M. Vasilevsky, and A. P. Nenashev, in *Proceedings of the 1st International Congress on Radiation Physics, High Current Electronics, and Modification of Materials, Tomsk, 2000.*

9. V. A. Ivanov and V. E. Privalov, *Application of Lasers in Instruments of Fine Mechanics* (Politekhnika, St. Petersburg, 1993) [in Russian].

10. E. I. Zababakhin, *Cumulation and Instability* (RFYaTs–VNIITF, Snezhinsk, 1998) [in Russian].

11. S. I. Krivosheev, N. F. Morozov, Yu. V. Petrov, *et al.*, in *Proceedings of the 5th International Conference on Zababakhin Scientific Talks, Snezhinsk, 1998* (RFYaTs–VNIITF, Snezhinsk, 1998).

12. S. I. Krivosheev, N. F. Morozov, Yu. V. Petrov, and G. A. Shneerson, Izv. Akad. Nauk, Ser. Énerg., No. 5, 165 (1999).

13. S. I. Krivosheev and Yu. V. Petrov, Preprint No. 142, IPMASH RAN (Institute of Problems in Machine Science, Russian Academy of Sciences, St. Petersburg, 1997).

14. A. A. Gruzdkov, S. I. Krivosheev, A. I. Razov, *et al.*, in *Proceedings of the LX International Workshop "Topical Problems of Strength," Velikiĭ Novgorod, 2002.*

Translated by V. Isaakyan

===================== **SOLIDS** =====================

Crystallization in the Al–Si, Al–Ge, and Al–Si–Ge Systems at Centrifugation

**V. N. Gurin*, S. P. Nikanorov*, M. P. Volkov*, L. I. Derkachenko*, T. B. Popova*,
I. V. Korkin*, B. R. Willcox**, and L. L. Regel'****

** Ioffe Physicotechnical Institute, Russian Academy of Sciences,
Politekhnicheskaya ul. 26, St. Petersburg, 194021 Russia*
e-mail: vladimir.gurin@mail.ioffe.ru
*** International Center of Gravitational Materials Science and Applications,
Clarkson University, Potsdam, New York 13699-5814, USA*
Received July 7, 2004

Abstract—Crystallization in the Al–Si, Al–Ge, and Al–Si–Ge systems at centrifugation is studied. Of them, the Al–Si system is the least prone to sedimentation. In the others, sedimentation considerably changes the structure of the alloys at the bottom of the ingots compared with their top. At certain concentrations of the constituents, the number of crystallites in the lower part of the ingot is larger than in the upper part and the crystallites at the bottom are coarser than at the top. The Si : Ge atomic ratio in the Al–Si–Ge system changes by a factor of 2–12 against the initial ratio (1 : 1) when the (Si + Ge) concentration changes as a result of centrifugation. Also, this ratio changes over the crystal surface (in the samples not subjected to centrifugation, this ratio remains unchanged over the surface). Crystallites in the Al–Si–Ge system are covered by Ge. © *2005 Pleiades Publishing, Inc.*

INTRODUCTION

Centrifugation of metallic melts has been extensively explored in a variety of systems from Al and Mg to Fe–C, Bi–Cd, Pb–Sb, and many others [1–3]. In all the cases, centrifugation was found to modify the structure and properties of the alloys crystallized. This process most significantly affects the constituent distribution in the upper and lower parts of the ingot: the greater the difference between the densities of the constituents, the greater the difference in constituent distribution at the top and bottom. This fact may be attributed to the different densities of the states in which the constituents are in the melt (associates, etc.) or to hydrodynamic flows appearing in the melts at centrifugation [4]. Direct experimental corroboration of such states and flows in multicomponent metallic melts is today absent. The nonuniform distribution of the components in the melt modifies the overall structure of the ingot crystallized, be it of eutectic, hypoeutectic, or hypereutectic composition. The ingot contains areas with a different amount of so-called colonial precipitates (eutectic, etc.), as a result of which the structure is greatly modified. Such inhomogeneity inevitably changes the properties of these materials.

In this work, we study the effect of centrifugation on the structure and composition in the Al–Si, Al–Ge, and Al–Si–Ge systems with various concentrations of Si, Ge, and (Si + Ge). The first of the systems listed is of great practical value, while the others, though not appli-

cable in practice yet, are good model systems for such investigation.

EXPERIMENTAL

The compositions of the systems studied were as follows: Al–Si (10, 12.7 (eutectic alloy), and 15 at.% Si), Al–Ge (20, 28.4 (eutectics), and 40 at.% Ge), and Al–Si–Ge (5, 10, 20, and 25 at.% (Si + Ge)). The starting materials were ingots of the same compositions grown by melting in the suspended state in a He atmosphere with subsequent quenching in a copper mold. The samples obtained had a length of 9 cm and a diameter of 6 mm. Starting Al and Ge were of $4N$ and $3N$ purity, respectively, and n-Si had a resistivity of $2000\ \Omega$ cm. The experiments were performed on a high-temperature centrifuge (Clarkson University, Potsdam, New York, USA) with an arm length of 150 cm. The acceleration was equal to $7\ g$. The weight of the alloys centrifuged was varied from 5 to 10 g. The material was placed into 14-cm-long alundum test tubes with an inner diameter of 6 mm, and the tubes were sealed in evacuated (rough vacuum) quartz ampoules (three tightly packed tubes in an ampoule). The test tubes contained small bars (6–8 cm long and ≈6 mm in diameter) of alloys of desired composition. The test tubes and the ampoule must be in intimate contact in order to prevent vibration at centrifugation, which may cause cracking and seal failure at high temperatures. The time it takes for the furnace to reach a maximal temperature was 2–3 h. The centrifuge was switched on at 420°C, when
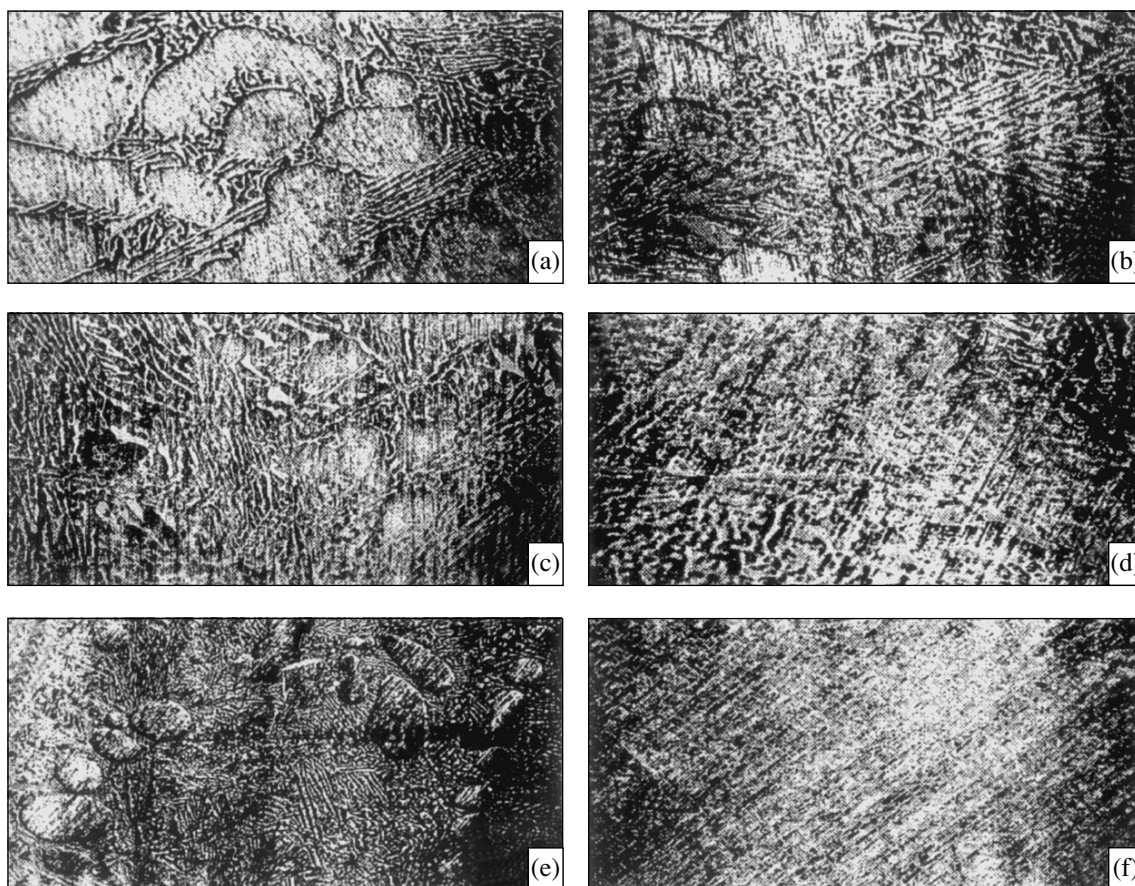
Fig. 1. Al–Ge system. (a, b) Top and bottom of the ingot with 20 at.% Ge (hypoeutectic composition), (c, d) top and bottom of the ingot with 28.4 at.% Ge (eutectic composition), and (e, f) top and bottom of the ingot with 40 at.% Ge (hypereutectic composition). ×100.

alloys that melt at the lowest temperatures (Al–Ge eutectics with a melting point of ≈420°C) and the Al–Si–Ge system (a melting point of ≈430°C) start melting. At a maximal temperature of 900–1000°C, the furnace was kept for 4 h. Then, it was switched off, the alloys were furnace-cooled to crystallization for about 1 h, and the centrifuge was switched off. After the experiment was completed, the alundum test tubes with the melt solidified were withdrawn from the quartz ampoule (which was continuously kept under a rough vacuum) and broken. From the upper and lower parts of the metallic bars (ingots), two pieces 5–7 mm long were cut off at a distance of 5–7 mm from the respective end of the ingot in order to reject a pipe cavity and a rounding at the bottom of the ingot (i.e., the part most distant from the axis of the centrifuge). Microsections made from these pieces by the conventional technique were examined in an optical microscope and in a Camebax microanalyzer to determine the amount of Si and Ge (lines KA and LA at 10 kV) in the crystallites.

RESULTS AND DISCUSSION

The optical microscopy examination corroborates the observation (see [1–3]) that acceleration, even as low as 7 *g*, influences the behavior of the systems.

The structure and mechanical properties of the Al–Si system with different Si concentrations was described in considerable detail elsewhere [4]; here, this system will be outlined only briefly. According to our data, Si (more specifically, a solid solution of Al in Si) accumulates in the upper part of the ingot, while Al (more specifically, a solid solution of Si in Al) concentrates mostly in its lower part. This is consistent with the values of the densities of these materials in the solid state: 2.70 g/cm^3 for Al and 2.33 g/cm^3 for Si. The published data are contradictory: some of the authors (we among them) argue that, after centrifugation, Si accumulates at the top of the ingot [1]; others reason that Si concentrates at the bottom [5]. Both statements seem to have the right to exist, since the result depends on the experimental conditions (on a melting technique, initial concentrations of Al and Si, temperature, how much the melt is heated over the liquidus temperature, heating and cooling rates, etc.).

In the Al–Ge system, the difference between the densities of the components is appreciable: 2.70 g/cm^3 for Al and 5.32 g/cm^3 for Ge). Therefore a considerable separation of the elements at centrifugation may be expected because of Ge sedimentation. Figure 1 shows the microsections made of the upper and lower parts of
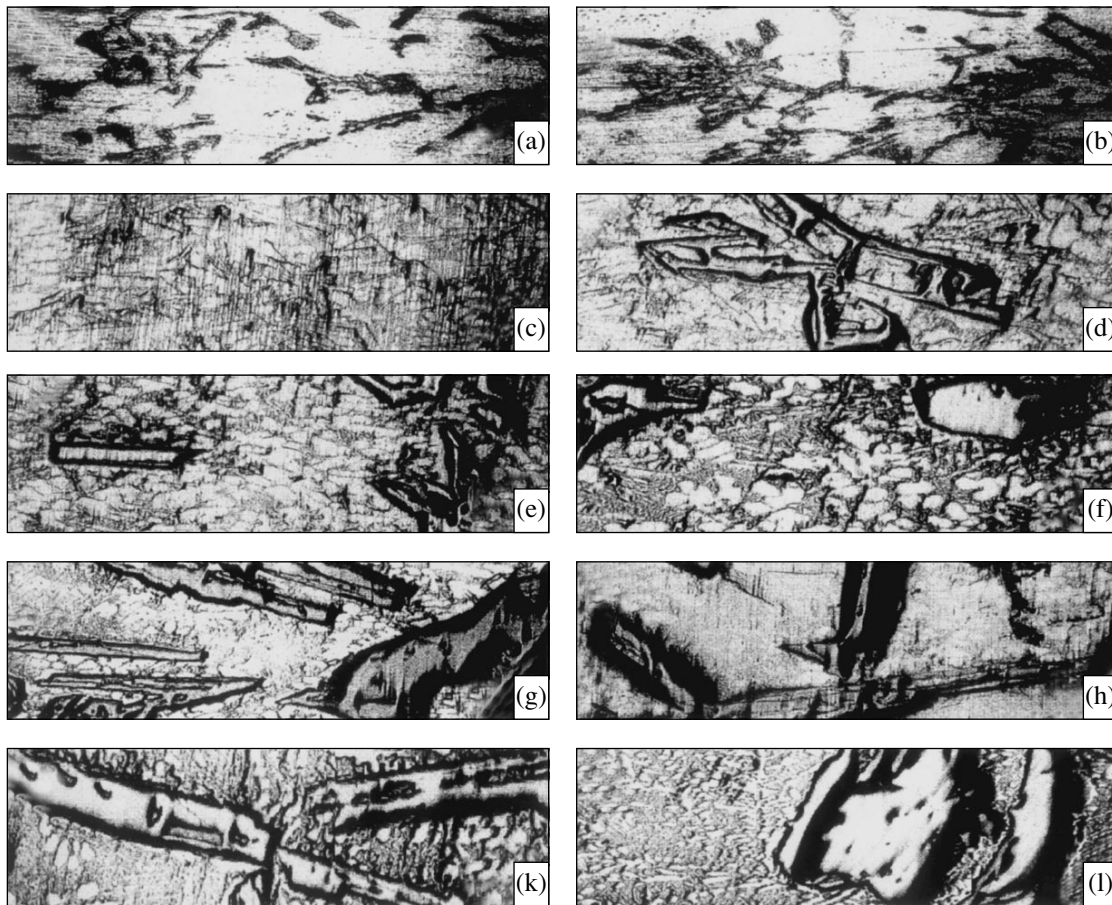
Fig. 2. Al–Si–Ge system. (a, b) Top and bottom of the ingot with (Si + Ge) = 10 (5 + 5) at.%, (c, d) top and bottom of the ingot with (Si + Ge) = 20 (10 + 10) at.%, (e, f) top and bottom of the ingot with (Si + Ge) = 30 (15 + 15) at.%, (g, h) top and bottom of the ingot with (Si + Ge) = 40 (20 + 20) at.%, and (k, l) top and bottom of the ingot with (Si + Ge) = 50 (25 + 25) at.%. ×100.

the Al–Ge ingots with different Ge concentrations. In the alloy of hypoeutectic composition (20 at.% Ge) (Figs. 2a, 2b), the amount of bright oval precipitates (up to 500 μm across) of a solid solution of Ge in Al (hereafter, Al) at the top is higher than at the bottom; in other words, the amount of a solid solution of Al in Ge (hereafter, Ge) at the bottom is higher, which indicates sedimentation. The top of the eutectic composition (28.4 at.% Ge) (Fig. 2c) also differs from its bottom (Fig. 2d) by the presence of oval areas of Al. These areas are easily distinguishable by thin unidirectional hatches, which are the traces of fine polishing of Al by a paste with 0.05-μm Al_2O_3 grains (such a paste is extremely difficult to remove completely). At the bottom of this ingot, a high density of Ge dendrites is seen but ovals are virtually absent. In the hypereutectic ingot (40 at.% Ge), oval Al areas at the top (Fig. 2e) are smaller in size than in the previous cases, while at the bottom (Fig. 2f), such areas are absent but the density of Ge crystallites is very high. It is noteworthy that large Ge crystallites are observed along the circumference of the eutectic and hypereutectic compositions at the bottom (in the former case, individual crystallites

are seen; in the latter, the density of the crystallites is high and their size reaches 1.4 mm). Thus, centrifugation of this system results in sedimentation and, accordingly, makes its structure inhomogeneous (the structures of the upper and lower parts are different from each other).

The Al–Si–Ge system differs dramatically from the first two in type and composition of precipitates. Figure 2 shows the lower and upper parts of the ingots with different (Si + Ge) concentrations. Only when the (Si + Ge) concentration equals 10 at.% (5 + 5) are individual crystallites not observed in the microsections. However, the upper (Fig. 2a) and lower (Fig. 2b) parts differ in density of needles (which actually are plate crystals), "asterisks" (when the rays issue from the same center) of the α solid solution of Al in Si + Ge, and oval precipitates of the β solid solution of Si + Ge in Al (hereafter, the α and β phases will be referred to as Si + Ge and Al, respectively). Accordingly, the (Si + Ge) concentration is higher in the lower part of the ingot. The bright oval Al areas and dark Si + Ge needles were first to be analyzed on the Camebax microanalyzer. In the phase diagram depicted in Fig. 3a, where the initial and final
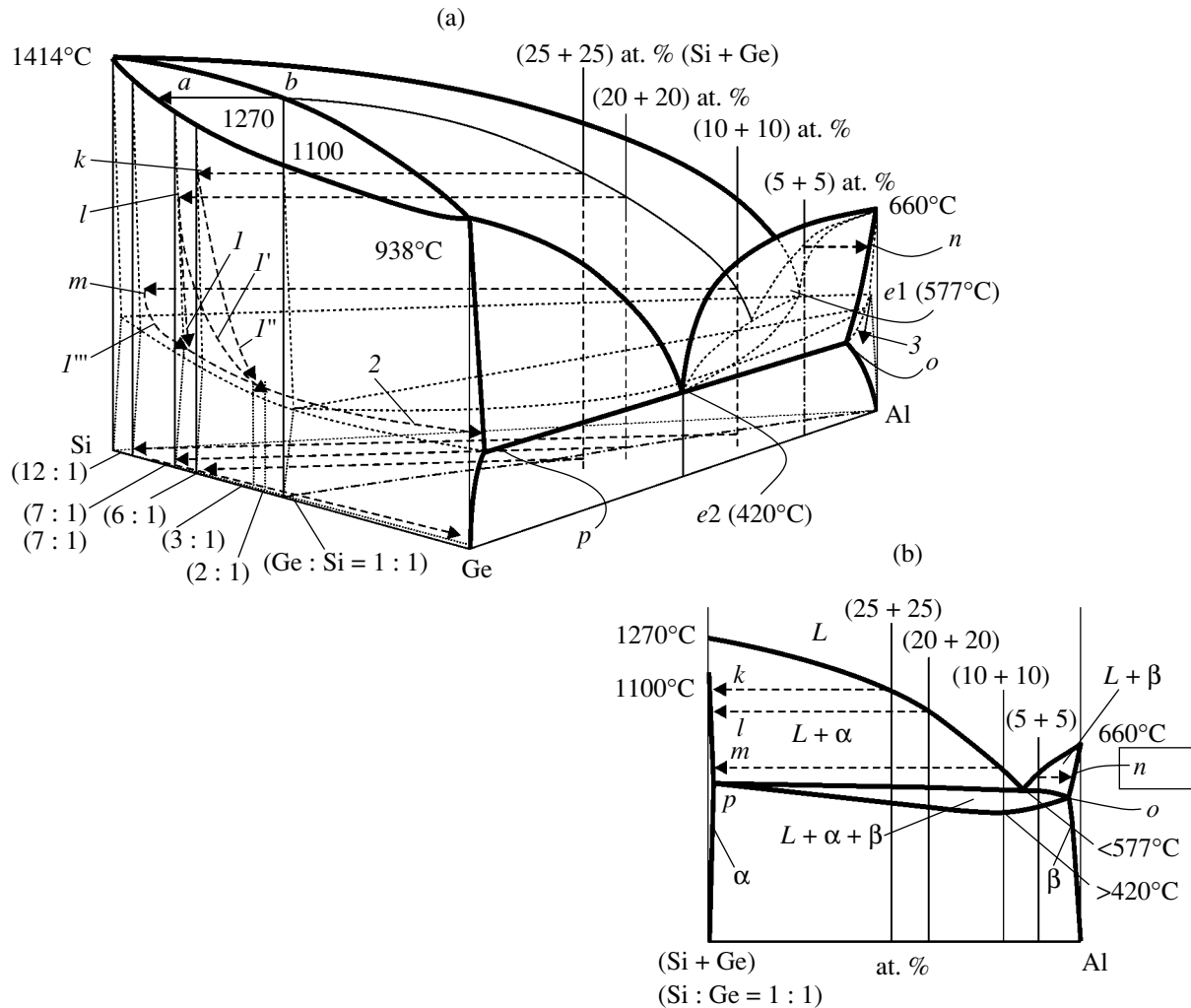
(a)

Fig. 3. (a) General view of the ternary Al–Si–Ge phase diagram with a limited solubility of the components in two binary systems and unlimited solubility in the third binary system [8]. *e*1 and *e*2, eutectic points in the Al–Si and Al–Ge systems. The arrows indicate alloys crystallizing at Si + Ge = (5 + 5), (10 + 10), (20 + 20), and (25 + 25) at.%, as well as the temperature–concentration routes of crystallization of these compositions (curves *1, 1', 1", 1'", 2,* and *3*). The concentration (5 + 5) is on the right and the others on the left of the intereutectic recess (the depression of the liquidus surface between the Al–Si and Al–Ge eutectics). The same compositions are represented in the polythermal section. In the concentration triangle, the projections of the curves with arrows, as well as the ratios Si : Ge found by chemical analysis, are shown. (b) Polythermal section of the ternary Al–Si–Ge phase diagram that passes through the line connecting the point of Si : Ge = 1 : 1 (initial ratio) with the Al corner (in panel (a), this dash-and-dot line is in the middle of the triangle at the base of the diagram). The regions $(L + \alpha)$ and $(L + \beta)$ are regions of primary crystallization (in panel (a), the solidi of these regions are shown by thin continuous lines). The region $(L + \alpha + \beta)$ is the region of secondary crystallization (in panel (a), it is shown as a dotted extended segment). Points *k, l, m,* and *n* in both panels are the points of beginning of the phase transformations and growth of (Si + Ge) and Al crystallites at different initial (Si + Ge) concentrations. Points *o* and *p* are the points where the crystallization of these compositions in the region of secondary crystallization is completed.

(point *o* in curve *3*) crystallizing compositions are indicated, this composition is on the right of the recess between the eutectics in the Al–Si and Al–Ge systems. The results of chemical analysis differ radically from those for the remaining concentrations of Si + Ge (see below). For example, Al contains from 1.4 to 2.8 at.% (Si + Ge) both at the top and at the bottom of the ingot. The spread in concentration may be associated with the fact that Al successively crystallizes first from the primary $(L + \beta)$ crystallization region along line *no* (1.4–1.7 at.%) and then from the secondary $(L + \alpha + \beta)$ crys-

tallization region (2.0–2.8 at.%) at the lowest temperature (Fig. 3b). In the needles, the Al content varies from 0.01 to 0.60 at.% and the ratio Si : Ge, from almost pure silicon to almost pure Ge (the amount of the latter is somewhat higher at the bottom). Unfortunately, too small sizes of crystallites (5–10 μm) in this ingot allow chemical analysis only at one site. Thus, the combined content of Si and Ge dissolved in Al does not exceed the solubility of pure Ge in Al (2.8 at.% [5]).

The chemical analysis data for the ingots with other (Si + Ge) concentrations (20, 40, and 50 at.%) are con-
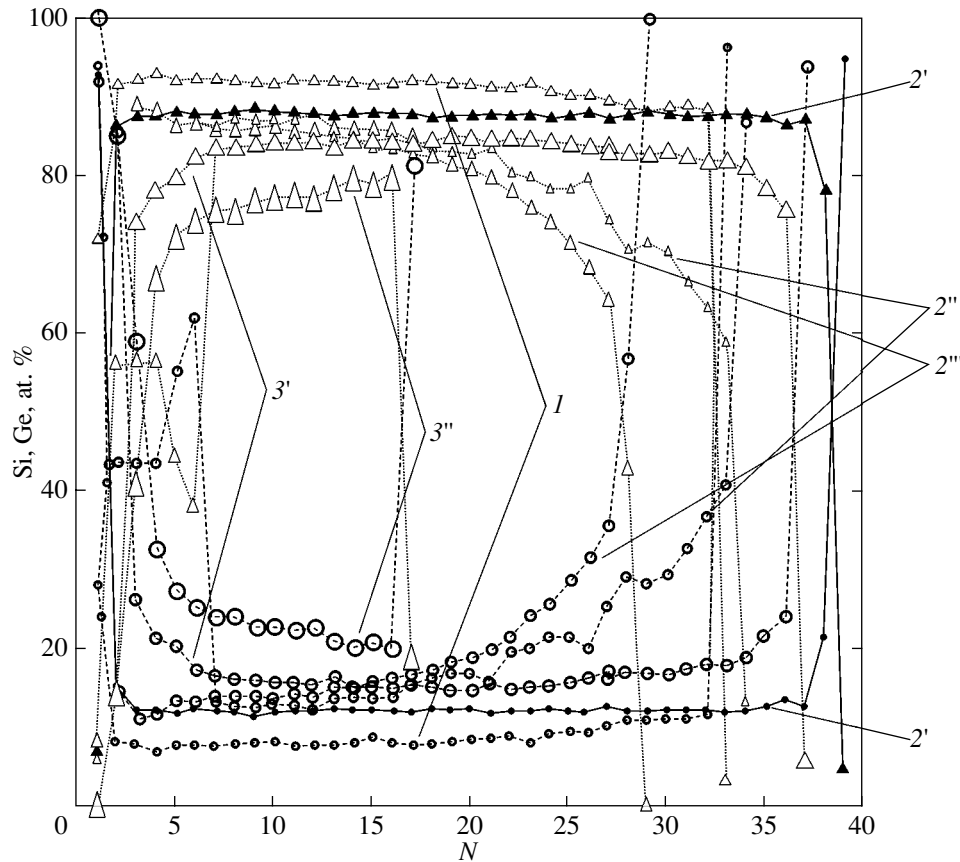
Fig. 4. Chemical analysis (Camebax microanalyzer) data for (Si + Ge) = (*1*) 20 (10 + 10) at.% (top and bottom), (*2'*) 40 (20 + 20) at.% (uncentrifuged sample), (*2"*) 40 (20 + 20) at.% (top of the centrifuged sample), (*2'''*) 40 (20 + 20) at.% (bottom of the centrifuged sample), (*3'*) 50 (25 + 25) at.% (top of the ingot), and (*3"*) 50 (25 + 25) at.% (bottom of the ingot). The continuous lines and filled symbols (triangles for Si and circles for Ge) refer to the uncentrifuged sample (Si + Ge = 20 + 20). The tops and bottoms of the ingots are shown in the figure. *N*, points on the crystallite surface.

siderably different from those reported above. It comes as no surprise since the crystallites precipitated here (α solid solutions of Al in Si + Ge) lie on the left of the recess between the eutectics (Figs. 3a, 3b).

At a (Si + Ge) concentration of 20 at.% (10 + 10) (Fig. 2d), rather large composite crystallites (quarter-foils) arise along the circumference at the lower part of the ingot; at the top, a high density of the needles (plate crystallites) is observed (Fig. 2c). Starting from a concentration of 30 (15 + 15) at.%, individual crystallites precipitate in both the upper and lower parts of the ingot. Some of the crystallites at the bottom (Figs. 2f, 2h, 2l) are coarser than those at the top (Figs. 2e, 2g, 2k). The space between these coarse grains is filled with eutectics that are finer than those at the top. At 30 at.%, individual crystals are observed largely along the perimeter, while at 40 (20 + 20) and 50 (25 + 25) at.% (Si + Ge) they occupy the entire surface of the microsection. Thus, as a result of centrifugation-induced sedimentation in the ternary Al–Si–Ge system, the top and bottom of the ingots with initial (Si + Ge) concentrations of 30 (15 + 15) at.% or lower become quantitatively and qualitatively dissimilar. To estimate

changes in the ratio Si : Ge, we analyzed the chemical composition of the tops and bottoms of the ingots with 20, 40, and 50 at.% (Si + Ge). As a reference, we took an ingot with 20 at.% (Si + Ge) that was not centrifuged.

As follows from Fig. 4, the initial ratio Si : Ge = 1 : 1 changed, depending on the concentration, to (12 : 1)–(7 : 1) for (10 + 10), (7 : 1)–(2 : 1) for (20 + 20), and (6 : 1)–(3 : 1) for (25 + 25). In addition, the ratio Si : Ge varied over the surface of crystallites in the ingots centrifuged. In the reference (uncentrifuged) ingot, this ratio remained the same throughout the surface (filled dots in Fig. 4). All the crystallites indiscriminatively were coated by Ge. The composition of the coatings over the crystal was the same (≈100% Ge), as demonstrated by Camebax measurements at three to five points on the surface, while the thickness of the coatings was estimated as varying between 10 and 40 μm. Note also that the difference between the top and bottom of the ingots widens with increasing initial (Si + Ge) concentration.

We also checked the Al content in the ingots with Si + Ge = 20, 40, and 50 at.%. It turned out to be insignificant, no higher than 0.02 at.% (the ultimate solubil-

ity of Al in Si and Al in Ge is, respectively, 0.016 and 1.2 at.% [5]). One thus may conclude that the solubility of Al in Si–Ge solid solutions is close to its ultimate solubility in Si.

It should be noted that an excess of Si in the crystalline precipitates was also observed in other works [6, 7] for low initial (Si + Ge) concentrations, 2(1 + 1) and 1 (0.5 + 0.5) at.%, and initially equiatomic (1 : 1) ratio Si : Ge in the Al–Si–Ge ingots obtained without centrifugation. The precipitates in the works cited were also covered by Ge.

The results can be explained from the phase diagram for the Al–Si–Ge system. Figure 3 shows its general view (Fig. 3a) and polythermal section (Fig. 3b). The general view gives an insight into phase transformations (at points k, l, m, and n) in the concentration range studied. The arrows indicate transformation routes and crystallizing compositions (in the concentration triangle and along the Si–Ge axis). The ratio Si : Ge in the forming crystals is seen to differ greatly from the initial value. The situation is roughly the same as in the binary Si–Ge system (thin continuous line *ab* inside the "disk"), where this ratio in the emerging compositions far exceeds the initial ratio Si : Ge = 1 : 1. It may be supposed that the crystallization of the α solid solutions in our case is akin to that in the binary system and may proceed in two ways. The former does not imply centrifugation: first, crystallization goes along line *1* (Fig. 3a) and the composition of the ingot (in our case, the sample with (20 + 20) at.% was studied) remains nearly constant (the Al content during crystallization varies insignificantly). After the system has reached the solidus, it quickly solidifies (slides down to point *p* along line *2*) and the crystallites are covered by Ge. This is confirmed by the data of chemical analysis (the continuous curves and filled dots in Fig. 4): the ratio Si : Ge in the crystallites remains almost the same. The second way (curves *1'*, *1"*, and *1'''*) is possible at centrifugation: acceleration results in variable compositions of the crystallites, and, as a result of Ge sedimentation, they grow along the "inclined curve": throughout the concentration range, the Ge content (and the ratio Si : Ge) varies over the crystallite surface (Fig. 4). Here, as in the former case, once the system has reached the solidus (but now at a point where the ratio Si : Ge is smaller), it quickly solidifies (slides down along line *2* to point *p*) and the crystallites are also covered by Ge. The polythermal section (Fig. 3b) shows the region of secondary crystallization, in which precipitation of α and β solid solutions is completed. In the former case (Fig. 3a), the crystallites are covered by nearly pure Ge (Fig. 4). In the latter (Fig. 3b), the crystallites appear as aluminum ovals and bright areas between the needles in Figs. 2a and 2b.

CONCLUSIONS

(1) Centrifugation of the Al–Si, Al–Ge, and Al–Si–Ge melts with different concentrations of Si, Ge, and (Si + Ge) at a low acceleration of $7g$ in the temperature interval 900–1000°C for 4 h causes intense precipitation of a solid solution of Si in Al (β solid solution for the Al–Si system) and α solid solutions (Al in Ge and Al in Si + Ge for the Al–Ge and Al–Si–Ge systems, respectively). For a (Si + Ge) concentration of (10 + 10) at.% in the Al–Si–Ge system, the crystallites at the bottom of the ingot are coarser than at the top. In general, the crystallites at the bottom of the Al–Si–Ge ingot contain a somewhat higher Ge concentration than at the top. These results are associated with sedimentation of heavier components (Al, Ge, and Si + Ge), which shows up as solid-state crystallites or colonies (associates) in the starting melts.

(2) As a result of centrifugation-related sedimentation, the ratio Si : Ge varies over the surface of the crystallites grown from the Al–Si–Ge melt with Si + Ge = (10 + 10), (20 + 20), and (25 + 25) at.% (recall that this ratio remains unchanged in uncentrifuged ingots). For (Si + Ge) = (5 + 5) at.%, the crystallites of the α solid solution (Al in Si + Ge) contain no more than 0.02 at.% in both the upper and lower part of the ingot. The oval-shaped precipitates of the β solid solution (Si + Ge in Al) contain no more than 6 at.% (Si + Ge). These figures do not exceed the ultimate solubilities of Al, Ge, and Si in the related binary systems.

REFERENCES

1. A. A. Vertman and A. M. Samarin, *Methods of Studying the Properties of Metallic Melts* (Nauka, Moscow, 1969) [in Russian].

2. G. B. Stroganov, V. A. Rotenberg, and G. B. Gershman, *Al–Si Alloys* (Metallurgiya, Moscow, 1977) [in Russian].

3. G. Müller, *Convection and Inhomogeneities in Crystal Growth from the Melt* (Springer-Verlag, Berlin, 1988; Mir, Moscow, 1991), pp. 267–278.

4. M. P. Volkov, V. N. Gurin, S. P. Nikanorov, *et al.*, Fiz. Tverd. Tela (St. Petersburg) **47**, 886 (2005) [Phys. Solid State **47** (2005)] (in press).

5. *State Diagrams of Binary Metal Systems: A Handbook*, Ed. by N. P. Lyakishev (Mashinostroenie, Moscow, 1996) [in Russian], Vols. 1–3.

6. F. Loffler Jorg, S. Bossuyt, A. Peker, *et al.*, Appl. Phys. Lett. **81**, 4159 (2002).

7. D. Mitlin, U. Dahmen, V. Radmilovich, *et al.*, Mater. Sci. Eng., A **301**, 231 (2001).

8. V. Ya. Anosov, M. I. Ozerova, and Yu. Ya. Fialkov, *Fundamentals of Physicochemical Analysis* (Nauka, Moscow, 1976) [in Russian].

Translated by V. Isaakyan

OPTICS,
QUANTUM ELECTRONICS

Production of the Hg-196 Isotope by a Photochemical Method

Yu. V. Viazovetski

Russian Research Center Kurchatov Institute, pl. Kurchatova 1, Moscow, 123182 Russia
e-mail: viazov@kiae.imp.ru
Received June 22, 2004

Abstract—An experimental setup and photochemical approaches used for extracting highly enriched mercury isotopes at the Russian Research Center Kurchatov Institute are described. In the extraction process, selectively excited mercury atoms are oxidized in the presence of 1,3-butadiene. Along with the Hg-198, Hg-199, Hg-200, and Hg-202 isotopes, the least abundant mercury isotope, Hg-196, has been produced for the first time with a concentration as high as 97%. © 2005 Pleiades Publishing, Inc.

INTRODUCTION

The home and world markets demonstrate a burgeoning demand for mercury isotopes, which are applied in various fields of science and technology. The consumption of the Hg-198, Hg-199, Hg-200, and Hg-202 isotopes has greatly increased to date, since, in a number of countries, they are being used to solve the problem of environmental protection against industrial mercury and mercury compound waste [1, 2].

Initially, interest in the Hg-196 isotope was related to its usage in medicine for disease diagnosis. Then, mercury enriched by Hg-196 to 2–4% was used in light sources in an attempt to raise their efficiency [3]. Wider usage of Hg-196, e.g., in light sources for photochemical devices or in mercury analyzers, was retarded because of the impossibility of increasing its concentration to 96% or more.

Mercury enriched by Hg-196 with a photochemical method was first produced by French researchers in 1968 [4]. They designed an experimental separator that produced the Hg-196-enriched product with an output of 1 mg/day, measured a number of basic constants characterizing the process, and carefully investigated photochemical oxidation of mercury by oxygen in the presence of 1,3-butadiene (C_4H_6). It turned out that isotopically enriched mercury is produced with the participation of the $[HgO_2]^*$ excited complex (the asterisk denotes the excited state). The reaction scheme suggested in that work is shown in Fig. 1.

In this context, of interest are works of German scientists [5, 6] who also used the photochemical reaction of mercury oxidation in the presence of 1,3-butadiene to produce Hg-196. As a light source, they applied a low-pressure lamp filled with Hg-198-enriched mercury. The emission line of this lamp was broadened so that the Hg-196 isotope was excited by the wing of this line.

In spite of the impressive results achieved in the laboratory conditions, little is known about the commercial introduction of the photochemical processes. One of sparse examples is the pilot-scale photochemical technology of mercury isotope separation.

The author developed a technology and designed an experimental setup for extraction of highly enriched mercury isotopes [7, 8]. Along with the Hg-198, Hg-199, Hg-200, and Hg-202 isotopes, the mercury isotope Hg-196 was produced for the first time with a concentration as high as 97%. A number of novel physical and technical approaches made it possible to automate the enrichment process, render it continuous, and minimize operating personnel [9].

The essence of the experimental process is photochemical oxidation of excited mercury atoms by oxygen in the presence of 1,3-butadiene. The atoms are excited by the resonance radiation (wavelength $\lambda = 253.7$ nm) from a low-pressure mercury lamp. This reaction provides a high selectivity of separation, which is of special importance in concentrating mercury isotopes with (partially or completely) overlapping resonance lines.

First, emphasis was on developing production technology for the most abundant and most expensive Hg-196 isotope.
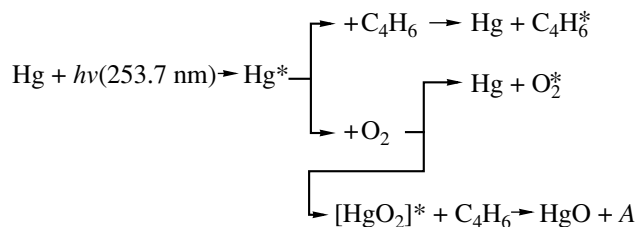
$$Hg + h\nu(253.7\ nm) \rightarrow Hg^* \begin{cases} +C_4H_6 \rightarrow Hg + C_4H_6^* \\ +O_2 \rightarrow Hg + O_2^* \end{cases}$$
$$[HgO_2]^* + C_4H_6 \rightarrow HgO + A$$

Fig. 1. Route of the photochemical reaction (*A* stands for by-products).
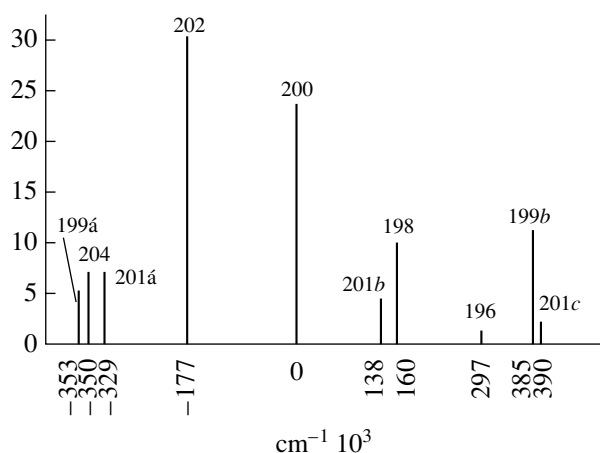
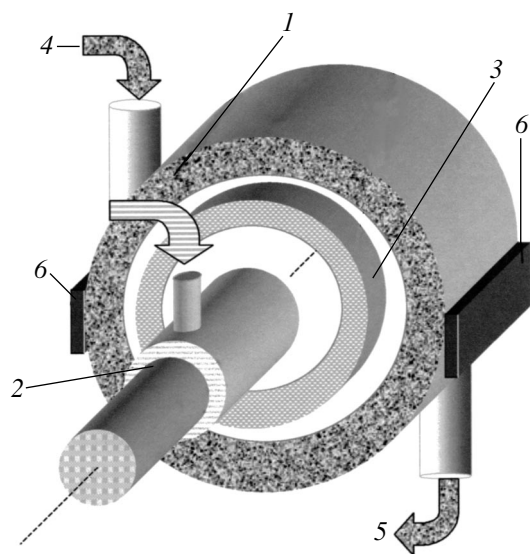**Fig. 2.** Hyperfine structure of the 253.7-nm resonance line of mercury.

Fig. 3. Photochemical separating unit: (*1*) photochemical cell, (*2*) low-pressure mercury-vapor lamp, (*3*) isotope filter, (*4*) inlet pipe, (*5*) outlet pipe, and (*6*) electrodes.

SEPARATION OF THE Hg-196 ISOTOPE

Enrichment of mercury by Hg-196 is a specific process, since natural mercury contains this isotope in small amounts (0.146%) and the spectral situation is rather complicated. The hyperfine structure of the mercury resonance line at 253.7 nm is shown in Fig. 2. The center of the absorption line of Hg-196 is offset from the absorption line components of Hg-199 and Hg-201 by 0.088 and 0.093 cm^{-1}, respectively, and from the lines of Hg-198 and Hg-201 by 0.137 and 0.150 cm^{-1}, respectively. Therefore, not only the desired isotope Hg-196 but also the Hg-198, Hg-199, and Hg-201 isotopes are enriched.

Enrichment of mercury by Hg-196 proceeds in several stages, with the product enriched at the previous stage being used as a raw material at the next one.

The efficiency of the setup to a great extent depends on the design of the separating unit (Fig. 3), which contains photochemical cell *1*, low-pressure mercury-vapor lamp *2*, and isotope filter *3* (if necessary).

The low-pressure mercury-vapor lamp with desired light characteristics was designed specially for initiating the photochemical reaction and represents a quartz tube with cathodic areas and a cooling-water jacket soldered on the tube. The lamp is mounted at the axis of the separating unit.

The simplest design of the photochemical cell represents a two-wall volume between two coaxial quartz tubes soldered to each other or flange-sealed at the side faces. The cell is configured with inlet pipe *4* for reagent delivery (oxygen, mercury, and 1,3-butadiene) and outlet pipe *5* for removal of the enriched mercury and reaction products. On the outer surface of the cell, two electrodes *6* made of nickel foil are placed facing each other. One of them is grounded, and the other is under a varying potential of frequency 50–60 kHz and amplitude 6–10 kV when it is necessary to initiate a spatially uniform high-frequency discharge in the inner space of the cell to remove the recovery or clean the cell from organic deposits in the oxygen atmosphere. The working gap was selected in such a way that the radiation of the mercury lamp is utilized most effectively. At the first cycle of mercury enrichment by Hg-196, when the optical density in terms of this isotope is low, cells with a wide (25 mm or more) gap are used. At the second and subsequent cycles, the gap is usually not wider than 5–6 mm.

The isotope filter, which is applied for filtering out the radiation from the lamp, is placed between the cooling jacket and the inner wall of the cell. Structurally, the filter represents two coaxial quartz tubes 8–9 mm apart that are soldered to each other at the ends. The filter is filled with mercury of natural isotope composition (the concentration of the desired Hg-196 isotope is 0.146%). The efficiency of the filter depends on its working gap and cold-point temperature, as well as on the molecular weight and pressure of the quenching gas. Hydrogen, which has a large cross section of quenching the 253.7-nm resonance line and prevents scattering of the mercury-absorbed radiation, served as a quenching gas most frequently. Sometimes, when it was necessary to broaden the mercury absorption line in the filter, a heavier gas, e.g., nitrogen, or a gas mixture (hydrogen and argon, nitrogen and argon, etc., in various proportions) was used. The mercury absorption linewidth in the filter may also be controlled by varying the cold-point temperature. Significantly, as the cold-point temperature rises, the absorption of the lamp radiation at the center of the line of transparency is enhanced, which may reduce the output of the setup.

The enrichment process consists in the following. A working mixture of oxygen and 1,3-butadiene circulates in the closed loop of the setup, entraps the mercury vapor from the evaporator, and supplies it to the separating units, which are connected in series, in parallel, or in series parallel depending on the operating conditions. In the separating units, mercury atoms excited by the mercury lamps are oxidized and the oxide deposits on the inner surface of the photochemical cells. The mercury depleted by the desired isotope or by several isotopes (waste) remains in the cooled trap. Hydrogen is pumped through the separating units at regular intervals, a high-frequency discharge is initiated, and the mercury oxide enriched by the desired isotope is reduced to the metal. The reduction of enriched mercury from its oxide is described in [10]. The hydrogen flow entrains the metallic mercury vapor and carries it to the liquid-nitrogen-cooled collector. The setup may switch the operating conditions according to the supervisory program inserted. Necessary operating conditions are set with the circuits that are controlled by signals from the automatic control unit [11].

The filter–lamp system was optimized in only one parameter, the cooling water temperature. Since the lamp is mounted on the inner tube of the filter, the cold-point temperature of the filter was specified by the cooling water temperature.

SEPARATION OF THE Hg-196 ISOTOPE BY THE DIRECT ENRICHMENT METHOD

In the direct enrichment method, the desired isotope, which is collected in a separated-isotope collector, is excited by mercury lamp and enters into the chemical reaction of oxidation.

In the production of Hg-196, we used four parallel-connected photochemical separating units with a gap of 25 mm, an isotope filter with a gap of 8 mm that was filled with mercury of natural isotopic composition, and hydrogen as a quenching gas.

When the mercury was enriched by Hg-196, we tried the following expedients: filtering-out of the lamp radiation, process cyclization, and successive replacement of the depleted mercury in the lamps by the enriched mercury extracted from the isotope collector.

The feasibility of enrichment process cyclization was studied in an attempt to produce mercury with a Hg-196 concentration as high as possible. After the first cycle, the Hg-196 concentration in the product was 5–7%. This mercury was used as a raw material for the second cycle of enrichment, etc.

The Hg-196 concentration in the enriched product, C, versus Hg-196 concentration C_0 in the raw material is shown in Fig. 4. From cycle to cycle, the enrichment factor for Hg-196 declines, while the enrichment factors for foreign (impurity) isotopes (especially for Hg-200 and Hg-202) increase. This is because the mercury
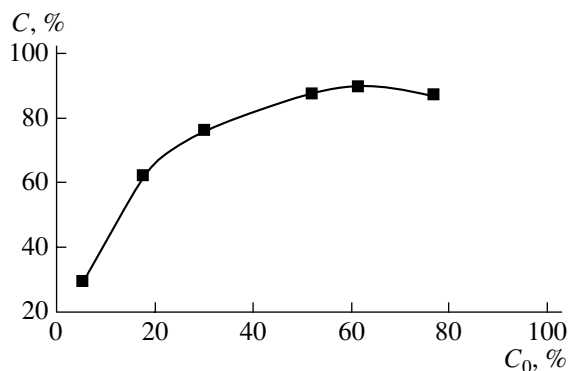

Fig. 4. Hg-196 concentration C in the product vs. Hg-196 concentration C_0 in the raw material.
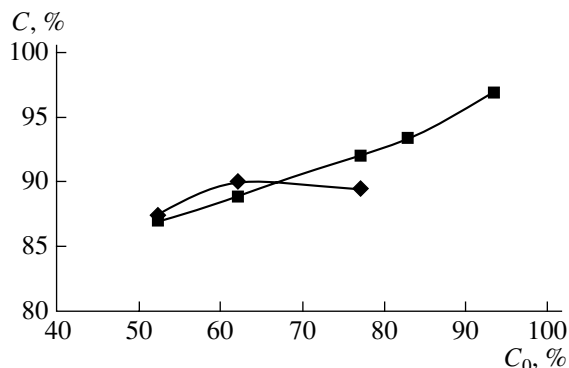

Fig. 5. Hg-196 concentration C in the product vs. Hg-196 concentration C_0 in the raw material. (◆) Direct and (■) negative method.

atom density at the entrance to the reaction cells must be decreased in each of subsequent cycles.

In the last cycle but one, the Hg-196 concentration in the mercury reached 90% but reduced to 87.5% after the last cycle. This mercury was then used in mercury-vapor lamps. Further enrichment by Hg-196 turned out to be impossible, since, when the rate of evaporation is low, the product is heavily contaminated by isotopes of the raw material used in the current cycle and also in the previous cycles.

The cost of the mercury thus enriched was extremely high. The experiments performed demonstrated that direct enrichment is appropriate if the desired isotope concentration does not exceed 60–62%. Isotopes of higher concentrations (<90%) may be obtained with the negative enrichment method, in which impurity (and not desired) isotopes are excited and extracted from the raw material.

SEPARATION OF THE Hg-196 ISOTOPE BY THE NEGATIVE ENRICHMENT METHOD

In this method, a mercury-vapor lamp of certain isotopic composition excites impurity isotopes, which are

then oxidized, while the desired isotope is collected in the trap as waste.

In this case, we employed a lamp filled with Hg-196-depleted mercury (0.08%). Impurity isotopes were extracted without using an isotope filter.

In these experiments, the process was also cyclic. The dependence of Hg-196 concentration C in the product on Hg-196 concentration C_0 in the raw material is presented in Fig. 5 for the direct and negative enrichment processes. Clearly, the efficiency of negative enrichment reaches a maximum when the raw material is preenriched to 50–55%. Therefore, Fig. 4 shows the final stages of enrichment of Hg-196.

The method of negative enrichment is seen to be more efficient in separating Hg-196, since the mercury vapor density at each subsequent cycle is higher than in the preceding one. Accordingly, at each subsequent cycle, the output of the setup increases, the losses of the valuable raw material decline, and the probability that the product will be contaminated by the background mercury decreases.

CONCLUSIONS

The basic result of this work is that the Hg-196 isotope is produced in high concentrations (up to 97%) for the first time. This became possible owing to the joint application of two, direct and negative, enrichment methods and also to the application of original physical and technical approaches in designing the setup. With light sources that contain a high concentration of Hg-196, one can further optimize the photochemical method both in terms of extracting isotopes with overlapping resonance lines from naturally occurring isotope mixtures and in terms of raising the output of the photochemical setup for large-scale production of the Hg-196 isotope. Production of highly enriched Hg-196 offers considerable scope for its application in other areas of applied and fundamental physics, as well as in pollution prevention programs, geology, etc.

REFERENCES

1. http://www.umanitoba.ca/institures/fisheries/METAALI-CUS1.html.
2. http://sofia.usgs.gov/geer/posters/merc_cycle/.
3. J. Maya, M. W. Grossman, R. Laguchenko, *et al.*, Science **226**, 435 (1984).
4. J. P. Morand, M. Wacogne, and E. Poth, Energia Nucleare **10**, 362 (1968).
5. G. Müller *et al.*, J. Photochem. **13**, 109 (1980).
6. G. Müller *et al.*, Isotopenpraxis **17**, 200 (1981).
7. Yu. V. Viazovetski, RF Patent No. 2,074,017 (1993).
8. Yu. V. Viazovetski, RF Patent No. 2,074,018 (1993).
9. Yu. V. Viazovetski and A. P. Senchenkov, Zh. Tekh. Fiz. **68**, 67 (1998) [Tech. Phys. **43**, 60 (1998)].
10. A. P. Senchenkov and V. I. Boloshin, USSR Inventor's Certificate No. 714,697 (1982), Byull. Izobret., No. 38 (1982).
11. Yu. V. Viazovetski, Candidate's Dissertation (Russian Research Center Kurchatov Institute, 1995).

Translated by V. Isaakyan

Effect of the Parameters of the Plasma Channel Produced by a High-Current Relativistic Electron Beam in Dense Gaseous Media on the Beam Transportation Stability

N. A. Kondrat'ev and V. I. Smetanin[†]

Research Institute of Nuclear Physcs, Tomsk Polytechnic University, Tomsk, 634050 Russia

e-mail: alex@npi.tpu.ru

Received November 14, 2003; in final form, July 2, 2004

Abstract—Results are presented from experimental studies of the time evolution of the plasma channel produced by a high-current electron beam (with an electron energy of $E_e = 1.1$ MeV, a beam current of $I_b = 24$ kA, and a pulse duration of $t = 60$ ns) in helium, nitrogen, neon, air, argon, krypton, xenon, and humid air (air : H_2O) at pressures from 1 to 760 Torr. It is shown that, in gases characterized by a small ratio of the collision frequency to the gas ionization rate u_i, the electron beam produces a broad high-conductivity plasma channel, such that $R_b/R_p < 1$, where R_b and R_p are the beam and channel radii, respectively. As a result, large-scale resistive hose instability is suppressed. © 2005 Pleiades Publishing, Inc.

INTRODUCTION

Particular interest in application of relativistic electron beams (REBs) propagating in gaseous media is motivated not only by their unique capability of transporting high-density energy fluxes through gases, but also by the possibility of using them to initiate a number of selective plasmochemical reactions or synthesize compounds in beam plasmas [1–3]. However, stable transportation of an REB through a gaseous medium can be disturbed or even terminated because of the onset of large-scale instabilities, among which the most dangerous is resistive hose instability (RHI) [4]. This instability has been the subject of many theoretical and experimental studies [5–8]. In studying mechanisms responsible for RHI, particular attention has also been paid to the processes accompanying the formation of the plasma channel produced by the beam in a gas [9–13]. These studies were performed, however, for a limited number of gases (air, nitrogen, and argon) within a narrow pressure range. Therefore, it is rather difficult to reveal general features of REB transportation stability in different gases at different experimental conditions. The determination of these general features and taking them into account can help to develop methods for suppressing RHI in various technological applications with the participation of high-current electron beams.

EXPERIMENTAL SETUP

Experiments were carried out on a Tonus accelerator [14], generating REBs with an electron energy of $E_e = 1.1$ MeV, a current of $I_b = 20$–24 kA, a current pulse duration of $t_e = 60$ ns, and a diameter at the exit from

the accelerator of 5 cm. The generated high-current REB was injected through an titanium anode foil of thickness 50 μm into a 9.2-cm-diameter metal drift tube (DT) filled with a gas (helium, nitrogen, neon, air, argon, krypton, xenon, or humid air (air : H_2O)) at a pressure from 1 to 760 Torr (Fig. 1). Experiments were performed at two different DT lengths: $L_1 = 0.4$ m and $L_2 = 1.4$ m. Varying the DT length, we could perform necessary measurements at distances from the accelerator anode at which large-scale instabilities insignificantly affected the beam propagation (L_1) and at distances at which the REB propagation was substantially
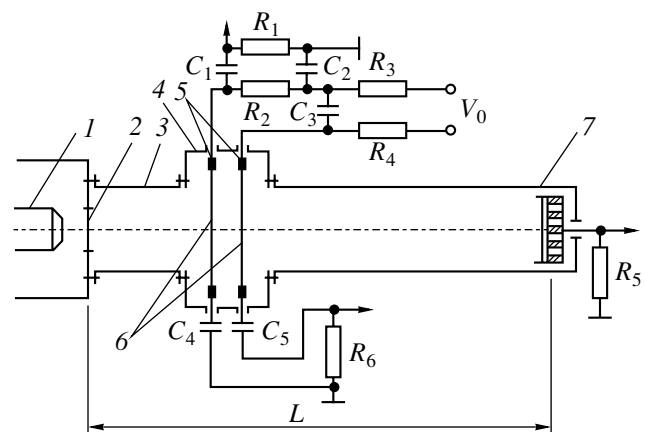

Fig. 1. Scheme of the experimental setup and the measurement circuits: (*1*) accelerator cathode, (*2*) anode, (*3*) drift tube, (*4*) experimental chamber for measuring the conductivity, (*5*) annular clamps for foils, (*6*) measurement foils, (*7*) sectioned evacuated Faraday cup, (C_1–C_5) measurement and compensating capacitors, and (R_1–R_6) measurement resistors.

[†] Deceased.

Table 1

Gas	Molecular mass	ρ, kg/m^3	ν, 10^9 s^{-1}	U_0, eV	σ_g, 10^{-16}cm^2	E_{thr}, kV/cm	E_t/P, V/(cm Torr)	α, ion s/cm^3
He	4.0	0.17	6.69	24.5	2.83	2.4	13.0	1.7×10^{-8}
Ne	20.1	0.90	4.20	21.5	4.14	5.3	1.9	2.1×10^{-7}
N$_2$	28.1	1.25	7.45	15.5	7.80		46.0	1.4×10^{-6}
Air	28.9	1.29		16.3		31.2	42.0	2.5×10^{-6}
Ar	39.9	1.78	5.90	15.7	6.46	7.5	3.6	3.0×10^{-7}
Kr	83.8	3.74	5.30	14.0	7.54	17.5		6.0×10^{-7}
Xe	131.3	5.58	5.80	12.0	9.16	18.2		2.0×10^{-6}
Air + H$_2$O			13.9			25.0		

Notes: ρ is the mass density, ν is the collision frequency at 15°C and a pressure of 760 Torr, U_0 is the ionization energy, σ_g is the gas-kinetic ionization cross section, E_{thr} is the static breakdown field, E_t/P is the breakdown threshold at pressures close to atmospheric, and α is the dissociative recombination coefficient.

affected by the onset of instability (L_2). The REB transportation efficiency through the DT (defined as the ratio I_b/I_{inj} of the beam current I_b measured by an evacuated Faraday cup at the end of the DT to the beam current I_{inj} at the exit from the accelerator) was determined at the distances L_1 and L_2 from the accelerator anode. The distribution of the beam current density across the transportation channel was measured by a sectioned Faraday cup (see [15]). We also measured the time evolution the plasma channel produced by the REB in a gas and the radial profile of its conductivity by the method described in [16].

PARAMETERS OF THE GASES USED

When a high-current REB propagates through a dense neutral gas, the conductivity and the time evolution of the formed plasma channel depend on the character of atomic and molecular processes occurring in the gas. It is well known that the number of these processes is more than one hundred. Among those, the most important are electron-impact ionization (including elastic and inelastic collisions and electron energy loss through the excitation of vibrational and rotational atomic levels); stepwise dissociation; photoionization; avalanche ionization by secondary electrons and ions, by plasma electrons acquiring energy in high-frequency Langmuir oscillations, and also due to energy gained from molecular vibrations; electron–electron and electron–ion recombination; the formation of clusters and negative ions; and selective chemical reactions proceeding in the REB transportation channel. The character of these processes depends not only on the parameters of the REB itself (the electron energy, beam current, and beam diameter), but also on the pressure and sort of the gas. With the set of gases used in our experiments, we could study the beam transportation through media that differed markedly by their basic parameters and constants. The gaseous media used in our experiments are listed in Table 1 in order of increas-

ing molecular mass and mass density ρ (kg/m^3). The table also presents a number of the gas constants that are most important in our opinion. It is obvious that we are interested, first of all, in the parameters determining the ionization processes: the ionization energy U_0, the collision frequency ν, and the gas-kinetic ionization cross section σ_g. For the process of gas breakdown by an REB, the most important parameters are the static breakdown field E_{thr} and the breakdown threshold E_t/P at pressures close to atmospheric (where E_t is the breakdown field and P is the gas pressure) [17].

RESULTS AND DISCUSSION

Figure 2 shows distributions of the REB current density j_e across the transportation channel. The distributions were measured with the help of a sectioned Faraday cup for DTs of lengths $L_1 = 0.4$ m and $L_2 = 1.4$ m. For the sake of clearness, the figure also shows the radial profiles of the conductivity of the beam plasma σ for a DT of length $L_1 = 0.4$ m. In our experiments, the gas pressure ranged from 1 to 760 Torr; however, because of the limited space of this paper, Fig. 2 presents only the data for a gas pressure of $P = 300$ Torr, which reflects all the characteristic features of the results obtained. The measured current transportation efficiency I_b/I_{inj} through the gases under study for a DT of length $L_2 = 1.4$ m is presented in Table 2.

The fairly high values of the REB transportation efficiency at a DT length of L_1 for most of the gases under study can be explained in terms of the REB propagation stability. The interaction of the REB with the generated plasma ensures almost full charge neutralization and a high degree of current neutralization f_m, which is defined as $f_m = I_p/I_b$, where I_b is the electron beam current and I_p is the plasma current induced by the vortex electromotive force [18]. In this case, the electron beam current is lost predominantly due to ionization and scattering by gas atoms at an increased gas
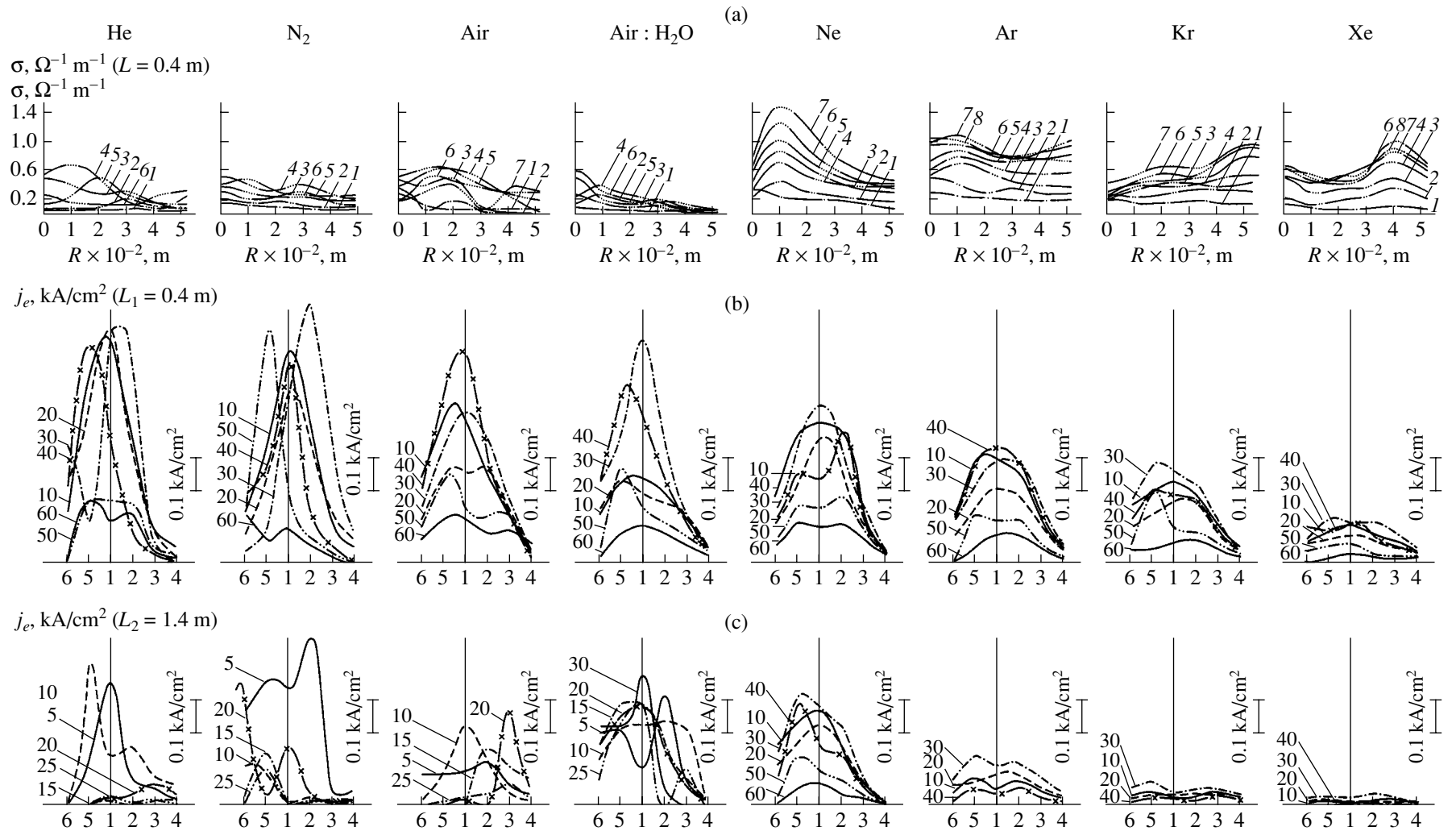
Fig. 2. (a) Measured radial profiles of the conductivity σ of the plasma channels produced by REBs in different gases for a DT of length $L_1 = 0.4$ m at the following instants: (*1*) 10, (*2*) 20, (*3*) 30, (*4*) 40, (*5*) 50, (*6*) 60, (*7*) 70, and (*8*) 80 ns. (b, c) Distributions of the current density j_e (measured with the help of a sectioned Faraday cup) across the transportation channel of a high-current REB in different gases for DTs of lengths (b) $L_1 = 0.4$ m and (c) $L_2 = 1.4$ m at the following instants: (*10*) 10, (*20*) 20, (*30*) 30, (*40*) 40, (*50*) 50, and (*60*) 60, ns. The time is counted from the start of the REB pulse. The numbers of the lamellas of the sectioned Faraday cup, which are shown on the abscissa, correspond to the following radii R: (*1*) 0, (*2*) 1.15, (*3*) 3.15, (*4*) 4.15, (*5*) 2.15, and (*6*) 4.25 cm.

Table 2. Current transportation efficiency I_b/I_{inj} and the calculated degree of current neutralization f_m in the gases under study for $L_2 = 1.4$ m

Gas	1 Torr		10 Torr		100 Torr		300 Torr		760 Torr	
	I_b/I_{inj}	f_m	I_b/I_{inj}	f_m	I_b/I_{inj}	f_m	I_b/I_{inj}	f_m	I_b/I_{inj}	f_m
Ne	0.70	0.78	0.70	0.75	0.60	0.70	0.50	0.68	0.40	0.67
Ar	0.68	0.72	0.60	0.68	0.56	0.64	0.45	0.62	0.30	0.60
He	0.67	0.70	0.65	0.65	0.40	0.63	0.20	0.59	0.10	0.59
Air	0.68	0.72	0.58	0.68	0.32	0.65	0.30	0.60	0.28	0.58
N_2	0.75	0.70	0.50	0.67	0.20	0.62	0.22	0.58	0.18	0.58
Air : H_2O	–	–	0.45	0.60	0.35	0.58	0.30	0.56	0.10	0.54
Kr	0.45	0.70	0.45	0.68	0.15	0.65	–	–	–	–
Xe	0.45	0.68	0.28	0.64	0.10	0.60	–	–	–	–

pressure in the DT. A change in the character of REB propagation is reflected in the beam transportation efficiency at a DT length of $L_2 = 1.4$ m. In most of the gases, the most probable process considerably reducing the REB transportation efficiency is the onset of large-scale instability, which manifests itself as a displacement of the electron beam from the DT axis or even as the forcing of the beam onto the DT wall (Fig. 2c). Small transverse oscillations of the REB at a distance of $L_1 = 0.4$ m from the accelerator, which are most pronounced for He, N_2, and air (Fig. 2b), grow considerably with increasing pressure and transportation length (to $L_2 = 1.4$ m). The disturbance of the beam propagation is certainly related to the onset of large-scale resistive instability. The mechanism for the onset of RHI in a finite-conductivity plasma can be explained as follows: The beam particles moving in their own magnetic field are affected by the centrifugal force arising at small random oscillations (bends) of the beam. Under the action of this force, the REB is displaced in the transverse direction over a distance on the order of its radius over a time longer than the diffusion time of the magnetic field in the ambient plasma, $t_d = 4\pi g r_e/c^2$, where g is the plasma conductivity and r_e is the beam radius. The velocity with which the magnetic field is displaced depends on the plasma conductivity, so the REB magnetic field shifts in the transverse direction more slowly than the REB itself and is retarded in phase with respect to the beam displacement. The motion of the beam relative to its own magnetic field induces a reverse plasma current I_p, which is spatially separated from the REB current I_b. Due to the repulsive interaction between these oppositely directed currents, the amplitude of the beam displacement increases further. As a result, RHI develops, which manifest itself in the increase in the amplitude of transverse oscillations of the REB. Such oscillations lead to the termination of the beam transportation at distances that do not exceed one to three betatron lengths $L_{bet} = \pi r_e(I_A/I_b)^{0.5}$, where I_A is the Alfvén current [19]. Under our experimental conditions, L_{bet} is on the order of 0.3–0.35 m. The results presented in Fig. 2 certainly indicate the growth of such REB transverse oscillations, whose amplitude is initially (at L_1) small and then (at L_2) increases due to the onset of RHI to such a high value that the beam is expelled onto the DT wall, so its transportation becomes impossible.

In [20], the development of RHI of an REB with parameters comparable to those in our experiments was studied. An electron beam with a particle energy of $E_e = 1$ MeV and a current of $I_b = 2$–10 kA was injected into air at pressures of 0.1–630 Torr. The velocity of the transverse displacement of the REB was determined with the help of inductive detectors as a function of the gas pressure P and transportation length L. The minimal velocity of displacement $U = 10^7$ cm/s corresponded to $P = 0.77$ Torr. In this case, the displacement amplitude was as low as 1.0–1.2 mm and the frequency of hose oscillations was $f_{hose} = 30$ MHz. As the gas pressure was increased further, the velocity of displacement sharply increased and reached a value of $U \sim 10^9$ cm/s at $P = 100$ Torr. At $P = 630$ Torr, the amplitude of the transverse oscillations of the beam far exceeded its diameter ($L > 0.7$ m, $f_{hose} = 180$ MHz).

Obviously, the onset or suppression (or a substantial retardation) of RHI of a high-current REB propagating through different gases depends on the conductivity of the formed plasma channel and on the character of the interaction of the fields induced in the beam–plasma system. Thus, in [21, 22], using the results from preliminary experiments and numerical simulations based on a "hard beam" model, which allowed one to analytically study the dispersion properties of RHI, it was shown that RHI is suppressed when the radial profile of the equilibrium plasma current R_p is substantially broader than the electron beam profile R_b (i.e., when $R_p \gg R_b$). On the other hand, when $R_p = R_b$, there is an additional mechanism for enhancing RHI. It is evident that, for $R_b/R_p > 1$, the instability increases substantially because the reverse plasma current is concentrated

mostly inside the beam. As a result, the repulsive interaction of the oppositely directed beam and plasma currents is very efficient and leads to a displacement of the REB from the conducting channel. If $R_b/R_p \ll 1$, then, due to avalanche ionization, most of the plasma current flows outside the beam; this is favorable for confining the REB near its propagation axis. Apparently, it is these plasma processes that are responsible for our experimental results obtained for Ne and Ar (Fig. 2). In this case, small (with an amplitude less than the beam radius) transverse oscillations of the REB are not enhanced as the gas pressure and the transportation length increase. At the same time, in N_2, He, and air, transverse oscillations of the REB terminate the beam transportation. A high-current beam propagating in Ne, Ar, Kr, and Xe produces a uniform and broad ($R_b/R_p <$ 1) high-conductivity plasma channel with a characteristic maximum at the periphery of the beam (Fig. 2a). The latter indicates that the gas breakdown occurs in the radial direction. The plasma channel ensures the stable propagation of the REB and the suppression of its transverse oscillations over the entire propagation length. On the other hand, in He, air, and N_2 and in an air : H_2O mixture, the radius of the conducting channel tends to $R_p = R_b$ with increasing pressure and the radial profile of the conductivity undergoes synchronous oscillations correlating with the transverse oscillations of the REB; as a result, the current transportation efficiency is substantially reduced. Taking into account that the parameters of high-current REBs injected into different gases were the same, we can conclude that the significant difference in the shapes of the measured radial conductivity profiles of the plasma channels in these gases can only be explained by different plasma-production mechanisms. The general features of the formation of the plasma channels and their influence on the REB propagation in different gases can be described as follows.

When a high-current REB with parameters corresponding to our experiments is injected into a neutral gas at a pressure of 1–760 Torr, the leading part of the beam is broken under the action of the unneutralized radial electric field. The electrons from this part of the beam have time to ionize the gas, so the charge of the following part of the beam is neutralized. The slow secondary electrons and ions generated in the course of ionization are more strongly affected by the space charge field and, up to $f_e = 1$, move predominantly in the radial direction and leave the region occupied by the beam. After the space charge of the REB is completely neutralized, the secondary electrons no longer escape from the beam and participate in ionization, being accelerated in the longitudinal electric field E_z. In our case, the time during which the space charge is completely neutralized does not exceed 1–4 ns [18].

The maximal density of the plasma produced by gas breakdown is determined by the balance between the ionization rate u_1 and the loss of charged particles by diffusion, recombination, deposition on the DT wall, etc. Gas breakdown is characterized by the well-defined threshold; i.e., breakdown occurs only at fields that exceed a certain value of E_t/P, which depends on the experimental conditions, including the sort of gas (see Table 1). The existence of the threshold is explained by the fact that the rate u_i of electron-impact ionization of atoms depends strongly on the electric field and that there are mechanisms hindering the development of an avalanche. The avalanche is retarded by both electron energy losses and the loss of electrons themselves. In the former case, the electrons gain energy sufficient for ionization more slowly; in the latter case, the chain multiplication reactions are broken. The electrons expend their energy on the excitation of the atomic and molecular electronic states and molecular vibrations and lose it in elastic collisions. As an example of such a redistribution of energy, Fig. 3 shows data obtained for nitrogen and air [17]. These results were confirmed by numerical simulations [23], which showed that a broad ($R_b/R_p < 1$) plasma channel forms in gases in which the ratio of the collision frequency to the ionization rate u_i is sufficiently small (i.e., when $\upsilon/u_i < 1$). Our results obtained for Ar, Ne, Kr, and Xe can be regarded as an experimental verification of this numerical model. We compared the data presented in Table 1 (V and E_t/P) and the radial profiles of the conductivity to the corresponding parameters for other gaseous media. The high ionization rates u_i characteristic of Ne and Ar determine the low breakdown thresholds E_t/P for these gases at pressures close to atmospheric (1.9 and 3.6 V/(cm Torr), respectively). The ionization features of these gases are also confirmed by the results from studies of their static breakdown voltages in a plane anode–cathode gap. These results, which were obtained at different gas pressures P and gap lengths d and which are known as Paschen curves, are presented in Fig. 4 [17]. Over a wide range of gas pressures, the breakdown voltages V_t for Ne and Ar are the lowest.
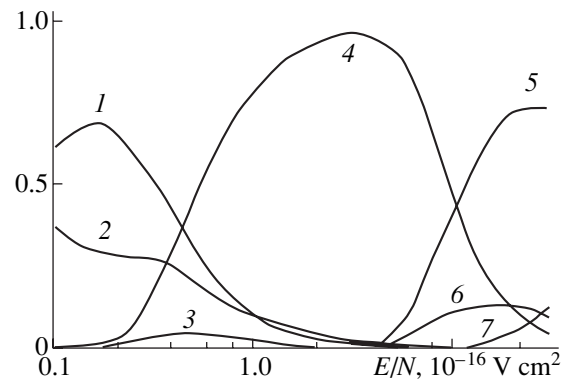

Fig. 3. Fractions of the electron energy expended on (*1*) O_2 vibrations, (*2*) O_2 and N_2 rotations, (*3*) elastic losses, (*4*) N_2 vibrations, (*5*) N_2 and (*6*) O_2 electronic excitations, and (*7*) ionization of O_2 and N_2.
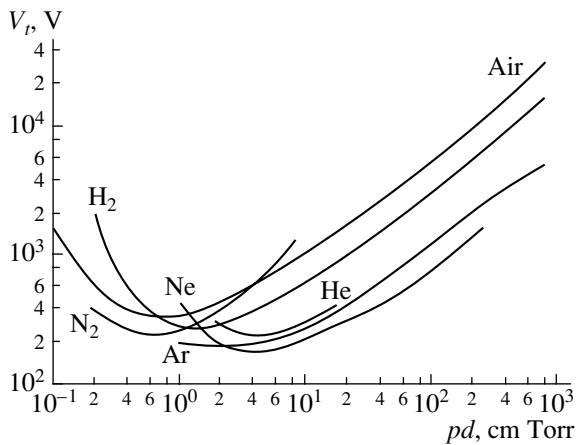
Fig. 4. Threshold potentials V_t of different gases as functions of the pressure p and discharge gap length d (Paschen's curves).
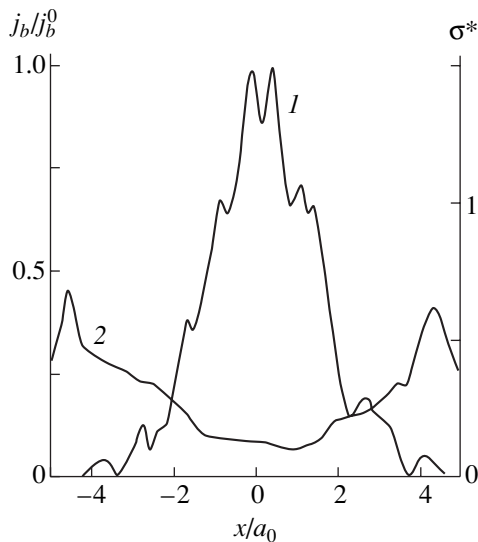

Fig. 5. Formation of the conducting channel around the REB: (*1*) the radial profile of the REB current density $j_b(x)$, normalized to the maximal REB current density j_b^0 at the point of injection and (*2*) the radial profile of the plasma channel conductivity $\sigma^*(x)$ (in arb. units). The radial coordinate x is normalized to the initial REB radius a_0.

It is evident that, in addition to the above mechanism for plasma channel formation, we should also take into account the effect of the radial component of electric field, which is equal to

$$E(r) = U/r\ln(r_2/r_1),$$

where U is the voltage, r_2 is the DT radius, and r_1 is the beam radius.

Under our experimental conditions, $E(r)$ is on the order of $\sim 10^5$ V/cm. In [24], it was shown that, in this case, the radial electric field is displaced to the periph-ery of the beam in the course of charge neutralization. The electric field $E = (E_z^2 + E_r^2)^{1/2}$ reaches its maximum at the beam edge, and the avalanche multiplication of electrons results in the formation of a conducting channel surrounding the beam and suppressing RHI (Fig. 5). It is transverse breakdown that forms a maximum in the radial profile of the plasma conductivity at the periphery of an REB propagating in Ar, Ne, Kr, or Xe. After breakdown, the conductivity of the plasma produced is very high and the electric field decreases to several hundred V/cm and lower.

Our results are qualitatively confirmed by the results obtained in [25, 26], where spatiotemporal behavior of the plasma conductivity was numerically reconstructed from the measured density distributions of the plasma and beam currents, $J_p(r, t)$ and $J_b(r, t)$. It was shown that, when an REB with a maximum of the current density at the beam axis is injected into air or argon, the plasma current has a maximum at the periphery of the plasma channel. This effect is explained by the avalanche ionization that develops in the space charge field displaced to the DT wall.

CONCLUSIONS

The main results from our experiments on studying the effect of the parameters of the plasma channel produced by a high-current REB on the beam transportation stability in dense gases can be formulated as follows:

(i) In gases in which the ratio of the collision frequency ν to the ionization rate u_i is small (i.e., $\nu/u_i < 1$), a high-current REB forms a broad high-conductivity plasma channel such that $R_b/R_p < 1$, where R_b and R_p are the beam and channel radii, respectively. As a result, large-scale RHI is suppressed. For gases in which $R_b/R_p > 1$, RHI is enhanced.

(ii) The formation of a broad ($R_b/R_p < 1$) high-conductivity plasma channel is preceded by the displacement of the maximum of the electric field $E = (E_z^2 + E_r^2)^{1/2}$ (where E_z is the longitudinal electric field and E_r is the radial electric field) to the REB periphery, where gas breakdown then occurs. The formed plasma channel, with a maximal conductivity at the beam edge, also suppresses the onset of RHI.

REFERENCES

1. G. E. Norman, L. S. Polak, P. I. Sopin, and G. A. Sorokin, in *Mechanisms of Plasma-Chemical Reactions between Hydrocarbons*, Ed. by L. S. Polak (Inst. Neftekhim. Sint. Akad. Nauk SSSR, Moscow, 1985) [in Russian].

2. V. D. Rusanov and A. A. Fridman, *Physics of Chemically Active Plasma* (Nauka, Moscow, 1984) [in Russian].

3. G. E. Remnev, A. I. Pushkarev, and M. A. Pushkarev, Izv. Vyssh. Uchebn. Zaved. Fiz., No. 7, 91 (2001).

4. M. N. Rosenbluth, Phys. Fluids **3**, 932 (1960).

5. H. S. Uhm and M. Lampe, Phys. Fluids **23**, 1574 (1980).

6. E. P. Lee and J. E. Brandenburg, Phys. Fluids **31**, 3403 (1988).

7. E. R. Nadezhdin and G. A. Sorokin, Fiz. Plazmy **14**, 619 (1988) [Sov. J. Plasma Phys. **14**, 365 (1988)].

8. E. H. Choi and H. S. Uhm, J. Appl. Phys. **65**, 3356 (1989).

9. N. A. Kondrat'ev, G. I. Kotlyarevskiǐ, and V. I. Smetanin, Zh. Tekh. Fiz. **59** (1), 118 (1989) [Sov. Phys. Tech. Phys. **34**, 450 (1989)].

10. A. W. Ali, Laser Part. Beams **6**, 105 (1988).

11. K. R. Davey, Phys. Fluids **26**, 1919 (1983).

12. G. F. Kiuttu, R. J. Adler, and R. J. Richter-Sand, Phys. Rev. Lett. **54**, 1668 (1985).

13. E. K. Kolesnikov and A. S. Manuǐlov, Zh. Tekh. Fiz. **67** (6), 69 (1997) [Tech. Phys. **42**, 648 (1997)].

14. I. Z. Gleǐzer, A. N. Didenko, L. P. Dronova, *et al.*, At. Energ. **36**, 378 (1974).

15. N. A. Kondratiev, V. I. Smetanin, and Yu. P. Surikov, Nucl. Instrum. Methods Phys. Res. **53**, 229 (1991).

16. N. A. Kondratiev, G. I. Kotliarevskiǐ, V. I. Smetanin, and Yu. P. Surikov, Phys. Lett. A **148**, 89 (1990).

17. Yu. P. Raizer, *Gas Discharge Physics* (Nauka, Moscow, 1992; Springer-Verlag, Berlin, 1991).

18. A. V. Agafonov, Atom. Tekh. Rubezhom, No. 10, 31 (1973).

19. E. A. Abramyan, B. A. Al'terkop, and G. D. Kuleshov, *Intense Electron Beams* (Énergoatomizdat, Moscow, 1984) [in Russian].

20. E. J. Lauwer, R. J. Briggs, and T. J. Fessenden, Phys. Fluids **21**, 1334 (1978).

21. R. F. Hubbard, R. F. Fernsler, S. P. Slinker, *et al.*, in *Proceedings of the 5th International Conference on High Power Particle Beams (BEAMS-83), San Francisco, 1983*, pp. 370–372.

22. E. K. Kolesnikov and A. S. Manuǐlov, Zh. Tekh. Fiz. **60** (3), 40 (1990) [Sov. Phys. Tech. Phys. **35**, 298 (1990)].

23. G. A. Sorokin, *Collective Methods of Acceleration and Beam–Plasma Interaction* (RI AN SSSR, Moscow, 1982) [in Russian].

24. G. Yu. Kurevlev and G. A. Sorokin, Teplofiz. Vys. Temp. **28**, 436 (1990).

25. Yu. F. Bondar', V. I. Klimov, G. P. Mkheidze, *et al.*, Tr. IOFAN **45**, 110 (1994).

26. G. P. Mkheidze, A. A. Savin, and G. A. Mesyats, in *Encyclopedia of Low-Temperature Plasma*, Ed. by V. E. Fortov (Nauka, Moscow, 2000), Vol. 4, pp. 108–126 [in Russian].

Translated by N. Larionova

EXPERIMENTAL INSTRUMENTS
AND TECHNIQUES

Effect of the Transverse Size of a Laser-Induced Plasma Torch on Material Processing

I. V. Blonskyy, A. Ya. Danko, V. N. Kadan, E. V. Orieshko, and V. M. Puzikov

Institute of Physics, National Academy of Sciences of Ukraine, pr. Nauki 144, Kiev, 03650 Ukraine

e-mail: kadan@iop.kiev.ua

Received March 10, 2004

Abstract—Projection microprocessing of materials by Nd : KGW laser shots (1.06 μm) is considered. Specifically, a practically feasible method of processing transparent materials (sapphire, fused quartz, and glass) by means of a laser-induced plasma is suggested. These materials are marked, in particular, by applying a controllable liquid-crystal mask on them. Also, a relief diffraction grating of period 3 μm is patterned on their surface. The effect of the transverse size of the area illuminated on the processing parameters is studied. It is established that the density and temperature of the laser-induced plasma grow with increasing transverse size of the torch, with the energy density of the laser radiation being the same. The plasma torch reverses the pressure and wavelength dependences of the rate of ablation of transparent materials as compared to those of metals. © 2005 Pleiades Publishing, Inc.

INTRODUCTION

Material processing by nanosecond laser pulses cannot be described in simple terms, since the resulting physical pattern is very complicated. The basic processes arising when a laser pulse strikes a transparent material are shown in Fig. 1. The overall process can be subdivided into separate sequential stages (which is sometimes incorrect, since the stages may proceed simultaneously), such as absorption of the pulsed radiation by the material and then its heating, melting, and sublimation. Intense sublimation generates a recoil pressure wave in the material. A high intensity of laser radiation may cause optical breakdown in the target vapor and, accordingly, a shock wave originating at the site of optical breakdown. Also, a plasma torch, which is capable of influencing the physical pattern of processing, may appear. Specifically, the plasma may absorb or completely reflect the radiation, depending on its temperature and density, thus screening the target and altering the thermal kinetics. Usually, plasma screening of the target should be minimized. However, the effect of plasma absorption may contribute to processing under certain conditions. An example is laser processing of transparent insulators, in which the radiation is not absorbed but its energy may be transferred to the material through the intermediate plasma phase. The transverse size of an area being processed is of great importance in processing of both metals and transparent insulators.

The aim of this work is to comparatively study how the transverse size of the plasma torch influences projection microprocessing of transparent insulators and metals. In addition, we suggest a practically feasible method of microprocessing transparent materials, such as sapphire, fused quarts, and glass, using a laser-induced plasma.
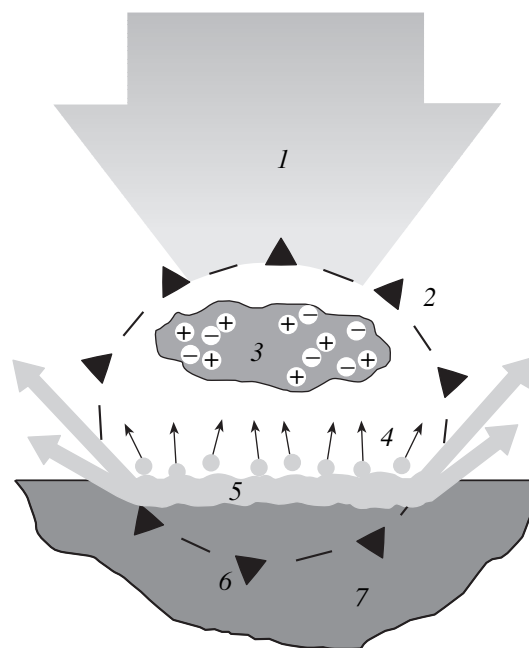

Fig. 1. Physical processes arising when a laser shot acts on a nontransparent material. (*1*) Laser beam, (*2*) shock wave front propagating from the site of ablation and optical breakdown, (*3*) plasma generated by optical breakdown in the material vapor, (*4*) material sublimation, (*5*) molten material splashed out beyond the laser spot under the action of the shock wave, (*6*) front of the recoil pressure wave in the material, and (*7*) nontransparent material.

EXPERIMENTAL SETUP

The optical scheme of the experimental setup is presented in Fig. 2. As a radiation source, we used a *Q*-switched water-cooled Nd : KGW laser of our own design that is pumped by a flash lamp. The laser output at a wavelength of 1.06 μm may reach 100 mJ, and the pulse duration is 10 ns. A polymer amplitude mask [1] and a liquid-crystal digital panel were used as stencils. Since the cross-sectional diameter of the laser beam on the mask is 3 mm and the mask measures 25 × 25 mm, a need appears for scanning the beam over the mask. Scanning averages the intensity nonuniformity over the beam's cross section. We used two scan units (sets of mirrors) *2* and *3*, which were mounted on the axis of a step motor. A rotation of the motor axis causes the beam to move parallel to the *X* or *Y* direction. The scan parameters (the width and number of steps and the size of the scan zone) were controllably varied. Galilean telescope *5* is used to decrease the mask–objective distance and place the beam at the center of the objective during scanning. The image of the mask is projected onto specimen *8* (fixed on *x–y–z* adjustable table *9*) through quartz triplet objective *7* with a focal length of 5 cm. Positioning and processing of the specimen can be observed through a microscope composed of objective *7* and eyepiece *12*.
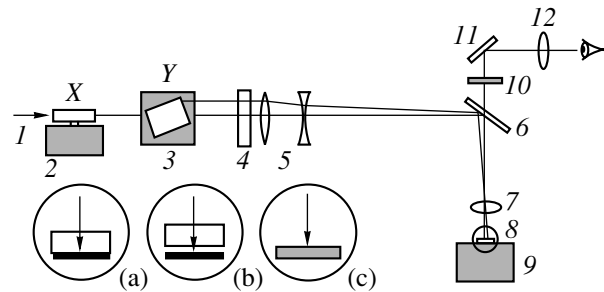
MICROPROCESSING OF TRANSPARENT MATERIALS

The method of microprocessing suggested in this paper is a modification of the method of laser-induced plasma-assisted ablation (LIPAA) elaborated by Zhang *et al.* [2, 3]. They processed transparent fused quartz in a vacuum chamber with a metallic target placed at a small distance from the specimen. The beam of a Nd : YAG laser (the second and fourth harmonics) passed through the specimen and fell on the target, causing its ablation and generating an ablation (metal-vapor) plasma. The plasma, in turn, contributed to the ablation of the rear (target-facing) transparent specimen surface, which is exposed to the same laser beam. With such an approach, Zhang *et al.* managed to pattern diffraction gratings of depth 0.9 μm and period 20 μm with a hole diameter of 0.7 μm in a 0.5-mm-thick fused quartz specimen. The advantage of this method is that there is no need for an expensive UV laser with photon energies above the absorption edge of a material; the disadvantage is the need for evacuating the chamber.

In our method, this disadvantage is eliminated by directly pressing a rubber target against the rear surface of a transparent specimen (Fig. 1a), which is in air under atmospheric pressure. We experimented with glass, fused quartz, and sapphire using the setup shown in Fig. 2. Figure 3 demonstrates an inscription (marking) engraved on the single-crystal sapphire specimen by the method suggested. Using a controllable liquid-crystal digital panel, similar micromarking was
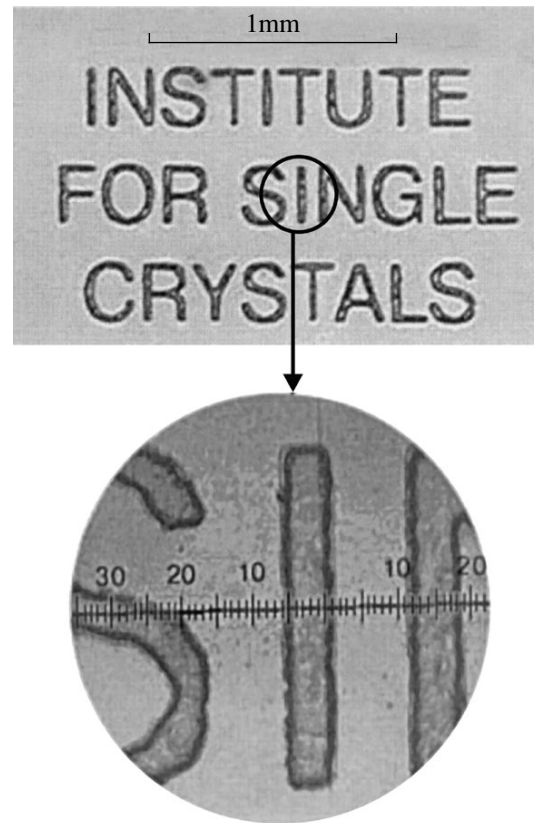

Fig. 2. Optical scheme of the experimental setup. (*1*) Nd : KGW laser beam, (*2*) *X* scanner, (*3*) *Y* scanner, (*4*) mask, (*5*) Galilean telescope, (*6*) mirror for the wavelength 1.06 μm, (*7*) projecting objective lens, (*8*) specimen, (*9*) *x–y–z* adjustable table, (*10*) protective light filter, (*11*) mirror, and (*12*) eyepiece for observation. (a) The specimen is a sapphire plate with a rubber target tightly pressed against the rear sapphire surface, (b) the specimen is a sapphire plate with a rubber target placed at a distance of 0.6 mm from the rear sapphire surface, and (c) metallic specimen.

Fig. 3. Inscription (micromarking) engraved on the sapphire specimen (5 μm per division).

engraved on the fused quartz and glass. The advantage of a liquid-crystal mask is that it makes it possible to change the surface pattern without being replaced.

Scanning of the mask took 15 s at a pulse repetition rate of 20 Hz. The pulse peak energy was 20 mJ. At a 13-fold demagnification provided by the projection system, the energy density reached 48 J/cm^2. In all the

cases, the processing resolution was 10 μm and the depth of marking, about 10 μm. Each point was processed by seven laser pulses. The ablation rate was found to be 1.4 μm per pulse (for LIPAA in a vacuum, it was no higher than 30 nm per pulse [2, 3]). Sapphire turned out to be more prone to cracking than quartz. Possibly, this is because the thermal expansion coefficients of these materials differ noticeably (0.5×10^{-6} deg^{-1} for fused quartz and 9.0×10^{-6} deg^{-1} for sapphire). In addition, crystalline sapphire is a birefringent material; therefore, two images corresponding to the ordinary and extraordinary rays appear on the rear surface at a certain orientation of the crystal and laser radiation polarization. In the experiments with a controllable slit, which will be discussed below, the rays diverge most noticeably: by 2–3 μm in the 5-mm-thick specimens. However, birefringence is not observed in the inscription shown in Fig. 3, because the specimen is thin (2 mm thick) and the resolution is closer to 10 μm.

Let us discuss the physical mechanisms behind our version of LIPAA (recall that it differs substantially from the original method [2, 3]). Laser breakdown generates a target-vapor plasma near the target and a transparent specimen. The temperature and density of the plasma grow in an avalanche-like manner (owing to laser radiation absorption in the process of inverse bremsstrahlung of electrons colliding with ions and neutral atoms) and may vary over wide limits. According to [4], the laser-induced plasma temperature during ablation of fused quartz varied from 15 000 to 60 000°C depending on the plasma torch geometry (the energy density of the 266-nm fourth harmonic of the Nd : YAG laser was 48 J/cm^2 and the spot diameter, 50 μm). The temperature and density of the plasma were the lowest at the ablation of a flat surface, i.e., for the freely expanding torch. When the ablation took place in a cylindrical cavity of diameter 80 μm, i.e., when the expansion of the plasma confined by the cylinder walls was nearly one-dimensional, its temperature and density were the highest. In our case, the energy density of the laser pulse also equaled 48 J/cm^2 and the plasma was severely confined in a microscopic cavity between the sapphire and rubber target, which arose because of ablation and deformation. Therefore, we may tentatively assume that the plasma temperature and density in our case are equal to the highest values reached in [4] ($T = 60\,000$°C, the electron density $n_e = 8 \times 10^{18}$ cm^{-3}). Contact transfer of the plasma energy to the transparent material seems to be the most plausible mechanism of energy transfer here. This assumption is corroborated by the following observation. Sometimes, when the energy density of the pulse exceeded 60 J/cm^2, the plasma pressure became so high that the plasma penetrated outside the processing spot between the target and sapphire, causing surface melting of the sapphire in areas beyond the reach of the laser radiation. Then, when the slit was projected onto the sapphire—rubber target assembly, the strip of the material removed was,

as a rule, 5 μm wider than the slit image; in other words, the material was removed from areas that were not directly exposed to the laser radiation. There lies a dissimilarity between our version and the original [2, 3] version of the LIPAA method (in the original version, a metallic target is several millimeters distant from a specimen in a vacuum). Zhang *et al.* [2, 3] wittingly used a plasma generated by an external laser (not participating in the process) and found that ablation takes place only if the laser radiation directly interacts with the plasma. That is, the plasma does not cause ablation in the absence of the laser radiation. It appears that, in our case, the plasma temperature and density are sufficiently high for contact ablation to proceed even in the absence of the radiation. This is quite natural, since not only is the specimen–target gap different in the two versions but also the energy density at the rear surface of the specimen (48 J/cm^2 in our version and as low as 7.7 J/cm^2 in [2, 3]). However, other ablation mechanisms where a plasma interacts with laser radiation must not be ruled out. It has been speculated [2] that, if the gap between a metallic target and a specimen is narrower than several hundreds of micrometers, the fast components of the plasma, such as ions, radicals, electrons, and clusters, may reach the surface during a laser pulse. In this case, energy and charge transfer to the specimen surface may give rise to short-lived centers absorbing the radiation. When the gap is wide, the specimen is first covered by an absorbing metallic field, which initiates ablation during subsequent irradiation. Ablation using a laser-induced plasma has one more feature that, to a great extent, governs its efficiency. Under the above conditions of plasma torch formation at the rear surface of the transparent material, the plasma temperature and density reach a maximum just near the surface. This is because the front of the plasma density and/or temperature maximum is known [5] to move toward the laser beam as laser-induced breakdown develops. Under direct ablation, the plasma front will move away from the surface, while, in our case, conversely, it will approach the surface of the transparent material, reaching a temperature and density maximum near it.

To see how the transverse size of the plasma torch influences the process of ablation using a laser-induced plasma, we designed a setup that is somewhat different from that shown in Fig. 2. Here, the beam of the same laser was directed (without scanning) to a controllable-width optical slit, which was placed instead of the mask, and the test specimen was placed in a sealed chamber with a quartz window. The chamber can be both evacuated and filled with air under an elevated pressure. The specimen was composed of a 6-mm-thick sapphire plate and a rubber target, which was offset by 0.6 mm from the rear surface of the sapphire (Fig. 2b) rather than being pressed against it. The image of the optical slit was projected with a 13-fold demagnification onto the rear surface of the sapphire plate. The laser pulse energy was kept constant at a level of 21 mJ,

the number of pulses was 30, the laser beam diameter on the slit was 2 mm, and the width of the slit was smoothly varied from 10 to 500 μm. The laser output density on the projection of the slit onto the sapphire specimen was 50 J/cm^2. The minimal width d of the slit projection at which ablation is initiated was measured as a function of the air pressure. From this dependence (Fig. 4), it follows that the minimal ablation-initiating width decreases with increasing pressure. Typically, the visually observable ablation of the sapphire exposed to the laser-induced plasma appears as follows. At a slit image width of 5 μm and a pulse energy density of up to 20 mJ, optical breakdown does not occur under atmospheric pressure: only a faint reddish glow is localized on the rubber target surface. Ablation is not observed either. When the pulse energy exceeds 20 mJ, the image of the slit on the sapphire undergoes optical breakdown: there appears a bright white glow of the plasma near the image of the slit the sapphire surface. Only then does sapphire ablation take place. This means that the target is needed only for generation of an initial slightly ionized "seed" plasma. The concentration and density of the plasma that are sufficient for the ablation of the specimen material are attained at its surface, where the electric field of the light wave is the highest.

Let us turn to the role of the transverse size of the processing zone. For a laser photon energy of 1 eV, the onset of an electron avalanche in a monoatomic gas with a neutral atom ionization potential of 10 eV is established with the empirical criterion [5]

$$\tau n E^2 \geq 10^{23}, \tag{1}$$

where τ is the laser pulse width (s), n is the density of the gas (cm^{-3}), and E is the strength of the light wave electric field (V/cm). If inequality (1) is met, an electron absorbing the photons in three-particle collisions with atoms and ions (inverse bremsstrahlung) takes the energy sufficient for ionization of a neutral atom during the action of the pulse. In practice, however, one should take into consideration electron energy losses, such as excitation energy losses, as well as those due to trapping of electrons by electronegative impurities and escape of electrons out of the irradiation zone. In our case, it is electron escape that is responsible for the threshold dependence of the ablation on the slit width. Therefore, the above criterion of onset of ablation should be complemented by the condition that the electron diffusion length during a pulse does not exceed the transverse size of the illuminated zone,

$$(D\tau)^{1/2} \leq d, \tag{2}$$

where D is the electron diffusion coefficient and d is the transverse size of the illuminated zone.

Condition (2) explains the threshold dependence of optical breakdown and ablation on the slit image width, and the pressure dependence of the threshold slit image
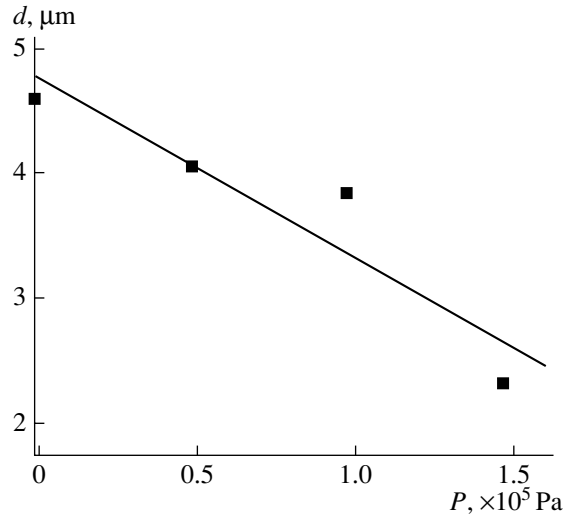

Fig. 4. Minimal width d of the slit image projection that is necessary for ablation initiation vs. air pressure P.

width follows from both criteria, since the diffusion coefficient depends on the gas density as $1/n$.

As the slit image width increases to 40 μm, atmospheric-pressure ablation by the laser-induced plasma changes to optical breakdown inside the sapphire, with the breakdown channel rapidly propagating across the specimen. This point deserves special consideration in view of the fact that the breakdown threshold, like the ablation threshold, also depends on the slit width in our experiment at the same laser energy density. It is known that the basic reason for optical breakdown in transparent materials is local heating of absorbing impurities by the laser beam [5]. Clearly, the heating of the centers is controlled by thermal diffusion. Taking into account that the thermal diffusion length in sapphire during the pulse is $l \sim 2(\xi\tau/\rho c)^{1/2}$, where ξ is the thermal conductivity, ρ is the density, τ is the pulse duration, and c is the specific heat, we have to accept that the onset of breakdown at an illuminated zone width of 40 μm does not fit in the model adopted. Indeed, widening of the illuminated zone above 0.6 μm would not radically change the thermal distribution near the absorbing centers but would merely increase their number. Therefore, we believe that, in the case considered, the UV radiation of the laser-induced plasma outside the specimen is the basic contributor to optical breakdown. Most of the energy of a high-temperature plasma may be reradiated in the vacuum ultraviolet range. The UV radiation may affect the ablation process, since it is absorbed by a transparent material and, thus, may stimulate absorption of the primary laser radiation by the formerly transparent material. Zhang *et al.* [6], who observed a similar phenomenon, used two lasers in experiments on fused quartz ablation: a low-output 157-nm F$_2$ laser and a high-output 248-nm KrF laser. The radiation of the former (157 nm) was absorbed by defect-related levels in the fused quartz, thereby inducing absorption of the
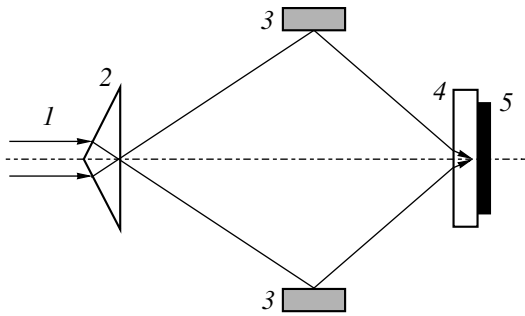
Fig. 5. Optical scheme for patterning diffraction gratings using the laser-induced plasma. (*1*) Laser beam, (*2*) Fresnel biprism, (*3*) mirror, (*4*) glass plate, and (*5*) rubber.
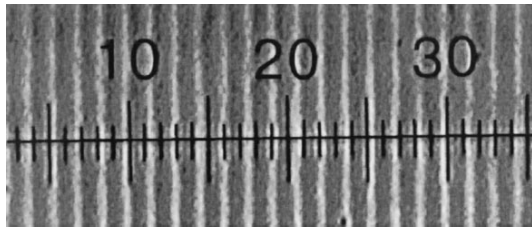

Fig. 6. Relief diffraction grating on the glass when viewed through an optical microscope. (2 μm per division).
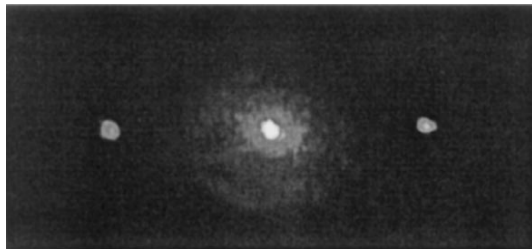

Fig. 7. Diffraction pattern in the far-field zone for the He–Ne laser beam diffracted by the diffraction grating depicted in Fig. 7.

248-nm radiation (which the material was initially transparent to). In our case, the plasma radiation in the vacuum ultraviolet range seems to play a major part in breakdown development, producing an induced-absorption layer before the propagation front. Zhang *et al.* believe that the plasma generated in their experiments by a laser beam providing an energy density of no higher than 7.7 J/cm² on the target cannot radiate in the vacuum ultraviolet range. In our case, such a possibility must not be ruled out, since the plasma is generated by a beam with an energy density of 48 J/cm² and is localized immediately at the surface of the material. Although the laser-induced plasma was not spectrally analyzed, we may assume that the plasma temperature reached 5.17 eV, starting from the results obtained in [4], where fused quartz ablation was accomplished under similar conditions. As follows from the Planck formula, such a plasma gives up most of its energy as radiation in the vacuum ultraviolet range ($\geq$6.2 eV). For

an absolutely black body with a temperature of 5.17 eV, the ratio of the radiant emissivity at $h\nu = 6.12$ eV to that at $h\nu = 5.17$ eV equals 1.3. As the width of the irradiation zone increases, energy losses due to electron escape out of it decline and, accordingly, the plasma temperature and density grow. Eventually, as the plasma torch widens, its UV radiation tends to shorter wavelengths and becomes sufficiently intense for optical breakdown to propagate from the plasma gas to the solid in a threshold-like manner.

We believe that the absorption induced by the UV radiation of the plasma is also of significance under subthreshold conditions as a contributor to the complex mechanism of ablation, which may be viewed as confined optical breakdown.

Let us now turn to experiments on patterning relief diffraction gratings on glass using our version of the LIPAA method (see Fig. 5). A laser beam (1.06 μm, 10 ns, 20 mJ) of diameter 3 mm was bifurcated with a Fresnel biprism, and then the two beams were brought to a 0.5×1.0-mm spot at the glass–rubber interface under atmospheric pressure. The number of laser shots was varied from one to five. Under these conditions, a relief diffraction grating with a spacing of 3.0 μm was patterned on the surface at the contact between the laser radiation and the laser-induced plasma. The image of the grating when viewed in an optical microscope is shown in Fig. 6. The diffraction pattern in the far-field zone observed for the diffraction of a He–Ne laser beam (632.8 nm) is demonstrated in Fig. 7. The angle between the zeroth- and first-order beams is 12.2°, which agrees with the microscopic measurements of the grating spacing. The total first-order diffraction efficiency is close to 9%. The absence of higher diffraction orders suggests that the shape of the grating is near-sinusoidal.

Let us return to the effect of the transverse size of the plasma torch on projection laser microprocessing. This point is of great significance both for transparent materials and metals, since the mask may have open areas of different size. We tackled this problem because of the need to explain the "edge effect" arising in conventional projection microprocessing of metals. It was noticed that, on large irradiated areas more than 20 μm across, the depth of material removal along its circumference is much greater than at the center. This appears to be an effect (detrimental in this case) of the laser-induced plasma. In the middle of an extended open area, energy losses due to the diffusion of electrons outside the irradiation zone are insignificant. Therefore, the plasma density may reach a critical value at which electron plasma frequency $\omega_p = (4\pi n_e e^2/m)^{1/2}$ (where n_e is the electron concentration, e is the electron charge, and m is the electron mass) becomes equal to the laser radiation frequency. Under this condition, the plasma is absorbed to the maximal extent, so that the target may be totally screened. At the edges, the situation is different. Here, the electron losses are high, since the elec-

trons diffuse out of the irradiation zone; accordingly, the plasma temperature and density are lower than at the center and it is more transparent to the laser radiation. The width of the graded zone is about 10 μm.

This effect was studied at length using the above scheme with a controllable-width slit. The specimen was 20-μm-thick nickel foil (Fig. 1c). The pulse energy was 21 mJ; the energy density on the target, 50 J/cm^2; and the width d of the slit on the foil surface was varied from 0 to 160 μm. We estimated the number of laser shots necessary for complete removal of the material from half the area occupied by the slit image. The number of shots versus the width of the exciting slit is shown in Fig. 8 for different air pressures in the chamber. As might be expected, the material is most effectively removed in a vacuum. The necessary number of shots (30) is minimal for a slit width in the interval from 10 to 20 μm at all the pressures. The slight increase in the number of shots for narrower slits is apparently due to objective lens aberrations and thermal diffusion, which travels a length of 1 μm for 10 ns in nickel. For d less than 2 μm, the material is removed incompletely. As d rises to 60 μm in a vacuum, the number of shots increases to 50 and then remains unchanged. At pressures of 4.9×10^4, 9.8×10^4, and 1.4×10^5 Pa, another situation is observed. For d larger than 20 μm, the number of shots increases drastically; the higher the pressure, the greater the increase. It is obvious that this observation, as in the case of the transparent materials, is a result of a correlation between the parameters of the laser-induced plasma and the transverse size of the processing zone. At small d (from 2 to 20 μm), the energy losses due to electron escape outside the processing zone are too high for optical breakdown to occur in the material vapor. As a result, the rate of material removal is the highest. As the slit image width increases further, the electron energy losses due to diffusion decline and a laser-induced plasma arises, which partially absorbs the radiation and, thereby, retards the rate of removal. When a critical plasma density is reached, the laser radiation cannot penetrate to the surface. Yet, ablation takes place at the edges of the slit image because of the edge effect. Such was indeed the case in the experiments. Through removal of the material was first observed at the edges, and the resulting "peninsula" gradually diminished in size due to edge ablation. The critical plasma density can be estimated from the relationship $n_c \lambda^2 \cong 10^{15}$ m^{-1} [7], where n_c is the critical plasma density and λ is the laser radiation wavelength. This estimator gives 10^{21} cm^{-3} for the critical plasma density at the center of the image. The rate of material removal as a function of the air pressure can also be found through the pressure dependence of the electron diffusion coefficient. When d exceeds 80 and 110 μm for pressures of 9.8×10^4 and 1.4×10^5 Pa, respectively, the number of shots remains the same or even decreases slightly. It seems likely that the material is mechanically removed by the shock wave of the expanding plasma.
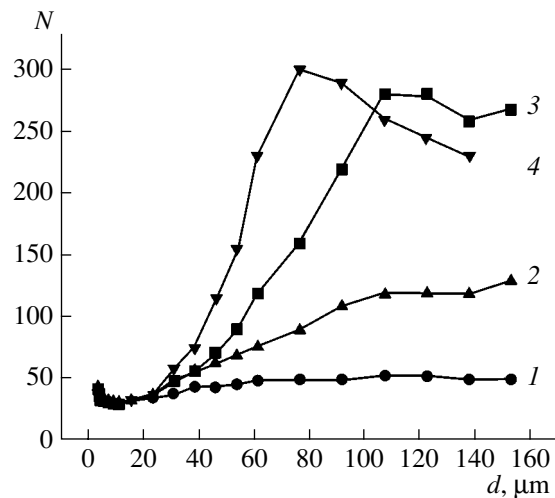

Fig. 8. Number N of laser shots necessary for removal of half the nickel foil vs. slit image width at (*1*) 0, (*2*) 4.9×10^4, (*3*) 9.8×10^4, and (*4*) 1.4×10^5 Pa.

CONCLUSIONS

Our study indicates the need for taking into account the transverse size of the plasma torch in designing tools for projection microprocessing of materials. The screening effect of the laser-induced plasma can be avoided if the characteristic size of the area being processed does not exceed 20 μm at a laser wavelength of 1.06 μm. Evacuation of the chamber with the specimen allows processing of a larger area.

When transparent materials are processed, the rate of ablation using a laser-induced plasma increases with transverse size of the plasma torch and the process culminates in laser breakdown of the material. The efficiency (rate) of ablation of transparent materials as a function of the air pressure and laser wavelength varies inversely to that of metals.

REFERENCES

1. *A Mask for Projection Laser Processing*, Ukr. Patent No. 547,14A.

2. J. Zhang, K. Sugioka, and K. Midorikawa, Appl. Phys. A **67**, 499 (1998).

3. J. Zhang, K. Sugioka, and K. Midorikawa, Appl. Phys. A **67**, 545 (1998).

4. X. Zeng, S. Mao, C. Liu, *et al.*, Appl. Phys. Lett. **83**, 240 (2003).

5. N. B. Delone, *Interaction of Laser Radiation with the Material* (Nauka, Moscow, 1989) [in Russian].

6. J. Zhang, K. Sugioka, T. Takahashi, *et al.*, Appl. Phys. A **71**, 23 (2000).

7. *Industrial Applications of Lasers*, Ed. by H. Köbner (Wiley-Interscience, New York, 1984; Mir, Moscow, 1988).

Translated by V. Isaakyan

BRIEF
COMMUNICATIONS

Kinetic Crossover of Coalescence Conditions in a Supersaturated Homogeneous Solution

P. Yu. Gubanov, Yu. V. Zheltov, I. L. Maksimov, and V. P. Morozov

Lobachevski State University, pr. Gagarina 23, Nizhni Novgorod, 603950 Russia
e-mail: ilmaks@phys.unn.ru
Received June 16, 2004

Abstract—Coalescence conditions under which the asymptotic behavior of the distribution function differs substantially from the Lifshitz–Slezov (LS) classical distribution are found in terms of an approach that includes the finiteness of the grain size during phase transitions. If the grain growth kinetics is controlled by monomer diffusion and grain dissolution, an intermediate asymptotic regime of coalescence may arise that eventually changes to LS-like diffusion. The change in the prevailing grain growth mechanism shows up in the crossover effect for scaling indices that describe the time dependence of the grain size. © *2005 Pleiades Publishing, Inc.*

Nucleation of a new phase due to supersaturated solid solution decomposition can be subdivided into two stages: the fluctuation growth of nuclei from the supersaturated solid solution and the stage of coalescence, at which coarser grains grow via dissolution of finer ones. Late in the phase transition, the latter stage (Ostwald ripening) dominates the former, so that the fluctuation stage may be neglected. The coalescence kinetics has been extensively studying since the classic paper by Lifshitz and Slezov was published [1]. They found the universal grain size distribution for the new phase to which any initial distribution tends in the limit $t \longrightarrow \infty$ (see also the monographs [2, 3] and review [4]). However, Lifshitz and Slezov implicitly assumed that grains may be infinitely large. Most of the works devoted to this problem consider a class of solutions meeting the (Lifshitz–Slezov (LS)) assumption. In a recent work [5], the coalescence kinetics was treated on the assumption that the grain size has an upper limit and it was shown that the asymptotic behavior of distribution functions (DFs) where the maximal grain size tends to zero by a power (of order m) law is radically different from the asymptotics considered by Lifshitz and Slezov.

In this work, we numerically and analytically investigate the coalescence kinetics in a supersaturated homogeneous solution, assuming that the maximal size of new-phase grains is finite. The time evolution of the grain size distribution is derived. The situations where the grain growth kinetics is controlled either by the rate of dissolution (the earlier stage of coalescence) or by monomer diffusion (the later stage of coalescence) are considered. The transition to the final distribution via an intermediate asymptotic coalescence regime is demonstrated, and the duration of this regime is estimated.

Consider the general case when the grain growth kinetics is governed by the competing processes of diffusion and dissolution. Then, the growth rate of a grain of radius a is routinely described by the dimensionless equation [5]

$$\frac{da}{dt} = \frac{D + \beta b_0}{D + \beta b_0 a}\left(\frac{1}{b} - \frac{1}{a}\right), \qquad (1)$$

where β is the rate of dissolution and D is the monomer diffusion coefficient.

In (1), quantities $b = \sigma/(n_0 - n_{00})$ and $b_0 = \sigma/(n_{0\infty} - n_{00})$ are the expressions for the grain critical radius ($\sigma = 2\varepsilon\nu n_{00}/(kT)$); n_{00} and $n_{0\infty}$ are the equilibrium monomer concentrations over the spherical and plane surface of a solute, respectively; n_0 is the initial monomer concentration in the solution; ε is the surface energy; ν is the specific volume of the monomer; T is the temperature; and k is the Boltzmann constant. Hereafter, the true (and critical) grain size comes in units of b_0 and the time, in units of $b_0^2(D + \beta b_0)/\nu D\beta\sigma$.

Generally, the kinetic equation of coalescence [1] and Eq. (1) cannot be solved jointly in analytical form. However, there are two extreme cases that allow for an asymptotic description. For one of them (the grain growth is controlled by monomer diffusion), the asymptotic DF was found in [5]. Let us consider the other case, when the grain growth kinetics is controlled by the rate of dissolution, $D \gg \beta a$ (the earlier stage of growth). Then, Eq. (1) reduces to

$$\frac{da}{dt} = \frac{1}{b} - \frac{1}{a}. \qquad (2)$$

In the general case, the DF is factorized in the same way as in the LS problem,

$$f(V, t') = N(t')P(V).$$

In the factorized form, it can be represented as the product of regularly varying (self-similar) function

$P(V)$ of distribution over grain size alone (where V is the ratio of the grain size to maximal grain size a_L, $V = a/a_L$) and nonstationary factor $N(t') = N_0 \int_{a_0^*}^{\infty} \varphi(a_0) da_0$, which equals the number of new-phase particles per unit volume. Finally, we will assume that the initial DF,

$$\varphi(a_0) = \begin{cases} \Phi(a_0) & 0 < a_0 < C \\ \dfrac{\Phi(C)}{(L-C)^m}(L-a_0)^m & C < a_0 < L, \end{cases} \quad (3)$$

exhibits a characteristic power-law behavior near a maximum initial grain size, $a_L(t = 0) \equiv L$, and vanishes at $a_0 > L$. Here, $\Phi(a_0)$ is an arbitrary function, m is an arbitrary number ($m > -1$), and $C < L$ is an intermediate size that specifies the area where the power tail of the initial DF is localized. Assumption (3) reflects a real experimental situation [6]. Indeed, in experiments [6, 7] with Ni–Pb and Fe–Cu solutions, the distribution like (3) with a characteristic grain size $L_1 = 50$ nm (the Ni–Pb system) and $L_2 = 30$ nm (the Fe–Cu system) was observed.

Solving the kinetic equation by the same method as in [5] in view of (2) and (3), we obtain

$$P(V) = \frac{3V(1-V)^m \lambda^{(m+1)\lambda}}{(\lambda - V)^{m+5}}, \quad (4)$$

where $\lambda = (m+4)/(m+1)$ is found from the condition of finiteness of the new-phase volume [5].

Note that the time dependences of the characteristic sizes are power functions with an exponent of 0.5,

$$a_L = \left(\frac{2}{\lambda}t'\right)^{\frac{1}{2}}, \quad b = \left(\frac{2}{\lambda}t'\right)^{\frac{1}{2}}\frac{m+4}{2m+5}; \quad (5)$$

for the density of new-phase particles, the exponent equals –1.5: $N(t') = B(2t'/\lambda)^{-3/2}$.

If the grain growth kinetics is controlled by monomer diffusion (the later stage of coalescence), the DF takes a more complicated form [5]

$$P(V) = \frac{3|V_2|^{A_2(m+1)}V_1^{A_1(m+1)}(1-V)^m V^2}{(V_1-V)^{A_1(m+1)+1}(V-V_2)^{A_2(m+1)+1}}, \quad (6)$$

where $\lambda = (2m+5)/(m+1)$, $A_{1,2} = 0.5[(\lambda - 1)\sqrt{1+4\lambda} \pm (\lambda + 1)]/\sqrt{1+4\lambda}$, and $V_{1,2} = (\sqrt{1+4\lambda} \mp 1)/2$. The time-dependent nucleus sizes follow the LS law,

$$a_L = \left(\frac{3}{\lambda}t'\right)^{\frac{1}{3}}, \quad b = \left(\frac{3}{\gamma}t'\right)^{\frac{1}{3}},$$
$$\frac{1}{\gamma} = b^2\frac{db}{dt'} = \frac{(2m+5)^2(m+1)}{27(m+1)^3}, \quad (7)$$
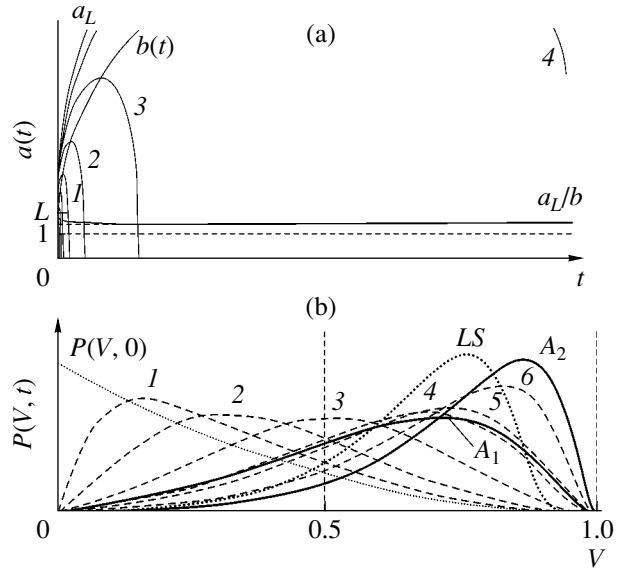
Fig. 1. Evolution of (a) the characteristic grain sizes and (b) distribution function $P(V)$ during coalescence in the homogeneous solid solution ($\chi = 10$, $m = 2$, $L = 2$). (a) $a_L(t)$ is the maximal grain size; $b(t)$ is the critical grain size; and (1)–(4) time evolution of new-phase grains, which are parametrized by initial grain size $a_0 = a$ ($t = 0$). (b) A_1 stands for distribution function (4); A_2, for distribution function (6); LS, for Lifshitz–Slezov distribution function [1]; and (1)–(6) time evolution of the distribution function calculated numerically.

accordingly, the new-phase particle density declines monotonically, $N(t') = B\lambda/t'$. Asymptotic distribution (6), which arises at the later stage of coalescence subject to the finiteness of the grain maximal size, differs substantially from the classical LS distribution [1]. This is because the tails of distributions that decrease too slowly may significantly alter the DF asymptotics [8, 9]. Note also that DF (6) passes to the LS distribution [1] in the limit $m \longrightarrow \infty$.

Comparing the exponents in expressions (5) and (7) reveals the crossover effect for the kinetic indices, which shows up when the prevailing grain growth mechanism changes. In fact, the square-root law $a_L \sim t^{1/2}$ and $b \sim t^{1/2}$, which is valid at the earlier stage (the grain growth kinetics is controlled by the rate of dissolution), changes to the LS classical law $a_L \sim t^{1/3}$ and $b \sim t^{1/3}$ later in the growth (the growth kinetics is controlled by monomer diffusion). It should be emphasized that ratio a_L/b does not change in time, indicating that the asymptotic DF found is self-similar. The crossover effect predicted in this work is bound to take place also in the LS classical model [1].

The numerical solution of the complete set of kinetic equations [5] supports the results of the asymptotic analysis. We found that an intermediate asymptotic regime of coalescence may set in in the general case, when the grain growth kinetics is governed by the

competing processes of monomer diffusion and grain dissolution. Time t_1 for which the DF approaches the asymptotics (curve *4*) and time Δt for which the DF remains close to it (with a deviation of no more than 10%) depend on ratio $\chi = D/(\beta b_0) \gg 1$: both t_1 and Δt grow with χ. In Fig. 1b, this situation is shown for $\chi = 10$. Here, the durations of the first and second stages are $t_1 \approx 212$ and $\Delta t \approx 188$ time steps, respectively. The time taken to reach final asymptotics (6) (with a deviation of $\approx 15\%$) is about 50 000 time steps. Comparison of the minimal sizes, $(a_L/b)_{theor} = 1.333$ and $(a_L/b)_{calc} = 1.391$, and self-similarity parameters, $\lambda_{theor} = 3$ and $\lambda_{calc} = 2.55$, demonstrates fairly good agreement between the theoretical and calculated values.

Analyzing the experimental data [6], one can estimate the typical value of χ for a specific two-phase system. Specifically, for the Pb–Ni system, $\chi \sim 10^3$; for the Fe–Cu system, $\chi \sim 10^4$. Then, it follows that the intermediate stage may last several tens of seconds under real conditions. On the assumption that $\Delta t \sim \chi^n$ (where $n \sim 1$), it is easy to check that the intermediate stage lasts $\Delta t \approx 2$ s for the Pb–Ni system and $\Delta t \approx 2$ s for the Fe–Cu system.

REFERENCES

1. I. M. Lifshitz and V. V. Slezov, Zh. Éksp. Teor. Fiz. **35**, 479 (1958) [Sov. Phys. JETP **8**, 331 (1958)].
2. V. A. Kukushkin and V. V. Slezov, *Disperse Systems on Solid Surfaces* (Nauka, St. Petersburg, 1996) [in Russian].
3. V. V. Slezov, Phys. Rev. **17** (2), 1 (1995).
4. V. A. Kukushkin and A. V. Osipov, Usp. Fiz. Nauk **168**, 1083 (1998) [Phys. Usp. **41**, 983 (1998)].
5. V. P. Morozov and I. L. Maksimov, Neorg. Mater. **35**, 1021 (1999).
6. Yu. V. Zheltov, V. P. Morozov, V. N. Dutyshev, *et al.*, Izv. Akad. Nauk SSSR, Met., No. 5, 31 (1990).
7. Yu. V. Zheltov, V. P. Morozov, A. A. Romantsov, *et al.*, Izv. Akad. Nauk SSSR, Met., No. 3, 52 (1988).
8. V. A. Kukushkin and A. V. Osipov, Zh. Éksp. Teor. Fiz. **113**, 2193 (1998) [JETP **86**, 1201 (1998)].
9. V. V. Slezov, J. Phys. Chem. **39**, 367 (1978).

Translated by V. Isaakyan

BRIEF
COMMUNICATIONS

H₂O/CuIn₃Se₅ Photoelectrochemical Cells: Fabrication and Properties

I. V. Bodnar'*, E. S. Dmitrieva*, V. Yu. Rud'**, and Yu. V. Rud'***

* Belarussian State University of Information Science and Radio Engineering, ul. Brovki 17, Minsk, 220027 Belarus
e-mail: chemzav@gw.bsuir.unibel.by
** St. Petersburg State Polytechnical University, ul. Politekhnicheskaya 29, St. Petersburg, 195251 Russia
e-mail: rudvas@spbstu.ru
*** Ioffe Physicotechnical Institute, Russian Academy of Sciences,
Politekhnicheskaya ul. 26, St. Petersburg, 194021 Russia
Received June 17, 2004

Abstract—Single-phase coarse-grained $CuIn_3Se_5$ ingots are grown by horizontal oriented crystallization from the near-stoichiometric melt. Photosensitive structures based on the interface between these crystals and an electrolyte (H_2O) are created. It is shown that the $CuIn_3Se_5$ ternary compound is a direct-gap semiconductor with an energy gap $Eg \simeq 1.1$ eV ($T = 300$ K). $H_2O/CuIn_3Se_5$ photoelectrochemical cells seem to be promising for efficient wide-band photodetectors of natural light. © 2005 Pleiades Publishing, Inc.

Fundamental research on I–III–VI₂ ternary compounds has led to the development of $ZnO/CdS/CuInGaSe_2$ thin-film solar cells with the highest quantum efficiency (19%) among photoelectric converters of this class [1, 2]. However, it has been shown that, along with I–III–VI₂ ternary compounds, there exist other, more complex, phases like $I–III_{2n+1}–VI_{3n+2}$, where $n = 1, 2, 3, \ldots$, in the class of I–III–VI compounds. Such coordination-ordered phases, which usually lie on $I_2VI–III_2VI_3$ pseudobinary sections of the related ternary diagrams, open up fresh opportunities for controlling the basic properties of compound semiconductors without doping [3–5]. Also, the above specific feature of atomic interaction in I–III–VI systems allows for coexistence of phases differing in coordination order [6]. Therefore, study of the new phases grown as bulk homogeneous crystals would help to elaborate new approaches to controlling the properties of compound diamond-like semiconductors up to providing conditions for self-organization of quantum-size inclusions. In this work, we report the results of pioneering experiments with optical electrochemical cells based on bulk $CuIn_3Se_5$ crystals.

(1) The crystals were grown by horizontal oriented crystallization of the near-stoichiometric melt. Dissociation in the liquid–solid–vapor system was suppressed by controlling the selenium vapor pressure in an evacuated quartz ampoule with the melt. The ingots grown were coarse-grained.

The phase composition of the crystals was determined with a Cameca-SX 100 X-ray spectral microprobe analyzer. The concentration of copper, indium, and selenium was in accordance with the chemical for-mula of the compound. The diffraction patterns taken from various areas of the ingots corresponded to the imperfect structure of chalcopyrite. The unit cell parameters calculated by the least squares method from reflections in the range $2\theta > 60°$ were found to be $a = 5.766 \pm 0.001$ Å and $c = 11.499 \pm 0.005$ Å, which agrees with the known data for this compound [4].

(2) As can be judged from the sign of the thermal emf, these crystals, like those grown by the vertical Bridgman method [3], have *p*-type conductivity at 300 K. However, the resistivity ρ of the horizontally grown ingots turned out to be several orders of magnitude higher than in the vertically grown ones. This is attributable to different offsets from the stoichiometry in the variously grown crystals.

Figure 1 shows the temperature dependence of ρ for one of the samples. In the temperature range 280–380 K, this dependence is exponential,

$$\rho = \rho_0 \exp(E_a/kT), \qquad (1)$$

where k is the Boltzmann constant and E_a is the activation energy of acceptor centers (under the assumption of heavy compensation by donors, it was estimated as $E_a \approx 0.52$ eV [7]).

It should be noted that, at thermal cycling, the curves $\rho(T)$ do not exhibit hysteresis throughout the temperature range under study irrespective of the rate and sense of temperature variation. This suggests that the coordination order of atoms in $CuIn_3Se_5$ crystals remains unchanged (i.e., the crystals do not experience first-order phase transitions) in the temperature range considered.
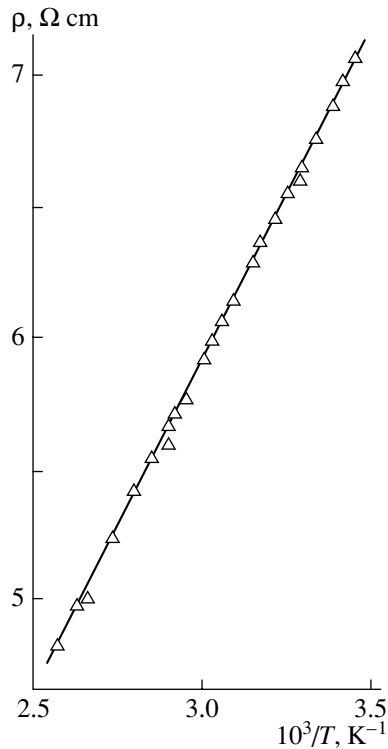
Fig. 1. Temperature dependence of the resistivity of the $CuIn_3Se_5$ crystal grown by the horizontal Bridgman method.

Fig. 2. Spectral dependences of the conversion quantum efficiency for (*1*) H_2O/p-$CuIn_3Se_5$, (*2*) In/p-$CuIn_3Se_5$, and (*3*) $ZnO : Al/p$-$CuIn_3Se_5$ structures at $T = 300$ K. The structures were illuminated by natural light from the side of (*1*) H_2O, (*2*) In, and (*3*) ZnO. The spectra are slightly shifted along the vertical axis to avoid superposition.

(3) Light-sensitive electrodes to the cells were made in the form of $0.1 \times 5 \times 10$-mm rectangular sheets. An ohmic contact was produced by thermally evaporating a pure silver film of thickness $d = 1$–2 μm on the $CuIn_3Se_5$ wafer, and the electrodes were soldered to the film with pure indium as a solder. To avoid direct contact with the electrolyte, the $CuIn_3Se_5$ surface with the ohmic contact was covered by an insulating lacquer. When the electrode thus prepared was immersed in the electrolyte, only the free front surface of the $CuIn_3Se_5$ crystal was in contact with the electrolyte. As a counter electrode of the photoelectrochemical cell, a sharpened platinum wire ($d \approx 0.3$ mm) or a quartz window covered by a high-conductivity transparent In_2O_3 film was used. The photoelectric response of the cells was studied in the fast photovoltage mode at a light flux modulation frequency $f = 20$ Hz. Distilled water served as an electrolyte.

As follows from the steady-state *I–V* characteristics, the rectification ratio (the ratio between the forward and reverse currents at a bias $|U| \approx 5$ V) of the cells equals ≈ 10 as a rule. Illumination of the cells reproducibly caused the photovoltaic effect. Importantly, the photovoltage sign is independent of the incident photon energy throughout the sensitivity range of the cells, photon fluence, and position of the light probe (≈ 0.4 mm in diameter) over the light-reception area.
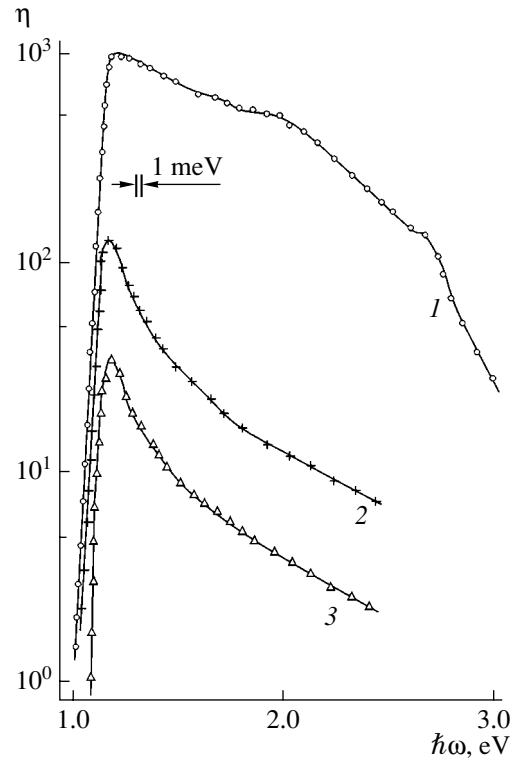
The open-circuit photovoltage and the short-circuit photocurrent are, respectively, the logarithmic and linear functions of the incident photon flux density. The cells were invariably more sensitive when exposed from the side of the electrolyte, and the best structures offered a sensitivity as high as $S_m = 7500$ V/W. This value exceeds the sensitivity value obtained in our earlier In/p-$CuIn_3Se_5$ and $ZnO : Al/p$-$CuIn_3Se_5$ solid-state structures (see table), which were made on the same crystals as the $H_2O/CuIn_3Se_5$ cells. It should be noted that $CuIn_3Se_5$-based cells do not exhibit any degradation of the photosensitivity. Therefore, there is reason to think that the $CuIn_3Se_5$ crystals under study, as well as other compound diamond-like semiconductors, are highly stable against photocorrosion [8, 9].

Figure 2 compares the typical spectral dependences of conversion quantum efficiency $\eta(\hbar\omega)$ (this efficiency is defined as the ratio of the short-circuit photocurrent to the number of incident photons) for the H_2O/p-$CuIn_3Se_5$ cells and In/p-$CuIn_3Se_5$ and $ZnO : Al/p$-$CuIn_3Se_5$ solid-state structures. The photoelectric parameters of both structures are listed in the table. From Fig. 2, it follows that the energy position of the long-wavelength photosensitivity edge, as well as the energy position of photosensitivity absolute maximum
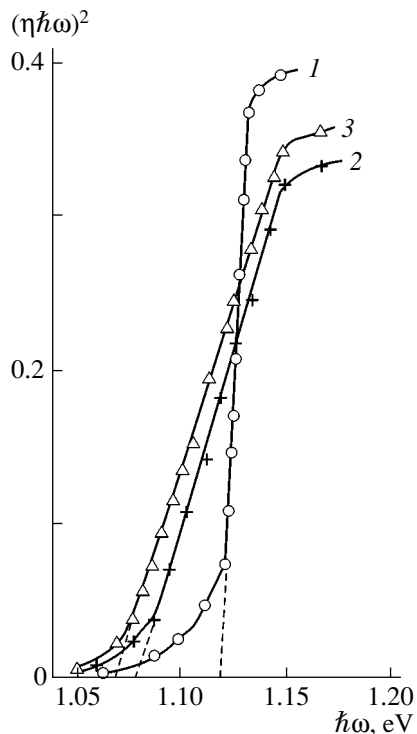
Fig. 3. $(\eta\hbar\omega)^2$ vs. $\hbar\omega$ for the structures based on the CuIn$_3$Se$_5$ crystals grown by the horizontal Bridgman method. (*1*)–(*3*) Mean the same as in Fig. 2.

$\hbar\omega^m$, do not change in going from the solid-state structures to the photoelectrochemical cells (see table). The fact is that the energy position of the long-wavelength edge in these structures, while so different, depends on band-to-band absorption in CuIn$_3$Se$_5$. Therefore, the long-wavelength edge of photosensitivity in all the structures is linearized in the coordinates $(\eta\hbar\omega)^2$–$\hbar\omega$ (Fig. 3) and extrapolation of the curves in the limit $(\eta\hbar\omega)^2 \longrightarrow 0$ yields close values of the cutoff energy. According to the theory of band-to-band absorption in semiconductors [10], this energy corresponds to the energy gap of the CuIn$_3$Se$_5$ ternary semiconductor compound (see table) and direct optical band-to-band transitions.

In the photoelectrochemical cells, the spectral range of high photosensitivity is wider than in the solid-state structures, as represented by the FWHM δ of the spectra $\eta(\hbar\omega)$ (see table). For the solid-state structures, this parameter is no greater than 0.34; for the cells, it is

Photoelectric properties of the CuIn$_3$Se$_5$-based cells at $T = 300$ K

Structure	$\hbar\omega^m$, eV	S_m, V/W	δ, eV	E_g, eV
In/CuIn$_3$Se$_5$	1.15	30	0.17	1.08
ZnO/CuIn$_3$Se$_5$	1.15	80	0.12–0.34	1.07
H$_2$O/CuIn$_3$Se$_5$	1.16	7500	0.9	1.12

nearly three times higher. This fact, combined with the photosensitivity value $S_m = 7500$ V/W, indicates that the interface in the photoelectrochemical cells is of lower recombination activity than that in the In/p-CuIn$_3$Se$_5$ and ZnO : Al/p-CuIn$_3$Se$_5$ solid-state structures.

Thus, even early samples of photoelectrochemical cells based on the CuIn$_3$Se$_5$ ternary compound with an ordered arrangement of vacancies offer a higher photosensitivity and a wider spectral range of high photosensitivity than well-known In/p-CuIn$_3$Se$_5$ [3] and ZnO : Al/p-CuIn$_3$Se$_5$ [11] solid-state structures. Our results demonstrate that these cells may be viewed as candidates for wide-band photoelectric converters.

REFERENCES

1. O. Lundberg, M. Edoff, and L. Stolt, in *Proceedings of the ISES World Congress, Göteborg (Sweden), June 14–19, 2003.*

2. T. M. Razykov, in *Proceedings of the ISES Solar World Congress, Götenborg (Sweden), June 14–19, 2003.*

3. I. V. Bodnar', V. F. Gremenyuk, V. Yu. Rud', and Yu. V. Rud', Fiz. Tekh. Poluprovodn. (St. Petersburg) **33**, 805 (1999) [Semiconductors **33**, 740 (1999)].

4. I. V. Bodnar', V. Yu. Rud', Yu. V. Rud', and M. V. Yakushev, Fiz. Tekh. Poluprovodn. (St. Petersburg) **36**, 1211 (2002) [Semiconductors **36**, 1132 (2002)].

5. G. Martin, R. Marques, and R. Guevara, Jpn. J. Appl. Phys. **39**, 44 (2000).

6. S. H. Wei, S. D. Zhang, and A. Zunger, Appl. Phys. Lett. **72**, 3199 (1998).

7. J. S. Blakemore, *Solid State Physics* (Cambridge Univ. Press, Cambridge, 1985; Mir, Moscow, 1988).

8. Yu. V. Rud' and M. A. Tairov, Fiz. Tekh. Poluprovodn. (Leningrad) **21**, 615 (1987) [Sov. Phys. Semicond. **21**, 377 (1987)].

9. D. N. Goryachev, Yu. V. Rud', and M. A. Tairov, Fiz. Tekh. Poluprovodn. (Leningrad) **23**, 312 (1989) [Sov. Phys. Semicond. **23**, 192 (1989)].

10. S. M. Sze, *Physics of Semiconductor Devices* (Wiley, New York, 1981; Mir, Moscow, 1984).

11. I. V. Bodnar', S. E. Nikitin, G. A. Il'chuk, *et al.*, Fiz. Tekh. Poluprovodn. (St. Petersburg) **38**, 1228 (2004) [Semiconductors **38**, 1192 (2004)].

Translated by V. Isaakyan

Stabilization of a Movable Magnet in the Field of a Stationary One by Rotation

I. V. Veselitskiĭ, V. S. Voronkov, G. G. Denisov, and R. V. Lin'kov

Research Institute of Applied Mathematics and Cybernetics,
Lobachevski State University, ul. Ul'yanova 10, Nizhni Novgorod, 603005 Russia
e-mail: voronkov@pmk.unn.runnet.ru
Received July 6, 2004

Abstract—It is shown that a rotating body containing a permanent magnet may be in stable noncontact equilibrium when placed in the field of a stationary magnet. It is assumed that the magnets are of a cylindrical shape and their magnetizations are aligned with the cylinder axis. The field of the magnets is simulated by two turns with direct current, which makes it possible to analytically find the forces and force moments acting on the movable magnet subjected to the field of the stationary one. Instability of the equilibrium state of a suspended body when its weight is counterbalanced by the repulsive force exerted by a stationary magnet follows from the Earnshaw theorem. It is demonstrated here that such instability may be removed with gyroscopic forces due to rotation of the suspended body. It turns out that the rotation of the movable magnet may stabilize not only its unstable angular but also translational degrees of freedom, which is a newly discovered effect. © 2005 Pleiades Publishing, Inc.

INTRODUCTION

According to the Earnshaw theorem [1, 2], a set of stationary particles that interact with forces that are inversely proportional to the particle spacing squared cannot be in stable equilibrium. The forces of interaction between electric charges, elementary currents, and permanent magnets, as well as gravitational forces, are examples. It is because of the Earnshaw principle that many attempts to design passive noncontact suspensions using permanent magnets have failed. In our case of two axially magnetized cylindrical magnets, this equilibrium state is easy to realize in practice. If the like poles of the magnets face each other (see Fig. 1) and the lower magnet is fixed, one can find a point on its axis where the weight of the upper (movable) magnet is counterbalanced by the repulsive force from the lower one. Figure 2 plots repulsive force $F(h)$ between two coaxial magnets against their center distance. The intersection of curve $F(h)$ with the straight line of constant weight mg gives two equilibria. The upper one (on the right of Fig. 2) is stable against vertical displacements.

However, the system possesses two double instabilities. The movable magnet tends to rotate through 180° and shift normally to the axis. Martynenko [3] showed that a charged particle being in unstable equilibrium in a static electric field may be changed to stable equilibrium when placed in a sufficiently high magnetic field, which acts in the same manner as gyroscopic forces. Denisov [4] demonstrated that the conservative stability of such a system may be raised to asymptotic stability by introducing dissipative forces in the rotating coordinate system.

In this work, we show that rotation of the movable magnet may transfer it to conservatively stable equilibrium. Unlike the standard gyroscopic stabilization techniques, the approach proposed provides stabilization not only of angular but also of translational degrees of freedom. The forces and force moments acting on the movable magnet when it is slightly offset from equilibrium are determined using the results of [5], where pon-
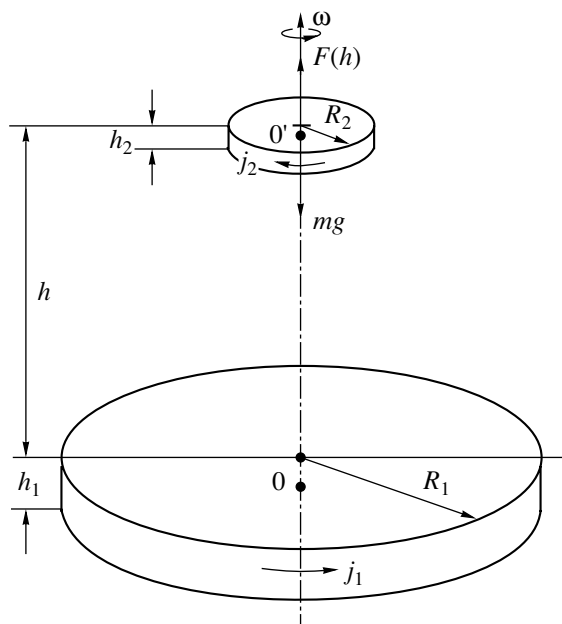

Fig. 1.

deromotive interaction between two cylindrical axially magnetized magnets was found.

1. PROBLEM DEFINITION AND ASSUMPTIONS

It is assumed that the movable magnet (which a coaxial rigid body is attached to) placed in the field of the coaxial stationary one is in equilibrium when the magnets are h distant from each other, h far exceeding the thicknesses $h_{1,2}$ of the magnets. The currents in the magnet-simulating turns can be written as $I_1 = j_1 h_1$ (stationary magnet) and $I_2 = j_2 h_2$ (movable magnet), where $j_{1,2}$ are the surface current densities, which depend on the magnet materials and produce their axial magnetization. The currents in the turns are in opposition to each other. In Fig. 3, the turns with the currents are shown together with translational and angular displacements. The stationary and movable turns (numbered 1 and 2, respectively) are related to coordinate systems $(0, \zeta, \eta, \xi)$ and $(0', \xi', \eta', \zeta')$ with their origins at the centers of the respective turns. The movable body is assigned a mass m (the center of mass coincides with the center of the turn), as well as axial, C, and equatorial, A, inertia moments.

In the generalized coordinates, the position of the movable body (given by vector $\mathbf{q}$) is specified by (i) translational displacements ξ, η, and $\zeta - h$ of its center of mass; (ii) Krylov angles of inclination, ϑ_1 and ϑ_2, of its axis $0'\zeta'$ to the 0ζ vertical axis of the stationary magnet (turn 1); and angle ϑ_3 of its own rotation about the $0'\xi'$ axis of symmetry of the movable magnet. In noncontact equilibrium (Fig. 1), the generalized coordinates (degrees of freedom) of the movable magnet have the values

$$\xi_0 = \eta_0 = 0, \quad \zeta_0 = h; \quad \vartheta_{10} = \vartheta_{20} = 0;$$
$$\vartheta_3 = \vartheta_{30}. \tag{1.1}$$

2. EQUATION OF MOTION OF THE MOVABLE MAGNET

To derive an equation of motion for the movable magnet, let us write the Lagrangean function [6] through deviations of the generalized coordinates from those corresponding to equilibrium:

$$L(q) = \frac{m}{2}\left[\left(\frac{d\xi}{dt}\right)^2 + \left(\frac{d\eta}{dt}\right)^2 + \left(\frac{d\zeta}{dt}\right)^2\right]$$
$$+ \frac{A}{2}\left[\left(\frac{d\vartheta_2}{dt}\right)^2 \cos^2\vartheta_1 + \left(\frac{d\vartheta_1}{dt}\right)^2\right] \tag{2.1}$$
$$+ \frac{C}{2}\left(\frac{d\vartheta_3}{dt} - \frac{d\vartheta_2}{dt}\sin\vartheta_1\right)^2 + U(q) - mg\zeta,$$

where

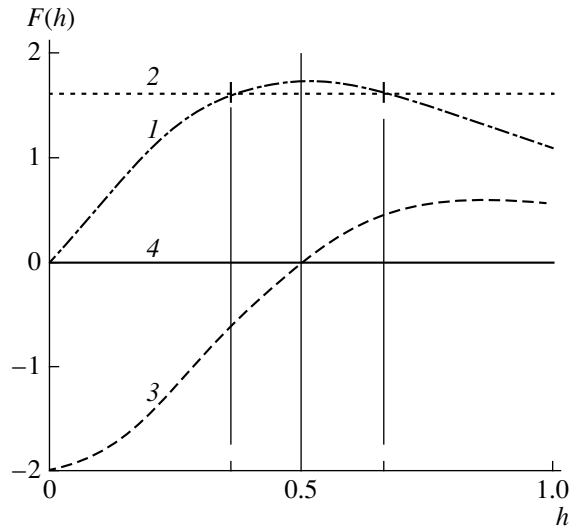$$U(q) = L_{1,2}(q_i)I_1 I_2 \tag{2.2}$$

Fig. 2. (*1*) $F(h)$; (*2*) $mg(h)$; (*3*) $k(h)$; and (*4*) $o(h)$.
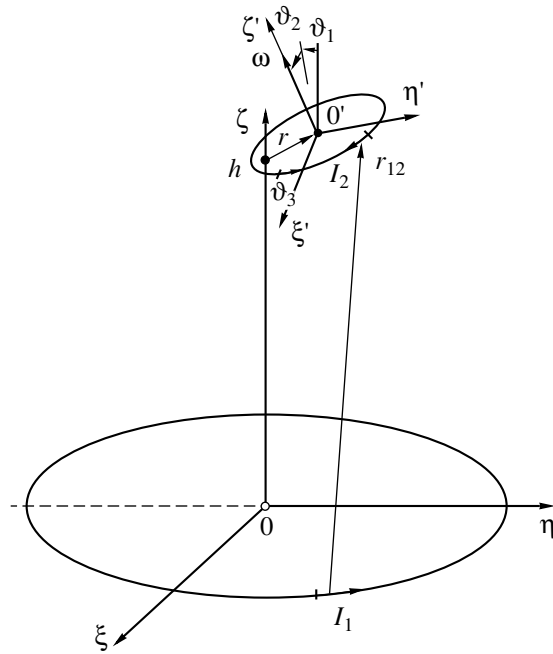
Fig. 3.

is the force function of ponderomotive interaction between two turns with currents I_1 and I_2 (which is similar to that considered in [5]) and $L_{1,2}(q_i)$ is the mutual induction of the turns with currents I_1 and I_2, which depends on all the generalized coordinates except angle ϑ_3. If the motion of a freely suspended body is assumed to be nondissipative, the Lagrangean equations will take the form

$$m\frac{d^2\xi}{dt^2} - \frac{dU}{d\xi} = Q_1, \quad m\frac{d^2\eta}{dt^2} - \frac{dU}{d\eta} = Q_2,$$

$$m\frac{d^2\zeta}{dt^2} - \frac{dU}{d\zeta} + mg = Q_3,$$

$$A\left[\frac{d^2\vartheta_1}{dt^2} + \left(\frac{d\vartheta_2}{dt}\right)^2 \cos\vartheta_1 \sin\vartheta_1\right]$$

$$+ H_0 \frac{d\vartheta_2}{dt}\cos\vartheta_1 - \frac{\partial U}{\partial \vartheta_1} = Q_4, \quad (2.3)$$

$$A\left(\frac{d^2\vartheta_2}{dt^2}\cos^2\vartheta_1 - 2\cos\vartheta_1\sin\vartheta_1\frac{d\vartheta_1}{dt}\frac{d\vartheta_2}{dt}\right)$$

$$- H_0\cos\vartheta_1\frac{d\vartheta_1}{dt} - \frac{\partial U}{\partial \vartheta_2} = Q_5,$$

where

$$H_0 = C\left(\frac{d\vartheta_3}{dt} - \frac{d\vartheta_2}{dt}\sin\vartheta_1\right) = \text{const} \quad (2.4)$$

is the magnitude of the kinetic moment vector for a rotating suspended body.

This vector is constant in magnitude, since angle ϑ_3 (through which the magnet rotates about its axis of symmetry) is a cyclic coordinate. Hereafter, it is assumed that dissipation and generalized forces Q_i are absent. Our aim is to provide stability in a conservative approximation. For Eq. (2.3) to be used, force function U still needs to be determined.

3. FORCE FUNCTION AND LINEARIZED EQUATIONS OF MOTION

The problem of finding force function $U(\mathbf{q})$ involved in the equation of motion (2.3) of the freely suspended magnet implies finding of the contour integral

$$U(q) = -\frac{\mu_0}{4\pi}I_1 I_2 \oint \frac{dl_1 dl_2}{|\mathbf{r}_1 - \mathbf{r}_2|}, \quad (3.1)$$

where μ_0 is the permeability of vacuum; $I_1 dl_{(1)}$ and $I_2 dl_2$ are differential current elements in the stationary and movable turns, respectively; and $|\mathbf{r}_1 - \mathbf{r}_2|$ is the distance between the current elements.

Physically, the contour integral in (3.1),

$$L_{12}(q) = \frac{\mu_0}{4\pi}\oint \frac{dl_1 dl_2}{|\mathbf{r}_1 - \mathbf{r}_2|},$$

is the mutual induction of two loops, which depends on the vector $\mathbf{q}$ of the generalized coordinates. Currents I_1 and I_2 are assumed to be constant and independent of the generalized coordinates. In the general case, the contour integral reduces to an elliptic integral. However, if R_2/h, ξ/h, η/h, ζ/h, ϑ_1, and $\vartheta_2 \ll 1$, this integral admits an analytical representation that is similar to that

found in [5]. Force function (3.1) can then be recast (up to terms of the second order of smallness in generalized coordinates) as

$$U = \frac{\pi\mu_0}{4}I_1 I_2 R_1^2 R_2^2\left[\frac{6h\zeta}{(R_1^2 + h^2)^{5/2}} + \frac{\vartheta_1^2 + \vartheta_2^2}{(R_1^2 + h^2)^{3/2}}\right.$$

$$\left. + \frac{3}{2}\frac{4h^2 - R_1^2}{2(R_1^2 + h^2)^{7/2}}(\xi^2 + \eta^2 - 2\zeta^2)\right] \quad (3.2)$$

$$+ \frac{\pi\mu_0}{4}I_1 I_2 R_1^2 R_2^2 3h\frac{\eta\vartheta_1 - \xi\vartheta_2}{(R_1^2 + h^2)^{5/2}}.$$

Function (3.2) allows for analytical expressions for the forces and force moments acting on the movable magnet from the field of the stationary magnet when the coordinates of the former deviate slightly from the equilibrium values given by (1.1). In equilibrium, the gravitational force is counterbalanced by the repulsive force between the magnets. According to (2.3), we get

$$mg = \frac{\pi\mu_0}{4}\frac{I_1 I_2 R_1^2 R_2^2 6h}{(R_1^2 + h^2)^{5/2}}.$$

We designate $d\vartheta_3/dt$ as ω, write the Lagrangean equation in complex variables $\theta = \vartheta_1 + i\vartheta_2$ and $u = \xi + i\eta$, and normalize them by introducing the time and length scales

$$t = \sqrt{\frac{2L}{g}}\tau, \quad L = \sqrt{\frac{A}{m}}, \quad u \longrightarrow u/L, \quad \zeta_1 = \frac{\zeta}{L}.$$

Eventually, we arrive at the dimensional equations of motion

$$\frac{d^2u}{d\tau^2} - ku - i\theta = 0, \quad \frac{d^2\theta}{d\tau^2} + iH\frac{d\theta}{d\tau} - \Xi\theta + iu = 0,$$

$$\frac{d^2\zeta_1}{dt^2} + 2k\zeta_1 = 0, \quad (3.3)$$

where

$$k = \frac{4h^2 - R_1^2}{R_1^2 + h^2}\frac{L}{h}, \quad H = \frac{C\omega}{A}\sqrt{\frac{2L}{g}}, \quad \Xi = \frac{2}{3}\frac{R_1^2 + h^2}{hL}.$$

A number of remarks regarding force function (3.2) and Eqs. (3.3) need to be made. First, in total agreement with the Earnshaw theorem, the sum of the longitudinal and two transverse stiffnesses equals zero. The parameters of the system should be taken such that the longitudinal stiffness in equilibrium will be positive (i.e., $k > 0$) and the equation for longitudinal coordinate ζ_1 stable. In transverse coordinates u, the stiffness is half as high (in magnitude) and negative, which causes instability. Another reason for instability is the destabilizing moment, which arises when the axis of the suspended magnet is inclined. This instability in angular variables

may be removed gyroscopically, i.e., by rotation. Second, the transverse translational and angular coordinates are interrelated (the term with $\eta\vartheta_1 - \xi\vartheta_2$ in force function (3.2)). It is this interrelation that allows us to look forward to stabilization by rotation in both angular and transverse translational coordinates. To show the possibility of such stabilization is, in essence, the goal of this work. Third, the conventional gyroscopic stabilization techniques are effective if the rotation frequency exceeds some critical value ($\omega > \omega_1$). In our case, conversely, a frequency is bound to exist (ω_2) above which stability is lost, since angular deviations tend to zero as $\omega \longrightarrow \infty$ (and, consequently, the interplay between angular and translational coordinates disappears). Fourth, the axial stiffness, being negative near the supporting magnet; decreases in magnitude with height, vanishes; and becomes positive (see Fig. 2, where lift $F(h)$ and axial stiffness $k(h)$ are plotted against normalized height $h = h/R_1$). The body may be stabilized by rotation at a small distance from the "zero point." Directly at the zero point, the lift is maximal and far exceeds the weight of the suspended magnet for high-coercivity materials. Then, there appears a broad possibility to control the weight of the suspended body so as to find the point in height where the stiffness has a desired value and also to provide a desired value of inertia moment A (and normalizing factor L). Fifth, since both the longitudinal and transverse stiffnesses at the zero point equal zero, the tempting idea of finding stable equilibrium in a nonlinear approximation (the Lyapunov critical case of linear approximation) arises. This, however, comes into conflict with one basic property of harmonic function U: its minimal or maximal value cannot be reached inside the domain where $\Delta U = 0$. Hence, an expansion of the force function in powers of small deviations in any order of smallness will fail.

If a solution to set (3.3) is found in the form $ae^{is\tau}$, the characteristic equations of this set take the form

$$s^4 - Hs^3 + s^2(k + \Xi) - kHs + k\Xi - 1 = 0, \quad (3.4)$$

$$-s^2 + 2k = 0. \quad (3.5)$$

For the suspension to be stable, it is necessary that the roots of Eqs. (3.4) and (3.5) be real. For (3.5) to be stable in longitudinal coordinate ζ, it is necessary that $k > 0$, i.e., that $4h^2 - R_1^2 > 0$, which is the case for the upper equilibrium state. One can check that (3.4) also has a finite domain of stability. In fact, if $k\Xi - 1 = 0$, Eq. (3.4) has a zero root and its characteristic equation reduces to a third-degree equation. It is known that a third-order equation has real roots if its discriminant is negative [7]. It is easy to check that it is negative if

$$H_1 < H < H_2,$$

$$H_{1,2}^2 = -k + \frac{5}{2k} + \frac{1}{8k^3} \pm \frac{1}{8}\left(\frac{1}{k^2} - 8\right)^{3/2}.$$

From these conditions, it follows that $H_{1,2}^2$ is real if $k^2 < 1/8$. Next, from the condition $k\Xi - 1 = 0$, it follows that the height of the suspension must be $h = 0.632R_1$. To eliminate the zero root, it is assumed that $k\Xi - 1 = \mu \ll 1$. Then, the least root of the characteristic equation is roughly equal to $s_1 = \mu/Hk$. The characteristic polynomial is divided by $s - s_1$, and the terms with s_1 to a higher power than the first are disregarded. Eventually, it can be represented as

$$s^3 + (b + s_1)s^2 + (c + bs_1)s + d + cs_1 = 0,$$

where $b = -H$, $c = k + 1/k + \mu/k$, and $d = -Hk$. The roots are real if

$$H_1^2 < H^2 < H_2^2,$$

$$H_{2,1}^2 = -k + \frac{5}{2k} + \frac{1}{8k^3} + \mu\left(\frac{2}{k} + \frac{1}{2k^3}\right)$$

$$\pm \frac{1}{8}\sqrt{\left(\frac{1}{k^2} - 8\right)^3 + \frac{8\mu}{k^2}\left(\frac{1}{k^2} - 8\right)^2}.$$

Thus, characteristic equation (3.4) has a finite domain of stability in parameters k, μ, and H.

4. FINDING THE DOMAINS OF STABILITY

It is assumed that Eq. (3.5) is stable; that is, $k > 0$. The domain of stability is sought from the condition that the roots of (3.4) are real. Equation (3.4) of the fourth degree has three parameters, k, Ξ, and H, which characterize the dimensionless transverse stiffness, dimensionless destabilizing moment, and dimensionless rate of rotation. The domain of stability was found by numerically calculating the roots. First, a value of Ξ was specified and then boundary values of H_1 and H_2 were found such that the roots remained real in some range of k. The sweep in k, Ξ, and H makes it possible to find the domain of stability in terms of these parameters. The results are summarized in Table 1.

The calculation show that there exists a lower bound for Ξ roughly equal to 2.62 ($\Xi = 2.63$, $k = 0.451$, $H_1 = 2.9407$, and $H_2 = 2.9417$ also belong to the domain of stability). For Ξ above this lowest value, there exist finite ranges of k and H that belong to the domain of stability. In Table 1, the largest value of k is taken as close to the upper bound of the domain of stability as possible, while its smallest value is close to the lower bound if $k > 0.01$ at this bound. Near the boundary values of k, those of H_1 and H_2 are almost coincident.

5. ANALYSIS OF A SPECIFIC SYSTEM

By way of example, let us consider a suspension consisting of permanent magnets made from Sm–Co alloy ($j_0 = 600$ kA/m) or 21SA320 strontium ferrite

Table 1. Boundary values of H_1 and H_2 vs. Ξ and k

$\Xi = 2.9$			$\Xi = 3.1$			$\Xi = 3.4$			$\Xi = 4.0$		
k	H_1	H_2	k	H_1	H_2	k	H_1	H_2	k	H_1	H_2
0.333	3.147	3.150	0.220	3.2812	3.2825	0.05	3.473	3.474	0.01	3.850	4.010
0.340	3.149	3.156	0.250	3.289	3.300	0.10	3.482	3.497	0.04	3.852	4.043
0.350	3.152	3.164	0.337	3.303	3.401	0.20	3.495	3.577	0.08	3.854	4.096
0.360	3.154	3.175	0.370	3.386	3.486	0.335	3.790	3.881	0.15	3.858	4.218
0.380	3.159	3.202	0.380	3.520	3.525	0.336	3.805	3.887	0.24	3.863	4.489
0.403	3.198	3.249				0.377	3.826	3.892	0.27	4.017	4.654
0.409	3.257	3.267				0.343	3.927	3.931	0.285	4.758	4.783
$\theta = 70$			$\Theta = 14.0$			$\Theta = 30.0$			$\theta = 60.0$		
0.01	5.235	7.866	0.01	7.465	21.104	0.01	10.949	67.096	0.01	15.490	202.49
0.04	5.236	8.109	0.02	7.465	21.639	0.02	10.949	71.781	0.015	15.490	222.49
0.12	5.236	9.122	0.03	7.465	22.247	0.03	10.949	78.821	0.018	223.652	243.51
0.15	7.586	9.869	0.05	7.465	23.789	0.035	66.511	84.592	0.0187	251.89	252.18
0.16	10.193	10.301	0.07	7.465	26.214	0.037	87.007	88.231			
0.161	10.325	10.361	0.08	28.425	28.541	0.0374	89.130	89.253			

Table 2. Parameters of the magnets and top

$j_1, j_2,$ kA/m	$d_2,$ mm	$m_{max},$ g	$m_1,$ g	$m_2,$ g	$R_2,$ cm	$A,$ g cm^2	$C,$ g cm^2	$L,$ cm	Ξ	k	H_1, H_2	$f,$ Hz
600	16	395	8.2	375	9.97			4.99	0.92	Unstable		
600	10	154	3.2	140	6.1			3.05	1.50	"		
600	5	39	0.8	30	2.82	59.6	119	1.41	3.25	0.26, 0.28	3.41–3.47	5.06–5.15
250	20	32	8.6	20	2.30	37.3	57.2	1.14	7.3	0.13, 0.14	5.66–10.03	12.2–21.6
250	16	21	5.5	12	1.78	16.5	20.8	0.97	8.6	0.10, 0.11	5.83–12.28	16.5–34.8

($j_0 = 250$ kA/m) and a Plexiglas inert mass (top) of density 1.2 g/cm^3 (Table 2). The diameter and height of the lower magnet are taken to be 55 and 15 mm (Sm–Co) or 100 and 15 mm (strontium ferrite), respectively. The respective heights of the suspended magnet and cylindrical inert mass are taken to be 5 mm and 1 cm. Our aim is to calculate the maximal lift (and the corresponding maximal mass m_{max} that can be held in place) and the mass m_1 of the suspended magnet for its different diameters d_2. Let inertial mass m_2 be such that the sum of this mass and the mass of the magnet is somewhat smaller than the maximal value. We start with calculating the radius R_2 of the inertial mass, inertia moments, reduced radius L, and (knowing the reduced radius) Ξ. From found Ξ and Table 1, one can judge whether the domain of stability is reached, as well as find permissible values of k and the range of rotation frequencies where the suspension is stable. In Table 2, for those values of Ξ belonging to the domain of stability, two values of k are shown at which the allowable range of rotation frequencies is rather wide. The calculated range of rotation frequencies, which is common for both k, is given in both dimensionless ($H_{1,2}$) and dimensional form (f, Hz).

From Table 2, it follows that, when the diameter of the upper Sm–Co magnet equals 10 and 16 mm, $\Xi < 2.62$ and the suspension is unstable. When the diameter of this magnet is 5 mm, the system becomes stable in a narrow range of large k. For the case of the strontium ferrite magnets (the diameter of the lower magnet is larger than in the case of the Sm–Co magnets), the destabilizing moment has a moderate value ($\Xi = 7.3$ and 8.6) and the system is stable in an appreciably wide range of rotation frequencies and at a not too low transverse stiffness.

CONCLUSIONS

Martynenko [3] demonstrated that the Earnshaw prohibition for stable confinement of a charge in the field of other charges may be removed by introducing a magnetic field. The Lorentz force arising in this case acts like gyroscopic forces. Stabilization is possible if the degree of instability is odd. Accordingly, the signs and arrangement of the charges are taken such that dis-

placements along the axis of the charges will be stable and those in two transverse directions unstable. In our case, the situation is similar, while somewhat more complicated. For two magnets with their like poles facing each other, axial displacements are stable and transverse displacements are unstable. However, instability in two angles is added in this case. The angular instability is removed by conventional means (gyroscopically, i.e., by rotation of the top). Unlike [3], "gyroscopic forces" here act in angular, rather than in transverse translational, coordinates. The feasibility of such stabilization is proved in this work. It is of fundamental importance that the transverse instability can be removed by rotation only if the angular instability takes place. It is easy to find an arrangement of the magnets such that the stabilizing, instead of the destabilizing, moment arises in the presence of the transverse instability. It suffices to interchange their positions and match the orientations of the fields. In such a system, stabilization by rotation is impossible.

ACKNOWLEDGMENTS

REFERENCES

1. I. E. Tamm, *The Principles of Electricity Theory* (Nauka, Moscow, 1976) [in Russian].

2. R. V. Lin'kov and M. A. Miller, in *Physics Encyclopedia* (Sov. Éntsiklopediya, Moscow, 1990), Vol. 2, p. 216 [in Russian].

3. Yu. G. Martynenko, Sorosovskiĭ Obrazovatel'nyĭ Zh., No. 3, 82 (1996).

4. G. G. Denisov, Izv. Ross. Akad. Nauk, Mekh. Tverd. Tela, No. 2, 183 (1998).

5. I. V. Veselitskiĭ, V. S. Voronkov, and S. A. Sigun'kov, Zh. Tekh. Fiz. **66** (5), 152 (1996) [Tech. Phys. **41**, 488 (1996)].

6. L. D. Landau and E. M. Lifshitz, *Course of Theoretical Physics*, Vol. 1: *Mechanics* (Nauka, Moscow, 1982; Pergamon, New York, 1988).

7. N. N. Bronshtein and K. A. Semendyaev, *Handbook of Mathematics* (Nauka, Moscow, 1986; Springer-Verlag, New York, 1997).

Translated by V. Isaakyan

BRIEF COMMUNICATIONS

Macrolocalization of Plastic Strain in Creep of Fine-Grain Aluminum

V. I. Danilov*, S. V. Konovalov, S. V. Zhuravleva**, L. B. Zuev*, and V. E. Gromov****

* Institute of Strength Physics and Materials Science, Siberian Division, Russian Academy of Sciences,
Akademicheskiǐ pr. 2/1, Tomsk, 634021 Russia
e-mail: dvi@ispms.tsu.ru
** Siberian State Industrial University, Novokuznetsk, 654080 Russia
Received May 28, 2004; in final form, July 20, 2004

Abstract—The evolution of the plastic strain macrolocalization pattern in low-temperature creep of commercial purity aluminum is studied. The localization pattern depends on a stage in the creep curve. At the stage of steady-state creep, localization zones propagate in the form of a wave traveling with a velocity proportional to the rate of buildup of the total strain. It is found that the volumes where the creep and strain localization wave propagation are activated equal each other. Based on estimates of the activation volumes, it is shown that the velocity of plastic strain localization waves is governed by thermally activated dislocation movement. © 2005 Pleiades Publishing, Inc.

INTRODUCTION

Macroscopic localization of plastic flow, which is observed throughout the process from the yield point to failure, may develop as a self-excited phase wave [1–4] when equidistant plastic flow zones move with a uniform velocity along an object under load. This type of localization was first discovered at the stage of linear hardening [1] in stretching of Cu–Ni–Sn single-crystal alloy in the state of supersaturated solid solution. Later, self-excited phase waves of strain macrolocalization at the stage of linear hardening under dynamic loading were observed in pure single-crystal and polycrystalline metals and alloys with different crystal structures. A dispersion relation for these waves was derived, and the dependence of their velocity on the strain hardening coefficient was found [2–4]. However, strain localization under other test conditions, e.g., under creep, has not been studied (the only exception is our work [5]).

Results of creep tests contain more information and, specifically, make it possible to determine the type and activation parameters of micromechanisms underlying plastic flow from macroscopic measurements [6]. In this work, an attempt is made to reveal the type of strain macrolocalization under creep.

EXPERIMENTAL

The specimens used were recrystallized A85 commercially pure aluminum crystals (for their chemical composition, see the table). Planar specimens, double blades with operating part dimensions of $40 \times 6 \times 1.8$ mm, were stamped out from cold-rolled sheets and then subjected to recrystallization annealing at 775 K for 2.5 h. The specimens recrystallized had grains of size $D = 75 \pm 8$ μm, and their conventional yield strength was $\sigma_{0.2} = 53 \pm 7$ MPa.

Creep tests were carried out on an Instron-1185 testing machine at different stress levels σ. From the time of load application on, the general elongation $\varepsilon(t)$ of the specimen as a function of time was monitored. Concurrently, the displacement vector (**r**) field for points on the surface of the specimen being deformed was recorded by the method of speckle interferometry [7]. Speckle images were taken in strain increments of 0.2%.

Numerically differentiating displacement field **r**(x, y) with respect to coordinates, one can obtain the components of the plastic strain tensor in the plane stress state (for details, see [3]). Here, we will keep track of local elongation ε_{xx} along the axis of tension, which is the most suitable component for studying the distribution of plastic flow macrolocalization and, at the same time, carries much information. The distributions

Chemical composition of the aluminum specimens studied in this work (wt %)

Si	Fe	Pb	Ga	Zn	V	Ti	Ni	Mn	Mg	Cu	Al
0.15	0.07	0.016	0.01	0.008	0.005	0.0035	0.0035	0.0025	0.002	0.0014	Remainder

of other important components (shear ε_{xy} and rotation ω_z) are much more complicated.

RESULTS AND DISCUSSION

We analyzed the creep curves shown in Fig. 1, which were obtained at stresses of 64.8, 62.5, and 60.2 MPa. The curves have three characteristic stages [7]. Fitting of the curves (Fig. 1, curve a, $\sigma = 64.8$ MPa) shows that $\varepsilon(t)$ can be approximated as $\varepsilon = 2 \times 10^{-2} \ln t + 0.2$ for the unsteady stage and as $\varepsilon = 5 \times 10^{-4} t + 0.25$ for the steady stage. Such behavior is consistent with the conventional concepts of creep [8]. Further on, we will concentrate on the steady stage, where the creep rate is constant, $\dot{\varepsilon} = \text{const}$, and is convenient to compare with the parameters of local strain distribution evolution.

At the steady stages of creep, the distributions of the component ε_{xx} of the plastic strain tensor over the specimen turned out to be periodic for all the stresses. These distributions are similar to the patterns observed at the stage of linear strain hardening under dynamic loading [1–4] (Fig. 2). At each time instant, the plastic strain is localized within particular equidistant zones of the specimen. Regions adjacent to the strained zones remain virtually intact (unstrained). The spatial period (the wavelength λ_{se} of the self-excited wave) of the set of localization zones remained constant throughout the stage of steady creep, 3.5 ± 0.5 mm. It did not change either when the applied stress was varied. The same pattern was observed earlier [5], but the wavelength of the self-excited wave in that work was 6.0 ± 1.0 mm.

The analysis of the local elongation distributions showed that the velocity of the localization maxima at the steady stage is uniform. For each of the stresses, the velocities of the localization zones were determined by the technique used in [3]; that is, the positions of the localization zones, x, were plotted against deformation time (Fig. 3). For each of the maxima of ε_{xx}, such a dependence is a straight line, the coefficients of correlation between t and x being no less than 0.99. From the slope of these straight lines, one can find the velocity of macrostrain localization zones (the velocity of the self-excited wave); from the spacing between the zones, the wavelength λ_{se} of the self-excited wave. It became obvious that traveling self-excited waves of macrostrain localization arise at the steady stages of creep, which are similar to those observed at the stages of linear hardening under dynamic loading.

For the stress interval studied, it is established that the velocity of the self-excited waves is a linear function of the creep rate at the stage of steady creep (Fig. 4). Earlier [5], this fact was observed for self-excited waves with one-order-of-magnitude-lower velocities, so that our findings correlate with the results of that work. The quantitative difference between them stems from the fact that, in [5], the experiments were performed on Al specimens with a grain size of
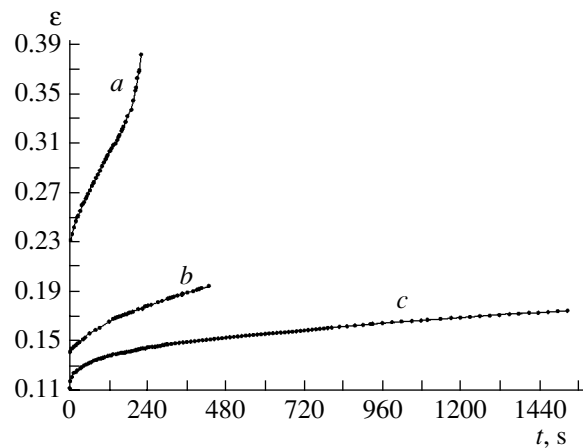

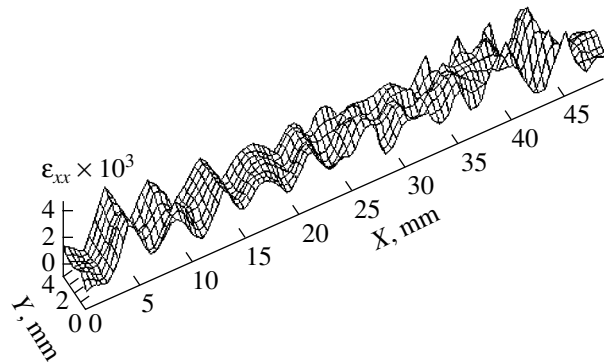**Fig. 1.** Creep curves obtained at (a) 64.8, (b) 62.5, and (c) 60.2 MPa.

Fig. 2. Local elongation distribution over the specimen at the steady stage of creep. $\sigma = 62.5$ MPa, $\varepsilon = 0.172$.
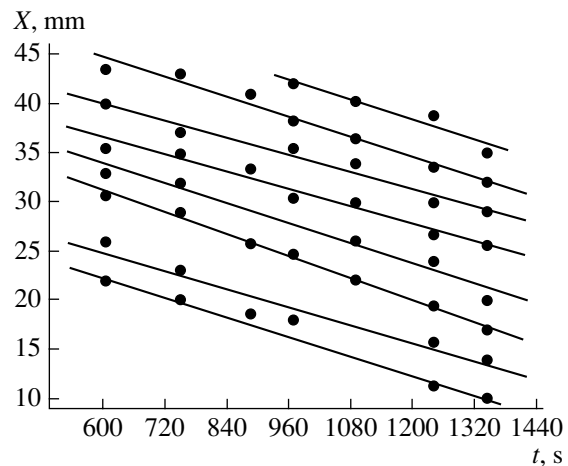

Fig. 3. Dynamics of strain localization zones at the linear stage of creep for the Al specimens at $\sigma = 60.2$ MPa.

≈ 10 mm. Because of this, the level of deforming stresses decreases by a factor of 1.5–2.0; accordingly, the creep rate is an order of magnitude lower. Moreover, the wavelength of the self-excited wave usually
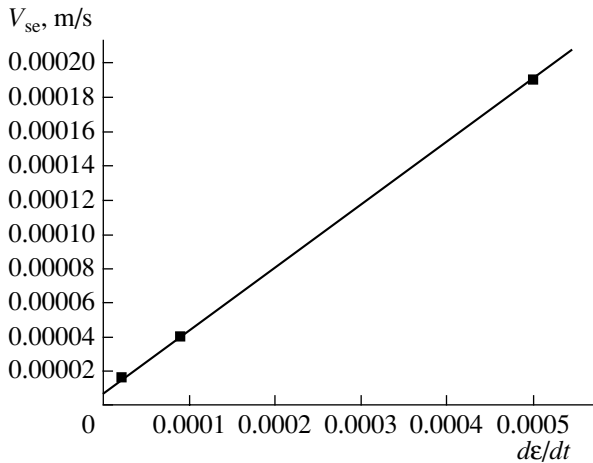
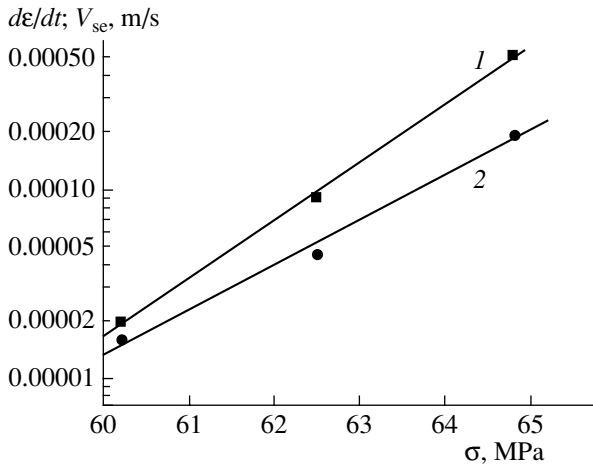**Fig. 4.** Velocity of the self-excited waves vs. creep rate at the steady stage.

Fig. 5. (*1*) Creep rate and (*2*) strain localization wave velocity under different stresses.

grows in coarser grains. The dependence $\lambda_{se}(D)$ for Al under dynamic loading was investigated in a wide range of D [3], and it was found that $\lambda_{se} \sim \ln D$ for $D > 50$ μm.

The proportionality between the velocity of self-excited waves and the creep rate suggests that the micromechanisms behind creep and propagation of self-excited strain localization waves are identical. It is known [8] that creep in metals is governed by thermally activated motion of dislocations and the creep rate is given by the kinetic relationship

$$\dot{\varepsilon}_c = \dot{\varepsilon}_\infty \exp\left(-\frac{U_c - \gamma_c \sigma}{kT}\right), \tag{1a}$$

where U_c is the activation energy of creep; $\dot{\varepsilon}_\infty$ = const; k is the Boltzmann constant; T is the temperature; and γ_c is the force constant [9], which is represented as the

product of the true volume of activation and the coefficient of atomic bond overstress. With this coefficient, average stresses can be converted to local stresses acting at the site of a thermal fluctuation event.

In fact, in coordinates $\ln\dot{\varepsilon}-\sigma$, the curve $\dot{\varepsilon}(\sigma)$ is approximated well by straight line *1* in Fig. 5. At the steady stage of creep, the V_{se} versus σ dependence is approximated by curve *2* in Fig. 5,

$$V_{se} = V_0 \exp\left(-\frac{U_{se} - \gamma_{se}\sigma}{kT}\right), \tag{1b}$$

where V_0 = const.

From the slope of straight lines *1* and *2*, one can estimate the values of γ_c and γ_{se} for creep and propagation of self-excited localization waves, respectively,

$$\gamma = kT\frac{\partial}{\partial\sigma}(\ln\dot{\varepsilon}). \tag{2}$$

The values $\gamma_c = 2.9 \times 10^{-26}$ m^3 and $\gamma_{se} = 2.2 \times 10^{-26}$ m^3 estimated with (2) are close to each other but differ from those obtained in [5] for coarse-grain Al.

According to [10], low-temperature creep (below 400 K for Al) proceeds via dislocation glide in a set of local obstacles (stoppers) that are overcome by thermal activation. In this case, $\gamma = bdl$ [9, 10], where b is the Burgers vector. If a stopper is $d \approx b$ across, one can assume that the overstress coefficient is proportional to the length l of a dislocation loop unpinned by thermal activation. In Al, $b = 0.286$ nm [10], and so $l \approx \gamma/b^2 \approx 270$ nm. The order of l can be estimated from the mean spacing between dislocations of a forest, $l \approx \rho^{-1/2}$, which act as pinning centers, at a reasonable dislocation density ($\rho \approx 1.5 \times 10^9$ cm^{-2}).

The coincidence of force constants γ_c and γ_{se} of the micromechanisms responsible for the creep rate and the propagation velocity of self-excited waves of plastic flow localization is hardly accidental. In a number of works [3, 11], we studied the velocity of plastic flow localization waves as a function of the coefficient of linear strain hardening under dynamic loading. It was found that this velocity depends on the ratio between the densities of mobile and sessile dislocations, as well as on the characteristic size of the dislocation structure being formed. Thus, the dislocation mobility plays an important part under both dynamic loading and creep. In the latter case, its effect seems to be more distinct.

CONCLUSIONS

(1) Plastic strain is macroscopically localized under creep as well. At the stage of steady creep, the wave pattern of strain localization is observed, which is generally similar to the pattern at the stage of linear hardening under dynamic loading.

(2) The velocity of localized plastic flow waves varies in proportion to the rate of steady creep.

(3) The coincidence of the activation volumes estimated from the stress dependences of the creep rate and self-excited wave velocity suggests that both creep and self-excited wave propagation have a dislocation nature.

REFERENCES

1. L. B. Zuev, V. I. Danilov, and V. V. Gorbatenko, Zh. Tekh. Fiz. **65** (5), 91 (1995) [Tech. Phys. **40**, 456 (1995)].

2. S. A. Barannikova, Zh. Tekh. Fiz. **70** (10), 138 (2000) [Tech. Phys. **45**, 1368 (2000)].

3. L. B. Zuev, V. I. Danilov, and B. S. Semukhin, Usp. Fiz. Met. (Ukr.) **3**, 237 (2002).

4. V. I. Danilov, S. A. Barannikova, and L. B. Zuev, Zh. Tekh. Fiz. **73** (11), 69 (2003) [Tech. Phys. **48**, 1429 (2003)].

5. V. I. Danilov, A. A. Yavorskiĭ, and L. B. Zuev, Izv. Vyssh. Uchebn. Zaved. Fiz., No. 4, 5 (1991).

6. A. J. Kennedy, *Processes of Creep and Fatigue in Metals* (Oliver & Boyd, Edinburgh, 1962; Metallurgiya, Moscow, 1965).

7. L. B. Zuev, S. N. Polyakov, and V. V. Gorbatenko, Proc. SPIE **4900**, 1197 (2002).

8. V. M. Rozenberg, *Creep of Metals* (Metallurgiya, Moscow, 1967) [in Russian].

9. V. P. Regel', A. L. Slutsker, and É. E. Tomashevskiĭ, *The Kinetic Nature of Hardness in Solids* (Nauka, Moscow, 1975) [in Russian].

10. R. W. K. Honeycombe, *The Plastic Deformation of Metals* (Arnold, London, 1968; Mir, Moscow, 1972).

11. L. B. Zuev, Ann. Phys. **10**, 966 (2001).

Translated by V. Isaakyan

BRIEF
COMMUNICATIONS

Generation of Autonomous Long-Lived Plasma Objects in Free Atmosphere

L. V. Furov

Vladimir State University, Vladimir, 600000 Russia
e-mail: golovn@vpti.vladimir.ru
Received October 23, 2003; in final form, June 16, 2004

Abstract—Results are presented from experimental studies of autonomous long-lived plasma objects in free atmosphere with a visible afterglow lasting 2 s. The experimental setup is described, and the energy conditions ensuring the generation of such plasma objects are determined. © *2005 Pleiades Publishing, Inc.*

INTRODUCTION

Studies of long-lived plasma objects (LPOs) are mainly related to the problem of ball lightning (BL). This problem has been actively studied over a long time both theoretically and experimentally [1–12].

Studies of LPOs that are remote from both the discharge chamber wall and energy sources are important for understanding the nature of BL, testing lightning protection systems, plasma chemistry, creating high-power pulsed open sources of optical radiation, and accumulation and transportation of electromagnetic energy.

Experimental studies aimed at generating plasma objets possessing some properties of BL (shape, size, color, velocity, lifetime, and decay) under laboratory conditions are reviewed in [13]. There are various means for generating LPOs: an erosion discharge [14, 15], a capillary discharge [16, 17], a microwave discharge and its modifications [18], etc. Since natural BLs occur in free atmosphere, most of the experiments were performed with atmospheric air.

Experiments in which the working medium is air saturated with water vapor seem to be the most promising, because such a medium most closely models natural conditions for the origin of BL. Using an erosion discharge, one can produce glowing objects with a diameter of 7–19 cm and lifetime of 0.5–1.0 s [19, 20]. It is shown experimentally that LPO lifetime depends on many parameters: the size and shape of the central electrode, the discharge voltage, the amplitude and duration of the current pulse, and the temperature and conductivity of the water deposited on the electrode [21].

In most experiments, a capacitor bank was used as a power supply (e.g., in [14], the capacitance was varied from 650 µF to 5 mF and the stored energy was varied from 50 to 200 J, while in [15], these quantities were 216 µF and 100 kJ, respectively) and the current pulse duration was a few microseconds. Over such a short

time, an LPO decays before it transforms into a stable structure.

The aim of this study was to produce LPOs with an afterglow time of up to 2 s in free atmosphere at normal pressure. For this purpose, an inductive energy storage unit with a current pulse duration of ~100 ms and high stored energy (of about 500 kJ) was used. No additives to the discharge plasma other than the products of electrode material erosion were used.

EXPERIMENTAL FACILITY FOR GENERATING LPOs

The experimental setup for producing and studying LPOs consisted of four main parts: a power supply, switches, a generator, and a system for monitoring the LPO parameters [12, 22, 23]. A schematic of the experimental setup is shown in Fig. 1. The storage inductance was fed from nine VAKG-12/6-3200 rectifiers connected in parallel. The parameters of the power supply were as follows: the input circuit voltage was 380 ± 38 V, the circuit frequency was 50 Hz, the rated output power was 38.4 kW, the rated rectified current was 3200 A, and the rated rectified voltage was 12 V (mode I)
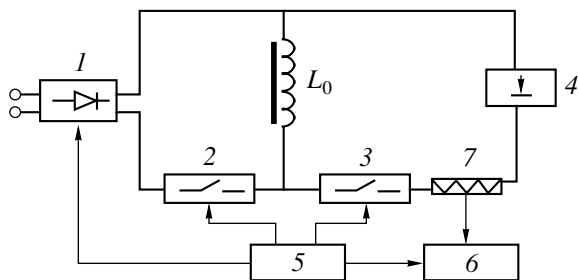

Fig. 1. Schematic of the experimental setup: (*1*) block of nine VAKG-12/6-3200 rectifiers, (*2*) MGG-10-U3 switch, (*3*) VMG-10 switch, (*4*) plasma gun, (*5*) program mechanism, (*6*) recording system, (*7*) 75ShSMUZ shunt, and (L_0) storage inductance.

or 6 V (mode II). Electric energy (about 500 kJ at a feeding current of 3000 A) was stored in the inductive storage with a total mass of 4000 kg. The power circuit was switched by an MGG-10-U3 switch (with a breaking current of 45 kA, turn-on time of ≤ 0.4 s, and clearing time up to arc extinction of 0.14 s) and a VMG-10 switch. LPOs were produced using a plasma gun made of nonmagnetic materials.

The facility operated as follows: After switch *2* was turned on, the storage inductance $L_0 = 6.5 \times 10^{-4}$ H was connected to rectifier bank *1*. When the stored magnetic energy reached a necessary value, the storage inductance was switched to load *4* (plasma gun) by switch *3*. After 0.07 s, switch *2* was turned off and the diaphragm of the plasma gun exploded under the action of the break induced current. The 0.07-s time interval was chosen in order for the diaphragm to remain undestroyed at a feeding voltage of 4 V and, at the same time, for switch *2* to provide a quite reliable contact. The switches, rectifiers, and recording system *6* were controlled by program mechanism *5*. The current in the discharge circuit was measured using shunt *7*.

The main component of the facility was a plasma gun used to generate autonomous LPOs in free atmosphere with an afterglow time of up to 2 s. A schematic of the plasma gun is shown in Fig. 2. The discharge was initiated with the help of 100-mm-diameter conducting diaphragm *4* composed of seven 8-μm Al foils. This number of foils was experimentally shown to be optimal. The diaphragm was placed on dielectric plate *3* (textolite, Plexiglas, cardboard, etc.), to which it was pressed by ring electrode *2*, made of a nonmagnetic material (stainless steel or brass). Electrode *1*, made of two to eight (depending on the experimental conditions) stranded wires with diameters of 1.0–2.4 mm, was connected to the diaphragm center. The opposite ends of the wires were connected (over a circle) to electrode *6*. To reduce the effect of the magnetic field generated by electrode *6* on the formation of LPOs, electrode *6* was placed below the discharge gap, whereas the current was supplied to electrode *5* via guide racks *7*. All the elements were made of nonmagnetic materials and set on support *8*. It was shown experimentally that the use of magnetic materials hindered the formation of stable LPOs; this was indicated by the fact that, in this case, the afterglow time was as short as a few tenths of a second. The design of the gun was rather compact and allowed one to vary the LPO size by changing the inner diameter D of the ring electrode from 60 to 150 mm.

The parameters of the experimental setup and LPO were simultaneously recorded on a UF-67-135 photo paper using a K-115 oscilloscope. Figure 3 shows typical waveforms of the current I, voltage U, and visible radiation intensity P recorded with the K-115 loop oscilloscope. The discharge current was recorded by the oscilloscope indirectly, using the voltage drop across the 75ShSMUZ shunt. The discharge voltage, including the electrode voltage drops, was measured
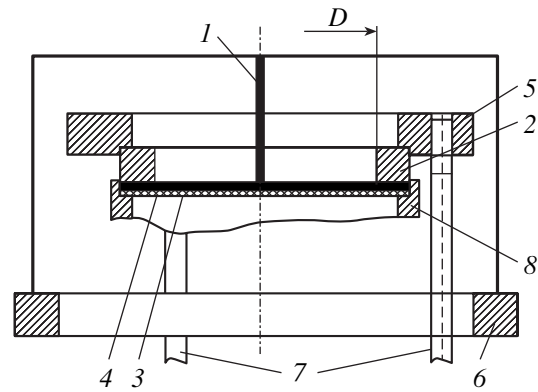

Fig. 2. Plasma gun: (*1*) central electrode, (*2*) ring electrode, (*3*) dielectric plate, (*4*) conducting diaphragm, (*5*, *6*) electrodes, (*7*) guide racks, (*8*) support.
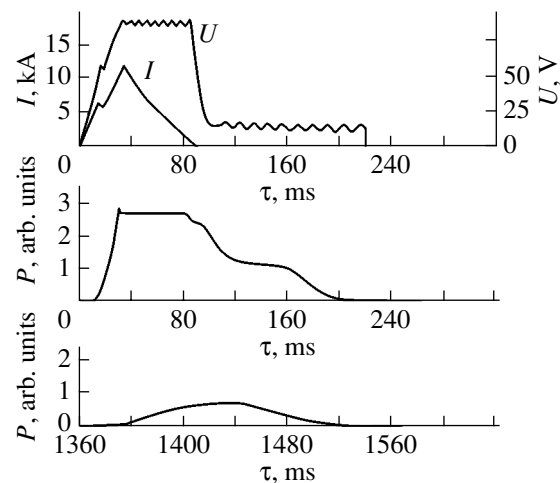

Fig. 3. Waveforms of the discharge current *I*, voltage *U*, and radiation intensity *P*.

between the axial and ring electrodes. The discharge current and voltage were recorded by the oscilloscope with the help of MO14-1200 galvanometers with an accuracy of 5%. The optical characteristics of LPOs were recorded using an AIETs2-S photometer with an F-2 vacuum photodetector. The operating spectral range of the photocathode (at a half-maximum level) was 320–600 nm. Special measurements showed that the time constant of the photometer was no more than 5 ms.

EXPERIMENT

Figures 4 and 5 show photographs of the experimentally obtained autonomous LPOs. The photographs were taken manually from a distance of 4 m on the Kodak-400 color film using a Zenit ET photo camera equipped with an MIR-1V lens (with a relative aperture of 8 and an exposure of 1/125 s). At the bottom of the photographs, parts of the plasma gun can be seen. In the
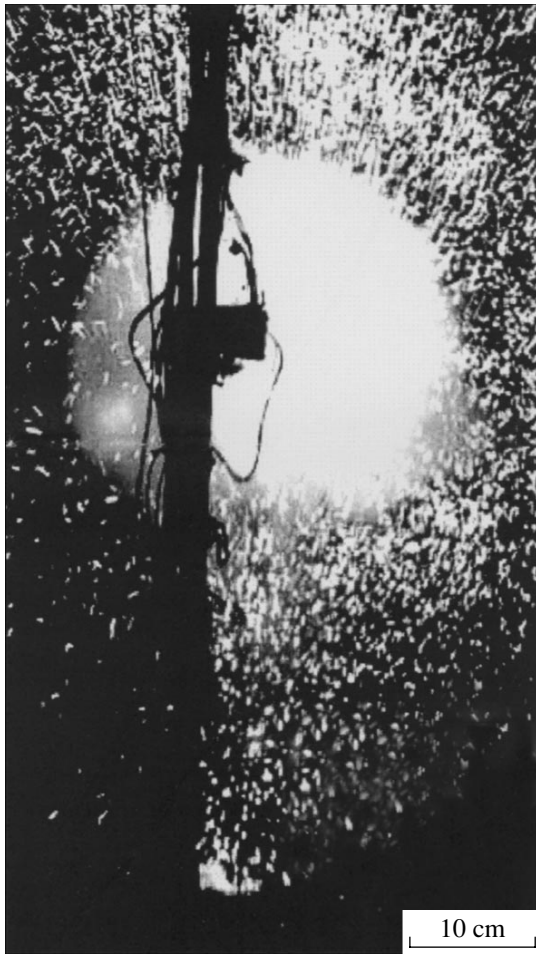
10 cm

Fig. 4. LPO in the initial stage of formation.

Fig. 5. LPO at the end of the formation stage.

initial stage, the LPO has a mushroom shape (Fig. 4), and by the end of the formation process, it transforms into a sphere (Fig. 5) with a diameter of 35–40 cm. It should be noted that the above photographs present the results obtained in different discharges. The dark vertical structure overlapping the periphery of the sphere is the holder of the measurement system. One second after the termination of the energy supply, the distance from the center of the sphere to the plasma gun was 70 cm. In the case at hand, the current amplitude was 10.2 kA and the current pulse duration was 100 ms.

Revealing physical processes responsible for the prolonged afterglow of the observed LPOs is beyond the scope of this study. Note, however, that photometric measurements of the LPO glow showed that the total radiation energy emitted by an LPO exceeds the sum of the thermal energy of particles, the ionization energy, and the energy of phase transformations in the condensed disperse phase. Depending on the experimental conditions, the radiated energy varied from 1.6 ± 0.7 to 10.8 ± 4.4 kJ. Hence, a fraction of the energy might be stored in, e.g., an electromagnetic field; i.e., an autonomous LPO can be regarded as a mirrorless photon trap.
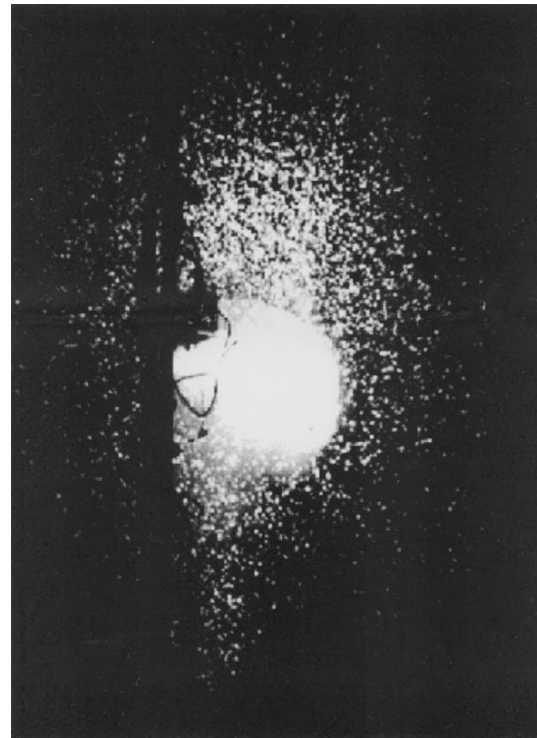
This is confirmed by the fact that, in about one-tenth of the experiments, the LPO glow intensity somewhat increased prior to its decay (a "hump" in the radiation intensity in Fig. 3). Such behavior cannot be explained using a cooling plasma concept.

Experiments showed that there were certain threshold parameters (or critical experimental conditions) under which LPOs arose in free atmosphere and existed for a rather long time. It was found in [19] that the duration of the LPO afterglow depended nonlinearly on the discharge energy (as well as on the discharge current). As a first approximation, the duration of the LPO afterglow on the discharge energy was assumed to be linear and was determined by the least squares method. The intersection of this linear dependence with the abscissa (where the lifetime is zero) gave an energy of 40 kJ, which corresponded to the discharge energy at a current of 10.4 kA. However, there is no sufficient reason to seek for the dependence of the LPO lifetime on the discharge energy in such a form. The actual behavior is more complicated, and the criterion for the formation of LPOs is still unknown. The observed statistical relationship between the LPO lifetime and the deposited electric energy can be regarded as fairly appropriate (the correlation factor is 0.32 for a significance of $\chi^2 = 0.1$). This means that the statistical relationship is determined by a more complicated combination of the parameters, which has yet to be found.

CONCLUSIONS

Experiments on the generation of autonomous LPOs with energy densities comparable to those typical of natural ball lightnings have been carried out. For autonomous LPPs with a diameter of 30 cm and stored energy of 10 kJ, the calculated energy density is ~ 0.7 J/cm^3, which agrees with the data for BLs [9]. In BLs, the energy density varies from 2×10^{-3} to 2×10^2 J/cm^3, the average energy density being relatively low, on the order of 1 J/cm^3.

An analysis of the video and photo information, as well as the waveforms of the glow intensity, shows that it is possible to obtain autonomous LPOs with a diameter of 30–35 cm and a visible afterglow lasting 2 s. Depending on the experimental conditions, the radiated energy varies from 1.6 ± 0.7 to 10.8 ± 4.4 kJ.

REFERENCES

1. A. I. Grigor'ev and T. N. Dunaeva, in *Ball Lightning: Problems, Hypotheses, Discoveries. Bibliographic Index from 1972 to 1992* (Odessa, 1992), Issue 41.

2. I. P. Stakhanov, *On the Physical Nature of Ball Lightning*, Ed. by A. A. Rukhadze and M. M. Fiks (Nauchnyi Mir, Moscow, 1996) [in Russian].

3. B. M. Smirnov, *Problems of Ball Lightning* (Nauka, Moscow, 1988) [in Russian].

4. O. A. Sinkevich, Teplofiz. Vys. Temp. **35**, 651 (1997).

5. O. A. Sinkevich, Teplofiz. Vys. Temp. **35**, 968 (1997).

6. I. M. Imyanitov and D. I. Tikhiǐ, *Beyond the Laws of Science* (Atomizdat, Moscow, 1980) [in Russian].

7. S. Singer, *Nature of Ball Lightning* (Plenum, New York, 1971; Mir, Moscow, 1973).

8. Y.-H. Ohtsuki, H. Ofuruton, N. Kondo, *et al.*, in *Proceedings of the 5th International Symposium on Ball Lightning, Tsugawa-Town, 1997*, p. 167.

9. J. D. Barry, *Ball Lightening and Bead Lightening: Extreme Forms of Atmospheric Electricity* (Plenum, New York, 1980; Mir, Moscow, 1983).

10. V. L. Bychkov, A. V. Bychkov, and S. A. Stadnik, Phys. Scr. **53**, 749 (1996).

11. A. I. Grigor'ev, I. D. Grigor'eva, and S. O. Shiryaeva, Khim. Plazmy, No. 17, 218 (1992).

12. V. N. Kunin, *Ball Lightning on Testing Ground* (Vladimir Gos. Univ., Vladimir, 2000) [in Russian].

13. *Ball Lightning in the Laboratory: Collection of Articles*, Ed. by R. F. Avramenko, V. L. Bychkov, A. I. Klimov, and O. A. Sinkevich (Khimiya, Moscow, 1994) [in Russian].

14. R. F. Avramenko, V. I. Nikolaeva, and L. P. Poskacheeva, in *Ball Lightning in the Laboratory: Collection of Articles*, Ed. by R. F. Avramenko, V. L. Bychkov, A. I. Klimov, and O. A. Sinkevich (Khimiya, Moscow, 1994), pp. 15–56.

15. A. F. Aleksandrov, Yu. Bakhgat, M. G. Skvortsov, *et al.*, Zh. Tekh. Fiz. **56**, 2392 (1986) [Sov. Phys. Tech. Phys. **31**, 1431 (1986)].

16. D. L. Kirko, P. V. Samonchev, and A. A. Martynov, Pis'ma Zh. Tekh. Fiz. **21** (10), 78 (1995) [Tech. Phys. Lett. **21**, 388 (1995)].

17. V. L. Bychkov, A. V. Bychkov, and A. B. Timofeev, Zh. Tekh. Fiz. **74** (1), 128 (2004) [Tech. Phys. **49**, 128 (2004)].

18. V. M. Shibkov, A. F. Aleksandrov, and A. A. Kuzovnikov, in *Ball Lightning in the Laboratory: Collection of Articles*, Ed. by R. F. Avramenko, V. L. Bychkov, A. I. Klimov, and O. A. Sinkevich (Khimiya, Moscow, 1994), pp. 136–150.

19. A. I. Egorov and S. I. Stepanov, Zh. Tekh. Fiz. **72** (12), 102 (2002) [Tech. Phys. **47**, 1584 (2002)].

20. A. I. Egorov and S. I. Stepanov, Preprint No. 2558/2004, PIYaF RAN (St. Petersburg Institute of Nuclear Physics, Russian Academy of Sciences, Gatchina, 2004).

21. G. D. Shabanov, Pis'ma Zh. Tekh. Fiz. **28** (4), 81 (2002) [Tech. Phys. Lett. **28**, 164 (2002)].

22. V. N. Kunin and L. V. Furov, Izv. Vyssh. Uchebn. Zaved. Fiz., No. 6, 119 (1990).

23. L. V. Furov, in *Proceedings of the 12th Scientific Conference of Ukrainian, Russian, and Belarussian Scientists on Applied Problems in Mathematics and Mechanics, Sevastopol, 2003*, pp. 57–61.

Translated by N. Ustinovskiǐ